UNIVERSITY OF SOUTHAMPTON

Faculty of Engineering and the Environment

The Use of Optical Techniques to Assess the Damage Tolerance of Composite Materials

Gary Battams

Thesis for the degree of Doctor of Philosophy

January 2014

UNIVERSITY OF SOUTHAMPTON

ABSTRACT

Faculty of Engineering and the Environment
Materials & Surface Engineering Group

Doctor of Philosophy

THE USE OF OPTICAL TECHNIQUES TO ASSESS THE DAMAGE TOLERANCE OF COMPOSITE MATERIALS

By Gary Battams

Experimental methodologies based on full-field optical techniques for the study of damage in fibre reinforced polymer (FRP) materials, during intermediate strain rate loading and subsequent fatigue loading are established. The methodologies are based on the synchronous use of digital image correlation (DIC) and infra-red (IR) thermography, allowing the collection of full-field kinematic and thermal surface data maps to provide a deeper insight into the damage mechanisms and a new capability for identifying damage in FRP materials and structures.

The study of damage initiation in FRP materials during intermediate strain rate loading requires the application of high speed cameras and the development of a novel loading rig capable of imparting a damaging load that does not fail the material. The rig design is fully validated. The application of DIC on images obtained using high speed cameras is evaluated. New approaches to identify the effect of sensor fill-factor on the accuracy of high spatial resolution DIC strain measurements are devised. Data captured from crossply carbon-epoxy and glass-epoxy specimens demonstrate the capability of combining DIC and IR-thermography in identifying damage during an intermediate strain rate loading event.

A novel semi-automated methodology for the accurate triggering of high resolution white-light and IR images during a fatigue test is described, which allows the synchronous capture of data that enables DIC and thermoelastic stress analysis (TSA) to be applied without the pausing of a cyclic load. The combined methodology is applied to crossply glass-epoxy and carbon-epoxy specimens, identifying various damage types including; transverse cracking, delaminations and longitudinal splitting, verified through the use of X-ray computed tomography (CT).

Finally, future improvements are recommended with an aim of future users applying the optical methodologies to a greater range of loading scenarios and to the study of a greater range of material types and laminate configurations, so informing on the future design of damage tolerant FRP structures.

Contents

List of Figures

List of Tables

Declaration of Authorship

I, *Gary Phillip Battams,* declare that this thesis entitled:

The use of optical techniques to assess the damage tolerance of composite materials

and the work presented in it are my own and has been generated by me as the result of my own original research. I confirm that:

1. *This work was done wholly or mainly while in candidature for a research degree at this University;*
2. *Where any part of this thesis has previously been submitted for a degree or any other qualification at this University or any other institution, this has been clearly stated;*
3. *Where I have consulted the published work of others, this is always clearly attributed;*
4. *Where I have quoted from the work of others, the source is always given. With the exception of such quotations, this thesis is entirely my own work;*
5. *I have acknowledged all main sources of help;*
6. *Where the thesis is based on work done by myself jointly with others, I have made clear exactly what was done by others and what I have contributed myself;*
7. *Parts of this work have been published (Appendix A)*

Signed:

Date:

Acknowledgments

I would like to thank my supervisors Professor Janice Dulieu-Barton and Dr Stephen Boyd for their support and advice throughout the PhD. I would also like to thank Duncan, Richard and Andy for putting up with my continuous questioning.

I would like to recognise the financial support provided by the Defence Science and Technology Laboratory (Dstl) and the Engineering and Physical Sciences Research Council (EPSRC).

Special thanks go to Ms Laura Jones for her advice throughout the project along with the members of the industrial advisory board. I am also very grateful for the technical support provided by Dr David Hollis (LaVision), Dr Richard Burguete (Airbus) and Professor Fabrice Pierron.

I would like to thank everyone in the EDMC and ISVR Electronics workshops for their technical support and advice at many times during the PhD. Thanks also go to Marcela and Paul for going out of their way to help in times of computer trouble.

Thanks go to my parents for all the support that they have given, especially when urgent electronics advice was required!

Thanks go to all the friends that I have made during my PhD; Marco, George, Shufeng, Rachael and Wei, not to mention Andy, Jay and Jim for the many good times had. Similarly, thanks to SUENS hockey for being the most awesome hockey team in the world….HONK!

Special thanks go to Kirsty and Sarah for their support during the final stages of thesis writing.

Finally, I would like to thank Kirsty for all her support during my PhD, for putting up with me being away from her for so long and just for being generally awesome.

Notation

Δ	a change
$\cdot$	a rate of change
α	Coefficient of Thermal Expansion
β_x, β_y	Scale Factors Relating the Pixel Size to Actual Surface Dimensions
ΔZ	Out of Plane Motion
ϵ	Emissivity
ε	Strain
$\varepsilon_{x,y,z}$	Strain tensor
$\varepsilon_{xx}(m,n)$	Transverse Strain at Grid Position (m,n)
η_{yx}	Shear coupling coefficient
$\eta(x,y)$	Displacement mapping (shape) function (x-direction)
θ	Ply Fibre Angle away from vertical axis
$\theta_{x,y,z}$	Rotation Angle From the Global Coordinate Axes
Λ	Correlation Value
λ	Wavelength
λ_1, λ_2	Wavelength detection limits of the Photodetector
ν	Poisson's Ratio
$\xi(x,y)$	Displacement mapping (shape) function (y-direction)
ρ	Mass Density
$\sigma_{x,y,z,}$	Stress Tensor
σ_{ij}	Stress Tensor
τ	Shear Stress
Φ	Radiant Energy
Φ_b	Radiated Energy of a Black Body
A	Surface Area
B	Stefan-Boltzmann Constant
c	Speed of Light
C_p	Specific Heat at Constant Temperature
C_ε	Specific Heat at Constant Strain
d	Laminate Thickness
D	Damage Parameter
D_{macro}	Macroscopic Damage Parameter
D_{micro}	Microscopic Damage Parameter
E^0	Young's Modulus for the Undamaged Material
E^D	Young's Modulus for Damaged Material
f	Focal Length
F	Load
F_c	Cut-off Frequency
V_f	Volume Fraction
F_g	Gauge Factor of the Strain Gauge
g	Step Size
$G_c^{(1)}$	Plane-strain mode 1 toughness of the 0° layer
$G_c^{(i)}$	0/90 Interface Toughness
G_d	Energy release rate for the deflection crack path into a 0/90 interface
G_p	Energy release rate for a penetrating crack into neighbouring 0° piles
h_s	Heat Transfer Coefficient
h	Planck's Constant

$H_{(u,v)}$	Image Data in the Frequency Domain
k	Boltzmann's Constant
k_{th}	Thermal conductivity
K_1, K_2	Thermoelastic Constants
l	Specimen Length
l_o	Original Specimen Gauge Length
(M, N)	Pixel locations within a subset in the vertical and horizontal directions
N	Number of Photons Emitted Per Unit Area for a Real Surface
N_b	Number of Photons Emitted Per Unit Area for a Black Body
$P(x_0, y_0)$	Subset Centre
Q	Heat
$\dot{Q}_{conv}$	Convective Heat Dissipation
$\dot{Q}_{cond}$	Conductive Heat Dissipation
r	Maximum Expected Error of Displacement Vector
R	Rotation Matrix
r_{abs}	Absolute Displacement Error
t	Time
T	Absolute Temperature
T_0, T_m	Absolute Mean Background Temperature
T_s	Temperature at the Area of Heating
$t_{x,y,z}$	Camera Translation Vector
u, v, z	Displacements in horizontal, vertical and out of plane directions
u_x, u_y, v_x, v_y	First Order Displacement Gradients of the Reference Subset
V	Velocity of Deformation
$v_x(m,n)$	The x Component of the Displacement Vector for the Cell Located at Grid Location (m,n)
$X_{S\ measured}$, $Y_{S\ measured}$	Locations of a Dot in acquired calibration images in the horizontal and vertical locations
$X_{S\ model}$	Dot location using a pinhole camera model
$\gamma_{x,y,z}$	Engineering Shear Strain tensor
Z	Object to Camera Distance
(C_x, C_y)	Coordinate Positions of the Centre of the Image Plane
(X_s, Y_s)	2D Sensor Coordinate Systems
(X_W, Y_W, Z_W)	3D Global Coordinate System

Abbreviations

ACK	Aveston, Cooper and Kelly Theory
ADC	Analogue to Digital Converter
APS	Active Pixel Sensors
ASTM	American Society for Testing and Materials
AVT	Allied Vision Technologies
BNC	Bayonet Neill-Concelman
CCD	Charge Coupled Device
CFRP	Carbon Fibre Reinforced Polymer
CLT	Classical Laminate Theory
CMOS	Complementary Metal Oxide Semiconductor
CT	Computed Tomography
CTOD	Crack Tip Opening Displacement
DAQ	Data Acquisition
DENT	Double Edge Notched Tensile (specimen)
DIC	Digital Image Correlation
DL	Digital Level (Units)
DSTL	Defence Science and Technology Laboratory
EPSRC	Engineering and Physical Sciences Research Council
ESPI	Electronic Speckle Pattern Interferometry
FAA	Federal Aviation Authority
FE	Finite Element
FEA	Finite-Element Analysis
FFT	Fast Fourier Transform
FPF	First Ply Failure
FRP	Fibre Reinforced Polymer
GFRP	Glass Fibre Reinforced Polymer
IR	Infra-Red
IRT	Infra-Red Thermography
LED	Light Emitting Diode
LSM	Least Squares Method
LVDT	Linear Voltage Displacement Transducer

NDE	Non Destructive Evaluation
NUC	Non-Uniformity Correction
PC	Personal Computer
PIV	Particle Image Velocimetry
PMMA	Poly(Methyl MethAcrylate)
PPT	Pulse Phased Thermography
RAM	Random-Access Memory
RMS	Root Mean Square
SEM	Scanning Electron Microscope
SHPB	Split Hopkinson Pressure Bar
SSD	Sum of Squared Difference
TSA	Thermoelastic Stress Analysis
TTL	Transistor-Transistor Logic
UTS	Ultimate Tensile Strength
VHS	Very High Speed
ZNCC	Zero normalised cross correlation

Chapter 1

Introduction

1.1 Background and Motivation

Fibre reinforced polymer (FRP) composites are a class of materials that were first used in structural roles during the 1940's with the development of polyester and epoxy based polymers. Their ability to form complex shapes led to their use in the manufacture of air ducts for aerospace applications [1]. With the development of materials such as aramids and carbon fibre reinforced polymer (CFRP), FRP composites have been used for the manufacture of a vast range of structural components due to their unique combination of material properties that often cannot be matched by simple monolithic materials [2]. FRP composites typically possess a high specific strength and stiffness, good environmental resistance and the ability to tailor material properties through the careful design of the laminate stacking sequence [2]. FRP's comprise of fibrous reinforcement within a polymer based matrix. The fibres typically have high strength and stiffness along their major axis under tension. The infusion of a polymer matrix creates a method of strain transfer between fibres, providing cohesion and determining much of the FRP's strength during compression and shear. The polymer also provides much of the environmental resistance of the final laminate. For these reasons, the final FRP composite has properties that are far superior to the constituent parts alone.

Even in the usually conservative civil aerospace sector there has been a rapid growth in the use of FRP composites, as shown in Figure 1 [3]. Where weight is at a premium, modern airframes, such as the Airbus A350 and the Boeing 787 Dreamliner, use high proportions of FRP material (up to 50% by weight). This leads to significant improvements in structural efficiency, and hence decreased fuel usage and cost savings.

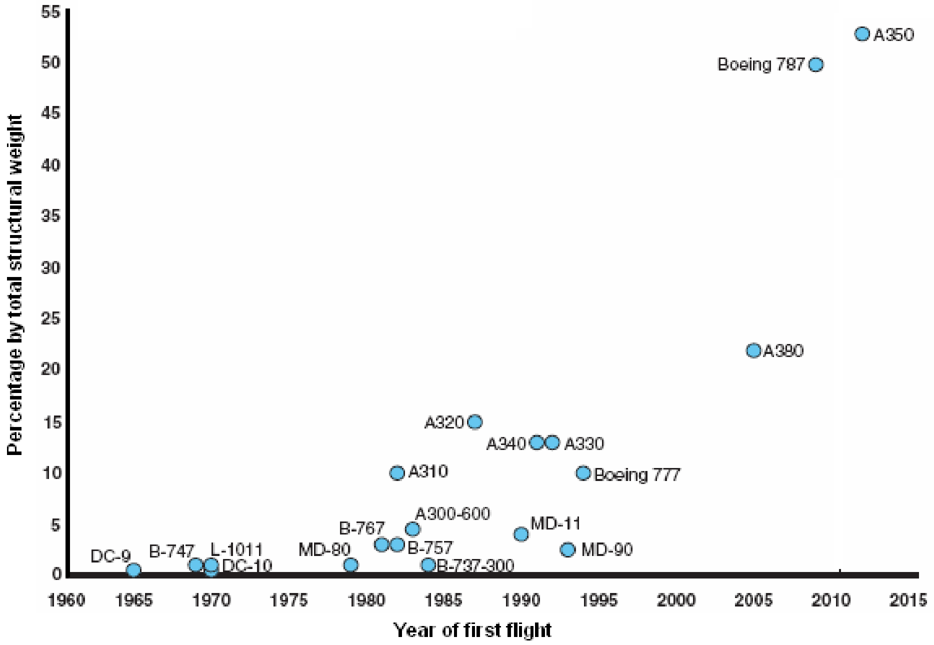

Figure 1: Increasing use of composite materials in civilian aircraft [4]

The quasi-static behaviour of FRP materials has been well studied [2] but their material responses at increased strain rates are less well defined, making it difficult for a designer to achieve a damage-tolerant design across all strain rates likely to be encountered [5]. Structural components are most often designed using material data collected at low strain rates (~10^{-4} s^{-1}), but intermediate (~1 s^{-1}) and high strain rate (>180 s^{-1}) loading often occur during service [6]. Instances may include a bird strike or hail impact on a wing leading edge, an explosive blast near a military vehicle or slamming encountered by small vessels in rough seas. Even a dropped tool during servicing may cause localised high strain rate loading.

One of the first applications of carbon FRP laminates was the use of *Hyfil* for composite fan blades on the Rolls-Royce RB-211 engine in the late 1960's. Much time and money were spent developing the blades to give weight savings and increased efficiency. However, during high strain rate testing (bird strike tests) the blades were found to fail in an extremely brittle manner and consequently, had to be redesigned using more conventional titanium [7]. Lack of understanding in the damage tolerance of such FRP structures (along with other factors) pushed the company to the verge of bankruptcy [8]. Although much work has since been carried out in the field, damage tolerance and the non-destructive evaluation

(NDE) of impact damaged FRP structures still remain key areas of research. A 2011 report investigating the Federal Aviation Authority's (FAA's) actions on the safety of composite aircraft highlighted four main safety concerns [4]. The first concern relates to a lack of standardisation in composite materials and the repair procedures employed, whilst the second highlights a need for greater worker training in dealing with aircraft manufactured from FRP materials, specifically in the repair and avoidance of damage. The third concern describes a current lack of information on FRP behaviour after damage due to a lack of in-service performance data. The fourth and final concern highlights the challenge in detecting and characterising damage in composite structures due to a lack of suitable NDE techniques. It is envisaged that the methodologies established in the thesis will help to address the third and fourth concerns through the development of NDE techniques for the study of damage in FRP components which could be used in the future for the analysis of real FRP components, helping to build confidence in the use of composite components through a greater understanding of damage evolution processes.

Many NDE and optical measurement techniques rely on digital imaging and specifically the charge-coupled device (CCD) or complementary metal oxide sensor (CMOS) sensors upon which they are based. Such sensor technology has developed rapidly in the last three decades giving improved sensitivity, higher frame rates and cheaper devices, so driving the growth of optical measurement techniques for material characterisation. Such techniques will typically apply an algorithm to a set of digital images and extract material data such as displacement, strain or stress from the spatial or intensity information captured within the image or image set. The resultant 'full-field' map of data contrasts with point measurement techniques such as strain gauges or thermocouples which typically give a single data point. One of the major advantages of such optical techniques is that they do not interact with the material/component/structure under investigation. Benefits are also gained by the number of data points available across a surface, giving a greater field of view and generally a finer spatial resolution than point measurements.

The current work uses the recent advances in imaging technology to develop an experimental methodology capable of capturing FRP behaviour as damage initiates during intermediate strain rate loading and to study how such damage subsequently propagates during simulated in-service loading. Intermediate strain rate loading is applied using an Instron very high speed (VHS) 80/20 servohydraulic test machine, specifically designed for the application of loads at high velocity. High speed white-light imaging combined with digital image correlation (DIC) is used to measure surface deformations and strains whilst a high speed infra-Red (IR) detector is used to measure surface temperatures during such intermediate strain rate tests. By using the two techniques it is envisaged that their synchronous application will provide a greater insight into the material behaviour, with greater confidence than a single technique alone. The thermoelastic stress analysis (TSA) technique, capable of providing full-field data related to the surface stress state, is also used to study the damage propagation behaviour of damaged FRP material combined with the DIC technique.

The thesis is part of a larger research project at the University of Southampton, funded by the Engineering and Physical Sciences Research Council (EPSRC) and the Defence Science and Technology Laboratory (DSTL), entitled ‘Full-field data-rich experimental approaches to explain composite material and structural performance and its damage tolerance’. Motivation for the project arises from the need for greater understanding of the behaviour of FRP materials subjected to intermediate strain rate events and the effect on structural performance. The project involves the work of two post-doctoral researchers and three post-graduate researchers. A flow diagram summarising each project and the interactions between researchers is presented in Figure 2. A description of each researcher’s role is shown in blue, whilst major work outcomes from a researcher or multiple researchers are shown in red. The end users of such work are highlighted by green arrows.

The thesis has developed two main bodies of work that were utilised by other researchers, namely the development of the slack adaptor for the repeatable loading of FRP coupons at intermediate strain rates and the evaluation of noise in DIC measurements when using high speed white-light cameras. The thesis also brings together work developed by several other researchers. The integrated end tab methodology developed by Mr Longana has been used for the manufacture of the majority of specimens discussed in the thesis, whilst the work conducted at intermediate strain rates uses the IR sensor calibration methodology developed by Dr Fruehmann and the camera triggering methodology developed by Dr Crump. The code with which to numerically apply strain to images, developed by Dr Crammond was also used in the verification of DIC measurements from high speed cameras.

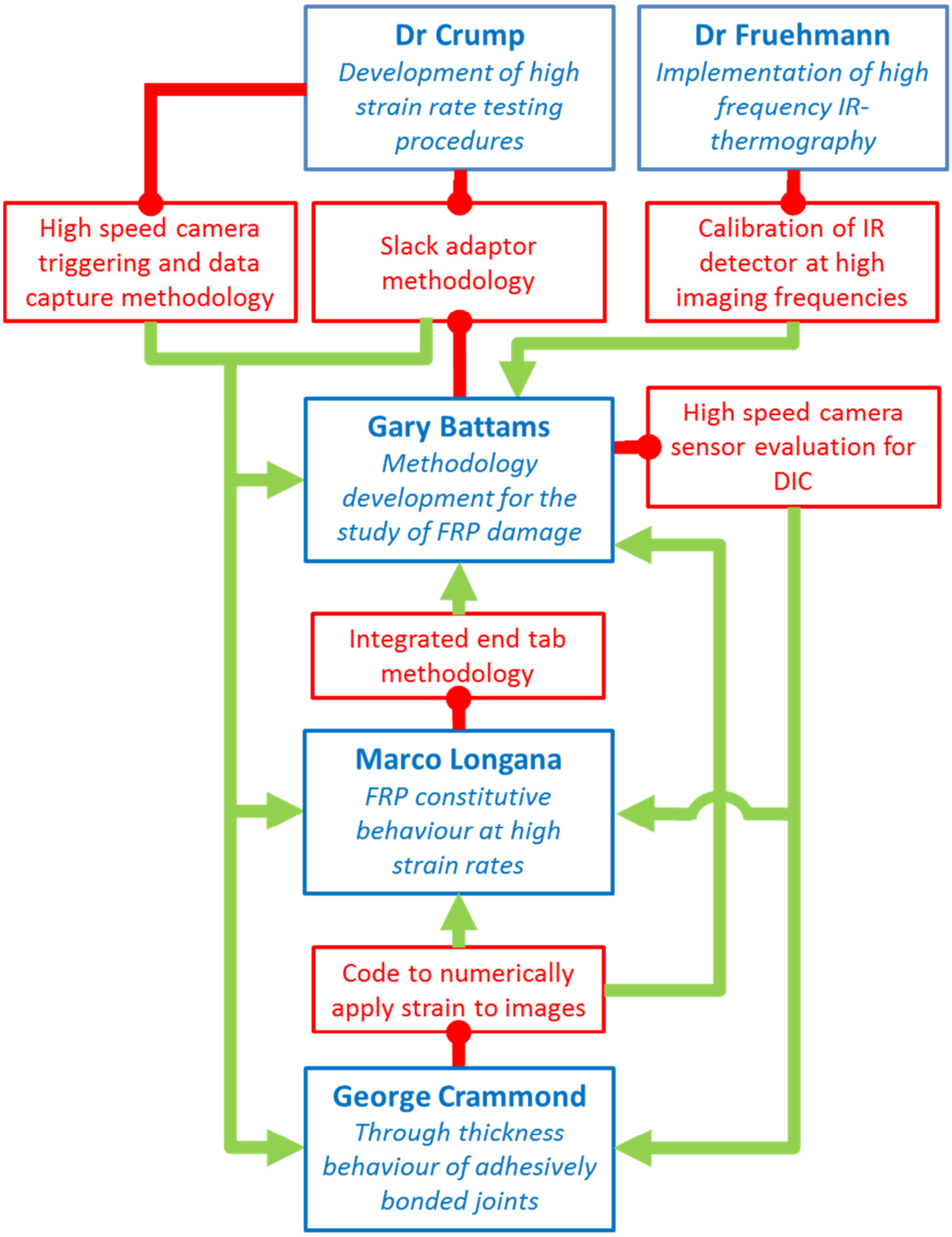

Figure 2: Researcher interactions within the EPSRC/DSTL project 'Full-field data-rich experimental approaches to explain composite material and structural performance and its damage tolerance'

1.2 Aims and Objectives

The main aim of the research described in the thesis is to establish an experimental methodology based on optical techniques to allow the study of FRP damage behaviour. This involves capturing and analysing data collected during intermediate strain rate loading and also during subsequent loading cycles at lower strain rates. The former aims to study how damage initiates during impact type loading, whilst the latter aims to investigate how damage evolves from such an event.

To establish the methodology, several objectives that must be covered were recognised:

1) Evaluate the characteristics and error sources of the digital imaging equipment and optical measurement techniques employed.
    a) To understand the characteristics of the high speed cameras and their limitations.
    b) To identify methods for reducing sources of error in the optical measurement techniques.
2) Establish a methodology for the study of FRP damage initiation during loading at elevated strain rates.
    a) Develop a controlled loading methodology for the application of an elevated strain rate load to FRP material. To know the limitations and error sources of the method.
    b) To apply high speed optical imaging and measurement techniques to capture the onset of damage during intermediate strain rate loading.
3) Establish a methodology for the study of damage evolution and propagation in predamaged FRP material through the application of optical measurement techniques during fatigue loading.

1.3 Novelty

The thesis demonstrates novelty in a variety of aspects, most notably in the application of multiple measurement techniques to the study of damage initiation and evolution in FRPs. During intermediate strain rate loading, both white-light and IR optical techniques are used to study the initiation of damage using high speed imaging. The benefit of using the techniques simultaneously stems from the two properties that are collected. DIC provides a surface strain map, whilst IR thermography allows insights into the surface stress state and the generation of heat from failure events. Although some previous studies have used high speed white light cameras and DIC, few have also used IR thermography to study FRP behaviour. IR cameras have only recently been able to achieve the frame-rates and sensitivities required for high speed imaging, through the use of reduced image sizes. The use of an IR detector outside of its usual operating conditions requires the use of a custom calibration procedure to obtain correct temperature measurements. Through the use of the calibration procedure developed by Dr Fruehmann, the thesis is one of the few examples that uses both quantitative thermal measurements and DIC based deformation measurements from high frame rate cameras.

Another area of novelty is in the application of DIC and TSA to cyclically loaded FRP specimens. The use of the two techniques allows the collection of surface strain and stress sum data, so giving greater confidence in the study of FRP damage propagation behaviour. Very few previous authors have used DIC to monitor a cyclically loaded FRP specimen and even fewer have simultaneously used TSA. A novel experimental methodology was developed to allow the automated collection of white light and IR images without the pausing of a fatigue cycle. The timing method developed allows the use of low cost, high resolution white light cameras, so giving strain maps of greater resolution after DIC analysis than possible using high speed white light cameras.

Although this thesis focuses on establishing experimental methodologies for the study of damage rather than the generation of material data, it serves as a basis for future projects for the collection of such data. It is envisaged that future projects will contribute to the damage tolerant design of FRP components using the methodologies developed in this thesis.

Two additional areas of novelty were generated as a result of the methodology development for FRP damage initiation at intermediate strain rates. The validation of high speed white light cameras for DIC measurements revealed previously unreported behaviour related to the sensor fill factor which was found to detrimentally affect recorded strains. A novel loading methodology was also developed to impart a purely tensile load at intermediate strain rates to FRP specimens.

In summary, the work described in this thesis demonstrates novelty in the following areas:

1. The use of high speed cameras for high resolution DIC strain measurement and the detrimental effect of reduced sensor fill factor on accuracy.
2. The development of an interrupted loading rig to apply purely tensile intermediate strain rate loading to standard sized FRP coupons, creating damage but without reaching final failure.
3. The application of high speed IR thermography and high speed white-light combined with DIC to the study of damage initiation of FRP during intermediate strain rate loading.
4. The conceptualisation and design of an automated and synchronised white-light and IR camera triggering methodology, enabling the evolution of damage to be captured during a fatigue cycle through the use of DIC and TSA without the need for a pause or change in the cyclic load.

1.4 Thesis Structure

The thesis consists of eight chapters. Chapter 1 is an introductory chapter outlining motivation, aims and novelty. Chapter 2 starts with a discussion of digital sensor technology, followed by a review of the theory of the full-field measurement techniques employed. It includes a discussion of the potential error sources of each technique identified from the literature, their advantages and limitations and also information about the specific equipment and software used in the thesis.

A literature review of damage initiation and evolution in FRPs is the focus of Chapter 3. Their typical mechanical response is stated followed by a discussion of their fracture behaviour. Emphasis is placed on the mechanisms that lead up to damage. The generally accepted behaviour of FRP materials when subjected to high strain rate loading is described along with a literature review of previous work using optical techniques to capture the onset of damage in FRP materials.

The equipment and methodology used for intermediate strain rate testing is discussed in Chapter 4. This includes an overview of the Instron Very High Speed (VHS) 80/20 servohydraulic test machine and the development of the slack adaptor system. The camera triggering method, developed by Dr Crump is presented, followed by a discussion on the design of the FRP specimens used throughout the thesis [9].

Chapter 5 discusses the application of DIC to images captured from high speed cameras, specifically focussing on the reduced accuracy encountered. The investigations into the cause are presented and the findings discussed.

Chapter 6 uses high speed white-light and Infra-Red (IR) cameras during quasi-static loading to validate a combined DIC and IR-thermography method for the identification of damage in crossply FRP specimens.

Chapter 7 presents the development and validation of the interrupted loading rig along with examples of tests conducted on CFRP and glass-fibre reinforced polymer (GFRP) specimens..

The methodology developed for automated and combined TSA/DIC measurements during the fatigue of FRP specimens is the focus of Chapter 8. Example data of fatigue tests conducted on previously undamaged CFRP specimens are presented and discussed. The chapter also includes subsequent damage propagation investigations conducted on previously damaged specimens using the methodology previously outlined in Chapter 7.

Finally, Chapter 9 summarises the main conclusions that can be drawn from the work conducted in the thesis. Also included are areas of potential future work. Such areas include; improvements to the interrupted loading rig allowing a greater range of strain rates and loads to be imparted, to gain FRP material performance data by applying the methodology to a variety of FRP materials and stacking sequences, and to diversify the types of impact loading from solely tensile loading. This may include the design of new methodologies to allow compression, shear and bending loads at intermediate strain rates to be applied and to investigate their affect on damage evolution.

Chapter 2

Full-Field Measurement Techniques

2.1 Introduction

The use of full-field optical techniques has grown rapidly in the past two decades due to the progress in digital camera performance and the dramatically increased computational power of modern PC systems [10]. Full-field techniques are based on image capture and are therefore very data-rich with the ability to obtain large amounts of data without modification of the mechanical behaviour of the specimen [11]. Full-field techniques are especially suited to the study of FRP materials as they are capable of identifying material heterogeneities [12].

Optical techniques can be divided into two types, interferometric and non-interferometric. The former includes the Moiré family of techniques which create fringe patterns through the superposition of a reference grating onto a second grating attached to a specimen surface [13]. Displacement resolutions as fine as 25 µm are achievable using a grating pitch of 40 lines per mm with white light illumination, which can be improved further to submicron levels through the use of coherent light sources [13]. Although such high resolutions are advantageous for a measurement system, interferometric techniques are highly susceptible to environmental disturbances, requiring the use of a bed isolated against vibrations [12]. For this reason interferometric techniques will not be used in the work conducted in the thesis.

Photoelasticity is a full-field technique that relies on the principle of birefringence, or double refraction of white light, in certain transparent materials [14]. Although the resin phase of many FRP materials exhibit birefringence, the addition of the fibre phase causes most FRP materials to become opaque. The material therefore requires a coating of birefringent material to be applied. This coating is likely to provide a reinforcing effect to the FRP surface and so change the surface damage behaviour of the material. Photoelasticity is therefore unsuitable to be used in the thesis.

The grid method is a full-field displacement measurement technique. Through a phase unwrapping process, changes in the spatial frequency of grid images can be related to the local displacements. The technique requires that flat specimen surfaces are coated in a grid to act as a spatial carrier with typically 6 pixels per grid element [10]. The smallest grid pitch possible for use with the technique is around is 0.1 mm, hence a spatial resolution of 0.017 mm is possible using this technique. Despite the high accuracy and spatial resolutions possible, the grid technique will not be used in the thesis for the following reasons. The use of the technique would considerably increase specimen preparation time due to the requirement of a bonded grid and experimental setup time would be increased due to requirement for accurate alignment between grid and camera sensor. Also, the use of an adhesive layer to affix a polymer grid coating may provide a reinforcing effect to the FRP surface and so change the surface damage behaviour of the material. Although an adhesive layer thickness of 0.1 mm is achievable [15], such a coating is also likely to have a detrimental influence on the thermoelastic measurements [16], as discussed in greater detail in section 2.8.1.

DIC is a versatile full-field displacement and strain measurement technique capable of a wide range of measurement sensitivities and spatial resolutions [17]. The method is applied to a set of images of a deforming surface by tracking the movement of small areas within the images to subpixel accuracy. To avoid matching errors (decorrelation) the technique requires that the deforming surface has a random pattern of surface contrast. This is typically created by coating the surface in a thin layer of acrylic paint or similar to create a speckle pattern. As the paint layer is thin and compliant it is not expected to significantly affect the behaviour of the underlying FRP material. DIC is therefore well suited to study of damage in FRP materials and is used extensively throughout the thesis.

IR thermography uses a camera sensitive to IR wavelength light to measure surface temperatures. The onset of damage in an FRP material may cause a surface temperature change due to the release of heat from the breaking of molecular bonds. It is envisaged that through the simultaneous use of DIC to measure surface displacements and IR-thermography to measure surface temperatures, greater confidence in the identification of damage will be achieved.

An extension of IR-thermography is thermoelastic stress analysis (TSA). TSA relies on the measurement of the small temperature changes induced by stress changes in an elastic solid, known as the thermoelastic effect and has been used in many studies to identify damage propagation in FRP materials [18-22]. The technique is especially suitable for the study of damage propagation as a cyclic load is required for the TSA measurement, allowing the effect of a dynamic load to be studied in real time [22, 23]. The primary output of the technique is the sum of the principal stresses and hence provides a different measurand to the DIC technique, so giving greater confidence in the identification of damage.

The chapter begins with an overview of digital sensor technology, followed by a detailed discussion of the DIC, IR-thermography and TSA techniques to be used in the thesis for the study of FRP damage.

2.2 Digital Sensor Technology

A typical digital camera system comprises of a lens and focusing system, one or more apertures, and a sensor. Digital cameras form the basis of measurement for the three full-field techniques to be used in the thesis and so warrant further discussion.

The principle behind a digital camera is to convert an optical image into an electronic signal. Semiconductor detectors rely on electrons becoming mobile in the semiconductor material due to an incident light photon creating a ‘hole’ in the valance band of the semiconductor material. Depending on the type of semiconductor material used, the detector can be sensitive to different wavelengths of light, so allowing the manufacture of IR detectors. When enough electrons become mobile, the conductivity of the semiconductor crystal increases. A single such element is known as a pixel. By combining many pixels, an array is formed to create a digital sensor. Such arrays are known as a charge-coupled device (CCD) or a complementary metal oxide semiconductor (CMOS) depending on the specific architecture used. Schematics of the two types of digital sensor are shown in Figure 3. Each pixel accumulates a charge over the image exposure time proportional to the intensity of incident light. The charge is converted to a voltage for each pixel and digitised using an analogue to digital converter (ADC). This voltage conversion takes place at each pixel in a CMOS sensor, whereas in a CCD sensor each charge packet is transferred sequentially to a buffer at the outer edges of the sensor [24]. The readout circuit converts the analogue data from each pixel into a logic signal which is subsequently sent to be processed and stored as an image on a personal computer (PC).

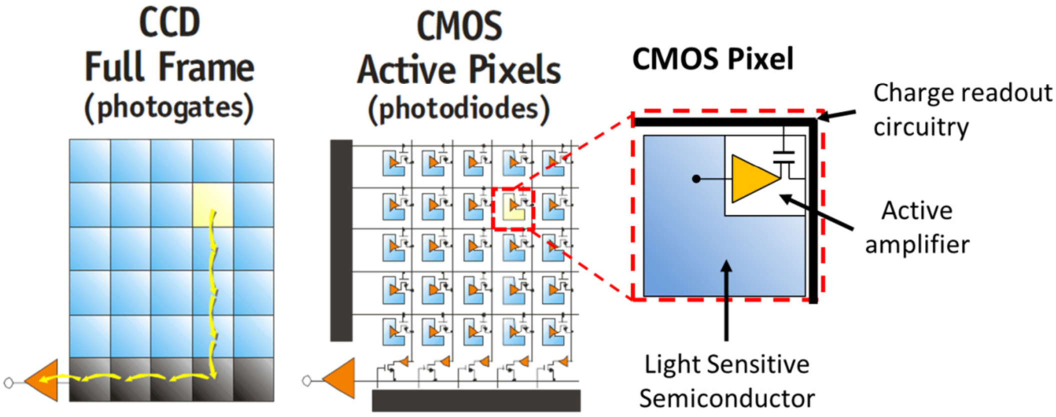

Figure 3: Schematic of CCD and CMOS sensors

There are a vast number of variables which determine the behaviour of CCD and CMOS sensors. The most important of which for the work conducted in the thesis are now discussed in more detail.

2.2.1 Sensitivity

The sensitivity of a sensor to incident light is a function of the quantum efficiency and pixel fill factor [25]. The quantum efficiency is the ratio of photon-generated electrons to the photons incident on the pixel area and is primarily a property of the type of semiconductor material. The fill factor is the ratio of a pixel area sensitive to light to the overall pixel area. The area sensitive to light is reduced in CMOS sensors by the use of charge amplification transistors and readout circuitry as shown in Figure 3. Some sensors use micro-lenses to achieve close to 100% fill-factor. This technology incorporates a small lens over each pixel which redirects the incident light onto the light sensitive potion of the pixel.

2.2.2 Exposure Time

The level of charge collected at each pixel is related to how long light is allowed to fall on the sensor. This length of time is known as the integration or exposure time. In older cameras reliant on photosensitive film, this time would be dictated by the opening and closing of a mechanical shutter. In digital cameras, the method of controlling the exposure time is controlled by first resetting the pixel charge to zero, waiting the designated exposure time and then reading out the pixel charge. This type of electronic shutter allows far greater imaging frequencies to be realised than the mechanical type. The transistors that are required to provide electronic shuttering are situated at each pixel in a CMOS sensor, further reducing the sensor fill-factor. Although maximising the exposure time is important for increasing image brightness, if motion occurs during the exposure time, the object is liable to become blurred. For this reason it is often beneficial to increase image brightness using other methods, such as improved illumination levels and wider lens apertures.

2.2.3 Dark Current

A major source of noise in digital sensors is dark current. Dark current is defined as the generation of electrons within the semiconductor material without any incident light. It occurs as a result of crystallographic defects and is more prominent at higher sensor temperatures. In a CCD sensor, the dark current doubles for every 7 K temperature rise [25]. An IR sensor uses a semiconductor material sensitive to IR wavelength light. At such wavelengths, the low energy of photons makes their detection more difficult above the dark current detector noise. Consequently IR detectors are typically cooled to cryogenic temperatures to minimise dark current noise and achieve the highest possible signal to noise ratio.

2.2.4 Dynamic Range

The dynamic range of a sensor is defined as the ratio of pixel saturation level to its minimum signal threshold [33]. Through the use of an ADC, the dynamic range is digitised into discrete intensity levels. The number of such levels defines the bit depth of a sensor and is the smallest change in intensity that a pixel can resolve. It is advantageous to use the full dynamic range available to give the greatest intensity resolution. A pixel which cannot collect any further charge is known as being saturated. Any information on the light intensity above this saturation point is lost and care should be taken to avoid such saturated pixels by adjustment of lens apertures and exposure times.

2.2.5 Uniformity

Due to variability in semiconductor material and circuit components, the response of an individual pixel will always be slightly different to those around it. This has implications on the accuracy on the recorded intensity levels. To counteract such an effect, a non-uniformity correction (NUC) is often applied by subjecting a sensor to a uniform light source and correcting the gain level for each pixel.

2.2.6 Bloom

When a sensor is exposed to bright light such that pixels become saturated, charge may leak to adjacent pixels, causing an increase in their recorded intensity. This effect is known as blooming and can be limited by avoiding pixel saturation. Some sensor architecture incorporate overflow drain devices to reduce blooming effects.

2.3 High Frequency Digital Imaging

A primary aim of the PhD is to use full-field techniques to identify damage during intermediate strain rate loading. The short duration of such tests requires the application of high speed cameras.

Ultra-high speed cameras incorporating multiple sensors and those which use image intensifiers are not used in the thesis as they typically operate at higher frequencies than that required for the current work. They also generate greater image noise, which after DIC processing have been found to result in strain error levels an order of magnitude greater than single CMOS sensor high speed camera systems [26].

High speed imaging is dominated by two factors; imaging frequency and image brightness. The imaging frequency is primarily governed by the pixel readout rate, whilst the image brightness is a function of the sensor sensitivity, exposure time, illumination levels and lens system.

Sensitivity can be increased through the use of larger pixels or the use of active pixel sensors (APS). This type of sensor uses an amplification transistor located at each pixel to boost the signal to noise ratio of the output.

CMOS sensors are generally able to image at higher frequencies than CCD sensors due to the majority of the charge collection and amplification circuitry being located at each pixel. This results in shorter delays between voltage readouts, at the cost of decreased fill-factor and correspondingly lower sensitivity [25]. For this reason, CMOS sensors are the architecture of choice for high speed cameras. Due to limitations in the data transfer rate to a PC, high speed cameras store images in local memory for later transfer to a PC.

An exposure method known as the rolling shutter technique is used in some high speed cameras, to maximise imaging frequency. The CEDIP Silver 480M IR camera used in the thesis uses this method. The rolling shutter alternates the exposure of odd and even lines of pixels, doubling the amount of charge collected and halving the time taken for charge transfer and image readout circuits to operate [25]. This comes at the cost of reduced resolution.

The pixel readout rate is often a limiting factor in the maximum imaging frequency. By reading out only a small fraction of the image area, the time taken for image readout is reduced and the maximum imaging frequency can be increased. This process is known as windowing and comes at the cost of reduced image size.

A further consideration which becomes more important at high imaging frequencies is the effect of lens aperture. A large lens aperture is advantageous for high speed imaging to produce images of greater brightness. It is however detrimental to the depth of the field. This is a major consideration when surfaces are imaged at an angle, such as that required during a stereo-DIC setup, as explained further in section 2.4.3.

2.4 Digital Image Correlation (DIC)

2.4.1 Introduction

The 2D DIC technique is typically applied to images collected from a single camera positioned normal to the surface under investigation. A typical setup is shown in Figure 4. As previously mentioned, the surface under investigation requires a contrast pattern to allow the correlation algorithm to successfully track the surface deformation. Some surfaces naturally possess such a surface pattern and no further surface preparation is required. The most common method for creating a speckle pattern and the method used throughout the thesis is to apply a light coat of acrylic spray paint.

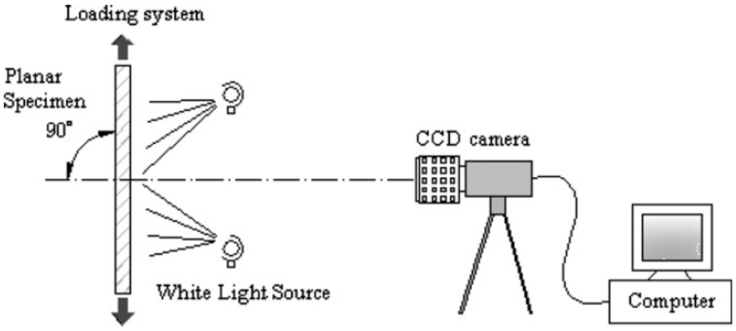

Figure 4: Schematic experimental setup for 2D DIC [17]

An overview of the DIC technique is now presented. A more detailed description of the DIC technique can be found in the book by Sutton *et al* [27] and the review papers by Pan *et al* [17, 28].

2.4.2 2D Correlation

To perform DIC, an initial reference image, taken at time *t,* is split into a regular array of regions known as subsets. The size of the subset can be set by the user, but an area of 20 x 20 pixels is typical. Each subset will ideally sample over multiple speckles on the specimen surface and have a unique distribution of pixel intensities. A second, deformed image taken at time $t+\Delta t$ is searched for the new subset position by comparing the intensity patterns of the two cells through use of a correlation function. This procedure is shown schematically in Figure 5, where a reference subset at initial position $P(x_0, y_0)$ composed of an intensity distribution of $f(x_i,y_j)$, moves by rigid body motion to position $g(x_i,y_j)$ at time $t+\Delta t$. The vector connecting points *P* and *P'* is the displacement vector of the subset, composed of the horizontal and vertical components, *u* and *v*.

The deformed subset will never be an exact match of the reference subset due to various factors, including subset rotation, camera noise and strain within the subset. The best match for the new subset position must therefore be found by an optimisation procedure.

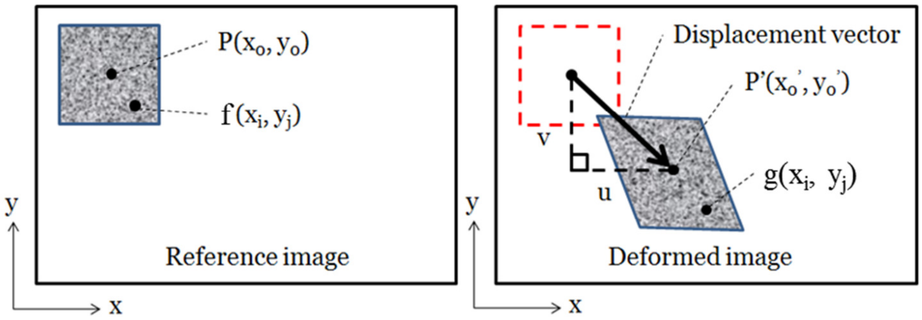

Figure 5: Schematic of a reference subset (left) at time t, and the same cell after a deformation (right) at time t+Δt

The exact function used depends on the DIC software employed. DaVis 8.1.3 by LaVision is used for all correlations described in the thesis. The software uses the least square difference (LSM) method (also known as sum of squared difference (SSD)). This is a common method used in many other DIC software and is explained in depth in multiple reviews [27-29]. The LSM method computes the position of the deformed subset to the nearest pixel accuracy by minimising the result of the following function [17]:

$$C_{SSD} = \sum_{i=-M}^{M} \sum_{j=-M}^{M} \left[f\left(x_i, y_j\right) - g\left(x'_i, y'_j\right) \right]^2 \qquad 2.1$$

where M is the size of the subset in pixels.

DaVis defines a correlation value to indicate the similarity between the reference subset and the deformed subset, with a value of 1 indicating a perfect match. The correlation value Λ, is defined as follows:

$$\Lambda = 1 - C_{SSD} \qquad 2.2$$

A plot showing the correlation values across a 150 x 150 pixel search area is shown in Figure 6 with the correct displacement location indicated by the centre maximum point. In cases where the subset has a low uniqueness, multiple maximum points may occur, increasing the chances of decorrelation.

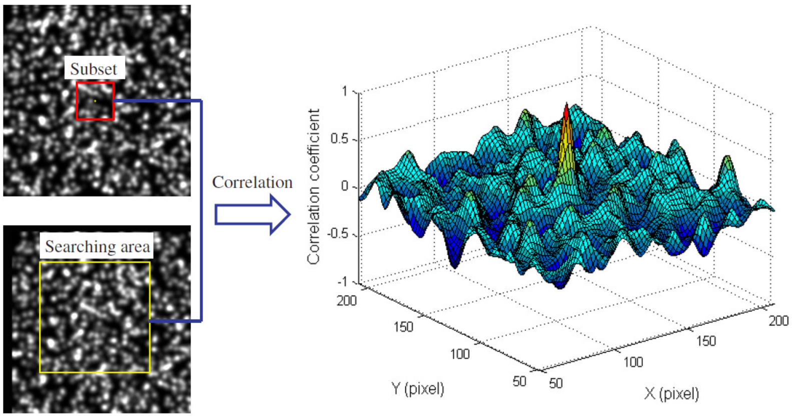

Figure 6: Correlation values for a search area of integer pixel displacements, showing the maximum value at the correct new cell location [17].

To compute the subset displacement to greater accuracy, grey levels values must be evaluated at subpixel locations using an interpolation method and the LSM method repeated in an iterative manner [29]. DaVis 8.1.3 allows the use of two subpixel interpolation methods; a bilinear approximation and a 6th order spline method. The former yields lower displacement accuracy but faster convergence, whilst the latter gives greater accuracy at the cost of greater computation time.

If the subset moves purely by rigid body motion, then the displacement of all pixels within the subset is equal. The displacement of pixels can therefore be defined as follows [17]:

$$\begin{aligned} x_i' &= x_i + \xi(x_i, y_j) \\ y_j' &= y_j + \eta(x_i, y_j) \end{aligned} \qquad 2.3$$

where the zero order displacement mapping (shape) function is defined as:

$$\xi_0(x,y) = u \qquad \eta_0(x,y) = v \qquad 2.4$$

To take into account translation, rotation, shear and normal strains within a subset, a first order (affine) shape function can be used [17]. Such a function is employed by DaVis 8.1.3:

$$\begin{aligned} \xi_1(x_i, y_j) &= u + u_x \Delta x + u_y \Delta y \\ \eta_1(x_i, y_j) &= v + v_x \Delta x + v_y \Delta y \end{aligned} \qquad 2.5$$

where $\Delta x = x_i - x_0$, $\Delta y = y_i - y_0$, u and v are the horizontal and vertical displacement components of the reference subset centre $P(x_0, y_0)$ and u_x, u_y, v_x, v_y are the first-order displacement gradients of the reference subset.

LaVision states an expected displacement accuracy when using a bilinear subpixel interpolation method within DaVis 8.1.3 as given in Table 1. Similar accuracy values when using a 6th order spline subpixel interpolation method were not available from LaVision.

Cell size (pixels)	Accuracy of 2D vectors	Accuracy of 3D vectors
128×128	0.005 pixel	0.01 pixel
64×64	0.01 pixel	0.025 pixel
32×32	0.025 pixel	0.05 pixel
16×16	0.05 pixel	0.1 pixel

Table 1: Accuracy of DIC displacement vectors calculated using DaVis 8.1.3 when using a bilinear interpolation method [30]

This correlation procedure is repeated across all subsets within an image and all images in a series to produce a series of full field displacement maps. To obtain high accuracy displacement maps it is beneficial to use larger cell sizes. The disadvantage is that small scale behaviour within a subset will not be identified. Most DIC software, including DaVis 8.1.3, offers the option of overlapping subsets whereby the subset size is maintained whilst the distance between subset centres is decreased. This distance between two adjacent subsets is referred to as the step size. A small step size allows a greater density of displacement vectors at the cost of decreased strain accuracy, caused by the decreased gauge length.

Strain maps are calculated from a DIC displacement map using the following relationships:

$$\varepsilon_{xx} = \frac{du}{dx} \qquad 2.6$$

$$\varepsilon_{yy} = \frac{dv}{dy} \qquad 2.7$$

$$\gamma_{xy} = \frac{du}{dy} + \frac{dv}{dx} \qquad 2.8$$

where du and dv is the difference between adjacent displacement vectors in the longitudinal and transverse directions, dy and dx are the distances between the centres of two adjacent cells and γ_{xy} is the engineering shear strain.

In the DaVis 8.1.3 software, a central difference algorithm is used to compute the strain values as shown below for the case of horizontal strain ε_{xx}:

$$\varepsilon_{xx}(m,n) = \frac{dv_x(m,n)}{dx} = \frac{\left(v_x(m+1,n) - v_x(m,n)\right) + \left(v_x(m,n) - v_x(m-1,n)\right)}{2g} \qquad 2.9$$

where $\varepsilon_{xx}(m,n)$ is the transverse strain at grid position (m,n), $v_x(m,n)$ is the x component of the displacement vector for the cell located at grid location (m,n) and g is the step size.

Equation 2.9 can be further simplified to give the following expression:

$$\varepsilon_{xx}(m,n) = \frac{(v_x(m+1,n) - v_x(m-1,n)}{2g} \qquad 2.10$$

The absolute error of the vertical strain is defined as follows [31]:

$$r_{abs} = \sqrt{\left(\frac{\sqrt{2}r}{g}\right)^2 + \left(0.0001\varepsilon_{yy}\right)^2} \qquad 2.11$$

Where r_{abs} absolute displacement error, r is the maximum expected error of displacement vector, as quoted in Table 1, and ε_{yy} is the magnitude of applied strain in the vertical direction.

When the absolute error is calculated for various cell sizes and overlaps, for the same spatial resolution a larger cell size with more overlap gives a more precise displacement vector compared to a smaller cell size without overlap. This result is summarised in Table 2. The disadvantage of using a large cell size is that the displacement vector will be a function of the displacement of all pixels within the subset, causing a loss in spatial resolution despite the additional vector density.

Cell size (Pixels)	**Overlap (%)**	**Step size (pixels)**	**Strain precision for 2D system (% strain)**	**Strain precision for Stereo camera system (% strain)**
128x128	88%	16	0.02210%	0.04419%
64 x 64	75%	16	0.04419%	0.11049%
32 x 32	50%	16	0.11049%	0.22097%
16 x 16	0%	16	0.22097%	0.44194%

Table 2: Absolute error of a DIC correlation based on cell size and overlap

2.4.3 Stereo Camera DIC

Stereo DIC uses a calibrated pair of stereo cameras and unlike 2D DIC, allows out of plane deformations to be separated from in-plane strains. To enable the previously discussed 2D DIC algorithm to be applied, 'corrected' images are calculated which are composed of the images produced from the two cameras after taking into account camera perspective, position and lens magnification. An important step to enable the differentiation between in plane and out of plane deformations is the calibration of camera positions relative to each other.

In the DaVis system, calibration requires the imaging a calibration plate with markers of known shape and position. A typical calibration plate for the DaVis system is shown in Figure 7. The use of a calibration plate also allows the lens distortion effects to be corrected for. DaVis uses a third order lens distortion model, explained in more depth in [32].

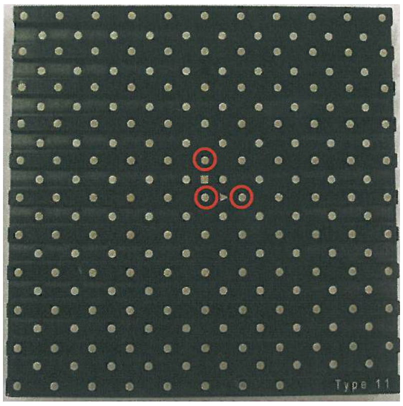

Figure 7: Front view of a Type 11 calibration plate used with the DaVis system [32].

The calibration process relates the 2D sensor coordinate systems, (X_s, Y_s) for each camera to the 3D global coordinate system (X_W, Y_W, Z_W), as depicted in Figure 8. This is carried out using a camera pinhole model which is discussed in more depth in [27]. The algorithm used by DaVis is as follows [32]:

$$X_S = C_x + f\beta_x \frac{R_{11}X_W + R_{12}Y_W + R_{13}Z_W + t_x}{R_{31}X_W + R_{32}Y_W + R_{33}Z_W + t_z}$$
$$Y_S = C_y + f\beta_y \frac{R_{21}X_W + R_{22}Y_W + R_{23}Z_W + t_y}{R_{31}X_W + R_{32}Y_W + R_{33}Z_W + t_z} \qquad 2.12$$

where (X_S, Y_S) and (X_W, Y_W, Z_w) are the sensor and world coordinates respectively, (C_x, C_y) are the coordinate positions of the centre of the image plane, β_x and β_y are scale factors relating the pixel size to actual surface dimensions, f is the focal length, R is a rotation matrix and $t_{x,y,z}$ is the translation vector defining the camera positions with respect to the global coordinate system.

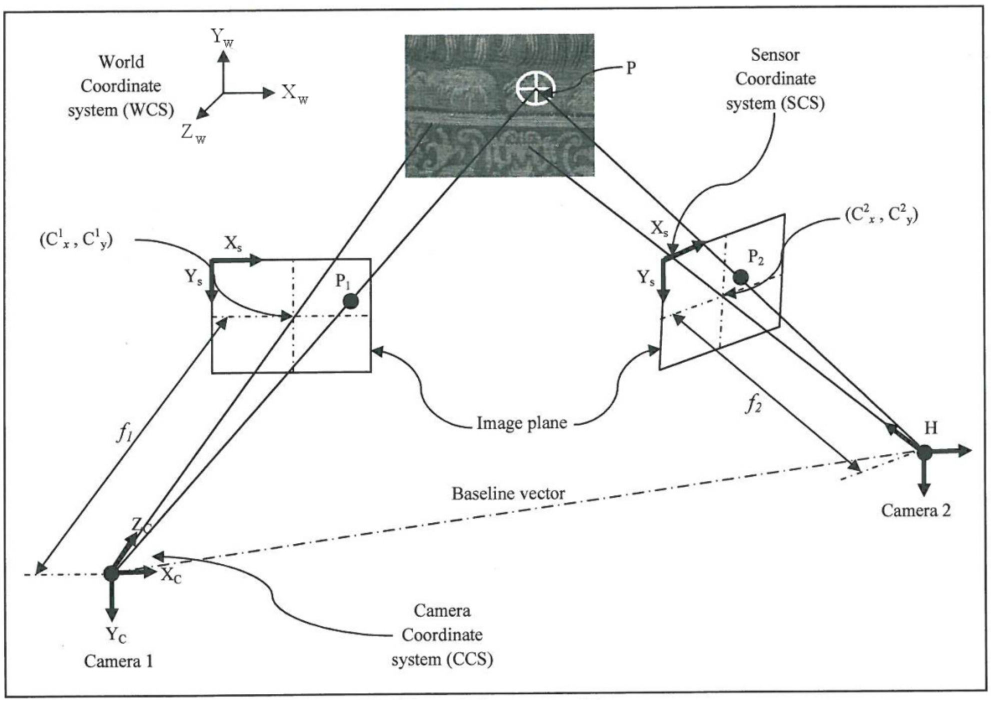

Figure 8: Schematic for a stereo DIC imaging system [32]

A rotation vector used to define the orientation of each camera in the global coordinate system [32] is:

$$\begin{bmatrix} R_{11} & R_{11} & R_{13} \\ R_{21} & R_{22} & R_{23} \\ R_{31} & R_{11} & R_{33} \end{bmatrix} = \begin{bmatrix} 1 & 0 & 0 \\ 0 & \cos\theta_x & \sin\theta_x \\ 0 & -\sin\theta_x & \cos\theta_x \end{bmatrix} \begin{bmatrix} \cos\theta_y & 0 & -\sin\theta_y \\ 0 & 1 & 0 \\ \sin\theta_y & 0 & \cos\theta_y \end{bmatrix} \begin{bmatrix} \cos\theta_z & \sin\theta_z & 0 \\ -\sin\theta_z & \cos\theta_z & 0 \\ 0 & 0 & 1 \end{bmatrix} \quad 2.13$$

where $\theta_{x,y,z}$ is the rotation angle from the global coordinate axes.

Calibration in the DaVis system is carried out by first acquiring a single image pair of the calibration grid. The origin of the global coordinate system is then defined as the centre of the calibration plate. The angles $\theta_{x,y,z}$ and the camera translation vector $t_{x,y,z}$ for each camera are found from the dots highlighted in red in Figure 7. This allows predictions of where the rest of the dots should be located if the system were a perfect pinhole camera model. These dot locations give $X_{S\ measured}$ for each dot in the grid (N) and each image (M). These ideal dot locations are compared to those measured in the images collected to give an objective function E, which provides a quantitative measure of displacement accuracy in the system [32]:

$$E = \sum_{i=1}^{M} \sum_{j=1}^{N} \left(\left(X_{S\ measured}^{ij} - X_{S\ \mathrm{model}}^{ij} \right)^2 + \left(Y_{S\ measured}^{ij} - Y_{S\ \mathrm{model}}^{ij} \right)^2 \right) \tag{2.14}$$

where M is the number of images, N is the number of dots, $X_{S\ measured}$ and $Y_{S\ measured}$ are the locations of a dot in the acquired images in the horizontal and vertical locations and $X_{S\ model}$ is the corresponding dot location using the pinhole camera model.

In order to differentiate between in plane strains and out of plane displacements a full-field map of surface height must be calculated and accounted for to produce the corrected image. This procedure is explained in depth in [27, 32]. Once the set of corrected images are produced, the 2D image correlation procedure described in section 2.4.2 can be applied.

2.4.4 DIC Error Sources

The accuracy of DIC is influenced by numerous factors, a full discussion of which can be found in [27]. Several of the most important error sources for the work conducted in the thesis are now reviewed.

Out of Plane Motion

A surface that moves away from a camera will appear to have been subjected to an isotropic compressive strain, whilst a surface moving closer will appear to undergo tensile strain. Such a strain will be in addition to and indistinguishable from any real in-plane strains. The effect of out of plane motion on the DIC recorded strain can be calculated as follows [27, 33]:

$$\varepsilon_{xx} = \frac{\partial u(\Delta Z)}{\partial x_s} \cong -\frac{\Delta Z}{Z} \tag{2.15}$$

$$\varepsilon_{yy} = \frac{\partial v(\Delta Z)}{\partial y_s} \cong -\frac{\Delta Z}{Z} \tag{2.16}$$

$$\gamma_{xy} = \left(\frac{\partial u}{\partial y_s} + \frac{\partial v}{\partial x_s} \right) \cong 0 \tag{2.17}$$

where Z object to camera distance and ΔZ is the out of plane motion.

A stereo DIC system does not encounter strain errors due to out of plane motion as in plane strains and out of plane movements can be separated and quantified, as previously described.

Camera Misalignment

For a 2D DIC system, a camera that is not aligned perpendicularly to the surface under investigation creates a uniform in-plane strain after correlation due to difference in magnification across the width [34]. For small angles this effect is small. Meng *et al* [35] concluded that a misalignment of 5° created a displacement error level smaller than 0.01 pixels. Since a camera alignment within 5° is easily achievable, camera misalignment should not be a problem for 2D DIC.

Speckle Pattern and Image Quality

Acquiring high quality images is paramount for achieving reliable DIC measurements. Certain artefacts are likely to increase the chance of decorrelation, all of which should be avoided. These include contamination on the lens, reflections on the specimen surface, sensor saturation and variations in lighting levels across the image [27]. Image blurring can also result in decorrelation due to a change in the imaged speckle pattern. It is also recommended that the image contrast is maximised through use of the full dynamic range of the sensor [17].

The speckle pattern is intrinsically linked to the spatial resolution of the image, and in turn, the spatial resolution of the camera and the lens magnification. Various parameters have been proposed to quantify the quality of a speckle pattern [36-38], as reviewed in [39]. Speckle size influences the useable subset sizes for DIC. Very large speckles are liable to contain an entire subset within their area, reducing uniqueness and giving a high chance of decorrelation. Speckles smaller than 2 pixels diameter are liable to encounter the pixel locking effect [40], whereby displacement vectors become biased towards integer pixel values. This is investigated further in chapter 5. As a general rule for accurate subset matching, a speckle should be sampled by at least a 3x3 array of pixels with each subset containing approximately 9 speckles [27].

Camera Hardware

As previously mentioned in section 2.2, digital sensors may introduce errors into the image as a result of random noise, which can be reduced by sensor cooling. The image noise produced varies greatly between camera manufacturers and models. High speed cameras with image intensifiers have been shown to be especially prone to high image noise [26]. Variations in pixel sensitivity across a sensor can cause a decrease in similarity between reference and deformed subsets after image correlation. For this reason a non-uniformity correction is recommended. Dead pixels in a digital sensor can similarly cause a decrease in similarity after image correlation. Such pixels are usually taken into account by defining the intensity value of a dead pixel as an average of its near neighbours. Cameras with low dead pixel counts are recommended for DIC.

Subpixel Interpolation

The use of a subpixel interpolation algorithm introduces a systematic error that is dependent on the subpixel position of the deformed subset [41]. The systematic errors of three types of subpixel interpolation method are shown in Figure 9.

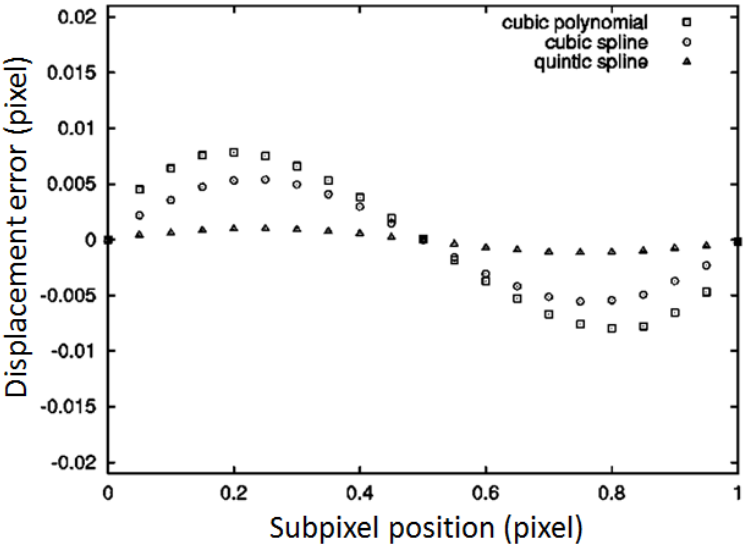

Figure 9: Displacement error as a function of subpixel displacement [41]

The displacement error is a minimum at integer and half integer pixel displacements, whilst the error is a maximum at 0.25 and 0.75 pixels of displacement. For speckle pattern images with a continuous grey level distribution, a quantic spline interpolation was found to produce the lowest displacement errors [41].

2.5 Infra-Red Thermography (IRT)

All objects above absolute zero emit heat in the form of electromagnetic radiation from their surface. As the temperature of an object increases, the amount of heat radiated increases. By measuring the amount of IR energy emitted from a surface, accurate temperature measurements can be made. The emissions of bodies at room temperature are strongest in the near and mid infrared range (between 1.5 and 20 μm) [42]. For this reason IR detectors are commonly used for temperature measurement. Two types of IR detectors exist, photon detectors and bolometers. Bolometers experience a rise in detector temperature from incident IR radiation, causing a change in a detector property, often resistance [43]. Bolometers are of a lower sensitivity and are therefore not considered in the thesis. Photon detectors rely on exciting a semiconductor material sensitive to IR wavelengths in the same way as white-light digital sensors, as described in section 2.2. The charge collected on each pixel can be related to the surface temperature through appropriate calibration. Photon detectors have greater sensitivity and faster response rates than bolometers and are therefore better suited for the study of short duration events.

Thermography is fundamentally different from white light techniques as it relies on surface emissions due to surface temperature rather than reflections [43]. IR reflections from the external environment are avoided as they contribute to errors in the measured surface temperature. In metals and other highly reflective materials, a matt paint layer is typically applied to ensure high and uniform emissivity and to avoid surface reflections. The emissivity is dependent on temperature and wavelength but can be assumed constant over the wavelengths and temperatures commonly encountered [44]. The emissivity is defined as the ratio between the emitted radiation of a body compared to the emitted radiation of a black body at the same temperature [22]:

$$\epsilon = \frac{\Phi}{\Phi_b} \qquad 2.18$$

where ϵ is the emissivity, Φ is the radiated energy of a body and Φ_b is the radiated energy on a black body at the same temperature.

FRP materials have an emissivity of around 0.9-0.92, which is high enough to not warrant additional surface coating [43].

The radiation at a given wavelength emitted from a blackbody over a hemisphere can be described by Planck's law:

$$\Phi_{\lambda,b} = \frac{2\pi c^2 h}{\lambda^5}\left(e^{\left(\frac{ch}{k\lambda T}\right)} - 1\right)^{-1} \tag{2.19}$$

where $\Phi_{\lambda,b}$ is the spectral emissive power for a black body, h is Planck's constant, c is the speed of light, λ is the wavelength, T is absolute surface temperature and k is Boltzmann's constant.

By integrating across all possible emission wavelengths, the Stefan-Boltzmann relationship is found, relating surface temperature to the total emitted radiation:

$$\Phi_b = BT^4 \tag{2.20}$$

where Φ_b is the emissive power per unit area of a black body over all wavelengths, T is the absolute surface temperature and B is the Stefan-Boltzmann constant:

$$B = \frac{2\pi^5 k^4}{15c^2 h^3} \tag{2.21}$$

The energy of a single photon is as follows:

$$E = \frac{hc}{\lambda} \tag{2.22}$$

Equation 2.19 can therefore be expressed in terms of the number of photons per unit area for a black body N_b:

$$N_b = \int_0^\infty \frac{2\pi c}{\lambda^4}\left(e^{\left(\frac{ch}{k\lambda T}\right)} - 1\right)^{-1} \partial\lambda \tag{2.23}$$

As photodetectors are only sensitive to IR radiation across a relative small wavelength band, Equation 2.23 is integrated over the receptive wavelength range to give the number of photons within this range. Due to the mathematics involved this is not possible to perform analytically, and must be carried out numerically. Since real surfaces are not blackbodies, emissivity is also taken into account:

$$N = \epsilon \int_{\lambda_1}^{\lambda_2} \frac{2\pi c}{\lambda^4}\left(e^{\left(\frac{ch}{k\lambda T}\right)} - 1\right)^{-1} d\lambda \qquad 2.24$$

where N is the number of photons emitted per unit area for a real surface and λ_1 and λ_2 provide the wavelength sensitivity limits of the photodetector.

When equation 2.24 is evaluated, the following relationship is found:

$$N = \epsilon B T^3 \qquad 2.25$$

where N is the number of photons emitted per unit area for a real surface, B is the Stefan-Boltzmann coefficient for photodetectors equal to $0.370B/k$ (1.52×10^{15} photons $s^{-1}m^{-3}sr^{-1}K^{-3}$ and ϵ is the surface emissivity.

When using modern photodetector systems, the surface temperature is related to the measured signal through appropriate calibration. The calibration procedures for the detector used in the thesis are explained in section 2.6.

2.6 The CEDIP Silver 480M IR Camera

The IR photodetector used in the thesis is a Silver 480M manufactured by CEDIP Infrared Systems (now FLIR). The detector comprises of a dual 320 x 256 array of indium Antimonide (InSb) elements sensitive to IR wavelengths between 3.6 and 5.1 μm cooled by means of an internal Stirling pump to 77 K [42, 45]. A summary of the detector characteristics is given in Table 3.

Sensor Material	**Pixel Size (µm)**	**No. of Pixels**	**Dynamic Range (bits)**	**Wavelength Band (µm)**	**Electronic noise equivalent (at 30°C)**	**Sensitivity (at 25°C)**	**Maximum imaging frequency (Hz)**	
							Full-frame	**64 x 4**
InSb	30 x 30	320 x 256	14	3.6 – 5.1	15.75 mK	4.2 mK	383	20000

Table 3: Overview of CEDIP Silver 480M characteristics [42, 45]

The Silver 480M camera system comes equipped with a 27 mm lens as standard allowing stand off distances between 150 mm and infinity [42]. A G1 lens may be added to reduce the stand off distance to approximately 10 mm so increasing the spatial resolution and giving an approximate field of view of 9.6 x 7.7 mm [46]. An intermediate lens was not available for the work conducted in the thesis.

The dual detector array of the Silver 480M, shown in Figure 10, allows one detector array to be exposed to radiation via an electronic shutter whilst a readout circuit extracts the intensity readings for the other array, allowing a high imaging frequency to be achieved [43]. By windowing, the frame rate can be increased further with the maximum limit being defined by the data rate capacity of the readout circuit. The charge of each pixel is converted to a digital level (DL) unit between 0 and 2^{14} levels by an on board ADC. As frequency is increased, the exposure time (integration time) over which incident IR radiation is collected must decrease. Whilst reflection based techniques can overcome this limitation by increasing illumination levels, the IR radiation emitted by an object cannot be increased without raising its temperature. This limit proves a major challenge for thermography operating at high imaging frequencies.

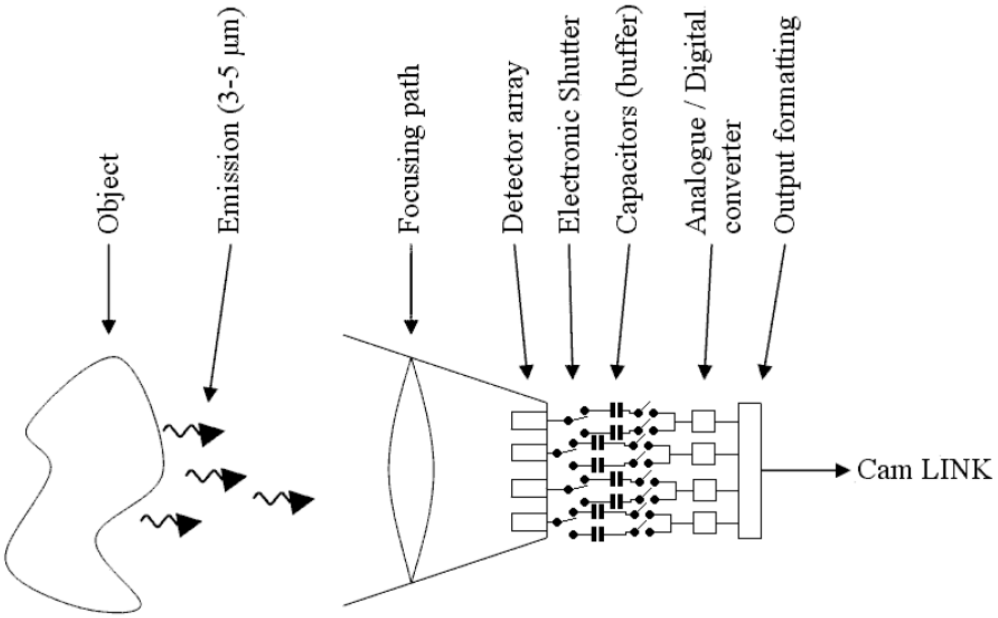

Figure 10: Schematic of the CEDIP Silver 480M IR detector [43]

Variations in pixel sensitivities are adjusted by means of a non-uniformity correction (NUC). This is carried out by exposing the detector to a uniform surface of high emissivity at two different temperatures. Any variations in pixel response can then be cancelled out by applying a custom amplification factor and offset to each pixel. This data is stored internally on the camera such that image data transferred to a PC already has the NUC applied.

The software provided with the Silver 480M camera includes calibration curves that relate the detector signal S to the surface temperature. This procedure uses a single curve and assumes uniform response across all pixels in the sensor. A schematic of typical calibration curves are shown in Figure 11.

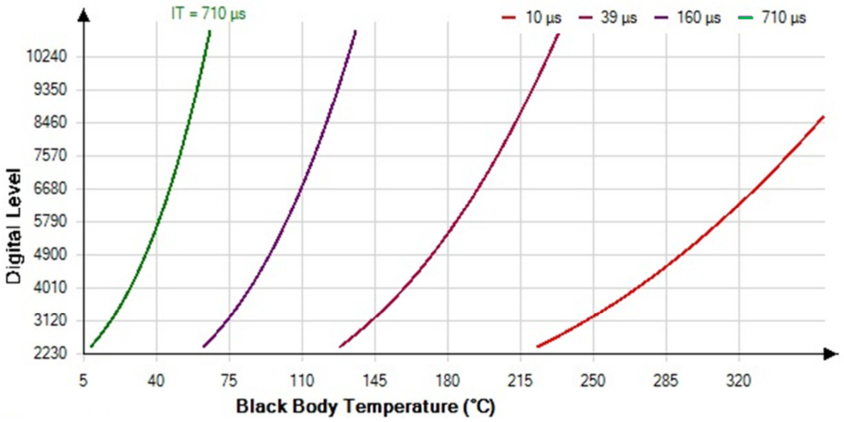

Figure 11: Calibration curves relating sensor response to surface temperature for various integration times

This standard calibration method is sufficient for most users, but the work described in the thesis requires the use of the camera at high imaging frequencies. As frame rate is increased the integration time decreases, reducing the pixel saturation to extremely low levels. The imaging of an object at 20°C at 15 kHz imaging frequency with a 60 µs integration time produces a detector response value of approximately 500 DL, just 3% of the dynamic range of the detector [47]. The manufacturer does not recommend extrapolating the standard calibration curves to such low saturation levels due to a non-linear detector response [47].

A custom calibration was therefore developed by Fruehmann *et al* [43] to obtain temperature measurements using the Silver 480M detector when operating at high imaging frequencies. The method operates in place of the standard temperature calibration and NUC procedure by applying two unique calibration curves for every pixel in the sensor array (one for each array) to take into account pixel response variations. A summary of the detector sensitivity and precision when using the high frequency calibration procedure is presented in Table 4.

Temperature (°C)	Sensitivity (°C/DL)	Precision (°C)
15	0.14	0.32
25	0.11	0.24
35	0.08	0.19
45	0.06	0.14
55	0.05	0.11
65	0.04	0.09
75	0.03	0.07

Table 4: Detector precision using the high frequency calibration procedure [47]

2.7 Thermoelastic Stress Analysis (TSA)

2.7.1 The TSA Relationship for Orthotropic Materials

A material which undergoes a change in applied stress will experience a change in temperature. This relationship between mechanical deformation and thermal energy in an elastic solid is known as the thermoelastic effect [44, 48]. By loading a material within the elastic range a full-field map of the small temperature changes can be measured simultaneously using an IR camera and the surface stress state calculated.

For a linear elastic, homogenous material, the rate of change of temperature in a material can be related to the applied deformation as follows:

$$\dot{T} = \frac{T_0}{\rho C_\varepsilon}\frac{\partial \sigma_{ij}}{\partial T}\dot{\varepsilon}_{ij} - \frac{\dot{Q}}{\rho C_\varepsilon} \quad \text{for } i,j = 1,2,3 \qquad 2.26$$

where T is the absolute temperature of the material, C_ε is the specific heat at constant strain, $\dot{Q}$ is the rate of heat production per unit volume, ρ is the mass density, σ_{ij} is the stress tensor and $\dot{\varepsilon}_{ij}$ is the rate of change of the strain tensor.

During TSA, a material is cyclically loaded at a sufficient frequency that the heat transfer term, $\dot{Q}$, can be neglected and the loading can be assumed to be adiabatic [49]. For most materials, the change in elastic properties, E and v, at room temperature are practically zero and can be neglected [49]. Also, the through thickness stress term for the surface ply, σ_{33}, is considered as zero as the surface ply is in a state of plane stress [50]. It can therefore be shown [44] that for an orthotropic material, a temperature directly relates to the rate of change of stress [19]:

$$\Delta T = -\frac{T_0}{\rho C_p}(\alpha_1 \Delta\sigma_1 + \alpha_2 \Delta\sigma_2) \qquad 2.27$$

where ΔT is the change in temperature, T_0 is the absolute temperature, α is the coefficient of thermal expansion, C_p is the specific heat at constant pressure and $\Delta\sigma$ is the change in stress, where the subscripts 1,2 and refer to the material coordinates.

For orthotropic materials such as laminated FRP, it is assumed that the principal material directions and principle stress directions are coincidental [11]. Equation 2.27 is often normalised by the mean background temperature T_0 to take into account any changes due to ambient temperature or heating at local damage sites [18, 51] :

$$\frac{\Delta T}{T_0} = K_1 \Delta\sigma_1 + K_2 \Delta\sigma_2 \qquad 2.28$$

$$\text{where} \quad K_1 = \frac{\alpha_1}{\rho C_p}, \ K_2 = \frac{\alpha_2}{\rho C_p}$$

The constants K_1 and K_2 are obtained empirically by measuring the thermoelastic response of the same material in a unidirectional lay-up loaded in tension, such that one of the principal stresses reduces to zero. Such calibration is not carried out in the thesis and as a result all thermoelastic data presented is proportional to the surface stress sum.

2.8 TSA Processing

To enable TSA analysis, a series of thermal images are recorded synchronously with the applied load signal across multiple loading cycles. The Silver 480M detector features a lock-in amplifier for this purpose. All IR images are converted to absolute temperature maps using the standard calibration procedure, stated in section 2.6.

The Altair-Li 5.90 software by CEDIP is used in the thesis to process IR image sets via TSA. The analysis is conducted by applying a fast Fourier transform (FFT) to the temperature values of each pixel in the image series to obtain the magnitude (ΔT) of each pixel. The use of the load reference signal helps to reduce noise in the calculated ΔT data and allows the phase difference between the thermoelastic response and the load reference signal to be found. Due to the characteristics of the test machine, load cell and IR detector, there is usually a constant phase offset between the load reference signal and the thermal signal [52]. Unlike some other thermography systems, this offset is not calibrated prior to image capture and post processing must be conducted using an area of known phase response [52]. An area of material that undergoes tensile loading with an increase in applied load will display a temperature response that is 180° out of phase with the load signal assuming adiabatic conditions [22]. Phase data can be useful in identifying locations of damage that may otherwise be undetectable due to localised departures from thermoelastic behaviour at regions of damage [52]. To relate the change in temperature to the surface stress state of a laminated FRP material, further calibration is required to determine the K_1 and K_2 thermoelastic constants. This procedure is not conducted in the thesis.

Since each pixel in an IR camera can be related to the surface stress sum, the full field data obtained using the TSA method will have a greater spatial resolution than the DIC technique when using images of equal spatial resolution. This is due to the DIC technique requiring a group of pixels (subset) for each data point.

2.8.1 Error Sources in TSA

Several potential areas of error were identified from the literature:

Non-Adiabatic Effects

One of the main drawbacks of TSA is that adiabatic conditions must be achieved to ensure that the measured temperature change is a response of the stress change alone [53].

A more complete form of the TSA equation can be given as follows [42]:

$$\frac{\partial T}{\partial t} = \frac{1}{\rho C_p}\left(k_{th}\nabla^2 T - T\alpha\frac{\partial \sigma_1 + \sigma_2 + \sigma_3}{\partial t}\right) \qquad 2.29$$

where k_{th} is the thermal conductivity and t is time

True adiabatic conditions are only created when the spatial heat transfer term, $k\nabla^2 T$, is zero, either when $k = 0$, or $\nabla^2 T = 0$. k is typically small but non zero in FRP materials. $\nabla^2 T$ may equal zero for certain load conditions, i.e. when the adiabatic temperature change in a material is uniform throughout a material, causing no temperature gradients [42]. In most applications approximate adiabatic conditions are generated by making ∂t small through the use of a high loading frequency [42].

At significant stress gradients, such as between 90° and 0° plies in crossply laminates or at locations of damage, heat transfer is increased and the adiabatic assumption may longer be valid [54]. In metallic specimens, a cyclic loading frequency of between 10 and 30 Hz has been shown to be sufficient for adiabatic conditions [55]. Due to the lower thermal conductivity of FRP materials, it would be expected that the frequency required for adiabatic conditions would be lower. However it has been shown in crossply CFRP laminates that due to the high stress concentration between layers, a loading frequency of greater than 30 Hz is required to create adiabatic conditions [54]. This is beyond the capacity of the test machines available for the work described in the PhD, therefore some non-adiabatic effects may be expected when testing FRP specimens.

Mean Stress Effect

Wong *et al* [56] re-evaluated the TSA equation to take into account the change in elastic properties with temperature, known as the mean stress effect:

$$\Delta T = -\frac{\alpha T}{\rho C_\varepsilon}\left(1 - \frac{1}{\alpha E^2}\frac{\partial E}{\partial T}\sigma_m\right)\Delta\sigma_x \qquad 2.30$$

In the case of steel is has been shown that for a 1% error in the derived stress, $\Delta\sigma_x$, the mean stress needs to equal 50% of the material yield stress [57]. In glass epoxy composites, a mean stress change between 0 and 189 MPa was found to result in a TSA stress response change of approximately 3% [58]. Zhang *et al* also found that the mean stress effect in crossply glass epoxy laminates was negligible in comparison to the effect of the cyclic stress range when $\Delta\sigma_x = 58$ MPa [59].

Surface Coating

Whilst epoxy based composite materials have a sufficiently high emissivity to not require a paint coating for TSA analysis, the DIC technique still requires use of a paint coating to give sufficient surface contrast.

Two types of behaviour are known to occur in TSA due to a coating; thermal lag and thermal drag-down [55]. Thermal lag is caused by the paint layer acting as a thermal insulator, causing a smaller measured ΔT at the paint surface than at the surface of the specimen. Thermal drag-down is a function of loading frequency and paint thickness. At high loading frequencies (or thick paint layers), heat does not have time to conduct into the coating, resulting in inaccurate thermoelastic measurements [16]. An extensive analysis of the effect of paint coating type and thickness on TSA measurements was conducted by Robinson *et al* on aluminium and steel specimens [16]. The study found that RS matt black paint gave the most consistent thermoelastic signal and that two to three passes (equivalent to 15 to 25 μm coating thickness) combined with a loading frequency of between 5 and 15 Hz was optimum for TSA analysis on metallic specimens.

It has been noted by some authors that the thermoelastic response of FRP laminates is from the isotropic 25 μm thick resin layer on the outer surface of a laminate [60]. This was shown not to be the case for different material types and manufacturing processes where the resin rich layer was not so thick, showing that the majority of the thermoelastic response is from the outer surface ply [23].

2.9 Conclusions

The chapter has provided justification for the use of a combination of DIC and thermographic techniques for the study of damage in FRP materials over other full-field techniques. DIC, IR-thermography and TSA have compatible surface preparation requirements, have relatively low experimental complexity and depending on the exact imaging setup should be able to give adequate sensitivity and spatial resolution for the identification of damage in FRP materials.

As these full-field techniques rely on the use of digital cameras, the chapter begins with an overview of digital sensor technology. Since the techniques are to be applied to intermediate strain rate tests, high speed digital sensors are also discussed along with their potential disadvantages.

The underlying theory of the DIC technique has been presented with a focus on the algorithms used by the image correlation software DaVis 8.1.3, used throughout the thesis. The principle behind IR-thermography is outlined, with its advantages and limitations discussed. The operation of the Silver 480M IR camera is presented and along with the two types of temperature calibration procedure used in the thesis. Finally an overview of TSA theory is presented along with potential error sources when used for identification of damage in FRP materials.

The literature review conducted is important for the work conducted in the PhD for the following reasons:

- Knowledge of the underlying theory of the measurement techniques is important to understand the influence of experimental variables, post-processing parameters and sources of error.
- An awareness of the known sources of error for the measurement techniques used is crucial to avoid such pitfalls and obtain reliable measurements in later chapters.
- A review of previous studies applying full-field methods to the study of FRP damage behaviour has been invaluable in understanding the advantages and limitations of the various techniques. It has also highlighted the current lack of full-field investigations into the damage behaviour of FRP at high strain rates.
- The review has confirmed that DIC and IR-thermography are compatible with each other in terms of experimental setup, specifically in surface preparation requirements.

Chapter 3

Damage Mechanisms in Fibre-Reinforced Composites: An Overview

3.1 Introduction

The chapter contains a review of the literature on the mechanics of damage in laminated FRP materials. The purpose of the chapter is to establish a basis for the interpretation and discussion of the results from the work conducted during the PhD presented in later chapters of the thesis. The focus of the PhD is to develop imaging methodologies to capture damage initiation, evolution and failure in FRPs, therefore material studies will be limited to simple uniaxial tension. Only literature that considers uniaxial tension will be discussed in the present review, with the emphasis on the behaviour of crossply carbon-epoxy and glass-epoxy laminates as these are used in most of the experimental work described in the thesis; the reasons for this material and lay-up choice are discussed further in Chapter 4.

The chapter begins with an overview of the damage sequence expected in unidirectional laminates, followed by the more complex and interacting damage behaviour of multiaxial laminates. The role of three-dimensional effects within multiaxial laminates is also discussed. Increased strain rates are known to cause a change in both the material properties and the damage behaviour within certain FRP materials and layup configurations, the mechanisms of which are discussed within the chapter. Later chapters aim to use IR-thermography to identify damage in FRP specimens. A section within this chapter is therefore devoted to a discussion of the causal mechanisms of heat generation within FRP materials.

The chapter places specific emphasis upon previous applications of full-field optical techniques to the study of FRP damage, both during quasi-static and elevated strain rate loading. The review aims to identify the advantages and limitations of the full-field techniques for FRP damage study, thus informing the design of the experimental methodologies developed in later chapters.

3.2 Damage Progression under Tensile Loading

Metallic structures often retain their structural integrity after overloading due to the energy dissipation and redistribution of stresses during plastic deformation [5, 61]. In contrast, overloaded FRP components typically do not exhibit gross yielding [61]. Energy is instead dissipated in FRP materials through the formation of complex and interacting types of damage, potentially causing significant performance degradation [18]. The onset of damage may result in an FRP structure no longer being functional, either due to a decrease in stiffness, strength or the increased risk of moisture or chemical ingress. Such contrasting behaviour in damage tolerance can be attributed to the complex and interacting damage behaviour in FRP materials.

The behaviour of monolithic materials to an applied load can broadly be described by one of the following responses: elastic, elastic-plastic, viscoelastic or viscoplastic [62]. Truly brittle materials exhibit an elastic response showing little plastic deformation prior to final failure. Examples include ceramics, certain polymers and some metals at low temperatures [63]. Typical fibre reinforcements such as carbon and glass fibre behave in a brittle manner and as a consequence, have a low fracture toughness [2, 64]. Commonly used FRP matrix materials, such as polyester and epoxy, show a more ductile viscoelastic or viscoplastic response [65] which becomes more important at greater applied strain rates [66]. The matrix phase is used to provide stress transfer between fibres and to protect the fibres from the environment [2, 65, 67]. When the constituent parts are combined into an FRP composite the material demonstrates a more progressive failure sequence [68]. This is due to the energy dispersing damage mechanisms that occur at the fibre and lamina scales [2].

3.2.1 Unidirectional Laminates Subjected to Longitudinal Tension

Damage is likely to initiate in FRP materials at the locations of defects, creating a local stress concentration effect [69, 70]. Fibres will typically have a random distribution of microstructural flaws, the severity of which is dependent on their size, shape, and location [64, 71]. Flaws within the resin matrix may include voids, inclusions or resin-rich areas [69], whilst flaws at the fibre-resin interface may be caused by contamination of the fibre surfaces or incorrect fibre surface preparation [72]. An isolated small flaw will usually be arrested by adjacent fibres [73], but in the case of a sufficiently large defect, or cluster of defects, a single failure location may dominate the failure sequence of the laminate [74].

When unidirectional FRP laminates are loaded under tension in the fibre direction, the phase to fail first is that which possesses a lower strain to failure value. In most FRP composites, this is the fibre phase [73]. Fibre breaks are usually not crucial to the overall strength of a laminate as load can be transferred to adjacent intact fibres by shearing of the matrix. However, in glass-epoxy and carbon epoxy laminates, a single fibre break has been shown to contribute to higher fibre loads within a local area, increasing the chance of additional fibre failures [73].

The types of failure mechanisms possible around a single fibre break are shown in Figure 12. A brittle matrix with a high interfacial strength will typically form a crack in the matrix before being arrested at the next fibre, as shown by image (a) in Figure 12. A weak interface combined with a relatively high fibre elongation to failure results in debonding between the fibre and matrix and subsequent fibre pullout as shown in image (b). A ductile matrix may result in a shear type failure through the matrix up to the next fibre, image (c) [2, 75].

As the tensile load increases, such failures increase in number and density. A fibre fracture occurs rapidly and induces a stress concentration effect on surrounding fibres due to the viscoelastic behaviour of the matrix. This shear loading is greatest in magnitude at the instance of first occurrence, dropping to a lower steady-state value [76]. This stress concentration effect may promote a cascading effect of fibre breaks which may lead to ultimate failure of the laminate [77].

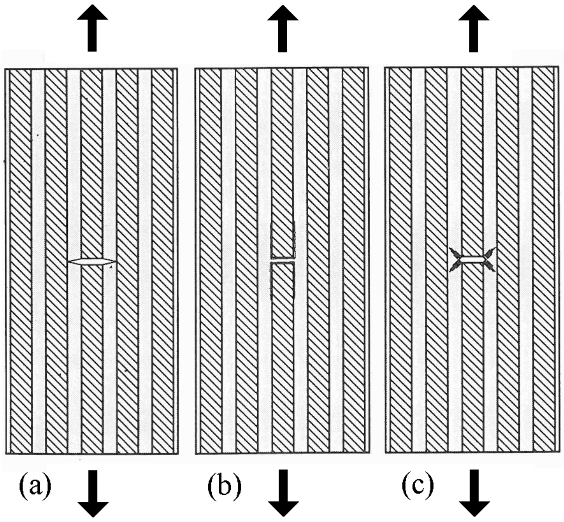

Figure 12: Potential failure mechanisms around a single fibre break in a unidirectional laminate under tension: (a) brittle matrix with a high interfacial strength, crack is arrested at next fibre, (b) weak interface with a high fibre elongation to failure resulting in fibre pullout, (c) ductile matrix resulting in a shear type failure of matrix [2]

According to Aveston, Cooper and Kelly (ACK) theory [78], a unidirectional FRP laminate may fail either due to a single fracture or multiple fracture events. For typical glass-epoxy and carbon-epoxy laminates of 0.55-0.65 fibre volume fraction, the laminate is predicted to fail due to a single fracture event [73]. Real laminates rarely fail across one clean fracture surface due to variations in fibre and interfacial strength [73]. Such variations can also cause multiple fibre breaks to occur. The coalescence of such fibre breaks may result in a macrocrack, causing total failure. This damage sequence is depicted in Figure 13.

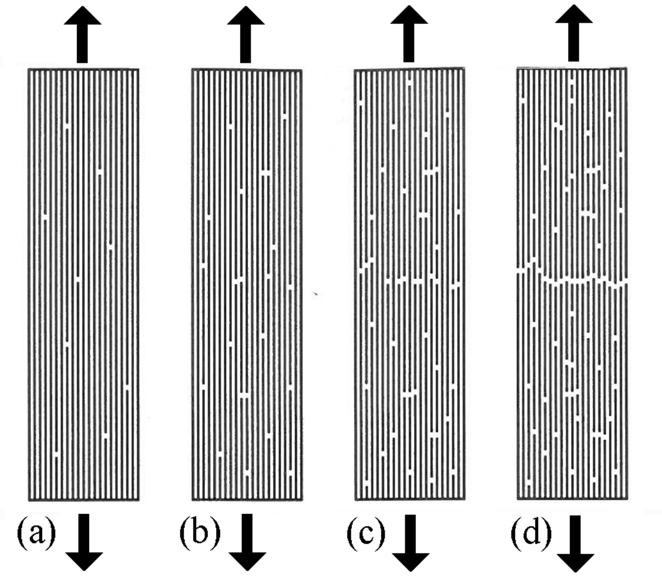

Figure 13: Progressive fibre failure in a unidirectional laminate under tension. (a) Initial fibre fractures, (b) increasing in density, (c) coalescing into cracks, (d) until eventual formation of a macrocrack and complete specimen failure [2].

Matrix cracks along the fibre axis, commonly known as longitudinal splitting may also occur in unidirectional laminates when a transverse load is created. Such loads may occur when the transverse contraction of a laminate due to the Poisson's ratio effect is restricted by end tabs or grip surfaces. This damage type is similar to that of transverse cracking discussed in section 3.2.2.

As the diameter of glass and carbon fibres are of the order of tens of micrometres [79], only high resolution examination techniques are able to resolve individual fibre breaks. The application of IR and white-light imaging to study individual fibre breaks would require the use of microscopic lenses, drastically complicating the experimental setup. It is therefore outside of the scope of the thesis to attempt to resolve fibre-scale damage. As longitudinal splitting tends to occur at a larger scale and affect a larger specimen area, it is more likely to be identifiable using optical techniques. The thesis therefore focuses upon the use of the optical techniques to study damage at the lamina scale and beyond.

3.2.2 Unidirectional Laminates Subjected to Transverse Tension

Unidirectional FRP laminates loaded in tension perpendicular to the fibre direction fail at a far lower load than when loaded parallel to the fibre direction. For this reason, transverse loading is generally avoided in unidirectional composites. This behaviour is due to the lack of reinforcement provided by the high strength fibres. The transverse strength of unidirectional laminates is less than that of pure resin due to the stress concentrations that develop around fibres [2, 80]. In GFRP laminates, the stress concentration factor may reach up to a value of 20, whilst in CFRP laminates, a maximum stress concentration factor of 4 is reached due to the lower transverse modulus of carbon fibre [81]. These values increase with greater fibre volume fractions [2]. Crack initiation may occur at the fibre-matrix interface or within the resin, as shown in Figure 14, depending on the interfacial strength of the composite and the presence and severity of any flaws. Fibre debonding has been shown to be the dominant mechanism for microcracks leading to transverse cracking in glass and carbon epoxy laminates [81].

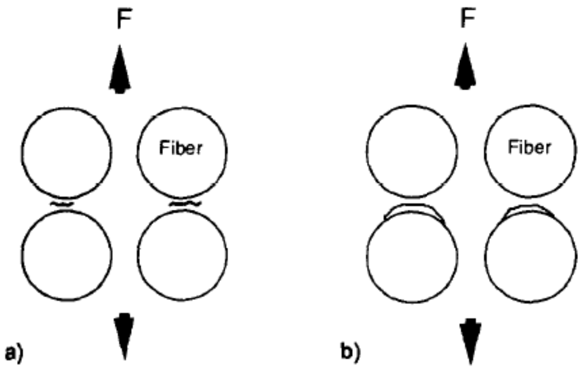

Figure 14: Damage initiation mechanisms for transverse cracks: (a) crack initiation in the matrix, (b) transverse crack initiation at the fibre/matrix interface [80].

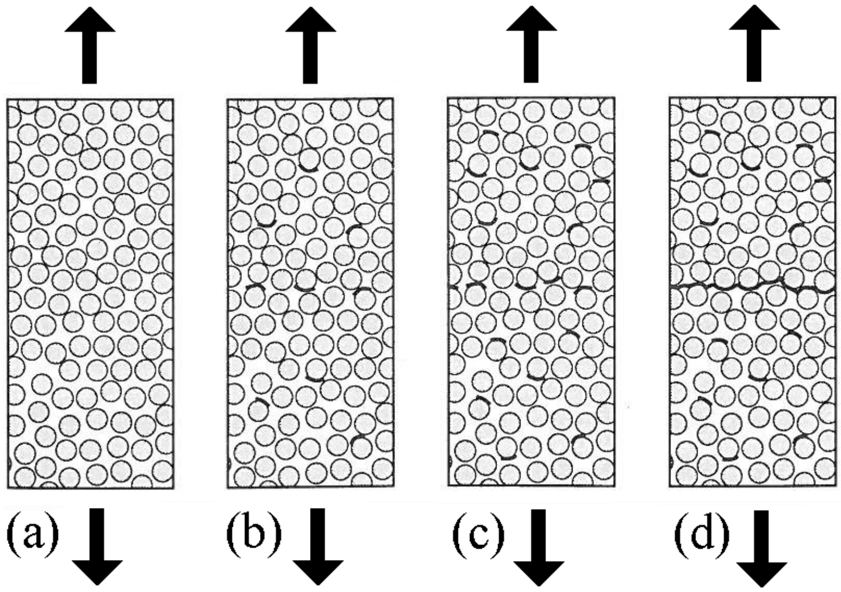

Figure 15: Progressive microcracking failure in a unidirectional laminate subjected to transverse tension, ranging from crack initiation in (a) and (b) leading to crack coalescence (c) and macroscopic failure (d) [2].

Given that a single large flaw is not present, further loading will cause microcracks to coalesce into a transverse crack and cause final failure in a unidirectional laminate. This progression is shown schematically in Figure 15. Due to the fibres providing little reinforcement in this orientation, the transverse tension performance is dominated by the matrix and interfacial strength properties [2]. When such a crack occurs in a multiaxial laminate (typically in a ply orientated 90° to the direction of loading) it is referred to as a transverse ply crack.

3.2.3 The Behaviour of Multiaxial Laminates Subjected to Tension

Multiaxial laminates consist of a stack of plies with the fibres orientated in different directions. Two commonly used stacking configurations are quasi-isotropic $[0,+45,-45,90]_s$ and cross-ply $[0,90]_{ns}$ [82]. The former has in-plane elastic properties that are approximately constant for all possible loading angles and the latter lacks any stiffness coupling between in-plane loading and out-of-plane deformation (bending) [2]. The laminate notation and coordinates used in this thesis are shown in Figure 16, where θ is the ply fibre angle away from the y axis. In the case of the crossply laminate discussed, the global coordinates are coincident with the material direction for the $0°$ plies and rotated by $90°$ for the $90°$ plies.

In contrast to unidirectional laminates, multiaxial FRP materials display complicated and interacting damage behaviour between plies that is inherently difficult to predict, as highlighted by the results of multiple world-wide failure exercises [83-85]. When subjected to uniaxial tension, the first ply failure (FPF) of most multiaxial laminates and the most common damage type in crossply laminates is transverse cracking [75]. This is due to the reasons previously discussed in section 3.2.2. Plies in which the fibres are parallel to the x axis have the greatest likelihood of transverse crack formation, with the first cracks occurring at the locations of the most severe material flaws [86]. Transverse cracks often promote the onset of further types of damage [87].

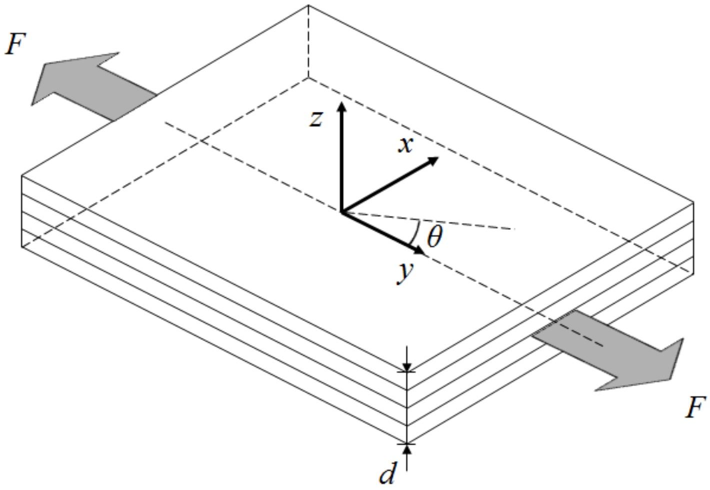

Figure 16: Laminate notation, where x, y, z are the laminate global coordinates, d is the laminate thickness, F is the tensile load in the y direction and θ is the ply fibre angle away from the y axis.

The tensile loading of a multi-axial laminate, as shown in Figure 16, generates a complex stress state due to the orthotropic stiffness response of each lamina. Each lamina experiences a combination of in-plane normal, (σ_x, σ_y) and shear stress (σ_{xy}) that can be predicted by classical laminate theory (CLT) [2]. CLT assumes that all layers are in a state of plane stress, i.e. the out of plane stress and other shear stresses are zero, $\sigma_z = \sigma_{yz} = \sigma_{xz} = 0$. This approximation is accurate at the centre of a laminate but at geometrical discontinuities, such as holes or close to laminate edges, such assumptions are not valid. The latter is known as the free-edge effect and is important in the initiation of damage in laminated structures.

As the focus of this thesis is the development of novel experimental methodologies, it was decided to use a specimen layup configuration with relatively simple and well known behaviour. Symmetric crossply specimens were therefore selected, as these have been the subject of extensive prior research [73, 75, 88-90].

The free edge effect can cause large perturbations to the predictions of CLT theory, especially within one laminate width of a free edge [91]. Therefore the free-edge effect has been extensively studied [92-96]. A review by Mittelstedt *et al* [91] outlines much of the research effort which includes approximate closed-form solutions and numerical models. Despite such efforts, no single exact elastic model exists to describe the 3D stress state at free edges [91].

To explain the free-edge effect, a $[0,90]_s$ crossply laminate is considered as not bonded between plies and subjected to a uniaxial strain ε_{11}. This is shown in Figure 17 (i). The laminate is taken as being sufficiently long in the y direction, such that stresses and strains in this direction are not a function of position. Poisson's ratio mismatches between $0°$ and $90°$ plies cause different elastic transverse strains ε_x where the major Poisson's ratio is defined as follows:

$$v_{yx} = -\frac{\varepsilon_x}{\varepsilon_y} \qquad 3.1$$

where v_{yx} is the major Poisson's ratio of a ply, ε_y is the normal strain in the y direction and ε_x is the normal strain in the x direction.

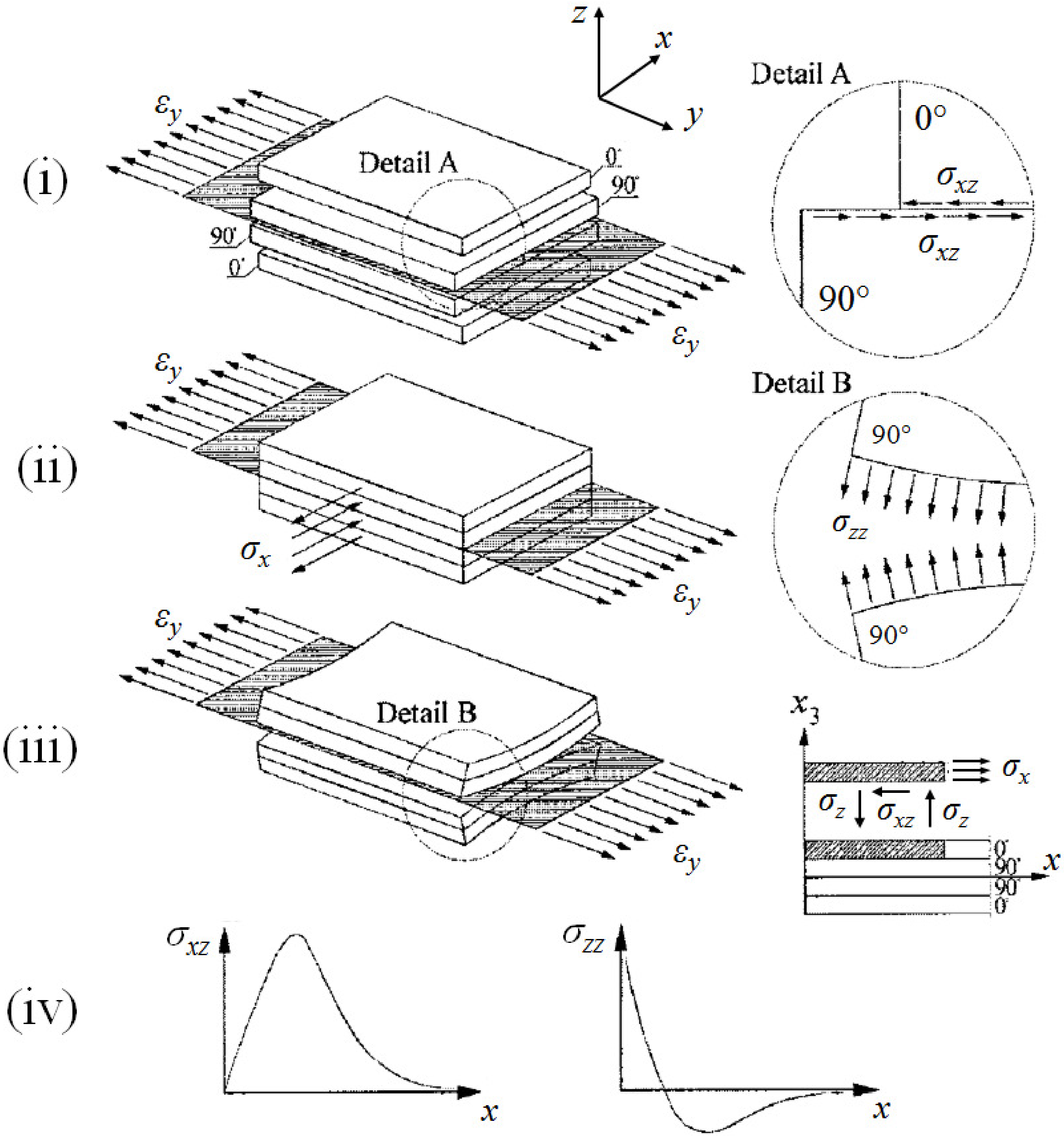

Figure 17: The free-edge effect in a $[0,90]_S$ *crossply laminate under uniaxial extension [91]*

In real laminates with bonded plies, a displacement continuity cannot exist and in-plane strain must match through all plies. Transverse stresses, σ_x, are therefore generated due to the stiffness mismatch between *0°* and *90°* plies. The transverse stresses, σ_x, generated in *0°* layers are tensile and compressive in *90°* layers. To maintain equilibrium, the transverse stresses, σ_x, are accompanied by an interlaminar shear stress σ_{xz}, at the 0/90 interface, as shown by detail A in Figure 17.

The transverse stress σ_x occurs through the ply thickness and the interlaminar stress σ_{xz} occurs at the ply interface, as shown by the free body diagram in Figure 17. They therefore do not share a common axis and a moment is created about the y axis. To maintain moment equilibrium, an interlaminar normal stress σ_z is created. The σ_{xz} and σ_z stress distributions along x are shown in Figure 17.

In theory the σ_z is infinite at the free edge, but in reality the stress levels are decreased due to the presence of an adhesive layer between plies [97]. Nevertheless, out of plane stresses are a maximum at the free edge and result in a tendency for crossply laminates to peel at free edges as depicted in Figure 17 (iii). Such a separation of two adjacent plies of a laminate is known as a delamination [98].

The shear coupling coefficient is defined as the ratio between the normal stress in the y direction, $\sigma_{y,}$ and the shear strain in the yx plane, ε_{yx}:

$$\eta_{yx} = \frac{\varepsilon_{yx}}{\varepsilon_y} = \frac{E_y \varepsilon_{yx}}{\sigma_y} \qquad 3.2$$

The work by Herakovich [97] found numerically that for angle-ply laminates, $[+\theta,-\theta]_s$, the Poisson's ratio mismatch between plies is a maximum when θ = 15° and the shear coupling coefficient is at a maximum when θ = 22°. In an experimental investigation, the first failure modes found to form at the free edges in θ = 10° and θ = 30° laminates were delaminations. When the angle is increased to θ = 60°, transverse cracking became the dominant edge failure mechanism. The shear coupling coefficient is therefore the dominant factor in edge stress generation for angle-ply laminates but for crossply laminates where the shear coupling coefficient is zero, delaminations occur solely due to interlaminar normal stresses, $\sigma_{z.}$ Such delaminations occur only at larger strains, well after that required to form transverse cracks.

3.2.4 Damage Development from Free Edge Effects

The free edge stress state is important when it comes to understanding the damage initiation process in FRP materials. Transverse cracks are usually the first type of damage to occur in a laminated composite subjected to tension [89] and will typically occur within the first 80 % of a component lifetime during fatigue tests [88]. Whilst they are often detrimental to a laminate's stiffness [99] and may promote the initiation of further damage types, the do not cause catastrophic failure alone.

As previously mentioned, various three-dimensional analytical and finite-element techniques have been developed to study the stress distribution due to the free edge effect in laminated materials, but no exact elasticity solution exists. The theoretical work by Tahani *et al* [100] predicts and confirms the earlier work by Wang *et al* [101] that the interlaminar normal stress σ_{33} and the interlaminar shear stress σ_{23} between plies in crossply laminates are of greatest magnitude at the free edge. There is a limitation to such models however as they tend to predict a singularity at ply interfaces at the free edge, which as discussed earlier, cannot exist and will either be dissipated by the adhesive layer between plies or cause damage to be created.

Yokozeki *et al* [89] found that transverse cracks initiate in both quasi-isotropic and crossply laminates at the free edges of specimens even after polishing free edge surfaces to eliminate the possibility of damage during manufacture. A crack that initiates at a free edge and only spans a small fraction of the entire width in a single ply is defined as an edge crack. Figure 18 (a) shows an X-ray image of such edge cracks in a quasi-isotropic glass-epoxy coupon, highlighted through the use of a penetrant dye. Edge cracks may propagate instantaneously across the entire width under quasi-static loading, to form a transverse crack, or propagate more progressively into the laminate width with increasing load or load cycles [89]. Several authors have noted that delaminations around edge cracks were found to reduce the chance of an edge crack developing into a full transverse crack [90, 102].

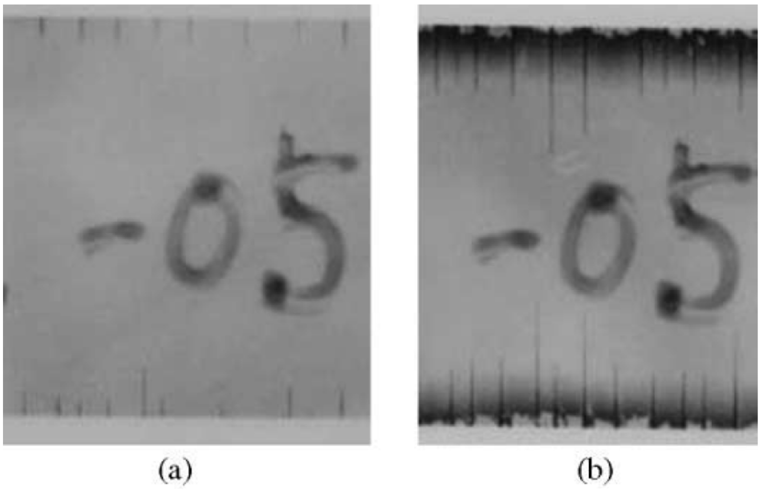
(a) (b)

Figure 18: X-ray images of edge cracks in [45/0/-45/90]s laminates showing: (a) edge crack saturation (at 3000 cycles), (b) crack propagation across the width (at 10000 cycles) [89].

Crossply laminates have a greater tendency than quasi-isotropic layups for edge cracks to form instantly into full-width transverse cracks [89]. The applied strain for first transverse crack formation in crossply laminates *[0,90]*$_s$ is related to the thickness of the inner *90*° block of plies [81, 103, 104]. As the thickness of the *90*° ply block increases, the constraint imposed by the *0*° plies becomes less significant and transverse cracks are found to form at lower applied strains. Transverse cracks were found to propagate quickly in laminates with thicker *90*° plies, whilst transverse cracks were found to initiate in laminates with thinner *90*° plies at low strains but not propagate until the application of higher strains [81]. The applied strain to first transverse crack formation in glass-epoxy was found to be 0.5% for *[0,90]*$_s$ laminates and 0.22% in otherwise identical *[90,0]*$_s$ laminates [81]. Three-dimensional finite element (FE) analysis has shown that this difference is due to the change in energy release rate associated with crack formation with an increase in edge crack length [89]. In quasi-isotropic laminates, the energy release rate is highest close to the free edges but approaches a steady-state value as the crack tip grows closer to the centre of the specimen width [89]. Such an edge effect cannot be predicted by a two-dimensional analysis. Crossply laminates were found to display a very small increase in energy release rate at the free edges, and as such, tend to propagate into transverse cracks immediately upon initiation in quasi-static tests [89]. Berthelot *et al* [88] has shown that it is possible to obtain stable transverse crack growth from edge cracks during fatigue loading of crossply laminates.

In the study by Yokozeki [89], crossply laminates were cyclically-loaded to study the behaviour of edge cracks. New edge cracks were found to form simultaneously with the propagation of existing edge cracks. Edge cracks were found to propagate stably into full-width transverse cracks under cyclic loading [89].

In a crossply laminate, the axial stress in the *90°* plies decreases in the vicinity of an existing transverse crack, so reducing the likelihood of further transverse crack formation [73]. As static load (or equivalently cyclic load number) increases, further transverse cracks form until a saturation point is reached. This state is known as the characteristic damage state of a laminate [2]. This progression is shown schematically in Figure 19. At this point of saturation, the minimum transverse crack spacing is usually of the same order as the layer thickness.

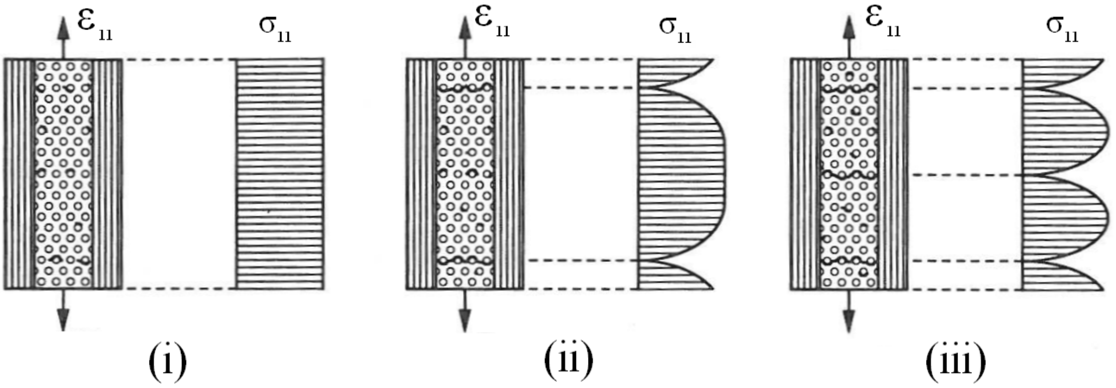

Figure 19: Schematic of crossply laminate subjected to an increasing uniaxial strain ε_{11}*. (i) Constant normal stress in 90° ply with initial microcrack formation at fibre-matrix interfaces, (ii) normal stress reduction in 90° ply due to the presence of transverse cracks, (iii) Saturation of transverse cracks occurring to give the characteristic damage state [2].*

It has been shown that when crossply laminates are subjected to fatigue loading, transverse cracks are often accompanied by delaminations and matrix cracks in *0°* plies as shown in Figure 20 [73, 90]. Such cracks, often known as longitudinal splitting, form due to the restraint of the Poisson's ratio contraction imposed by adjacent *90°* layers [73]. They extend only a short distance from the transverse crack from which they originate, indicating a local effect.

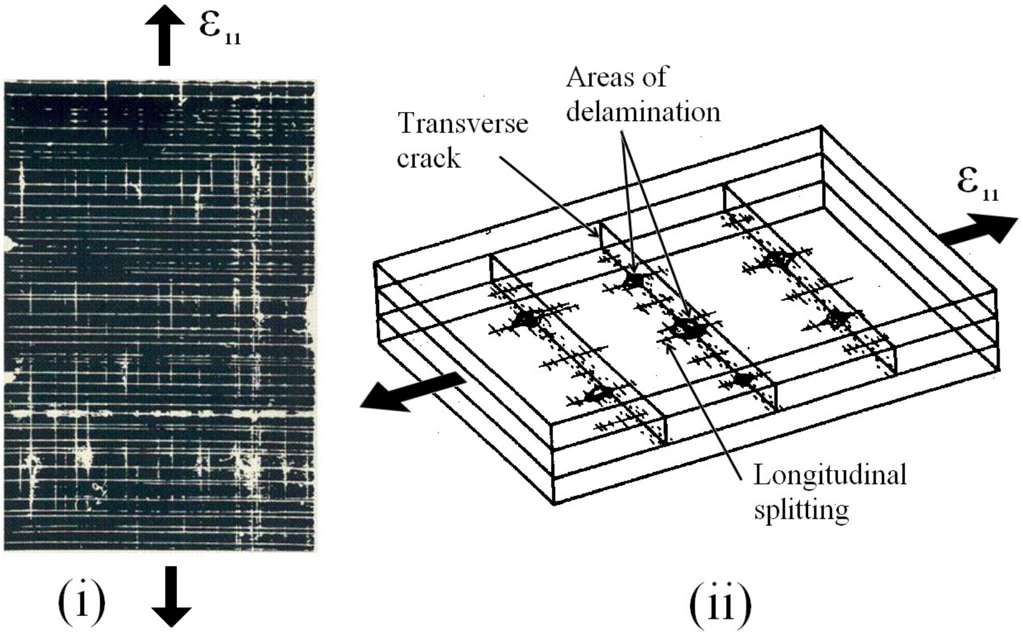

Figure 20: Longitudinal splitting and delaminations in a crossply laminate due to the presence of transverse cracks. (i) An X-ray radiograph of a laminate having undergone fatigue, (ii) a corresponding schematic showing the delaminations (dark areas) and longitudinal splitting emanating from transverse cracks [73].

Figure 21 (i) shows an idealised transverse crack in a crossply laminate where the crack tip ends at a *0/90* interface. Further loading causes the crack to propagate by one of two possible paths, as shown in Figure 21 (ii) for a crack penetrating into the *0*° layer and (iii) for a crack which is deflected into the *0/90* interface. The crack path taken depends on the energy release rates of each. When the following condition is satisfied, the crack is deflected into the interface.

$$\frac{G_d}{G_p} > \frac{G_c^{(i)}}{G_c^{(1)}} \tag{3.3}$$

where G_d is the energy release rate for the deflection crack path into the *0/90* interface, G_p is the energy release rate for a penetrating crack into neighbouring *0*° plies, $G_c^{(i)}$ is the *0/90* interface toughness and $G_c^{(1)}$ is the plane-strain mode I toughness of the *0*° layer [75].

When the ratio of deflecting to penetrating crack energy release rates is greater than the ratio of interface toughness to *0*° layer mode I toughness, the crack will be deflected into the interface. This implies that in a system with stiffer fibres, such as CFRP laminates, a transverse crack is more likely to penetrate into *0*° layers, eventually failing through the creation of a macrocrack through the entire laminate thickness [75]. A crack which is deflected into the *0/90* ply interface results in local delaminations [73]. Such a deflection may show a longer fatigue life. With further loading cycles, final failure will eventually occur due to cracks penetrating into 0° plies and eventual fibre fracture, at which point structural integrity is quickly lost [75].

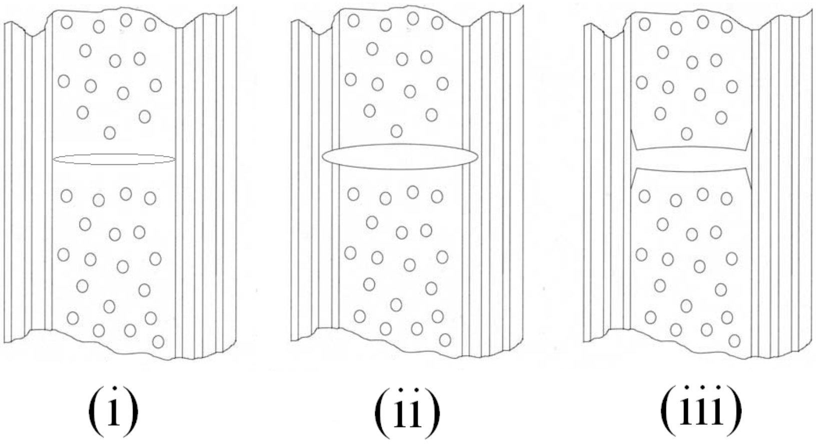

Figure 21: Possible crack paths in a crossply laminate from a transverse crack tip. (i) An idealised transverse crack ending at 0/90 interfaces, (ii) a penetrating crack propagating into 0° layers, (iii) a deflecting crack leading to delamination along 0/90 ply interfaces [75].

From the literature review thus far, it is clear that the damage sequence of crossply laminates under quasi-static and cyclic loading are well known and therefore such specimens are well suited for use in the thesis. Edge cracking, followed by transverse cracking is likely to be the first type of damage to occur in crossply laminates. As the full-field techniques to be employed are surface measurements, crossply laminates with external 90° plies are recommended to be used. Specimen details are discussed further in section 4.6.

3.3 FRP Strain Rate Sensitivity

Most FRP components are designed according to data gathered at quasi-static strain rates (~10^{-4} s^{-1}), but occasionally intermediate (~1 s^{-1}) and high strain rate (>180 s^{-1}) loading may occur [6]. Numerous studies have investigated the mechanical properties and the damage propagation of FRP materials under quasi-static conditions and as a result many failure criteria exist but none take into account strain rate effects [6].

The effect of strain rate on the mechanical properties of FRP laminates is determined by several factors including the rate dependency of the fibre and the rate dependency of the matrix, the fibre orientation and layup. The direction of loading and loading type also affect the strain rate dependency [5]. In situations where a unidirectional laminate is loaded in tension along the fibre direction, the fibre properties are expected to dominate the strain rate response [5]. The opposite is true for transverse and shear loading, whereby the matrix is expected to define the strain rate dependency. The effect of strain rate on the stiffness response of epoxy resin is shown in Figure 22, showing a distinct viscoelastic response with a stiffening effect at higher applied strain rates. Little work has been carried out on the strain rate dependency of fibres due to inherent difficulties with the testing of individual fibres and fibre bundles [5]. However as carbon and glass fibres do not behave viscoelastically, a strain rate dependent response is not expected. A complicating factor for multiaxial laminates is the possibility of strain rate dependent damage creation at fibre and ply interfaces [5].

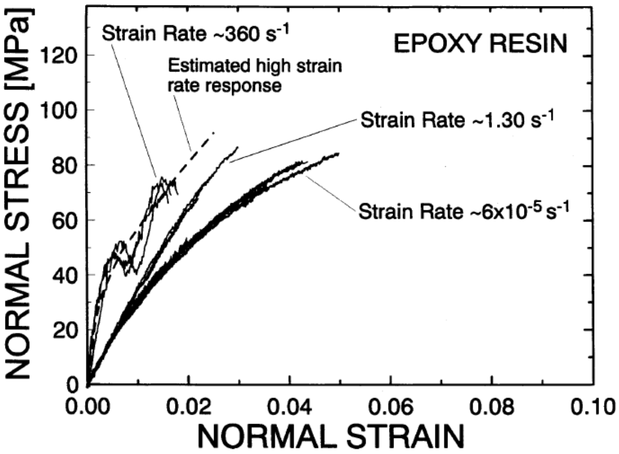

Figure 22: Stiffness changes according to strain rate for pure epoxy resin [105]

Many previous studies into the strain rate behaviour of FRP materials up to and beyond 1000 s^{-1} have used split-Hopkinson bars (SHB) [6]. These devices require small specimen samples of around 10 mm^2 to minimise inertia and wave-propagation effects within the specimen and so conflict with the need for FRP specimens to be large relative to the reinforcement [5]. Free-edge effects may also be more influential in such small specimens as they generally occur within a laminates width from the free edge [91]. A SHB is designed to load in compression unless significant adaptations are made. A tensile fixture requires minimal impedance mismatch across the fixture which is difficult to achieve in practice. As a result, most high strain rate work discusses the behaviour of FRP under uniaxial compression with small specimen sizes. The work by Daniel *et al* [106] and Gilat *et al* [105] are some of the few examples studying the tensile behaviour of FRP materials.

Gilat [105] used servo-hydraulic test machines to load carbon-epoxy samples up to rates of 1 s^{-1}, beyond which a SHB in tension was used to achieve strain rates up to 600 s^{-1}. Identical waisted specimens were used throughout all tests. Specimens with fibre angles of *10°*, *45°* and *90°* away from the axis of loading were tested. The different responses according to fibre angle are shown in Figure 23. An increase in stiffness and ultimate strength was found across all tests, with a more significant effect found in specimens of *45°* fibre angle. The work by Daniel *et al* [106] also studied the effect of fibre orientation on strain rate response using expanding ring type loading, coming to similar conclusions as that of Gillat [105]. Investigations into crossply CFRP laminates found that It has been shown for CFRP specimens that inertial effects are negligible at strain rates below 100 s^{-1}, accounting for 2% of the applied loading at this strain rate [66]. The majority of the strain rate dependent behaviour is attributable to the viscoelastic behaviour of the matrix material [66]. The greater stiffness of the matrix material at high strain rates increases the efficiency of stress transfer between fibres and decreases the ineffective length of broken fibres, so increasing the overall stiffness [107]. Although such work highlights the change in the global response to high strain rate loading, the effect on the damage initiation and propagation process is not investigated.

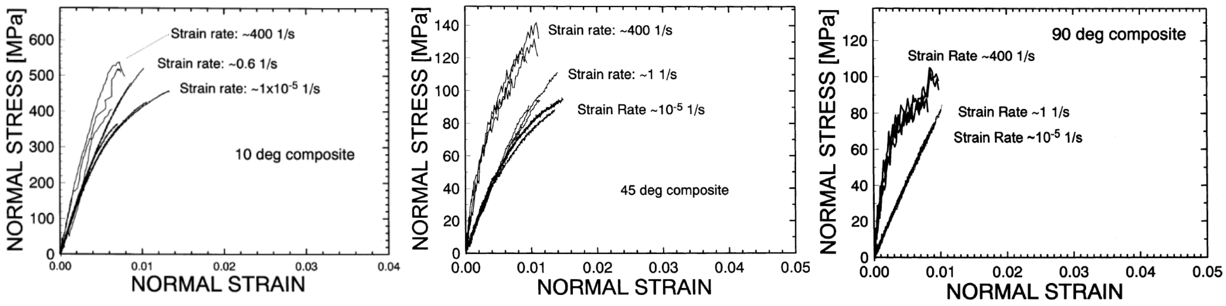

(a) (b) (c)

Figure 23: Strain rate sensitivity of CFRP according to fibre orientation: (a) 10°, (b) 45° and (c) 90° fibre angle away from axis of loading [105].

The work by Fitoussi *et al* [108] is one of the few studies that explores the effect of damage response at high strain rates in FRP materials. Complications in dynamic loading were addressed in the earlier work by Pardo *et al* [109] in terms of achieving a uniform loading and strain rate both spatially in the gauge length and temporally. Fitoussi [108] used an optimised specimen geometry and damping joint methodology to minimise stress wave effects induced from the dynamic loading to study the effect of strain rate on damage initiation. The author used a fuse type design in series with FRP specimens to achieve interrupted high strain rate loading, thus enabling the study of the effect of strain rate on the damage behaviour. The loading methodology is shown schematically in Figure 24. Both the global stiffness reduction and SEM imaging were used to quantify the damage response at the global and lamina scales for randomly reinforced glass-polyester and woven carbon fibre reinforced polymer (CFRP).

The author defined a stress and strain threshold level, above which the material stiffness response became non-linear at the onset of damage [108]. It was found that at higher strain rates, the onset of damage is delayed to higher applied strain levels. Damage was quantified using two methods, the first being a macroscopic reduction in Young’s modulus as shown in equation 3.4 and the second at the micro scale using a SEM to analyse a representative element volume. Image analysis was performed on the SEM data to quantify the number of matrix microcracks and fibre-matrix debonds and expressed as a micro damage parameter as expressed in equation 3.5.

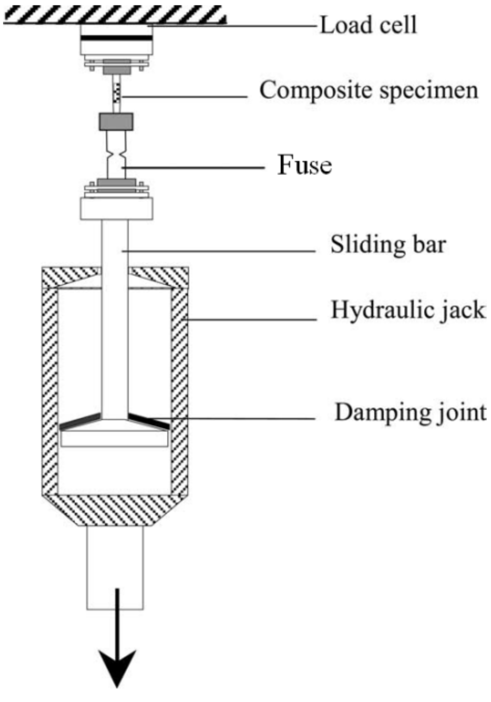

Figure 24: Interrupted high strain rate loading schematic utilising a mechanical fuse [108]

$$D_{macro} = 1 - \frac{E^D}{E^0} \tag{3.4}$$

where D_{macro} is the macroscopic damage parameter and E^0 and E^D are the Young's modulus for the undamaged and damaged material respectively [108].

$$D_{micro} = \frac{V_{f,d}}{V_{f,v}} \tag{3.5}$$

where D_{micro} is the microscopic damage parameter, $V_{f,d}$ is the volume fraction of debonded fibres and $V_{f,v}$ is the fibre volume fraction in the representative volume.

The effect of strain rate on the macroscopic and microscopic damage level for randomly reinforced glass-polyester specimens is shown in Figure 25. The decrease in damage propagation at higher strain rates was attributed to an increase in fibre matrix interfacial strength [108]. The same micro damage analysis was not carried out for woven CFRP specimens as damage was found to become heterogenous as loading strain rate was increased. Such damage localisation was attributed to the viscoelastic behaviour of the matrix material, causing an increase in stress around the initial damage site, contributing to further damage. Other previous studies have also linked increased damage localisation to the viscoelasticity of the matrix material [110].

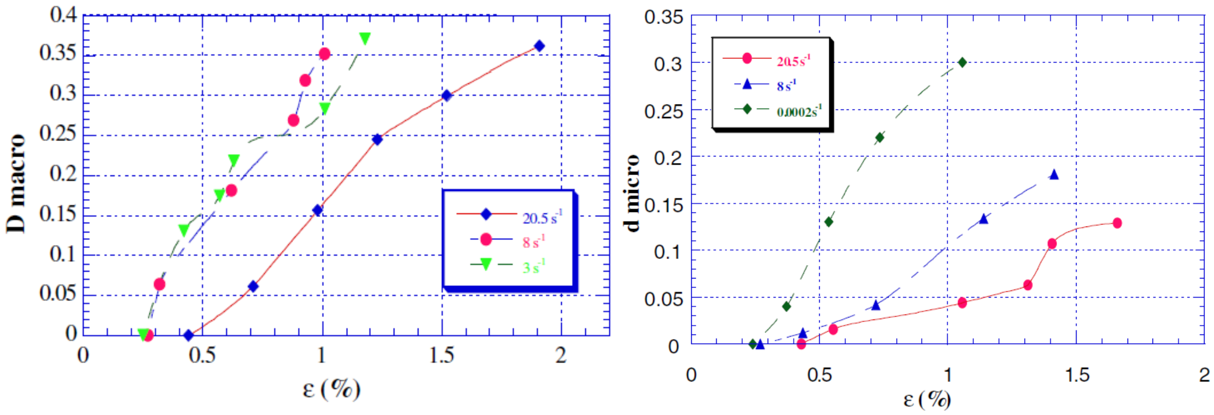

Figure 25: Evolution of the macro (left) and micro (right) damage parameters for randomly reinforced glass-polyester at various strain rates [108].

Whilst numerous studies have investigated the global response of FRP laminates subjected to high strain rate loading, it is clear from the literature review conducted that few studies have investigated the damage behaviour in FRP at high strain rates. From the study by Fitoussi *et al* [108], it is clear that damage becomes more localised in FRP materials at elevated strain rates, providing further motivation for the use of full techniques for damage identification.

3.4 Heating in FRP due to Damage

IR-thermography is to be used in the thesis for the identification of damage in FRP materials. It is therefore important to discuss the mechanisms that generate temperature rises within FRP materials.

Heat generation may occur in FRP due to a variety of mechanisms. The thermoelastic effect, as discussed in section 2.7, causes a change in material temperature due to a change in applied stress. Heat may also be generated due to damping caused by viscoelastic behaviour of the matrix [111] or the frictional sliding between fibre-fibre and fibre-matrix interfaces. This has been shown to cause a steady temperature increase of 32 K in fibre-reinforced ceramic composites under cyclic loading at 85 Hz [112]. A similar heat generation mechanism is likely to also occur in FRP composites after the onset of damage.

One of the most important sources of heat generation for the thesis is the heat generated during fracture. By identifying areas of heat generation, the sites of crack initiation and propagation in an FRP material can be found. For a crack to occur, the stress at the crack tip must be sufficient to overcome the atomic bond strength [113]. The amount of energy released varies according to the crack resistance of the material, which for polymers is approximately 10^3 J/m^2 [113, 114]. 60 – 80 % of the energy released is dissipated as heat with the rest of the energy being consumed by rearrangement of the material molecular structure [113]. The temperature rise during the fracture of PMMA and polystyrene specimens has been measured to be 500 °C [113].

If the crack velocity is sufficiently high [113], the relationship between the heat generated, ΔQ, and the resulting temperature rise, ΔT, can be calculated as follows [115]:

$$\Delta Q = \rho V C_p \Delta T \qquad 3.6$$

where ρ is the material density, V is the volume of material affected, and C_p is the specific heat capacity at constant pressure.

Typical properties of fibre and epoxy resin are given in Table 5, whilst estimated properties of carbon-epoxy and glass-epoxy laminates presented in Table 6 using a rule of mixtures approach.

Material	Density (kg/cm^3)	Mean fibre diameter (μm)	Thermal conductivity (W/mK)	Specific heat capacity (J/kgK)	Thermal expansion coefficient (/K)
Glass fibre	2400	15	1.03	800	0.5 x 10^{-5}
Carbon fibre	1700	7.5	15	800	0.08 x 10^{-5}
Epoxy	1200	N/A	0.049	640	11 x 10^{-5}

Table 5: Properties of selected FRP constituents and laminates [79]

Material	Density (kg/cm^3)	Specific heat capacity (J/kgK)
Glass-epoxy (assuming 45% V_f)	1740	712
Carbon-epoxy (assuming 75% V_f)	1628	760

Table 6: Estimated laminate properties based on a rule of mixtures approach

For slowly propagating cracks, heat dissipation effects cannot be neglected. Heat dissipation by radiation can be calculated using equation 2.20, whilst convective heat dissipation can be calculated using Newton's law of cooling [115]:

$$\dot{Q}_{conv} = \frac{\Delta Q}{\Delta t} = h_s A(T_s - T_{air}) \qquad 3.7$$

where h_s is the heat transfer coefficient, A is the surface area of the heat being transferred, T_s is the temperature at the area of heating and T_{air} is the temperature of the surrounding air.

Heat dissipation by conduction can be calculated using the Fourier heat equation which describes the temperature, T, of a material as a function of distance and time, t [115]:

$$\dot{Q}_{cond} = \frac{\Delta Q}{\Delta t} = -k\nabla T \qquad 3.8$$

where t is time and k is the thermal conductivity.

Equation 3.8 assumes a constant thermal conductivity in all directions. The thermal conductivity of GFRP and CFRP laminates however is dependent upon the fibre volume fraction and fibre direction [116]. For unidirectional carbon-epoxy laminates, the thermal conductivity was found to be an order of magnitude greater in the fibre direction than transverse to fibres, as presented in Table 7. Equivalent data for unidirectional glass-epoxy specimens could not be found in the literature but as glass fibres have a thermal conductivity half that of carbon, heat sources are expected to dissipated more slowly in glass-epoxy laminates.

Material	Thermal conductivity in fibre direction (W/mK)	Thermal conductivity in transverse direction (W/mK)
Carbon-epoxy	5~7	0.5~0.8

Table 7: Anisotropic thermal properties of unidirectional carbon-epoxy [116]

3.5 Application of Full-Field Techniques

Point measurement techniques can be used to study the behaviour of homogenous materials as the measurement is generally an accurate representation of the entire material. Damage in FRP materials occurs heterogeneously, making point measurements inadequate and driving the use of optical full-field measurement techniques for the study of damage [12, 117].

Coherent light techniques, such as shearography and electronic speckle pattern interferometry (ESPI) have proven capable of identifying hail damage and surface cracking in FRP materials [118, 119]. However, such techniques are highly susceptible to environmental disturbances and as a result, must be isolated against vibrations [12]. As GFRP laminates may fail at 2.8% strain or above [2], coherent light techniques are unsuitable for the current work as they are limited to the measurement of small strains.

X-ray computed tomography (CT) is a technique that has been used to characterise damage in FRP materials by analysing the spatial differences in X-ray attenuation [77, 120-123]. The technique allows damage to be identified in three-dimensions whilst achieving voxel resolutions of 2-3 μm [124]. The use of more a powerful synchrotron radiation source allows greater voxel resolutions of <1 μm to be achieved [124]. The technique is capable of identifying all types of FRP damage, including transverse cracking, longitudinal splitting, delaminations, single fibre breaks and even matrix micro-voids arising from fibre-matrix interface failure [120, 122, 125]. The technique requires specialist facilities and depending on the exposure time and the number of radiographs taken, a single scan may take over an hour to complete [126]. Additionally, the loading of specimens during scanning is difficult and requires the design of custom loading rigs. To achieve the highest voxel resolutions, samples must be cut to form matchstick sized specimens unless synchrotron facilities are employed [120, 124], so limiting the highest resolution scans to a post-mortem analysis. The technique is therefore not well suited to monitoring damage progression in FRP materials.

Ultrasonic methods are capable of providing full-field data of FRP damage behaviour and are especially suited to identify delaminations [127-129]. The technique is less suited for the study of in plane damage due to the lack of acoustic attenuation. Additionally a full-field image may take many minutes to acquire. To minimise losses, the object under investigation is immersed in liquid, or a suitable gel is used for acoustic coupling. For these reasons the technique is impractical to use during the fatigue loading of FRP specimens.

Pierron *et al* [130] used the grid method to resolve surface and subsurface cracks around a hole in quasi-isotropic, $[-45_4/90_4/45_4/0_4]_s$ and $[-45/90/45/0]_{4s}$ GFRP laminates. The technique was found to have sufficient sensitivity to identify the location of subsurface cracks based upon the outer surface deformation response only. This analysis can be applied to any full-field deformation measurement technique, given sufficient sensitivity. Surface cracks of 25 μm crack opening displacement were identified in the outer 45° ply using the grid technique, allowing the effect of ply clustering on damage tolerance to be studied. The avoidance of spatial aliasing was highlighted as a crucial factor for the correct analysis of grid images, requiring a prior knowledge of the expected deformations between frames. A study into the effect of paint coating thickness has previously shown that significant thermal drag down occurs for coating thicknesses above 25 μm [16]. The requirement for a grid to be attached to the specimen surface is therefore likely to be a limiting factor for the simultaneous application of the grid method and IR-thermography.

DIC has lower strain accuracy when compared to the interferometric techniques, leading Pan *et al* [17] to comment that it is unsuitable for the study of small heterogeneous deformations. Despite this, many authors have successfully used DIC to study damage in FRP materials [131-137]. Whilst the technique normally requires the application of a speckle pattern coating, fibres alone can be used as a surface texture [138]. At greater magnification levels, strain concentrations around individual glass fibres have been identified via DIC through the use of deposited submicron alumina particles on the FRP surface, allowing the study of the initial stages of damage [137]. DIC was used by Giancane *et al* [132] to calculate full-field maps of Young's modulus at various stages in the fatigue cycle of crossply GFRP specimens. Although a decrease in stiffness is likely to be attributable to damage, the authors did not carry out any validation studies to verify this conclusion or to determine the type of damage identified. In a separate study, Dattoma and Giancane [139] used DIC in combination with IR-thermography to evaluate fatigue damage in crossply glass-epoxy specimens. Full-field hysteresis data was obtained through analysis of the stress and DIC strain data whilst IR-thermography was used to obtain full-field temperature plots. Using this information, the energy absorbed by the material for the propagation of damage was calculated. This technique was able to identify increased damage evolution at notches and at the final stages of fatigue life.

Any type of image can be processed via DIC given that a suitable surface texture is achieved. In the study by Silva *et al,* [140] surfaces were speckle patterned using paints of varying emissivity. The IR images collected were processed using DIC to allow the simultaneous collection of thermal and kinematic data from various materials. Although this methodology allows for a simple experimental setup, the key advantage of using high resolution white-light cameras for DIC is lost. IR cameras generally have lower pixel counts when compared to white-light cameras and as a result, DIC data may lack the spatial resolution necessary for damage identification.

3.5.1 Thermography Techniques

Various authors have used IR-thermography to identify damage in FRP materials. Naderi *et al* [141] used IR-thermography at a macroscopic scale to identify damage evolution in thin woven glass-epoxy laminates during cyclic reversed bending at 10 Hz. Three stages of damage evolution were found in the study. In the initial stage, matrix cracking at material weak points was found to dominate the first 20 % of the fatigue life, showing a rise in surface temperature. The second stage, comprising of 75 % of the fatigue life was characterised by further matrix cracking, delamination and fibre-matrix debonding, showing a steady increase in surface temperature with damage evolution. The final stage shows a rapid temperature rise associated with fibre breakage [141]. A similar investigation was conducted by Broughton *et al* using the surface temperature rise as an indicator of the damage level in FRP materials. A similar three stage damage evolution behaviour was found in open-hole GFRP laminates [142].

Lisle *et al* [114], used IR-thermography to analyse damage and calculate energy release rates in woven glass-epoxy laminates. To minimise thermal effects from the surrounding environment, specimens were enclosed inside an opaque foam box and specimens were coated with matt black paint to maximise surface emissivity. Sensor noise was minimised using a 2D second order polynomial smoothing over an area of 5 x 5 pixels. The smoothing area chosen required a compromise between the adequate filtering of sensor noise and the identification of small heterogeneous heat sources. The spatial resolution necessary for identifying damage using IR-thermography is dependent on the scale of damage expected, in this case, the scale of the weave material [114]. Lisle *et al* was able to use IR-thermography of spatial resolution 0.16 mm/pixel to identify fracture in transverse weft yarns and the coalescence of such cracks [114]

Damage in woven carbon laminates has also been quantified using IR-thermography [143]. Single layer woven [0, +60, -60] carbon-polyimide laminates were monotonically loaded to failure whilst imaged using IR-thermography. Specimens were also cyclically loaded at up to 80% of the material UTS, with an IR image captured at the maximum load point of each cycle, thus eliminating the effect of any thermoelastic temperature change. The number and location of matrix cracks during monotonic loading in the +60 and -60 plies was determined by monitoring the number of thermal spikes. CFRP is expected to possess a greater thermal conductivity than GFRP laminates, resulting in heat rises being dissipated more rapidly [79]. However, it was found that an imaging frequency of 50 Hz was adequate to identify the instantaneous temperature rises as a result of crack initiation in woven CFRP laminates [143]. The authors do not comment on the spatial resolution of the IR images. Cyclic loading found that the majority of matrix cracks occur within 5000 cycles. Within this time, the surface temperature also reached a plateau as a result of frictional heating between fibre-matrix interfaces.

As the TSA technique requires a cyclic load to achieve adiabatic conditions, it is inherently suited to fatigue loading and hence damage study [52]. Various authors have used TSA to study damage in FRP materials [11, 18, 22, 42, 144-146]. Emery *et al* [18] used TSA to study the development of strain as a result of damage in crossply, quasi-isotropic and angle-ply glass-epoxy laminates. Although TSA was able to identify strain concentrations as a result of damage, without prior knowledge of the specimen layup it is likely to be difficult to distinguish between the various damage types based upon thermoelastic response alone. A thresholding procedure was used to monitor the cumulative damage in unnotched angle ply laminates, accurately predicting the final failure location.

TSA has been applied at high magnifications to the study of damage at the yarn scale in woven glass laminates, requiring the use of motion compensation [52]. The author was able to identify the initiation of transverse cracking in weft yarns and highlights the importance of phase data in investigating the damage response when the initial undamaged thermoelastic response is unknown.

One of the few studies to employ DIC and TSA together to study damage in FRP materials is undertaken by Goidescu *et al* [147]. Angle-ply and crossply woven carbon epoxy laminates were loaded using two routines; the first applies a quasi-static load to failure whilst the second is similar but returns the load to zero at several points during the quasi-static test. The author used a single IR camera positioned perpendicular to specimens to capture thermal data, whilst a stereo DIC system provided kinematic data. X-ray CT was used to verify damage during interrupted loading tests. A homogenous response was shown for all specimens during initial loading. From a load of 30% UTS onwards, thermal hotspots are identified as fibre breaks in the surface 0° layer of crossply laminates. The resulting strain behaviour was found to be within the noise threshold of the DIC measurement and therefore could not be identified. Fibre-matrix debonding in angle-ply laminates could not be observed in the thermal images. This is attributed to the low energy release of this damage type and the homogenous distribution over the specimen surface. The author notes that the use of high speed cameras would be advantageous to enable the dynamic study of damage.

3.6 Application of Full-Field Techniques at Elevated Strain Rates

Whilst numerous studies have used full-field optical techniques to study FRP damage behaviour during quasi-static and cyclic loading, far fewer studies have used the techniques during high strain rate loading. The lack of papers is attributed to the requirement for expensive high speed cameras powerful illumination and accurate triggering methods. The most common high strain rate loading method, the split-Hopkinson pressure bar (SHPB), is limited to the study of small specimens, making full-field measurements difficult due to a lack of optical access. As discussed in section 2.3, high speed cameras are less well suited to use with full-field measurements due to the increased noise levels and lower resolution when compared to low frequency CCD cameras [26].

The majority of work involving high speed cameras and DIC measures the out of plane deformation of panels as a result of shock or blast loading using a stereo camera system [148-150]. Fewer studies have used high speed DIC for damage identification. Koerber *et al* [151] used a single unintensified CMOS Photron SA5 high speed camera to characterise the damage behaviour of carbon-epoxy during transverse compression and in-plane shear loading using a SHPB. Images collected had a spatial resolution of 0.074 mm/pixel and correlations were carried out using the ARAMIS software using very small cell sizes of 10 x 10 pixels with a step size of 5 pixels. Shear dominated failure modes were clearly identifiable as regions of low strain in unidirectional off-axis laminates.

Lee *et al* [152] investigated the dynamic fracture velocities of edge-notched unidirectional carbon-epoxy specimens over a 30 x 30 mm area using a Cordin 550 high speed camera operating at 2.5 x 10^5 Hz. This camera type uses 32 individual CCD sensors, each with slight variations in alignment. For this reason, a reference image was required for each sensor, further complicating DIC processing. At crack initiation it was found that the crack driving force is higher in the dynamic loading case than during quasi-static loading, irrespective of the fibre orientation.

Crammond [11] used high speed DIC at 25 kHz to measure the transverse shear strains in a single lap joint loaded under tension. Transverse cracking of the 90° plies was identified in the central adherend. Final failure was identified from a crack initiating at the adhesive bond line.

IR camera technology is significantly less mature than that of white-light cameras. As a result, the maximum imaging frequency of most IR cameras is significantly lower than that of similarly priced high speed white light cameras. As described in section 2.6, the use of a commercial IR detector at high imaging frequencies requires the use of a reduced subwindow and a custom temperature calibration [47]. This methodology was used to investigate the thermal behaviour of double notched woven glass-epoxy specimens loaded to failure under tension at strain rates up to 100 s^{-1}. Using an imaging frequency of 15 kHz, four IR images were captured during loading. At lower actuator velocities, a noticeable drop in overall specimen temperature due to the thermoelastic effect was identified. Post-failure examination of the specimens after failure found that the temperature change at areas of delamination was 60 K, but only 30 K at areas dominated by fibre breakage. The measurements were found to lack the spatial resolution necessary to identify individual fibre breaks or matrix cracking at the yarn scale.

No previous combined usage of high speed IR-thermography and DIC for the identification of damage in FRP could be located in the literature.

3.7 Summary

The chapter has reviewed relevant literature on the progression of damage in FRP materials subjected to tensile loading and the effect of strain rate on the damage response. A specific focus has been placed upon crossply lay ups and carbon/glass-epoxy materials. Due to the free edge effect and the low strain to failure under transverse loading, the first damage type expected to initiate in crossply laminates are edge cracks in *90°* plies. Typically, such cracks propagate quickly into full-width cracks. Upon further loading, transverse crack density saturates until delaminations initiate. Finally, longitudinal splitting initiates in *0°* plies, followed by fibre breaks, eventually resulting in laminate failure. Strain rate effects due matrix viscoelasticity have been shown to result in increased ultimate failure strengths and stiffness and an increase of damage localisation, necessitating the use of full field measurement techniques.

The mechanisms of heat generation have been reviewed, with a focus on the heat released during crack formation. Although the majority of studies using IR-thermography have used the technique to monitor temperature rises due to frictional heating, some studies have used IR-thermography to measure the temperature rises associated with crack formation. One such study was able to identify the initiation and coalescence of cracks at the weave scale in GFRP laminates, noting that sensor noise was a major issue.

DIC has been proven by numerous studies to be capable of resolving surface damage during low speed loading in FRP materials but has rarely been applied to images captured from high speed cameras for this purpose.

TSA has been shown by various authors to be especially suited to the study of damage in FRP due to requirement of a cyclic load and the low surface preparation requirements. It is noted however that distinguishing between different damage types is difficult when using TSA, but use of phase data can be highly important when the initial undamaged thermoelastic response is not known. Also, motion compensation may need to be applied when imaging at high spatial resolutions.

Although a limited number of studies have used DIC and thermal techniques at low strain rates, no previous work has attempted to use IR-thermography and DIC together to identify damage during intermediate strain rate loading. The combined use of kinematic and thermal full-field techniques not only increases confidence in the identification of damage [11] but has also been shown to be capable of identifying more types of damage than a single technique alone [147], driving the use of a combined methodology for the current work.

Chapter 4

Testing Methodology at Intermediate Strain Rates

4.1 Introduction

This chapter outlines the equipment and methodology used to perform the intermediate strain-rate testing discussed in later chapters. The chapter begins with a review of the Instron VHS test machine, detailing its method of operation, specifications and the accessories required to perform simple uniaxial tests on FRP material to failure. The adaptations to the methodology required to provide interrupted loading to FRP specimens are discussed in detail in Chapter 7. Next, an overview of the high speed camera triggering methodology developed by Dr Crump is presented, followed by a discussion on lighting conditions for simultaneous high speed white-light and IR measurements, driving the development of a custom Light Emitting Diode (LED) lighting solution. The chapter concludes with a discussion on the test specimen design and motivation for the specimens used throughout the thesis.

An impact event on an FRP component in service is likely to result in a combination of many different loading types, including tensile, compressive, shear and out-of-plane forces. Although it would be preferential to establish experimental methodologies to investigate the damage response for all loading types, it was decided to concentrate solely on the tensile loading of specimens as a first step in the development of the optical measurement methodology. It is envisaged that the optical methodologies for the study of tensile damage developed in the thesis will be transferable to other loading scenarios in future projects, requiring only alterations to the loading methodology.

The strain rate applied to a material is a function of the gauge length and the velocity of the applied loading as follows.

$$\dot{\varepsilon} = \frac{d\varepsilon}{dt} = \frac{d}{dt}\left(\frac{l - l_0}{l_0}\right) = \frac{1}{l_0}\frac{dl}{dt} = \frac{V}{l_0} \qquad 4.1$$

where $\dot{\varepsilon}$ is the strain rate, t is time, l is the specimen length after an applied strain, l_0 is the original specimen gauge length and V is the velocity of the deformation.

To achieve greater strain rates, a higher loading velocity must be applied or shorter gauge length specimens must be used, or a combination of both. The use of short gauge length specimens is avoided where possible when using FRP specimens as they are often not representative of the behaviour of larger structures. Small samples may not include enough fibres or defects to be considered statistically representative of the bulk material [153]. Smaller samples have a lower chance of containing a significant defect within their gauge length and have been shown to have a significantly higher strength as a result [154]. This is true at both the fibre scale and the lamina scale. It is therefore preferable to use larger and consequently more representative FRP specimens loaded at greater velocities to achieve greater rates of strain. The free edge effect has also been shown to have an effect that is dependent on specimen geometry. As the ply thickness of quasi-isotropic laminates is increased it has been shown that edge delaminations initiate at a lower applied strain level [155].

Conventional test machines are limited to low strain rates due to inertial effects in the load cell and grips [156]. A variety of alternative loading techniques have been developed to apply intermediate and high strain rate tensile loading, each with their own inherent advantages and disadvantages when being used with FRP material. The typical strain rate regimes of the available techniques are shown in Table 8. One of the most common methods for high strain rate compressive loading which can also be adapted for tension is the SHPB. The device can typically load small specimen sizes of around 6 mm in length and requires careful interface design between the specimen and the bars to transfer load effectively [157]. A SHPB also has limited optical access, hindering the application of optical techniques. For these reasons it is not the preferred loading technique for the current work. Other loading techniques that operate at 10^4 s^{-1} would fail typical CFRP specimens within 2 μs. This requires the use of ultra high speed cameras to achieve more than a single frame during loading. Such cameras do not exist in IR wavelengths and ultra high speed white-light cameras bring about additional complications, including increased image noise resulting from image intensifiers and the use of multiple sensor arrays. Highly precise camera timing and synchronisation is also required for such cameras, bringing additional experimental challenges. For the many reasons stated it was decided to use a servo-hydraulic test machine to provide loading at intermediate strain rates between 10 – 100 s^{-1}.

Technique	Strain rate (s^{-1})
Conventional test machine	< 0.1
Servo-hydraulic machine	0.1 - 100
SHPB	100 - 10^4
Expanding ring	10^4
Flyer Plate	$>10^5$

Table 8: Experimental techniques for tensile high-strain rate testing [5]

4.2 The Instron VHS 80/20

The Instron Very High Speed (VHS) 80/20 is a servo-hydraulic test machine that was specifically designed for the application of intermediate strain rate loading of metallic specimens. The Fast Jaw gripping system, explained in detail later in this section, was found to be incompatible with FRP specimens due to the increased incidence of grip slippage and specimen failure at the point of gripping when compared to metallic specimens. To facilitate the testing of FRP specimens, a new slack adaptor gripping system was therefore designed, as discussed further in section 4.3.

The VHS machine has a maximum actuator velocity of 20 m/s and is capable of applying a maximum load of 80 kN. Although the machine is able to apply loading under both tension and compression, the methodology discussed in the thesis concentrates on tension for the reasons previously discussed in section 3.1.

The machine is capable of loading specimens up to 30 mm in width and approximately 4 mm thick. Specimen length is limited only by the maximum height of the crosshead, giving a maximum specimen/fixture length of approximately 1.15 m. The machine is therefore able to test specimens that fulfil the ASTM D3039 geometry recommendations for the quasi-static testing of FRP coupons [153]. To enable the safe testing of FRP specimens whilst improving optical access, a new protective enclosure around the VHS test machine was constructed. The larger size allows cameras, tripods and lighting equipment to be placed inside, eliminating the possibility of distortion as a result of imaging through the transparent enclosure panels, whilst also giving greater freedom of camera and lighting placement. The enclosure is designed to protect the operator from flying debris and uses interlock systems to ensure that tests cannot be conducted whilst an operator is inside. Figure 26 shows the VHS machine before and after the manufacture of the new enclosure.

Figure 26: The Instron VHS 80/20 machine and the old (left) and new (right) protective enclosure.

The VHS machine includes several design features to facilitate high speed testing. This includes a Kistler 9071A model piezoelectric load cell located on the machine crosshead, combined with a Kistler charge amplifier. Piezoelectric load cells are inherently suited to dynamic force measurements due to their small size and high stiffness [158]. Load data is collected using one of the input channels on a high rate National Instruments type 6110 DAQ card. The card comprises of four synchronised input channels operating at sampling rates of up to 4 MHz. A linear variable differential transformer (LVDT) provides actuator displacement data to one of these channels. In the work described in the thesis the other two channels are used to record strain gauge data and camera trigger data, as discussed further in section 4.4.

The most important feature of the Instron VHS machine is the ability to achieve constant actuator velocities ranging from 1 to 20 m/s. The actuator is accelerated over a distance of approximately 150 mm through the use of a fast response proportional valve and a high pressure accumulator, storing hydraulic oil at a pressure of 280 bar prior to each test. Although the valve allows a variable output, direct feedback between the actuator LVDT and the valve does not occur above actuator velocities of 1 m/s due to the short timescales involved. The Instron VHS actuator therefore operates in what is known as an ‘open loop’ configuration whereby feedback from an external sensor such as the actuator LVDT or load cell is not used to control the actuator during a test. The absence of such a feedback loop, combined with the high inertia of the actuator prevents the possibility of stopping the actuator at a predetermined load or position using the standard machine setup. The result is that any specimen clamped into the machine will be loaded to ultimate failure. A new loading methodology was therefore required to apply damage from an intermediate strain rate event without complete specimen failure. The interrupted loading methodology developed is discussed in detail in Chapter 7. With the absence of feedback control, the VHS actuator achieves a constant velocity prior to specimen loading through the use of a predefined calibration file relating valve control voltage to test time. Velocity calibration files are generated through the post processing of LVDT data across a series of repeated tests across a range of actuator velocities. The actuator is stopped at the bottom of its travel using a buffer.

To account for inertial effects of the actuator and grips, the actuator must be allowed a distance of approximately 150 mm to accelerate to the required velocity prior to specimen loading. As previously mentioned, the VHS machine originally included the ‘Fast Jaw’ gripping system for this purpose, a schematic of which is shown in Figure 27. The system relies on two gripping faces being initially held apart by a pair of angled wedges. The actuator initially accelerates downwards with the specimen passing freely between the grips. At the desired location the wedges are knocked out by a set of adjustable rods, as shown in Figure 27 (b). This action releases the force of four pretensioned bolts, so causing a set of grips to clamp onto the specimen surface, applying the high velocity loading, as shown in Figure 27 (c). This system was found to be challenging to use in practice due to the requirement for small clearances between jaw face and specimen surface and high bolt pretensions. Too little clearance results in the jaws dragging against the specimen surface, preventing the actuator from accelerating correctly and too large a clearance results in slippage against the specimen surface after wedge knockout.

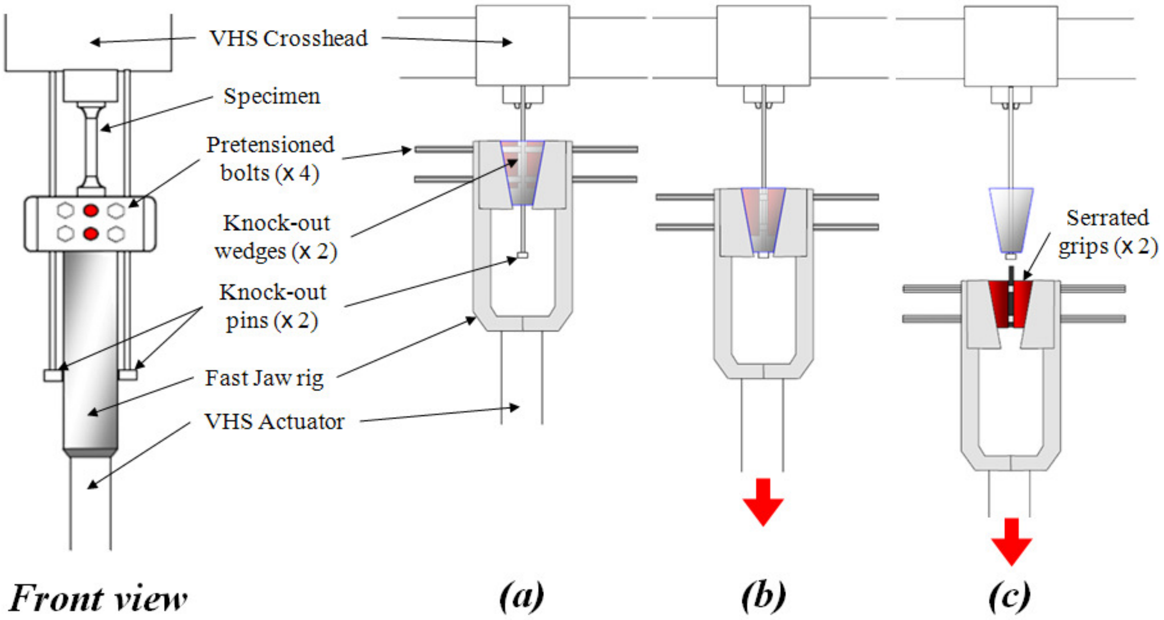

Figure 27: Method of operation for the Fast Jaw gripping system: (a) the Fast Jaw system prior to a test, (b) after 150 mm of travel, wedges are displaced by the end stops on two knock-out pins, (c) which release the pretension in four bolts, allowing grips to apply load to the specimen [159].

Greater challenges were found when using the system with FRP specimens. Since the actuator and jaws accelerate as they travel down the length of the specimen, FRP coupons need to be manufactured approximately 300 mm longer than their intended gauge length. It was also found that the jaws would either slip against the FRP surface, resulting in inconsistent and unrepeatable loading being applied, or cause failure at the gripping location. The problem was rarely found when using metallic coupons as the material is generally softer and the jaw faces were found to grip more successfully. A metallic tail clamped to the bottom of FRP specimens was found to partially alleviate the slipping problem at the jaw interface but caused slipping at the interface between the FRP specimen and tail. Due to these problems, an alternative slack adaptor design was developed, based upon previous designs developed by multiple researchers [108, 159-163].

4.3 The Slack Adaptor

The new slack adaptor loading methodology, as presented in Figure 28, uses the same upper gripping system as used in the previous fast jaw system, consisting of two hardened steel jaw faces situated in a titanium grip block. The block is bolted and tightened against the load cell located under the crosshead, allowing the wedge action jaws to grip the specimen. A similar gripping system was designed for the lower grip. The lower jaws were constructed from hardened BS4659 - B01 steel instead of titanium due to its prohibitively high cost. Consequently, the FRP specimen remains gripped at both ends throughout a test.

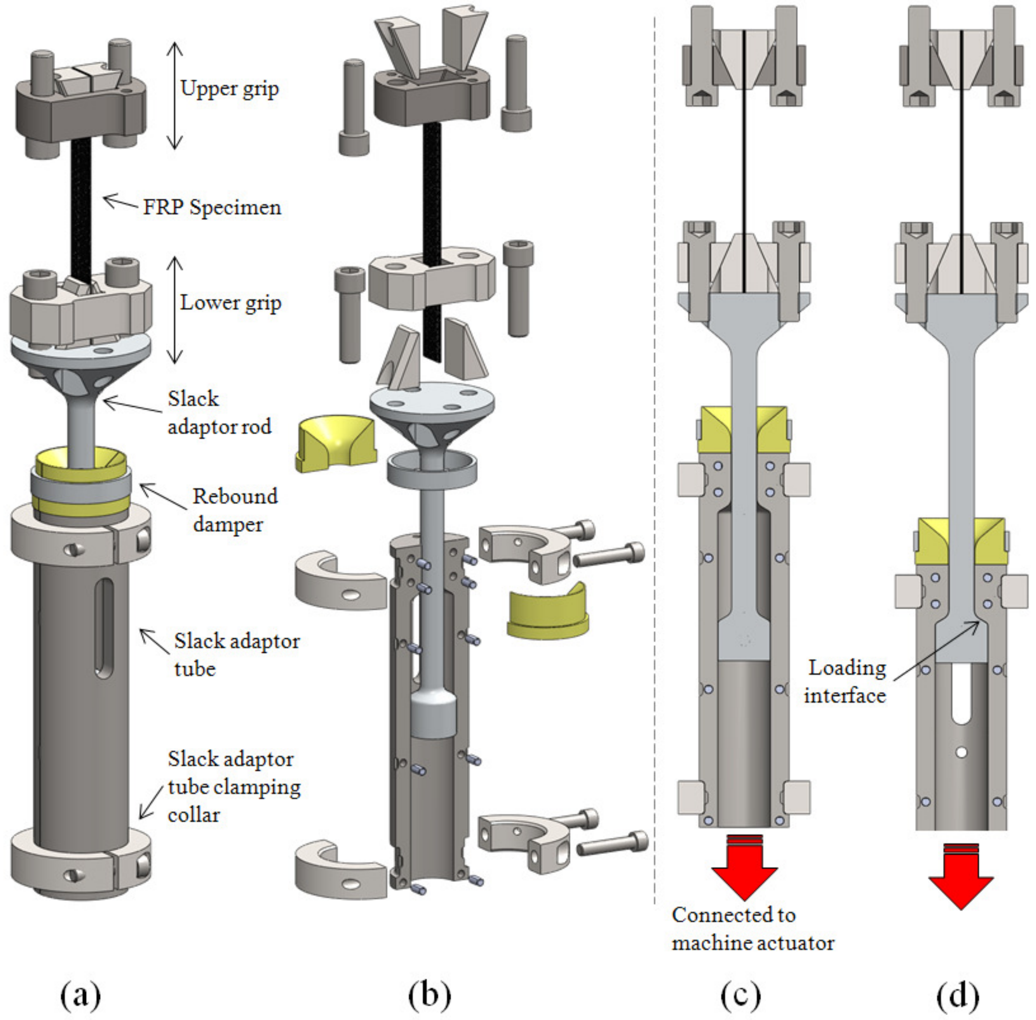

Figure 28: Slack adaptor parts, layout and function

A layout of the slack adaptor parts is shown in Figure 28 (a) including an exploded view with one half of the tube removed in Figure 28 (b). The slack adaptor design consists of two major parts, an aluminium 7075 rod and a two piece EN8 steel tube featuring a partially capped top. The rod is bolted to the lower grip block and remains free to hang from the specimen throughout the test. The two piece tube is held together by two clamping collars and is closed around the rod. The tube is allowed to pass freely over the rod. Once fully assembled, the tube is screwed onto the top of the VHS machine actuator, such that when the VHS machine is fired, the slack adaptor tube moves down with the actuator, accelerating to reach the required velocity within 150 mm. Loading begins once the tube has descended sufficiently for the inner surface of the tube end cap to reach the top of the piston. The load is then transmitted through the rod and lower grip to the FRP specimen. A cross section showing the slack adaptor prior to, and at the point of loading is shown in Figure 28 (c) and Figure 28 (d) respectively. Additions to the slack adaptor include a two-part rebound damper to prevent damage to the rod and tube after specimen failure and a 1 mm polyethylene washer at the loading interface. The washer was found to minimise the onset of load cell ringing, a phenomenon whereby the load cell and upper grip block enter into a vertical oscillation creating an oscillatory signal in the load trace.

A single piece aluminium rod was used to maximise strength through the elimination of weak points such as threaded joints. Earlier rod/piston designs were constructed from multiple parts and were found to fail after repeated tests through plastic deformation at the threaded interfaces. An important factor to note is that the single piece rod experiences loads far in excess of that of the failure load of the specimen when operating at high velocities. The lower grip block and single piece rod have a combined mass of 2.032 kg which must be accelerated by the actuator over a very short distance, imparting significant impulse loading to the rod. This loading is difficult to estimate numerically as it requires a dynamic analysis of the system whilst also taking into account the behaviour of the washer and specimen compliance. An experimental investigation was instead conducted using high speed imaging combined with DIC to investigate the acceleration of the lower part of the rod at various actuator velocities. This part was imaged through the window on the side of the slack adaptor tube. It was found that at an actuator velocity of 9.62 m/s, the acceleration was 54600 m/s^2, equating to a rod stress of 423 MPa, close to the material yield stress for aluminium-T651 of 462 MPa [164]. Any future usage above 10 m/s will therefore require a redesign to minimise the inertial mass and to give greater strength to the rod. One possible solution may be to substitute the rod material for a material such as Ti-6Al-4V or to redesign the lower grip block to reduce mass..

4.4 Camera Synchronisation and Data Capture Methodology

An important aspect of applying optical measurement techniques to high-speed events is ensuring that the optical data collected can be related temporally to other data sources. Since the VHS machine contains no in-built trigger system for such a purpose, a methodology was developed by Dr Crump [9] to allow the synchronisation of optical data to data collected from the VHS DAQ card, as outlined in Figure 2. The methodology developed relies on a custom designed circuit to trigger cameras at a specific point in a high speed test. A schematic showing the connections between cameras, the triggering system and the test machine are shown in Figure 29.

Prior to a test, the VHS actuator is moved to a height to allow approximately 10 mm clearance before loading takes place between the slack adaptor rod and tube. The voltage output from the LVDT at this actuator height is then entered into the console on the front of the triggering system by the operator. The actuator is then returned to the starting position ready for firing. Throughout a high velocity test, the LVDT voltage is read into the triggering system and once the voltage crosses the previously entered value, transistor-transistor logic (TTL) pulses are sent across four output channels. These channels are connected to high speed cameras which are preconfigured to record upon receiving a TTL pulse. One of the outputs of the trigger circuit is also connected to an input of the VHS DAQ card. This allows the TTL trigger pulse to be recorded in the VHS DAQ card data and allows temporal synchronisation between images and test machine data.

A known limitation of the high speed camera synchronisation methodology used in the thesis is the timing accuracy of the recorded images. Both the CEDIP Silver

480M IR camera and Photron SA1 white-light camera use an internal clock to time the exposure of images. The Photron camera clock runs continuously such that the cameras are always buffering at least one image in the onboard memory. When using the standard triggering mode, the camera starts recording images upon receipt of a TTL pulse. The first image in the series will be from the clock cycle immediately prior to the TTL pulse, resulting in a timing error of up to one frame period. This is illustrated in the top diagram of Figure 30.

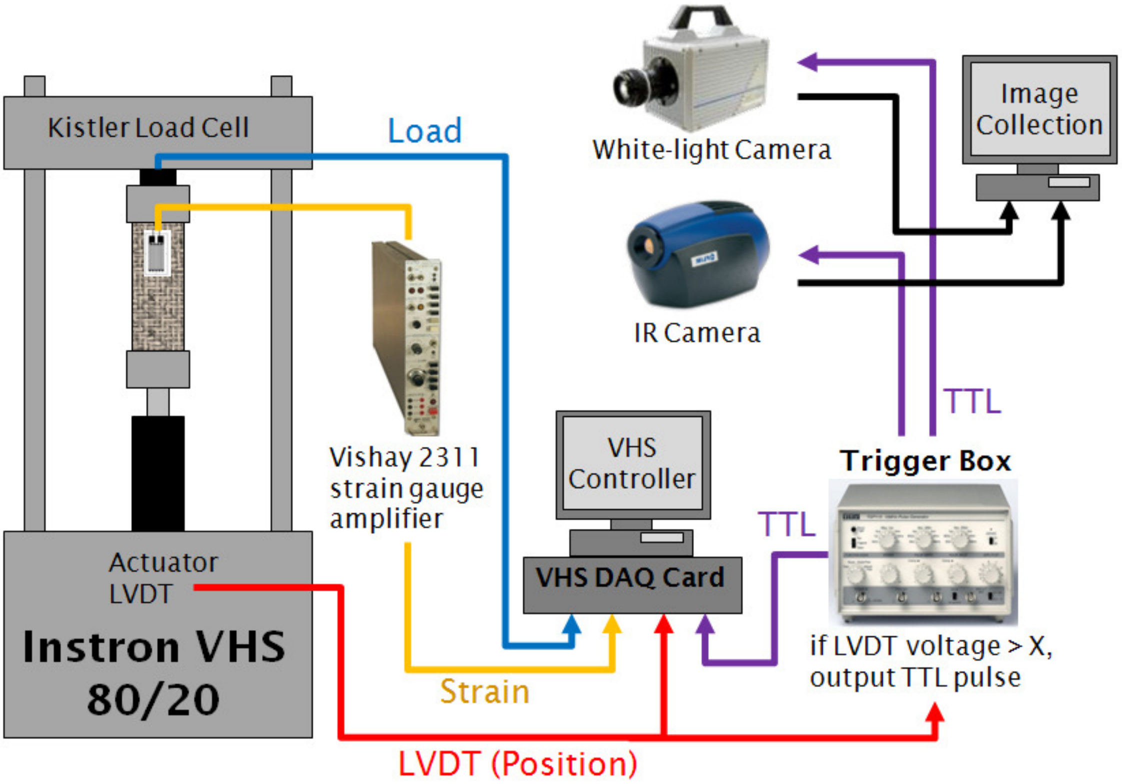

Figure 29: Camera triggering and data synchronisation with the Instron VHS

When operating at high frequencies, the CEDIP IR camera groups together approximately 120 frames into a single data packet for transfer to the PC memory. When a TTL pulse is received by the camera the PC starts saving the next data packet onwards, resulting in up to 120 frames after the trigger pulse being lost, so making image synchronisation impossible. For this reason it was found to be essential to set the CEDIP IR camera to operate in a circular buffer mode to be certain of capturing the true trigger point. The circular buffer operates by saving 500 frames of data onto the PC memory which are constantly overwritten as new image packets are received. When the camera receives the trigger pulse, the images on the PC are no longer overwritten and new images are saved to the PC memory. This results in an image sequence with approximately 500 frames of data prior to the camera receiving the trigger pulse. The CEDIP IR camera also features two voltage inputs which allow one sample of external data to be recorded with each IR image. The trigger signal was also recorded using one of these data inputs, so allowing the exact frame at which the trigger pulse is received to be determined through inspection of the recorded data. Since the trigger pulse may occur anywhere within the frame period, the timing error of the IR data is up to one frame period.

The internal clocks of the Photron cameras and the CEDIP IR camera are not synchronised and will therefore be out of phase with one another even when operating at the same imaging frequency. A potential way to overcome this limitation in any future use of the methodology is to make use of the ‘random reset’ trigger setting on Photron cameras combined with the ability to trigger individual frames on the IR camera. The ‘random reset’ setting resets the internal clock of the Photron camera upon receipt of a TTL trigger input such that the exposure of the first image occurs as soon as possible after the trigger, typically within 0.7 μs [165]. This behaviour is illustrated in the bottom diagram of Figure 30. For more accurate synchronisation between the CEDIP and the Photron cameras, a master-slave arrangement would need to be used, whereby the Photron camera is set to output a TTL pulse at the start of each clock cycle and the CEDIP camera is set to record a frame upon receiving each pulse. By setting the IR camera to record individual frames the internal clock is no longer used and the images are synchronised more accurately.

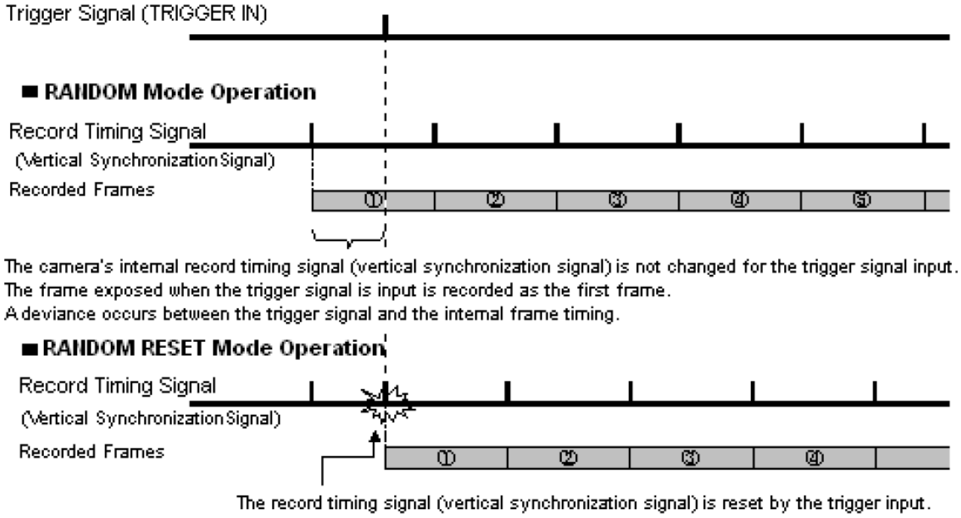

The camera's internal record timing signal (vertical synchronization signal) is not changed for the trigger signal input.
The frame exposed when the trigger signal is input is recorded as the first frame.
A deviance occurs between the trigger signal and the internal frame timing.

The record timing signal (vertical synchronization signal) is reset by the trigger input.

Figure 30: Timing principle for TTL triggered recordings on Photron high speed cameras [166]

Strain gauge measurements are conditioned using a Vishay 2311 strain gauge amplifier before being recorded by the VHS DAQ card. The Vishay 2311 is especially suited for use with dynamic tests due to possessing an extremely fast response time, with a typical output slew rate of 7.8 V/µs [167]. The device also provides the strain gauge excitation voltage, bridge completion circuitry and shunt calibration ability. Shunt calibration for all tests were carried out using a 2 kΩ shunt resistor giving a simulated strain level of 2.86% strain. All tests were conducted with an excitation voltage of 2.7 V in a quarter bridge configuration. Quarter bridge nonlinearity was corrected for using the following equation, as recommended in Vishay tech note 514 [168]

$$\varepsilon = \frac{2\tilde{\varepsilon}}{2 + F_G\left(\varepsilon_S - \tilde{\varepsilon}\right)} \qquad 4.2$$

where ε is the corrected strain, ε_s is the shunt calibration strain, $\tilde{\varepsilon}$ is the indicated strain and F_G is the gauge factor of the strain gauge.

4.5 Lighting

A crucial aspect in devising a successful imaging methodology for making kinematic measurements is to achieve adequate, uniform illumination that makes good use of the sensor dynamic range without saturation. This minimises bias and noise in subsequent DIC analysis [27]. When using high speed cameras the use of powerful illumination is essential for enabling greater imaging frequencies (and shorter exposure times) to minimise image blurring when studying dynamic events. Such blurring limits the subpixel accuracy achievable via DIC [27, 149]. More powerful illumination also allows the use of a smaller lens aperture, increasing the depth of field of the system and ensuring that more of the subject is in focus. The depth of field is usually not a consideration when imaging flat specimens with a single camera positioned perpendicularly. However, a calibrated stereo camera system requires that the cameras are situated at an angle to the specimen surface, and therefore a sufficient depth of field is required to ensure that the entire surface under examination remains in focus.

There are many possible methods of illumination for high speed imaging, including the use of lasers, spark sources and stroboscopes to name just a few [169]. For health and safety reasons in an open laboratory setting, lasers and spark sources were not trialled. Strobe lighting requires synchronisation between the strobe and camera shutter, complicating experimental setup. For this reason it was decided to only use constant light sources. A further consideration in the choice of lighting system is the physical size of the light unit, which in turn affects how close the lights can be placed to the surface under investigation and therefore the intensity of surface illumination. Adding lenses to the lighting system or fibre optics may allow a greater stand-off distance.

As one of the objectives of the work is to use white-light and IR imaging simultaneously, an important consideration is the effect of the lighting system on the thermal behaviour of the specimen and environment. To investigate this, a static unloaded specimen with a speckle patterned surface was imaged using a Redlake (now IDT Ltd.) Motionpro X3-plus high speed camera operating at 30 Hz frame rate. Two types of illumination were trialled; a single 1250 W tungsten halogen floodlight situated at 0.3 m stand-off distance and a 72 W LED floodlight situated at 0.5 m stand-off distance. Images were correlated in DaVis 8.1.3 using a cell size of 64 x 64 pixels and a step size of 16 pixels. A selection of DIC strain maps for the two types of illumination are shown in Figure 31. Since the specimen remained static and undeformed throughout, any calculated strain is error in the measurement system. The LED illumination was found to produce uniform strain maps across all images with a maximum variation of 0.03% strain, within the error level expected of the correlation algorithm. Halogen illumination was found to cause large errors, up to 0.5% strain. Similar behaviour is shown in the horizontal strain field. Such behaviour is caused by the high temperature of the halogen light and the integrated fan cooling system which directs hot air into the optical path. Such temperature variations cause density changes in the air, resulting in highly distorted images.

Using a CEDIP Silver 480M IR camera, it was found that the halogen illumination caused a near instantaneous temperature rise of 25 ℃ at first switch on, followed by a slow rise to an equilibrium temperature of 80 ℃ over 4 minutes. The initial apparent temperature rise was caused by IR reflections from the specimen surface. As the temperature effects were found to dominate both the white-light and IR measurements, the halogen illumination was set aside and LED illumination was explored further.

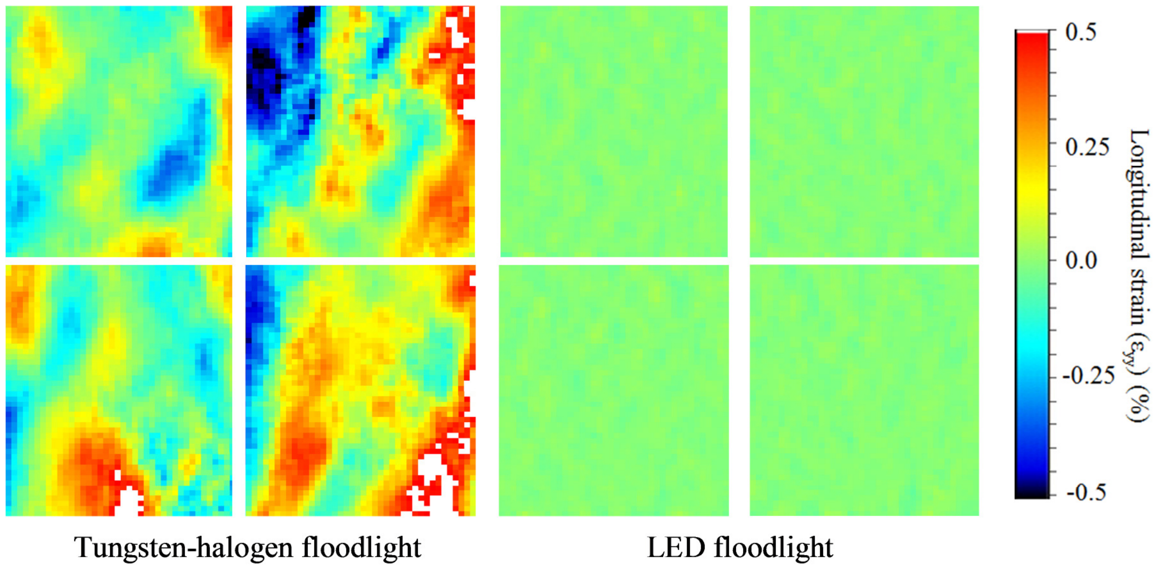

Figure 31: Effect of illumination type on the DIC measurement of a static, unloaded surface.

The physical size of the LED floodlight (approximately 0.4 x 0.4 x 0.1 m) was found to severely restrict its use with the Instron VHS. Since the illumination could neither be focussed adequately onto a specimen nor situated in close proximity, alternative LED solutions were investigated. Most commercial systems available control the LED modules using pulses of current at high frequency, varying the duty cycle to alter the LED output. Although the frequency is above that noticeable by the human eye, it is within the temporal resolution of high speed cameras. LED systems without pulsed control exist specifically for high speed imaging but are costly, hence a more cost effective solution was sought.

Two new LED lighting systems were designed and manufactured, the first using an array of 4 and the second using an array of 8 Intelligent LED Solutions ILH-ON01-ULWH-SC201 LED modules. Each LED module, outputting approximately 250 lumens, is combined with an acrylic lens of a full-width half maximum angle of 4.5° giving a concentrated column of light. Pulsed light output was avoided by wiring the LED modules in series and powering the modules directly using DC power supplies. The modules were cooled using a passive heat sink located at the rear of the unit to minimise the possibility of air distortion. Further information on the design of the LED lighting systems is included in Appendix C.

The larger LED lighting system was found to provide sufficient illumination for imaging at frame rates of up to 40 kHz using the settings described in Table 9. Images were again captured of a static, unloaded specimen with a speckle pattern and processed in DaVis 8.1.3 using a cell size of 64 x 64 pixels and a step size of 16 pixels. The strain data was found to be highly uniform and within ± 0.02 % strain with no evidence of distortion effects as previously found using halogen floodlight illumination.

Camera	Lens	Aperture	Imaging Frequency (kHz)	Exposure time (μs)	Camera stand-off distance (m)	LED unit stand-off distance (m)
Photron SA1.1	Sigma FX 105 mm macro	f 11	40	25	0.3	0.3

Table 9: Experimental setup for validation of custom LED lighting system.

A CEDIP Silver 480M IR camera was again used to assess specimen heating as a result of the custom LED illumination. Figure 32 (a) shows the surface temperature of a GFRP specimen without LED illumination, whilst Figure 32 (b) shows the surface temperature after LED illumination is applied and the specimen is allowed to reach thermal equilibrium.

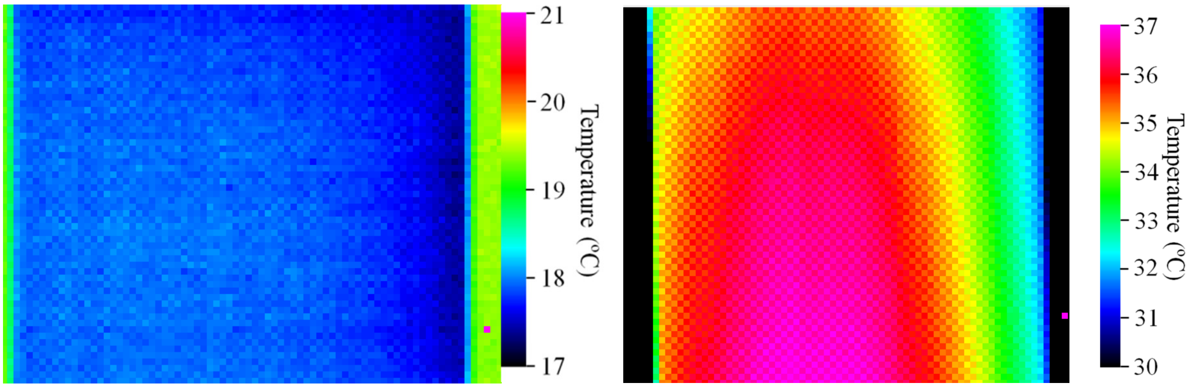

(a) (b)

Figure 32: Effect of custom LED lighting on the surface temperature recorded using an IR camera

It can be seen that the surface temperature in the centre of the specimen rises by approximately 19 °C and a temperature gradient of approximately 7 °C is created across the specimen. Although the surface temperature rise is undesirable, it is much lower than that found when using halogen illumination and is therefore less likely to influence the material behaviour or cause image distortion.

4.6 Test Specimens

Test specimens used in the thesis were manufactured from readily available carbon/epoxy and glass/epoxy pre-impregnated (pre-preg) material, as stated in Table 10. Both types of pre-preg comprise of a single layer of unidirectional fibrous reinforcement in an epoxy resin. Two different materials were used to prove that methodologies developed in later chapters are not limited to a single material type.

Manufacturer	**Resin Type**	**Fibre Type**	**Fibre weight (g/m^2)**	**Fibre Volume Fraction**	**Cured lamina thickness (mm)**
Gurit	SE84LV (epoxy)	Unidirectional HEC carbon fibre (Tensile strength > 4.8 GPa)	300	75%	0.281
Advanced Composites Group (ACG)	MTM28-1 (epoxy)	Unidirectional E-Glass (Tensile strength = 1.05 GPa)	200	45%	0.150

Table 10: Pre-preg material types used for specimen manufacture [170-172]

A symmetrical crossply lay-up was chosen for specimen manufacture to minimise many of the complicating effects arising from elastic coupling. The use of a symmetrical laminate eliminates elastic coupling between in-plane strains and out of plane deformation, minimising out of plane movement, whilst the use of a crossply laminate also eliminates shear coupling effects [2]. Another benefit of using a crossply configuration is that the damage behaviour of such material has been extensively documented, as previously discussed in Chapter 3, helping to simplify the interpretation of optical measurements.

Eight layers of glass/epoxy pre-preg material were used for laminate manufacture to give a $[90,0,90,0]_S$ lay up and a panel thickness of 1.2 mm. Four layers of the carbon/epoxy prepreg material were used to give a $[90,0]_S$ lay up and a similar panel thickness of 1.13 mm. Outer *90°* layers were used to promote surface damage in the form of transverse cracking when under load, as such damage should be resolvable by the optical measurement techniques. A classical laminate theory (CLT) analysis was conducted for the symmetric crossply laminates using the eSuite 1.0 software by ESP Composites [173]. Representative material data was provided by Daniel *et al* [2] for E-glass epoxy and carbon-epoxy. The use of increased ply clustering, i.e. a $[90_2,0_2]_S$ configuration rather than $[90,0,90,0]_S$, found no change in the lamina stresses. The use of thinner plies should therefore not influence the expected damage behaviour. However, CLT analysis does not take into account 3D effects such as that caused by a free-edge, or the additional constraining effects that are caused by a finer ply distribution. It also does not take into account reinforcement differences between the two material types such as fibre diameter and fibre volume fraction, both of which are likely to cause a difference in damage behaviour.

4.6.1 Geometry and End Tab Configuration

The use of dogbone shape specimens to promote specimen failure within the gauge length is generally avoided in FRP materials in favour of end tabs due to the 'shoulders' of waisted specimens often detaching from the rest of the specimen by longitudinal splitting prior to final failure. ASTM D3039 recommends the use of aluminium or woven glass end tabs adhered to composite laminates as a post-process [153]. Such a methodology was found to be inadequate when FRP specimens were tested at intermediate strain rates, with the majority of end tabs becoming detached from the specimen prior to final failure despite adequate surface preparation. An alternative methodology was developed by Longana *et al.* [174] to produce laminates with end tabs integrated into the panel using the same pre-preg material. An aluminium sheet of suitable thickness was used as a mould beneath the gauge section, so preventing bending of the specimen during curing. The integrated end-tab methodology was found to be superior to the ASTM D3039 end tab method at promoting failure within the gauge length and was used for both the GFRP and CFRP panels, as shown in Figure 33 and Figure 34 respectively. All laminates were cured in an autoclave with vacuum assisted consolidation using the manufacturers recommended cure cycle. Specimens were cut from panels using a diamond coated saw to a width of 25 mm and 20 mm for GFRP and CFRP specimens respectively. CFRP specimen width was decreased to 20 mm to reduce the specimen failure load, allowing an easier implementation of the intermediate strain rate damage methodology as discussed further in Chapter 7.

All specimens to be tested at intermediate strain rates were equipped with a single CEA-06-240UZ-120 Vishay strain gauge located at the centre of the specimen width. The gauges have an active length of 6 mm and are the recommended choice for FRP material testing, withstanding strains up to 3-5% when bonded with cyanoacrylate adhesive. The bonding surface was prepared according to the strain gauge manufacturer's instructions for FRP materials [175]. Additional wiring terminals were also bonded to the specimen above the strain gauge. The use of such terminals allows smaller wires to be soldered to the strain gauge terminals, minimising the chance of strain gauge debonding due to solder reinforcement.

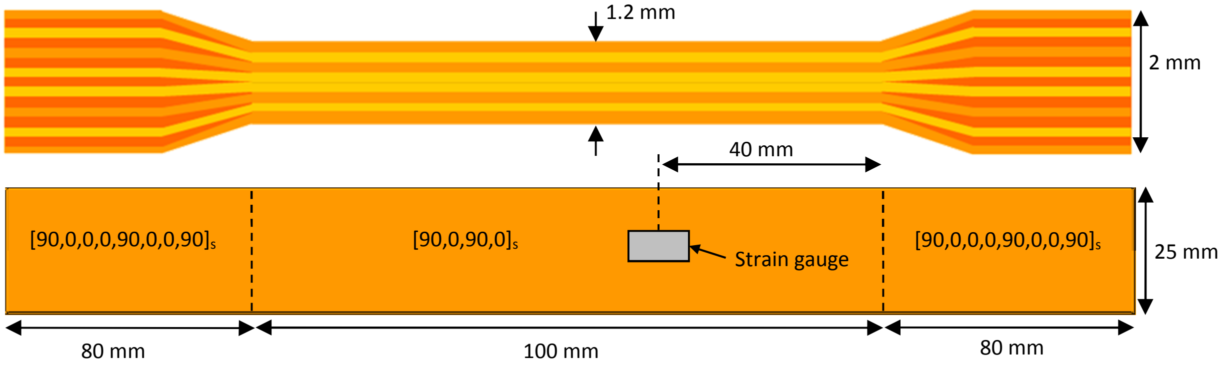

Figure 33: GFRP integrated end tab specimens with nominal dimensions

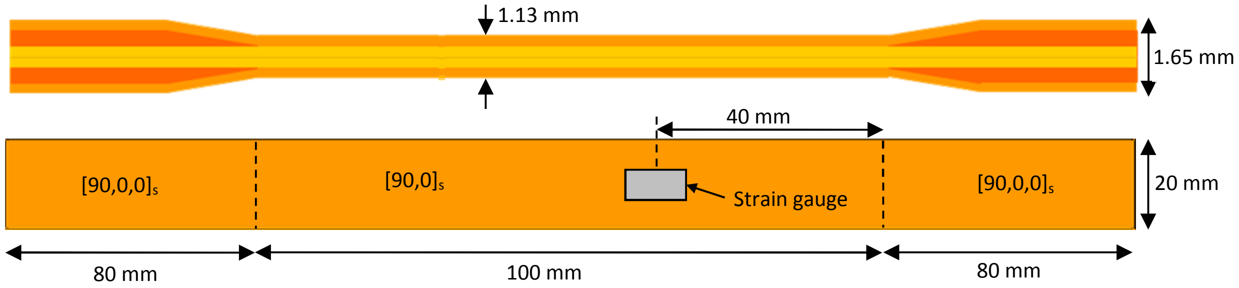

Figure 34: CFRP integrated end tab specimens with nominal dimensions

4.6.2 Speckle Pattern Application

To facilitate DIC analysis, a speckle pattern was applied to the specimen gauge section using readily available acrylic spray paints. All specimens were coated using three passes of RS matt black paint and once dry, a light coat of Ambersil RAL9010 matt white paint was applied to create a fine speckle pattern suitable for use with high resolution cameras. A non-standard 2 mm diameter nozzle was used to produce larger speckle size, more suitable for imaging with high speed cameras due to the generally decreased spatial resolution. The use of this coating methodology has been previously found to give a homogenous emissivity distribution suitable for TSA analysis. It is important to note that the application of a consistent speckle pattern is highly dependent on the experience and skill of the user. Speckle patterns were inspected visually for consistent speckle size and distribution. Any speckle patterns found to be inconsistent were removed using acetone and the speckle pattern application repeated.

4.6.3 Young's Modulus Characterisation

A total of twelve CFRP and twelve GFRP specimens were tested to failure in order to evaluate the Young's modulus and failure stress at quasi-static and an intermediate strain rate. Specimens were loaded in an Instron 5569 servo-mechanical test machine at an actuator velocity of 2 mm/min (3.33 x 10^{-4} s^{-1}) with strain measurement provided by a 50 mm gauge length extensometer. Six specimens were also tested in the Instron VHS at an actuator velocity of 3.2 m/s (a nominal strain rate of 32 s^{-1}). Strain was measured using the attached strain gauge and the Vishay 2311 strain gauge amplifier using the methodology previously discussed in section 4.4 A summary of the material properties found are stated in Table 11.

Specimen Type	**Actuator Velocity (ms^{-1})**	**Nominal Strain Rate (s^{-1})**	**Young's Modulus (GPa)**	**Failure Stress (MPa)**
CFRP $[90,0]_S$	3.33 x 10^{-5}	3.33 x 10^{-4}	71.20 ± 1.31	951 ± 27.50
	3.20	32.00	66.17 ± 2.95	1073 ± 60.21
GFRP $[90,0,90,0]_S$	3.33 x 10^{-5}	3.33 x 10^{-4}	21.04 ± 0.38	512 ± 30.5
	3.20	32.00	25.47 ± 1.16	728 ± 45.8

Table 11: Crossply CFRP and GFRP material properties at quasi-static and intermediate strain rates

4.7 Summary

The chapter has presented an introduction to the high strain rate testing of FRP materials and describes the methodology used in later chapters for the intermediate strain rate testing of FRP materials. The reasoning for using the Instron VHS machine in the thesis has been described along with an in depth discussion of the operation of the machine. This includes machine specifications, limitations and an overview of the slack adaptor loading system developed at the University of Southampton. An important aim of the thesis is to use high frequency imaging to study damage behaviour during intermediate strain rate loading. The method by which cameras are triggered and synchronised to test machine data is therefore described in detail along with validation of the illumination methodology. Finally the test specimens used in the thesis were described.

Chapter 5

Investigation of High Speed Camera Sensor Architecture

5.1 Introduction

A key objective of the work described in the thesis is to establish a full-field experimental methodology for identifying damage in FRP material during high velocity loading. The short test durations during high velocity loading necessitate the use of high speed cameras to capture a sequence of images for subsequent DIC analysis. DIC analysis of the images intends to identify areas of high strain or changes in strain distribution that may be indicative of damage.

The majority of previous materials research implementing DIC has been carried out with high resolution, low speed cameras using CCD sensor architectures [176, 177]. Fewer studies have used high speed cameras, primarily based on CMOS sensors [26, 151, 178-181]. As previously discussed in section 2.3, many high speed cameras have inbuilt features that have a serious detrimental effect on the image quality, and as a consequence, on the accuracy of DIC measurements [26, 182]. Image intensifiers have been shown to generate high noise levels in captured images, whilst the use of rotating mirror systems with multiple CCD arrays can cause errors due to differences in the sensors and misalignment between the sensors [26, 182]. For these reasons, only high speed cameras using a single unintensified CMOS sensor were used in the work described in the thesis.

CMOS sensors generally have a lower sensitivity, larger pixel sizes and a greater dark current than CCD sensors and are consequently less suitable than CCD based cameras for DIC [25]. However, CMOS sensors are still the architecture of choice for high speed imaging due to their faster charge readout rate and the ability of random pixel access, enabling smaller window sizes to be selected and greater imaging frequencies to be used [25, 183].

Although high speed cameras have been used for many years, they have generally been used for qualitative examinations. As outlined in section 3.6, authors that have applied DIC to images captured using high speed cameras generally do not aim to identify small scale damage behaviour. The use of high speed cameras and DIC for such a purpose therefore warrants further investigation to be confident in the identification of FRP damage in later chapters.

5.2 Camera and Sensor Architecture

Two types of high speed single CMOS sensor cameras were investigated for their suitability for use with DIC. A low speed CCD camera was also used as a comparison. An overview of the camera specifications are presented in Table 12.

Camera Manufacturer	Model	Sensor Type	Pixel Size (μm)	No. of Pixels	ADC Bit Depth	Fill-Factor
Redlake	MotionPro X3Plus	CMOS (other properties unknown)	12 x 12	1280 x 1024	12	Unknown
Photron	SA5	CMOS - Active Pixel Sensors	20 x 20	1024 x 1024	12	52% [184]
LaVision	Imager E-Lite 5M	Progressive scan CCD – Sony ICX625	3.45 x 3.45	2448 x 2050	12	~ 100% [185]

Table 12: Overview of camera specifications used for validation trials [186-188]

Sensor architecture details are often proprietary information and rarely disclosed in detail in manuals or datasheets. Further information of the MotionPro sensor architecture could not be sourced either in the literature or from the manufacturer. The Photron SA5 sensor uses all active pixels with no interpolation. Pixels have a fill factor of 52%, which is the same in the horizontal and vertical directions [184]. The Sony sensor used in the E-Lite camera has a fill factor close to 100% with the use of microlenses [185]. Such lenses are situated above the sensor array and gather incident light over the entire pixel area onto the active area, as shown in Figure 35.

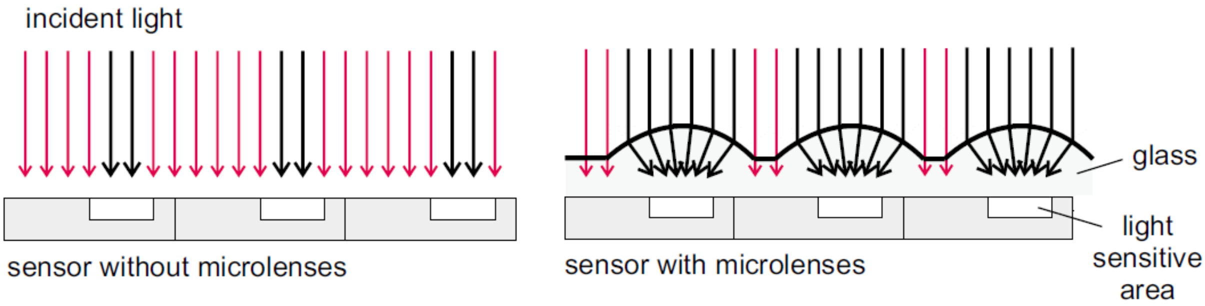

Figure 35: Schematic of microlenses, as used in the Imager E-Lite 5M camera [186]

5.3 Initial Experiments

A series of tensile tests were conducted using the three types of camera previously described. All three cameras were fitted with a Sigma 105 mm lens. A single unidirectional $[0]_4$ GFRP specimen was repeatedly loaded quasi-statically to 1.2 % strain using an Instron 5569 servo-mechanical test machine. During loading the specimen was imaged by each of the three cameras in turn. Tests were also repeated with the cameras rotated by 90° to investigate for any sensor asymmetry. As the applied load is within the elastic region of the material, damage should not occur over the limited number of loading cycles. A small 100 N preload was applied prior to each test to minimise any out of plane motion of the specimen due to grip realignment.

The specimen was coated in two passes of RS matt black paint with a further light coat of matt white paint to provide a random speckle patterned surface for DIC analysis. A 50 mm gauge length extensometer was attached to the rear surface of the specimen to validate the strains determined by DIC. Sets of 400 images were taken during the loading sequence using each of the three cameras. The spatial resolutions were kept nominally constant at 0.038 mm/pixel throughout all tests by adjusting the camera stand-off distance, so keeping the speckle pattern nominally identical across all tests. The image sets were processed in DaVis 8.1.3 and correlated relative to the first image in the series, using a cell size of 31 x 31 pixels and a step size of 8. Correlations were performed using the standard bilinear subpixel interpolation method. The final strain maps for each camera type and camera orientation are presented in Figure 36.

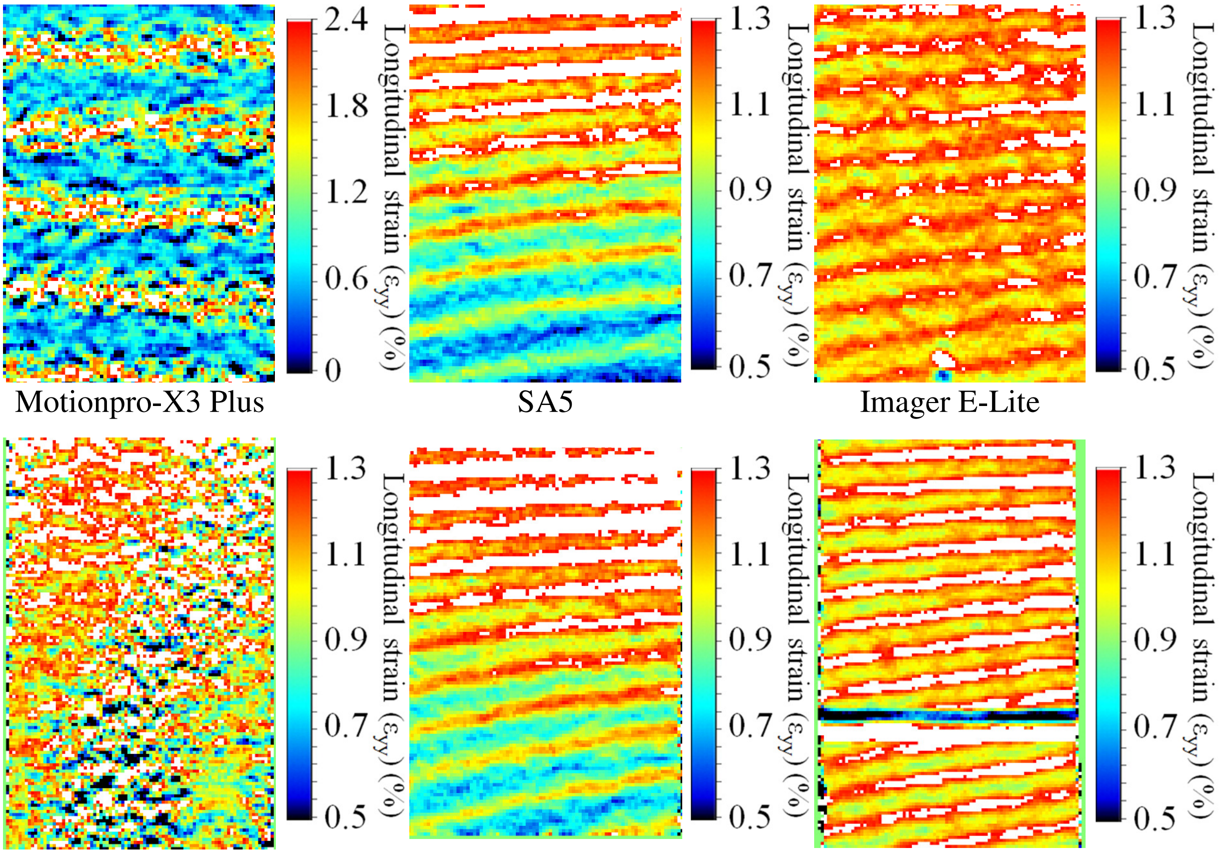

Motionpro-X3 Plus SA5 Imager E-Lite

Motionpro-X3 Plus (Rotated 90°) SA5 (Rotated 90°) Imager E-Lite (Rotated 90°)

Figure 36: DIC strain maps using a bilinear subpixel interpolation method of a unidirectional GFRP specimen loaded to 1.2% strain, imaged with three camera types at two different camera rotations.

A pattern of horizontal bands were found across all cameras tested except the Motionpro camera when rotated. This camera and orientation was found to exhibit high noise levels, potentially masking the banding effect. Please note the different scale for the Motionpro camera when in its normal orientation. The bands were found to increase in density with increasing applied strain and to move relative to the specimen surface. They therefore cannot be attributed to real behaviour of the material. Whilst the strain bands are of greatest magnitude in the data from the Motionpro camera when in its normal orientation, similar behaviour can be noted across all camera types. A vertical strain gradient can also be noted in the SA5 data. This is likely to be caused by camera misalignment. The horizontal band in the E-Lite data is a known issue, attributable to a tapshift correction not being applied. This correction is required to take into account the slight gap between the two sensor arrays used in this sensor type.

No change in the position or the spatial frequency of the pattern could be noted with the use of other subset or step sizes, as shown in Figure 37. The use of subset sizes above 63 pixels was unable to identify individual band patterns, whilst the use of subset sizes below 16 pixels was found to result in high noise levels resulting in the patterns becoming indistinguishable.

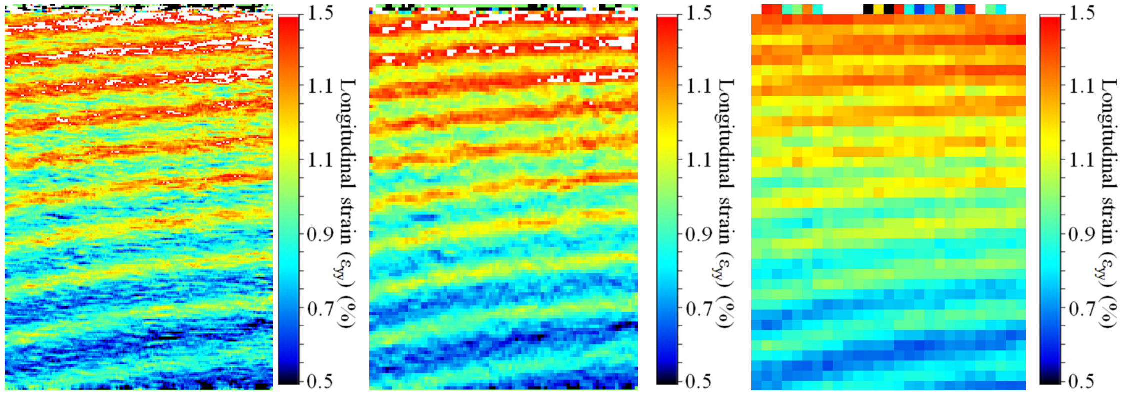

Subset size: 31 x 31 pixels
Step size: 4 pixels
31 x 31
8
31 x 31
24

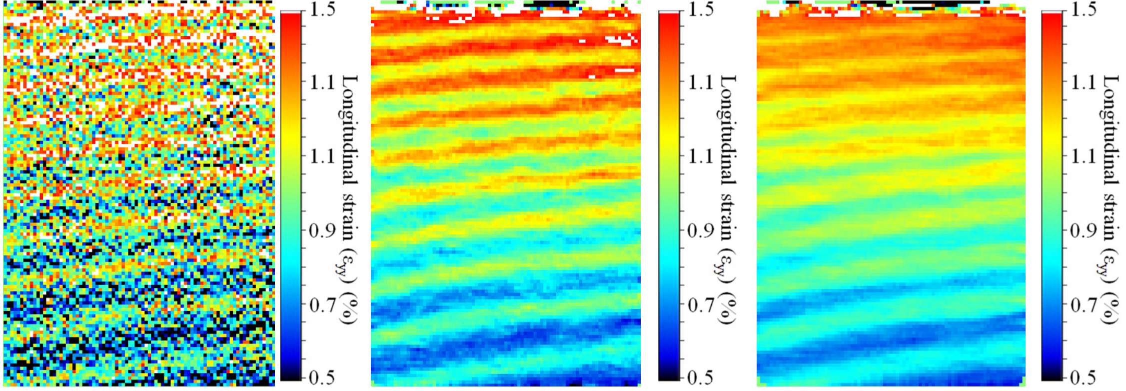

Subset size: 12 x 12 pixels
Step size: 8 pixels
41 x 41
8
63 x 63
8

Figure 37: Final SA5 image processed using various cell and step sizes.

As the bands are liable to disguise real material behaviour, or worse, be interpreted as material damage, methods for reducing or eliminating the effect were investigated.

As described in section 2.4.4, a sinusoidal variation in the subpixel accuracy of DIC is well known to occur for each pixel of applied displacement [41, 189]. It was therefore hypothesised that the behaviour occurred due to correlation algorithm inaccuracies. The periodicity of the bands were therefore investigated further by inspection of the longitudinal displacement maps from which the plots in Figure 36 are derived.

The following analysis was conducted for the final displacement map of each camera an orientation. As a uniform strain is applied to the specimen, the displacements on the specimen surface are expected to increase linearly along the specimen height. Any deviation from these displacement values are as a result of error in the DIC measurement. These errors were calculated and presented in Figure 38 for the Motionpro and SA5 cameras in the usual upright orientation.

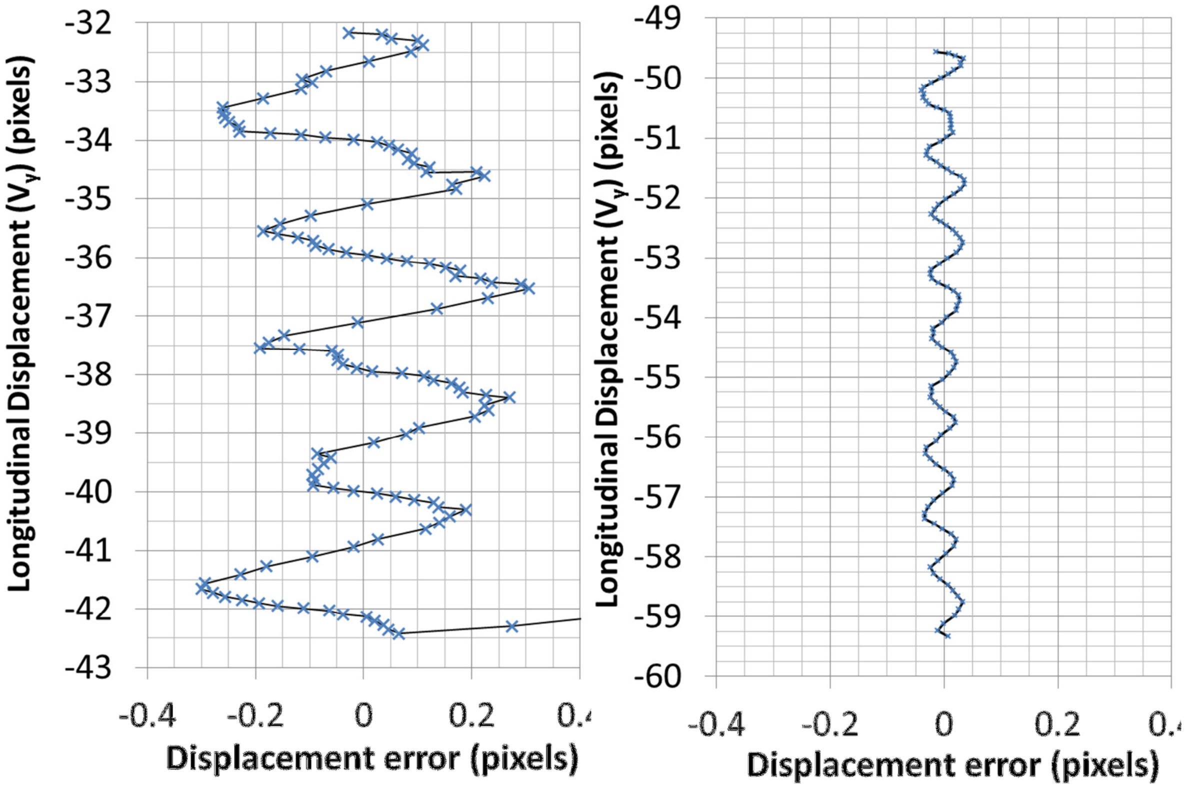

Redlake Motionpro-X3 Photron SA5

Figure 38: Error in calculated displacement as a function of applied displacement when using a bilinear interpolation method.

A periodic error behaviour was found for all cameras types. The SA5 and E-Lite cameras displayed a full period for every 1 pixel of applied displacement with the greatest accuracy occurring at integer and 0.5 pixel displacements. Such behaviour is typical of correlation algorithms [41, 189]. The Motionpro data when upright displayed a period for every 2 pixels of applied displacement. This behaviour was unexpected and is investigated further later in the chapter.

5.4 Application of Higher Order Subpixel Interpolation Method

In an effort to minimise the banding effect, correlations were repeated using a high accuracy 6th order spline subpixel interpolation method. Figure 39 and Figure 40 present a selection of longitudinal strain maps for the three camera types in the two orientations when using the high accuracy subpixel interpolation method. Whilst the periodicity and the magnitude of the banding patterns remain unaffected in the Motionpro data, the bands previously exhibited in the E-Lite data are eliminated by use of the high accuracy subpixel interpolation. Banding patterning of a lower magnitude is still apparent in the SA5 data.

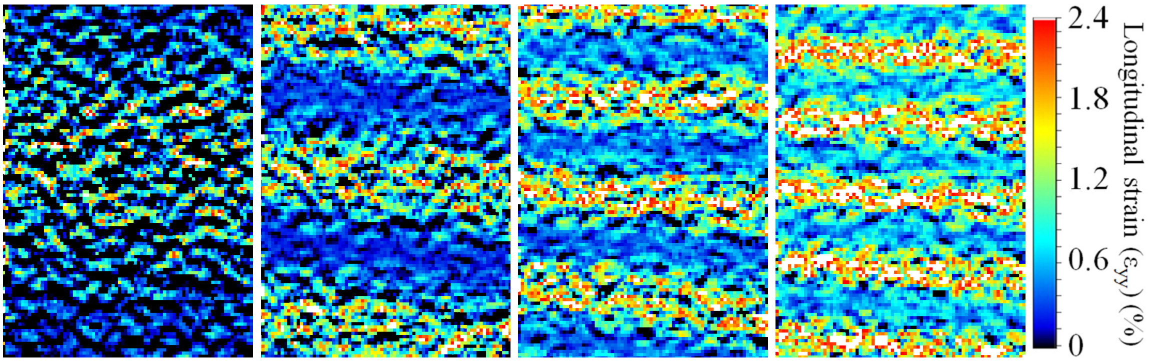

Motionpro-X3 Plus

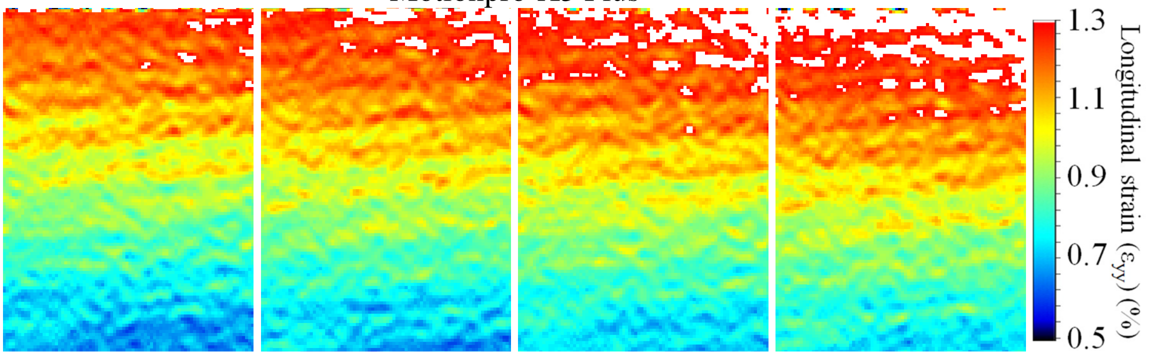

Photron SA5

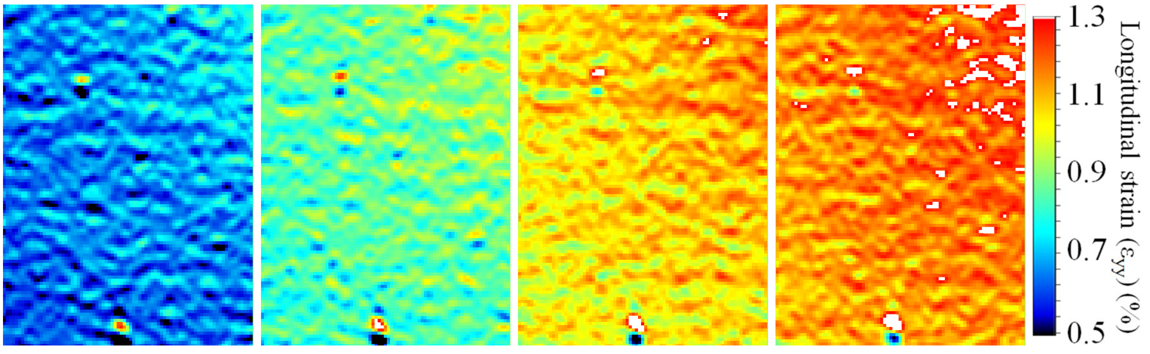

Imager E-Lite

Figure 39: DIC strain maps using a 6th order spline subpixel interpolation of a unidirectional composite specimen loaded to 1.2% strain

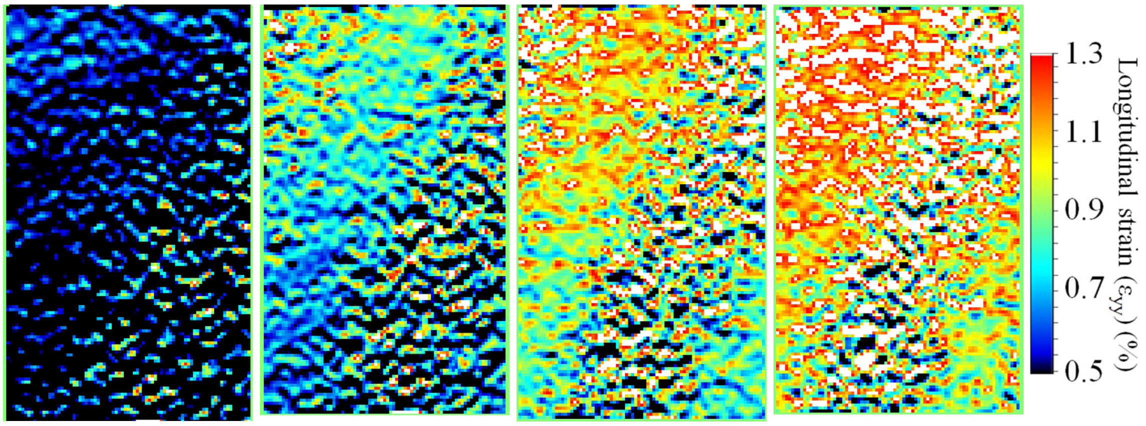

Motionpro-X3 Plus (Rotated 90°)

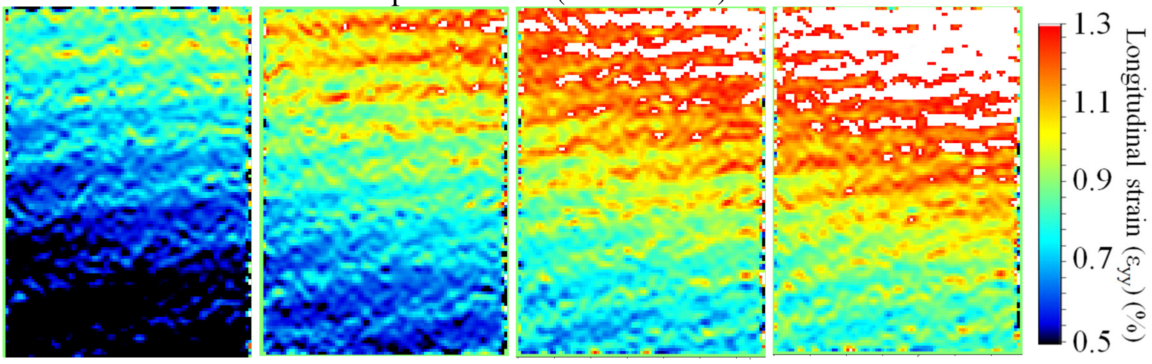

Photron SA5 (Rotated 90°)

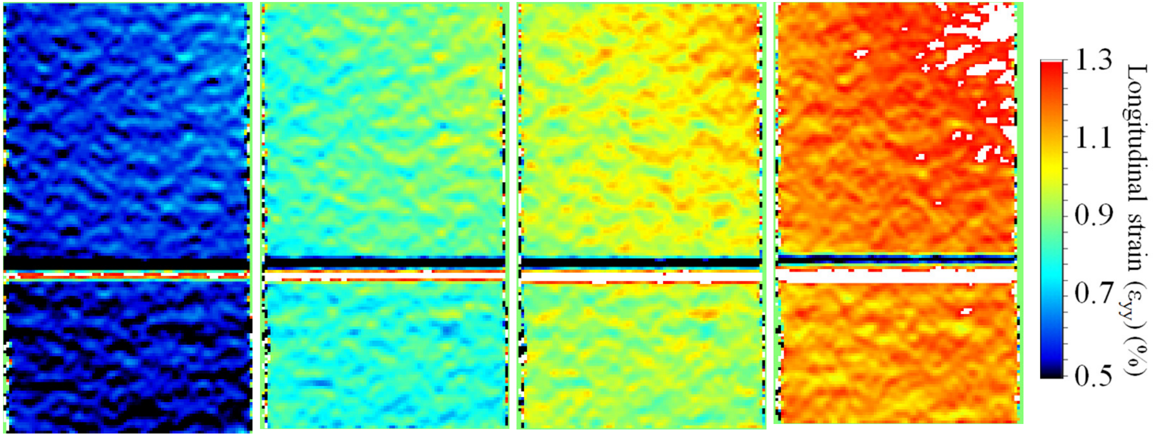

Imager E-Lite (Rotated 90°)

Figure 40: DIC strain maps using a 6th order spline subpixel interpolation of a unidirectional composite specimen loaded to 1.2% strain, showing the effect of camera hardware and camera rotation.

Correlations were also carried out using MatchID [190] using a subset size of 21 pixels and a step size of 10 pixels. The correlation was carried out using the ZNCC correlation method with a bicubic interpolation method. Figure 41 shows the final longitudinal strain map from the Imager E-Lite camera in an upright orientation. The bands are still apparent despite the change in correlation software.

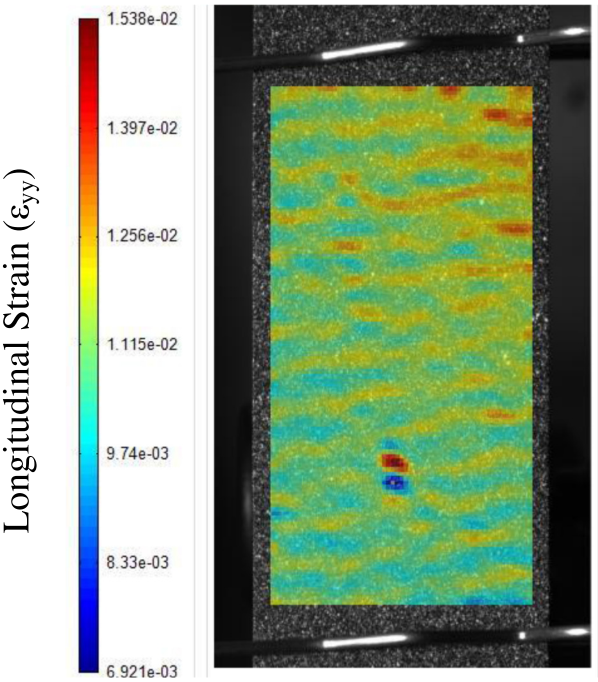

Figure 41: Final longitudinal strain map of the Imager E-Lite in the upright orientation.

Using the same procedure as discussed previously to produce Figure 38, the displacement errors were calculated when using the high accuracy interpolation method in DaVis 8.1.3 for all cameras and orientations. Figure 42 shows the change in periodic behaviour when the high accuracy method is used for the SA5 data when orientated upright. The error is much decreased when using the 6th order spline method but not entirely eliminated. The use of this method was also found to cause a phase shift of half a pixel. Similar behaviour was found from the SA5 data when rotated. The error was found to reduce to negligible levels for the Imager E-Lite camera when using the high accuracy method in both orientations. The large errors found from the Motionpro data was found to be unaffected by use of the high accuracy method.

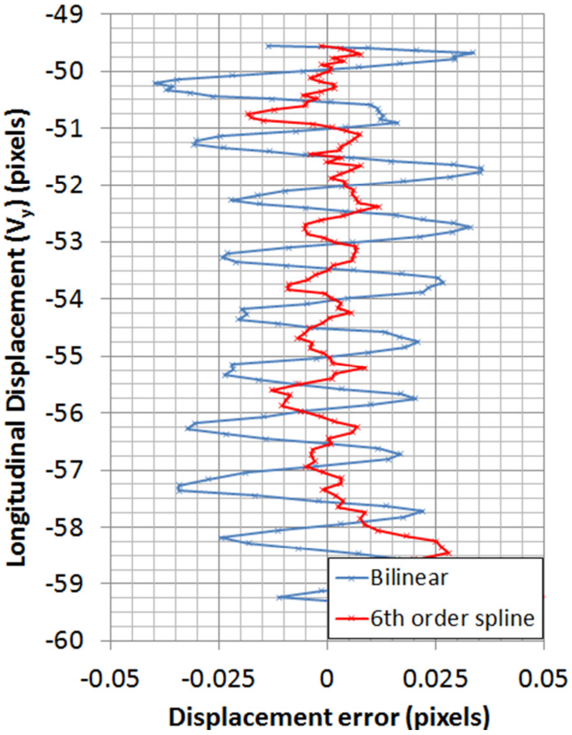

Figure 42: Comparison of displacement errors in SA5 data when using bilinear and 6^{th} order spline subpixel interpolation methods.

5.4.1 Correlation Strength

In an effort to further understand the remaining error after the application of the high accuracy interpolation method, maps of the correlation strength were studied (See section 2.4.2 for a description of correlation strength). Upon study of the correlation strength maps, a similar banding pattern was found to that previously found in the longitudinal strain maps. Figure 43 presents maps of correlation strength for the final correlated image of each camera type and orientation when using the high accuracy subpixel interpolation (Note the different scales for each type of camera.)

In the Motionpro and SA5 data, the lowest correlation values were found to coincide with the regions of greatest displacement error. The correlation strengths of the E-Lite camera data were found to be generally higher than those of the SA5 camera which in turn, were found to be greater than those of the Motionpro camera, as shown by the different scales used in Figure 43. Banding in the SA5 correlation strength maps (and to a lesser extent in the Imager E-Lite) was found in both the vertical and horizontal directions. Upon study of the horizontal strain maps, it was found that similar bands in the strain data also occur in the horizontal direction due to the horizontal displacement of the specimen surface due to material contraction under axial loading. The bands in correlation strength were found to occur at every integer pixel displacement in both the x and y directions.

Bands in the correlation strength maps could not be noted in the horizontal direction for the Motionpro camera when upright. This is believed to be due to the large range of correlation value in the vertical direction masking any smaller changes in the horizontal direction.

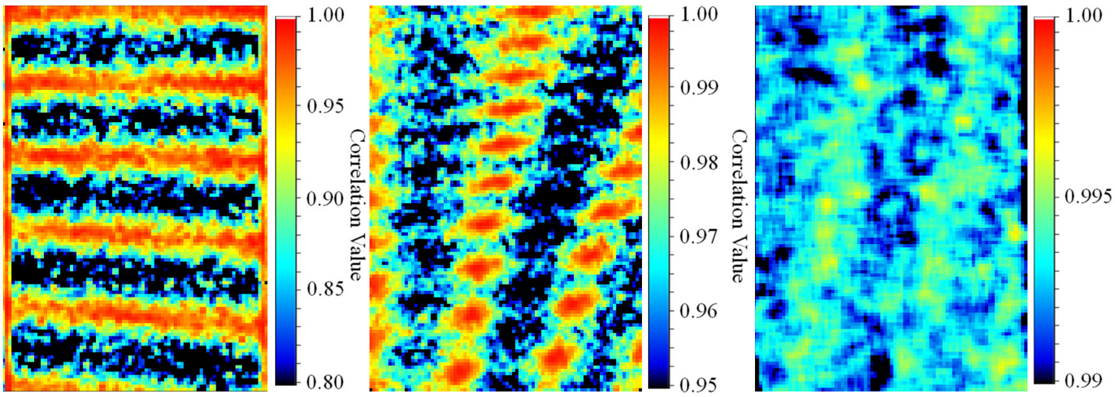

Motionpro (Upright) SA5 (Upright) E-Lite (Upright)

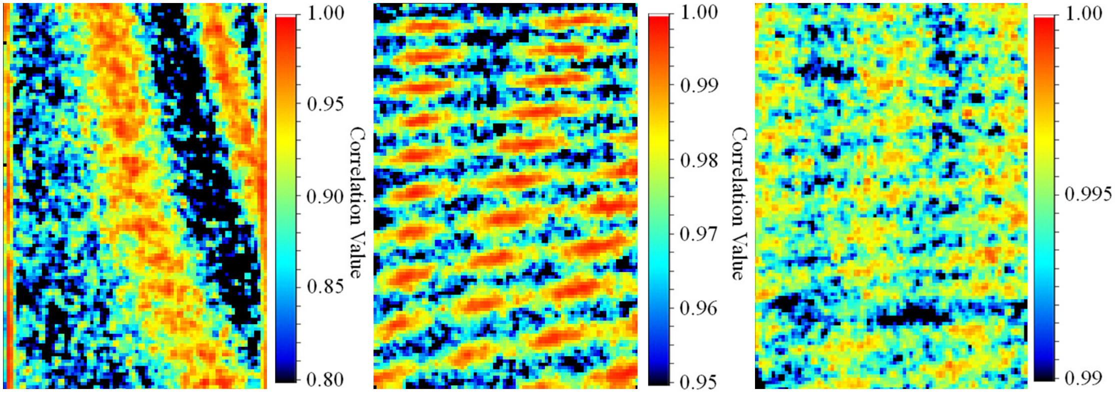

Motionpro (Rotated) SA5 (Rotated) E-Lite (Rotated)

Figure 43: Correlation strength maps for the final image in each of the 6 tensile tests conducted when using the 6th order spline subpixel interpolation

The use of the 6th order spline subpixel interpolation method was found to significantly reduce the systematic errors when using the SA5 and to reduce the behaviour to negligible levels when using the Imager E-Lite camera, the Motionpro data was largely unaffected. It is therefore recommended that work requiring DIC and high speed cameras should use the Photron SA5 camera combined with the high accuracy subpixel interpolation method. Due to camera availability, similar Photron SA1 cameras are used in later chapters.

Although the effect of systematic errors has been significantly reduced, such that real material behaviour is distinguishable from systematic error, the cause of the behaviour is unclear. The pixel locking (mean bias) effect, as defined in section 2.4.4 was ruled out as the cause of the systematic errors as the effect is dependent on speckle size and correlation algorithm only. Since the speckle size was kept constant by using the same specimen and the same spatial resolution for all tests, the effect of pixel locking would also be expected to be constant across all tests. The systematic errors would also not be expected to change as a result of camera choice or camera rotation if the effect was due to pixel locking.

5.5 Investigations of Pixel Locking

The investigations discussed in the previous sections were complicated by camera alignment and the horizontal material contraction as a result of a vertically applied strain. To remove these effects it was decided to develop a numerical stretching process.

The numerical image stretching algorithm was implemented in Matlab by frequency domain zero padding. This method is well known in digital signal processing (also known as 'exact interpolation') [191, 192] and is usually used to interpolate 1D time-domain signals, but can equally be applied to 2D image data.

An important point to note is that any image can be represented as a superposition of sinusoidal waves. A discrete Fourier transform of an image measures the "spatial frequencies" in the image, returning the real and imaginary parts, commonly referred to as magnitude and phase respectively when image processing. An image composed only of a one sinusoidally varying intensity, such as those presented in Figure 44 (i) and (ii) (top), will return three magnitude values when processed using an FFT.

The centre value is the DC value and corresponds to the overall brightness of the image. The points either side of this value give the spatial frequency component of the image. Two points are given as the FFT is always symmetrical. The centre image of Figure 44 has a greater spatial frequency. The values in the magnitude FFT therefore move closer to the outer edges. A speckle pattern is composed of many spatial frequencies, hence the resulting FFT magnitude image is much more complicated. Large speckles contribute more low frequency data whilst small speckle contribute more high frequency data.

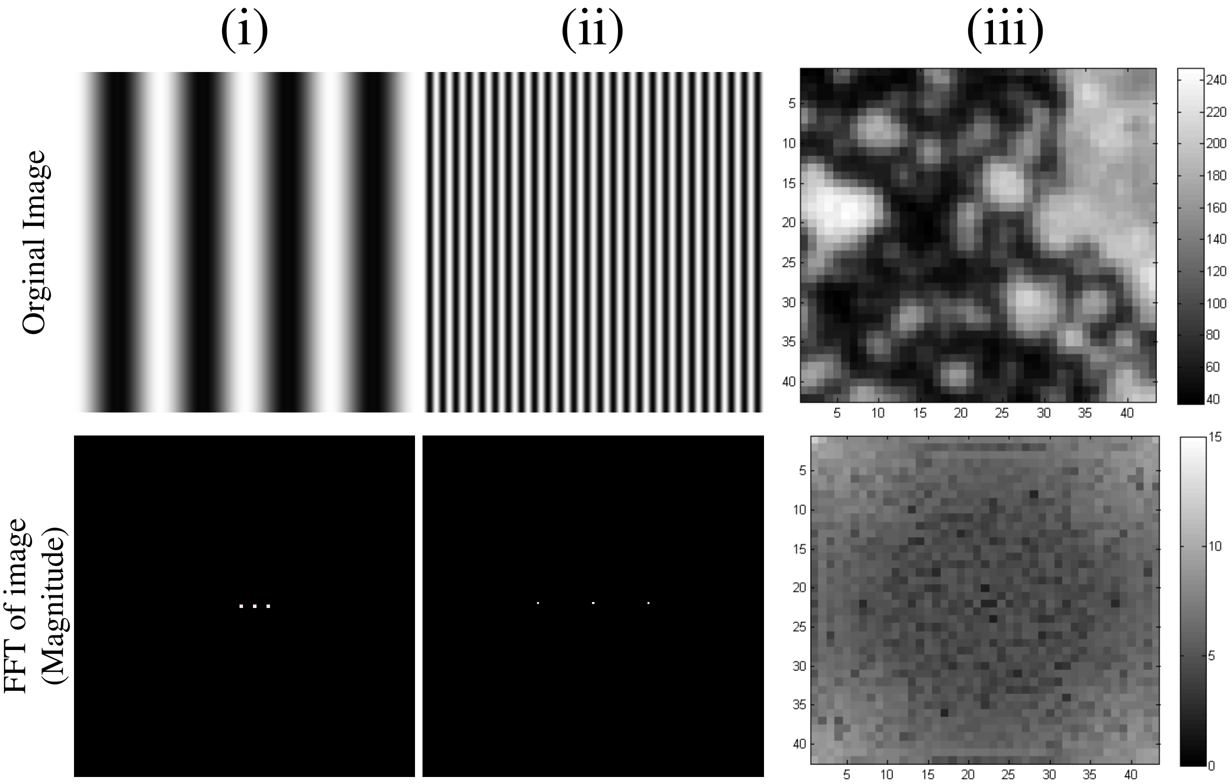

Figure 44: FFT of various images showing the effect of spatial frequency content

The image stretching procedure will now be explained using a 1D image as an example. A high spatial resolution image with a sinusoidally varying intensity is shown as (a) in Figure 45, whilst a lower resolution (1 x 20 pixel) image is shown as (b) in Figure 45.

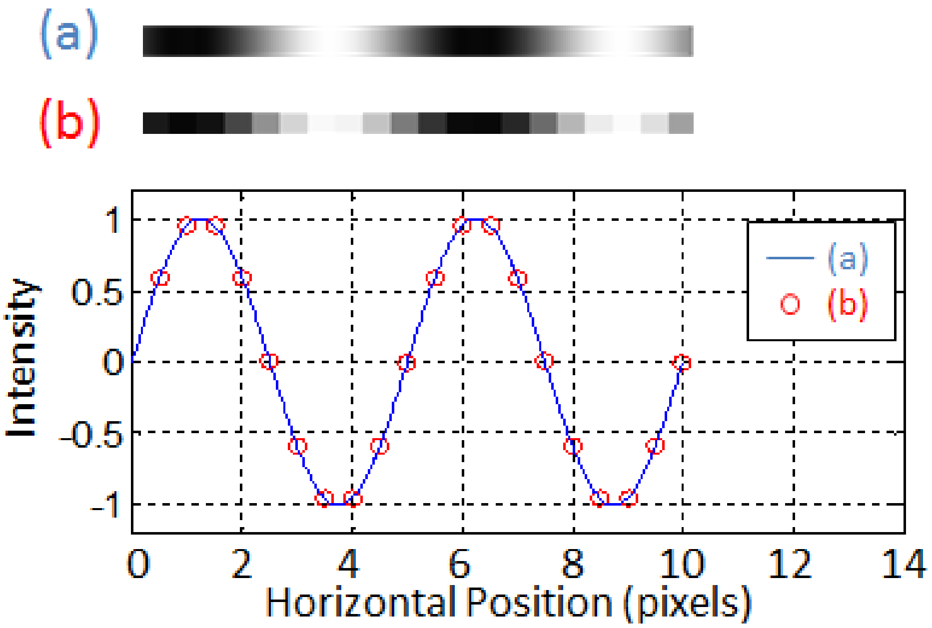

Figure 45: Discretisation of an image with a sinusoidally varying intensity. (a) High spatial resolution image, shown by a blue line in lower figure. (b) 1 x 20 pixel image represented as red points in lower figure.

The set of 20 samples within the low resolution image are converted from the spatial (image) domain to the frequency domain using a discrete FFT. This is shown in (b) and (c) of Figure 46 for the real (magnitude) and imaginary (phase) components respectively. The magnitude and phase samples are then padded with zeros at the centre of the set. This is essential to maintain spectral symmetry [191]. Zero values are highlighted in black in (d) and (e) for the real and imaginary components. An inverse discrete FFT is applied to the padded frequency data to convert back to the time domain. The resulting data, shown in (f) is now interpolated at a greater number of sampling points, resulting in an elongated sine wave. The example shown adds four zeros to the 20 sample set to give 20% elongation after conversion back to the spatial (image) domain. It follows that padding the 20 point data set with 10 zeros results in a 50% signal elongation.

A key feature of this technique is that the zeros added to the frequency domain data contain no frequency content. Therefore no additional data is added to the image and the interpolated images are composed of exactly the same frequencies as the original image [191]. Therefore no data is added or lost. This is a key advantage over other image stretching algorithms in order to avoid additional noise.

An artefact of the zero padding process is a decrease in the signal amplitude directly proportional to the percentage of elongation. To compensate, the amplitude of the signal is increased as a post process. A second artefact is that the resulting stretched data is larger than the original. Images stretched using this algorithm must therefore be cropped prior to image correlation.

A new, higher resolution (4000 x 2800 pixel) speckle pattern image was captured and manipulated using the numerical stretching algorithm. A higher resolution image was required in order to maintain an adequate image size after fill-factor simulations, to be discussed in section 5.6.

A speckle pattern was applied to a matt white surface using RS matt black paint. A larger nozzle diameter was used to increase the speckle size produced. The surface was imaged using a Pentax K-x digital SLR camera combined with a 300 mm macro lens at a stand-off distance of approximately 2.5 m. The 4000 x 2800 pixel speckle pattern image was artificially strained using the zero-padding algorithm to produce a series of 100 strained images in steps of 0.01% up to 1% strain. The strained images were processed in DaVis 8.1.3 using a cell size of 31 x 31 pixels, a step size of 8 pixels and a 6th order spline subpixel interpolation method. Figure 47 presents a selection of the strain maps between 0.1 to 0.18 % of applied strain.

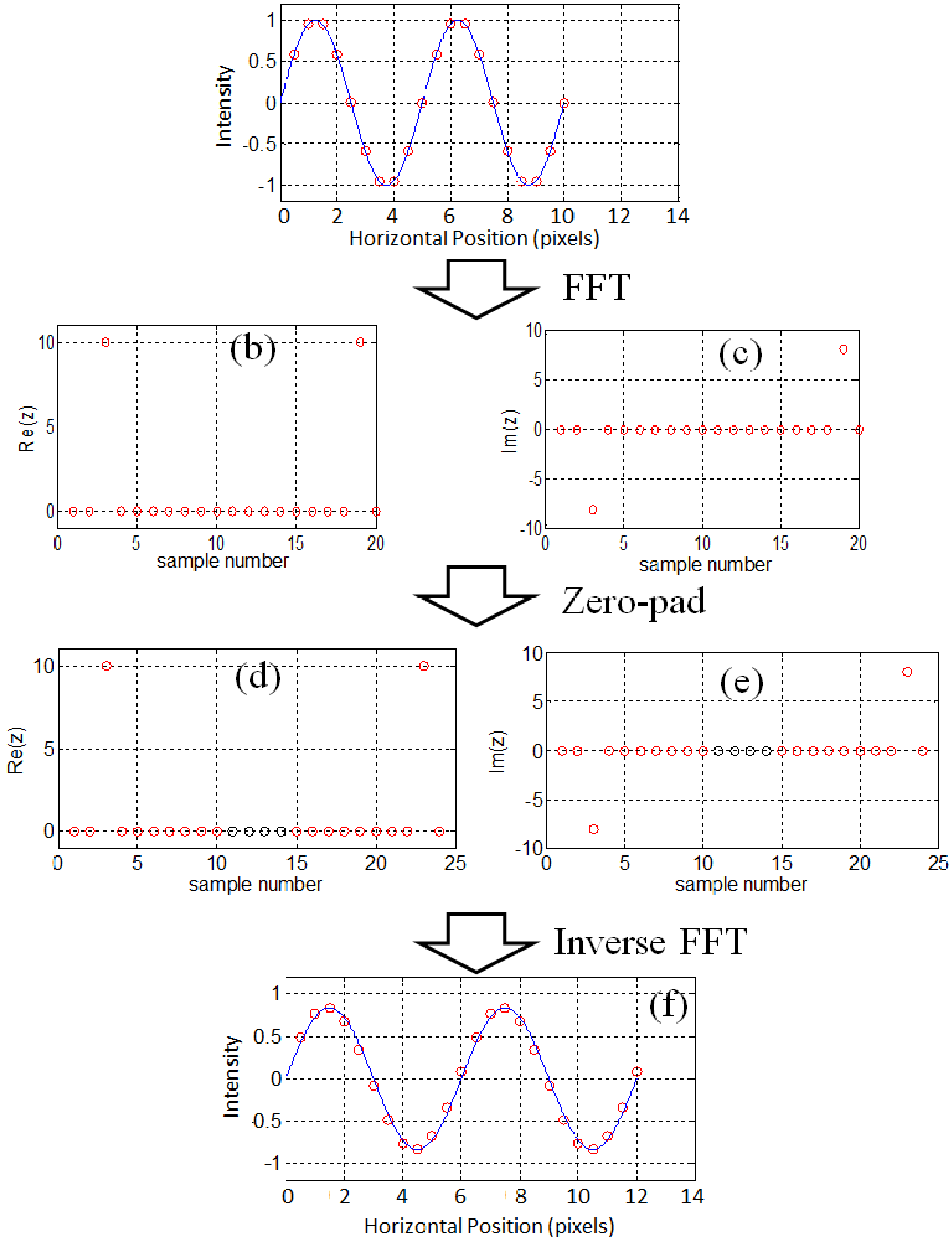

Figure 46: Example of zero-padding a 1D image in the frequency domain.

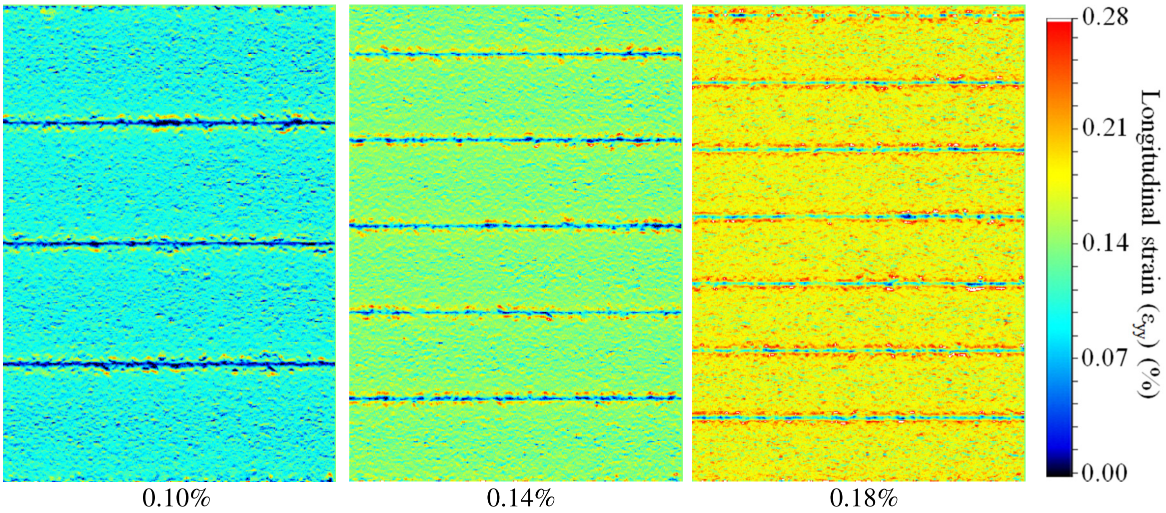

Figure 47: Selection of DIC Strain maps from artificially stretched images showing the reoccurrence of band patterns.

The bands were found to still occur, although at a much lower magnitude than those found during tensile tests. Also, the bands were found to occur at every integer pixel displacement.

Schreier *et al* states that a reduction of the high frequency content in the speckle pattern image through use of a low pass filter can be used to reduce systematic errors such as pixel locking [41]. A 2D Gaussian low pass filter was therefore applied on the original speckle pattern image prior to applying the zero-padding algorithm. The filter was implemented using the following algorithm in the frequency domain,

$$\mathrm{H}(\mathrm{u},\mathrm{v}) = \mathrm{e}^{\left(-\frac{\mathrm{r}^2}{2\mathrm{F_c}}\right)} \qquad 5.1$$

where
$$\mathrm{r} = \sqrt{\mathrm{m}^2 + \mathrm{n}^2}$$

where $H(u,v)$ is the image data in the frequency domain for columns u and rows v, F_c is the cutoff frequency, m is the vertical distance (pixels) from the data centre and n is the horizontal distance (pixels) from the data centre.

The original speckle pattern image was filtered using the low pass filter with a cutoff frequency of 400 Hz. A small 120 x 120 pixel area of the image is shown before and after the application of the low pass filter in Figure 48. The filter has the effect of reducing high frequency content, such as small speckles and camera noise. Even when large speckles are imaged some high frequency content is unavoidable, as can be seen in Figure 48.

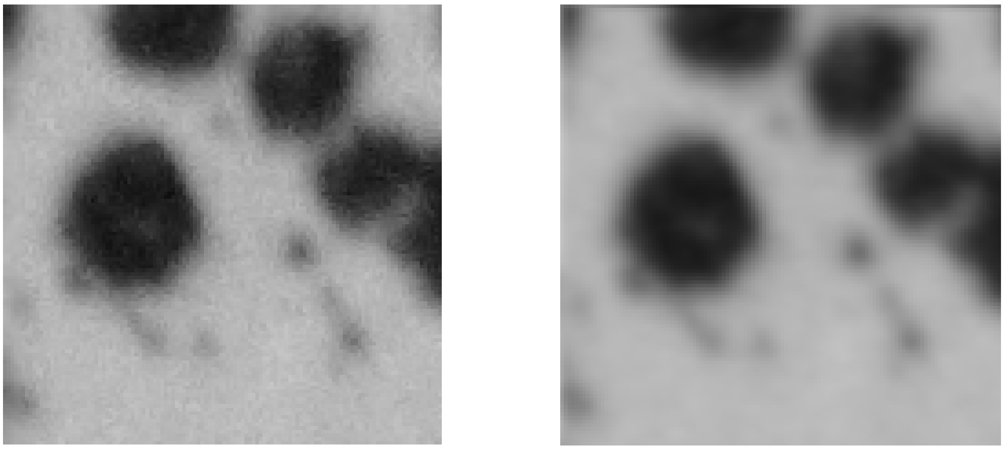

No filtering 400 Hz low pass Gaussian filter

Figure 48: 120 x 120 pixel areas of the speckle pattern image before and after applying Gaussian filtering.

The filtered image was numerically stretched using the same procedure and the resulting images were correlated using identical settings as in the previous investigation. The strain maps produced are presented in Figure 49. It can be seen that the bands are no longer evident. This finding shows that the occurrence of these systematic banding errors occur at least in part due to the high frequency content of images. The displacement maps from which Figure 47 and Figure 49 were produced were analysed for pixel locking by extracting the subpixel component of all displacement vectors and plotting the values in a histogram. The results are shown in Figure 50. Clear pixel locking behaviour is evident for the unfiltered image data, as shown by the increased number of displacement vectors close to 0 and 1 pixel. This behaviour is significantly reduced by the application of the low pass filter.

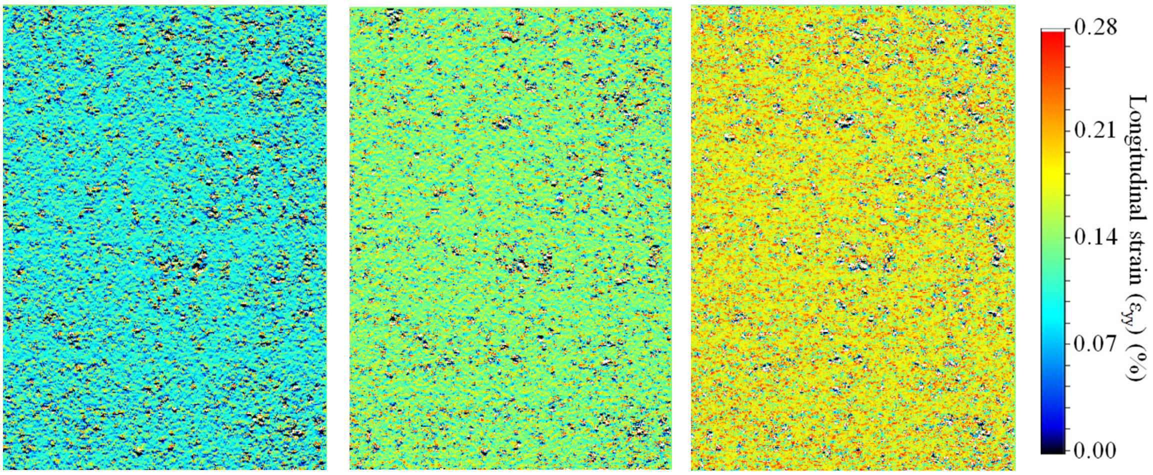

0.10% 0.14% 0.18%

Figure 49: Selection of DIC Strain maps from artificially stretched images filtered using a 2D low pass filter of 400 Hz.

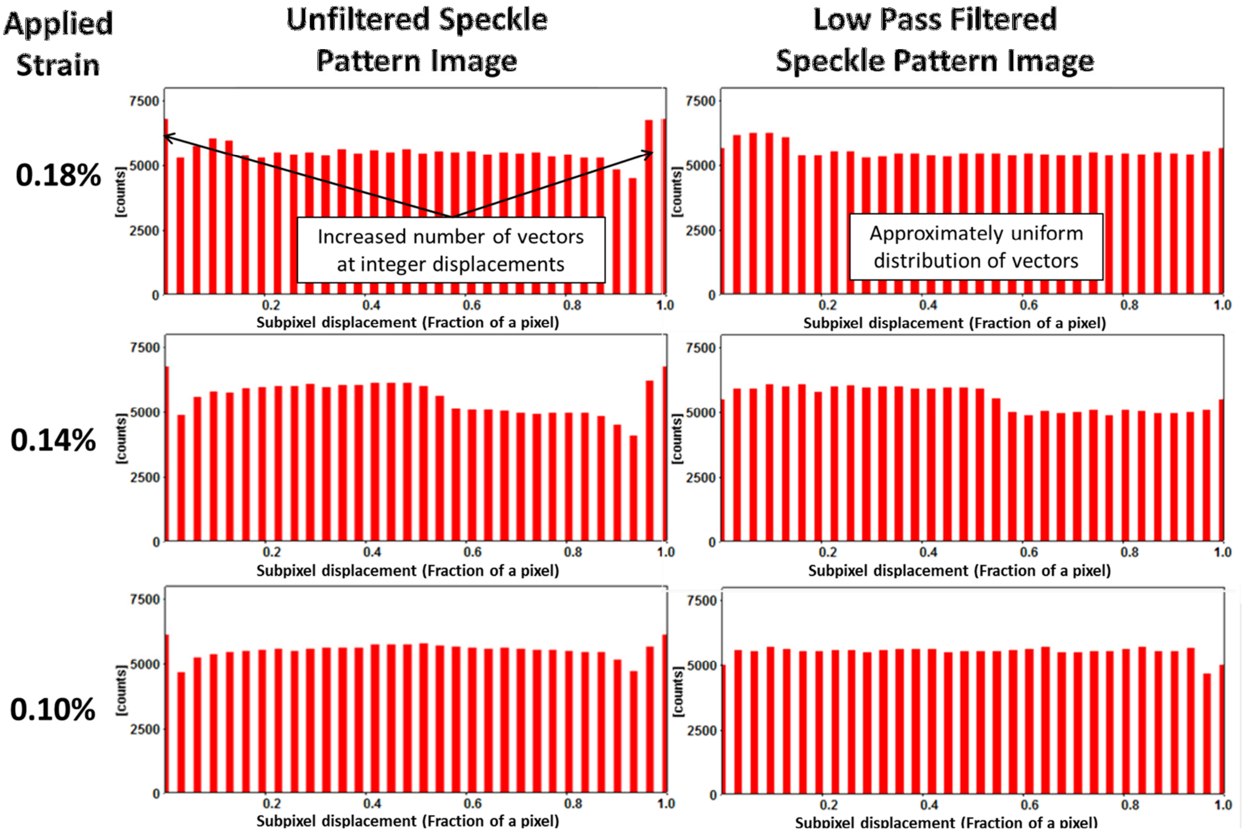

Figure 50: Histogram plots of the subpixel displacement component to investigate pixel locking.

Pixel locking cannot be the sole cause of the bands found during the tensile tests presented in section 5.4 as the bands were found to change according to the camera used and camera orientation. This is despite the same speckle pattern being imaged at the same spatial resolution. The effect must therefore be arising as a result of sensor architecture.

5.6 Fill Factor Simulations

The change in systematic error due to camera choice and rotation suggests an underlying cause arising from the sensor architecture. It was considered that the sensor fill-factor may be the cause of the banding seen in the correlated images that could not be attributed to the accuracy of the subpixel interpolation algorithm or pixel locking. It was hypothesised that as the Motionpro camera behaves differently when rotated, the fill factor may be greater in one direction than the other. This was investigated further through numerical simulations.

The set of 100 numerical stretched images were processed using a separate algorithm to simulate the effect of sensor fill factor (discussed shortly). The use of the numerical stretching procedure is essential for this analysis as it eliminates the need for a real camera to produce a set of strained images. The camera has its own inherent sensor fill factor and so would conflict with the simulated fill factor. Use of the numerical stretching also avoids experimental complications such as camera and loading misalignment.

The fill factor simulation was developed in Matlab by first dividing the image into areas of 4 x 4 pixels. For each area, the following procedure is applied. For the case of a 25% fill factor, the intensity values of the upper left quadrant of 2 x 2 pixels is extracted and the mean intensity calculated. This 2 x 2 area is analogous to the light sensitive area of a pixel in a real camera sensor with 25% fill factor. This mean intensity value is placed into one pixel in a new, separate image. A schematic of this procedure for 25% and 100% fill factors is shown in Figure 51. This algorithm was repeated for each 4 x 4 area and each image in the series. A 56% fill factor was simulated by applying the same procedure but using an active area of 3 x 3 pixels over which the mean intensity value is calculated. To simulate a 100% fill factor, all 16 pixels in a 4 x 4 area are used. All of the simulated fill factor images are therefore a quarter of the size of the original image, hence the need for a large original speckle pattern to obtain a usable speckle pattern for DIC analysis.

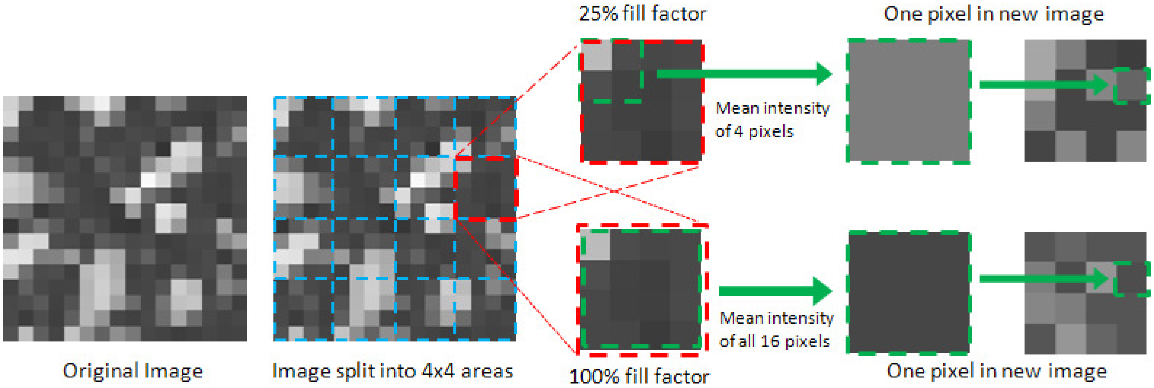

Figure 51: Methodology for numerically simulating camera fill factors

The simulated fill factor procedure was applied to the image set generated using the zero-padding technique. The use of numerically stretched images allows exactly the same set of images to be sampled at exactly the same points using various fill factors. This would be impossible to achieve in reality using different cameras, due to slight variations in pixel sensitivities, pixel sizes, spatial resolution, alignment etc.

A number of variables were investigated in turn for their effect on the systematic errors. Fill factors of 100%, 56% and 25% were simulated using the procedure previously described. The effect of non-regular active areas was also investigated as a possible cause of the orientation dependent banding in the images captured by the Motionpro camera. A schematic demonstrating the layout of regular and non-regular active areas is shown in Figure 52.

The effect of speckle pattern size was also investigated by down-sampling the original 4000 x 2800 pixel speckle pattern image to 75% (3000 x 2100 pixels) and 50% (2000 x 1400 pixels) of the original size, prior to numerical stretching. The resampling was carried out in Matlab using a bilinear interpolation method whereby the output pixel values are a weighted average of pixels in the nearest 2 x 2 neighbourhood. Table 13 presents a test matrix of all the variables investigated. All tests were conducted twice, the first without filtering and the second using a 400 Hz low pass Gaussian filter applied during zero-padding.

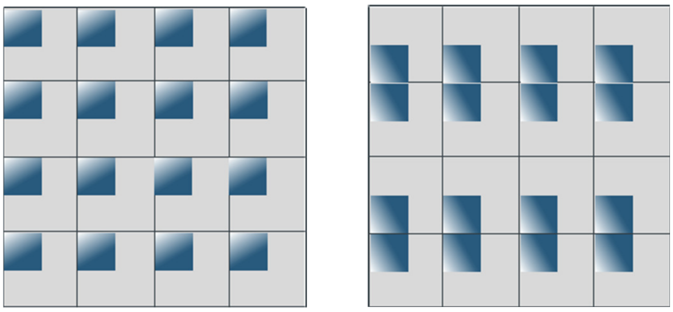
Regular sensor array of 4x4 pixels with 25% fill factor

Non-regular sensor array of 4x4 pixels with 25% fill factor

Figure 52: Schematic showing regular and non-regular active area locations on a sensor

	Image size (pixels)	**Active areas position**	**Fill factor**		**Image size (pixels)**	**Active areas position**	**Fill factor**		**Image size (pixels)**	**Active areas position**	**Fill factor**
(a)	4000 x 2800	Regular	100%	**(g)**	3000 x 2100	Regular	100%	**(m)**	2000 x 1400	Regular	100%
(b)	4000 x 2800	Regular	56%	**(h)**	3000 x 2100	Regular	56%	**(n)**	2000 x 1400	Regular	56%
(c)	4000 x 2800	Regular	25%	**(i)**	3000 x 2100	Regular	25%	**(o)**	2000 x 1400	Regular	25%
(d)	4000 x 2800	Non-Regular	100%	**(j)**	3000 x 2100	Non-Regular	100%	**(p)**	2000 x 1400	Non-Regular	100%
(e)	4000 x 2800	Non-Regular	56%	**(k)**	3000 x 2100	Non-Regular	56%	**(q)**	2000 x 1400	Non-Regular	56%
(f)	4000 x 2800	Non-Regular	25%	**(l)**	3000 x 2100	Non-Regular	25%	**(r)**	2000 x 1400	Non-Regular	25%

Table 13: Test matrix of simulated fill factor trials

Two potential routes for processing the simulated fill factor images were determined:

1. To use cell and step sizes that are decreased in proportion with the downsampled image size, i.e. if the full size image sets are processed using a cell size of 31 x 31 pixels and a step size of 8, then the 2000 x 1400 image sets are processed using a cell size of 15 x 15 pixels and a step size of 4.
2. To use the same cell size and step size regardless of image downsampling.

Option one has the benefit of keeping exactly the same speckles inside each subset, so only the speckle size is changed as downsampled images are used. However, it is impossible to differentiate between errors caused by the change in speckle size and errors introduced as a result of the decreased precision of smaller cell and step sizes.

The result of option two is that the expected strain accuracy is constant across all correlations. However, the number of speckles within each cell will change according to the level of downsampling. Also, the number of displacement vectors in the correlated maps decrease with greater downsampling.

Although both routes were evaluated, the second route was determined to be the only feasible method to quantitatively compare the effect of speckle sizes on the systematic errors. The artificially strained image sets, outlined in Table 13, were processed using a cell size of 23 x 23 pixels, a step size of 6 pixels and a 6th order spline subpixel interpolation method.

Figure 53 presents examples of strain maps from tests (a), (b), (c), whilst Figure 54 presents tests (m), (n) and (o), all without use of the low pass filter. Figure 53 shows that the banding behaviour becomes greater in magnitude as lower fill factors are simulated. Similarly to the investigations presented in section 5.4, the number of bands in a strain map was found to be equal to the number of pixels of applied displacement, with the lowest error and the maximum correlation value found at integer pixel displacements. The periodic behaviour of 1 pixel period is is similar to that previously exhibited by the Photron SA5 camera and to a lesser extent the imager E-Lite camera, which is different to the errors caused by pixel locking where the greatest errors were found at integer pixel displacements.

A similar banding pattern occurs (see Figure 54) when the speckle size is halved using a 50% downsampling and applying the fill factor algorithm. The strain maps again display one error band for every pixel of applied displacement. As the downsampled images have half the number of pixels and hence half the spatial resolution, the same applied strain level causes half the number of pixels of displacement. This therefore manifests itself as half the number of bands in the images. Plots of correlation value, presented in Figure 55, show that the bands coincide with the areas of decreased correlation value, with a lower fill factor and a smaller speckle size contributing to further decreases in correlation value.

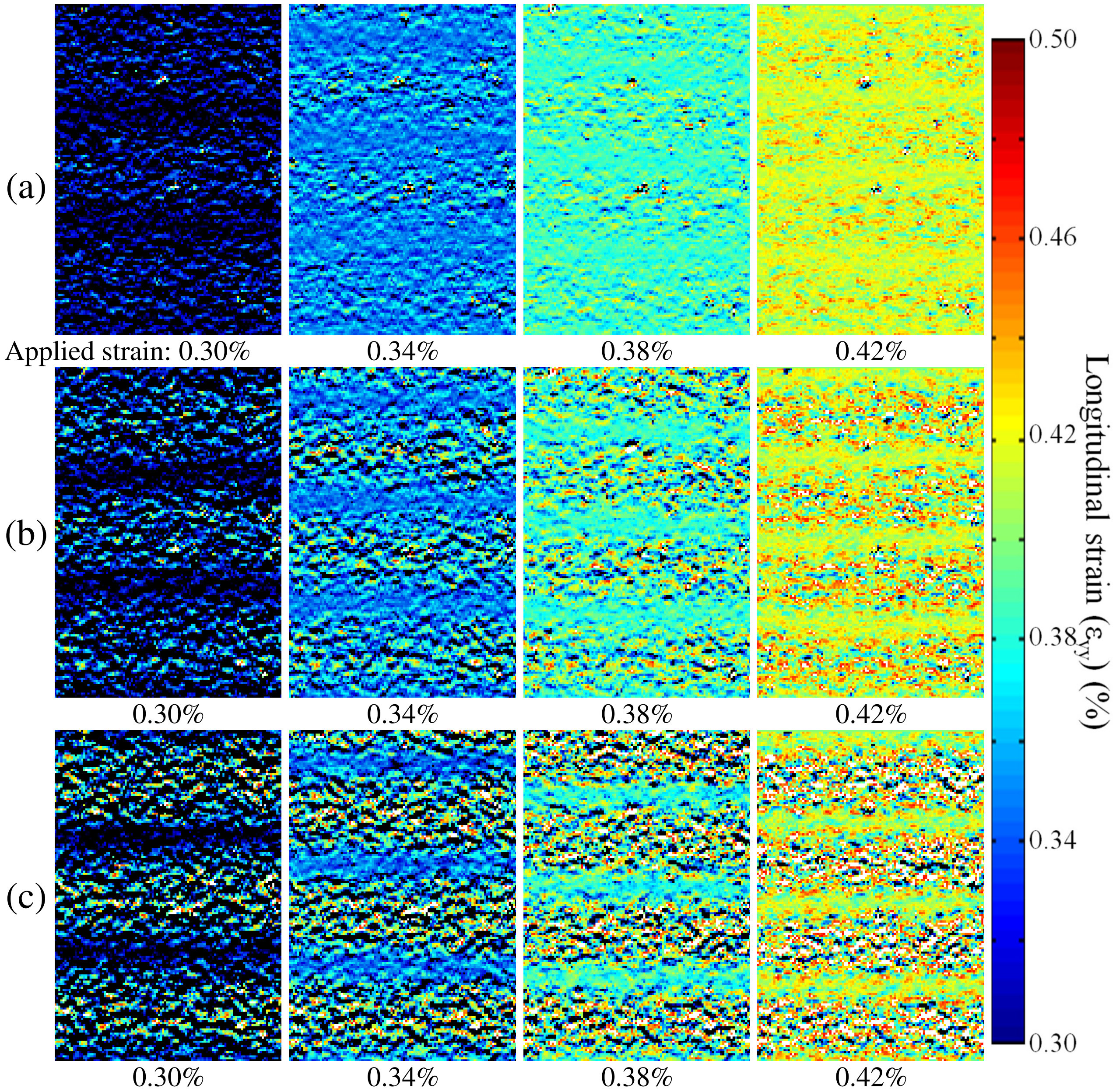

Figure 53: Selection of DIC Strain maps from artificially stretched images with fill factor simulation, showing the effect of sensor fill factor on systematic error behaviour.

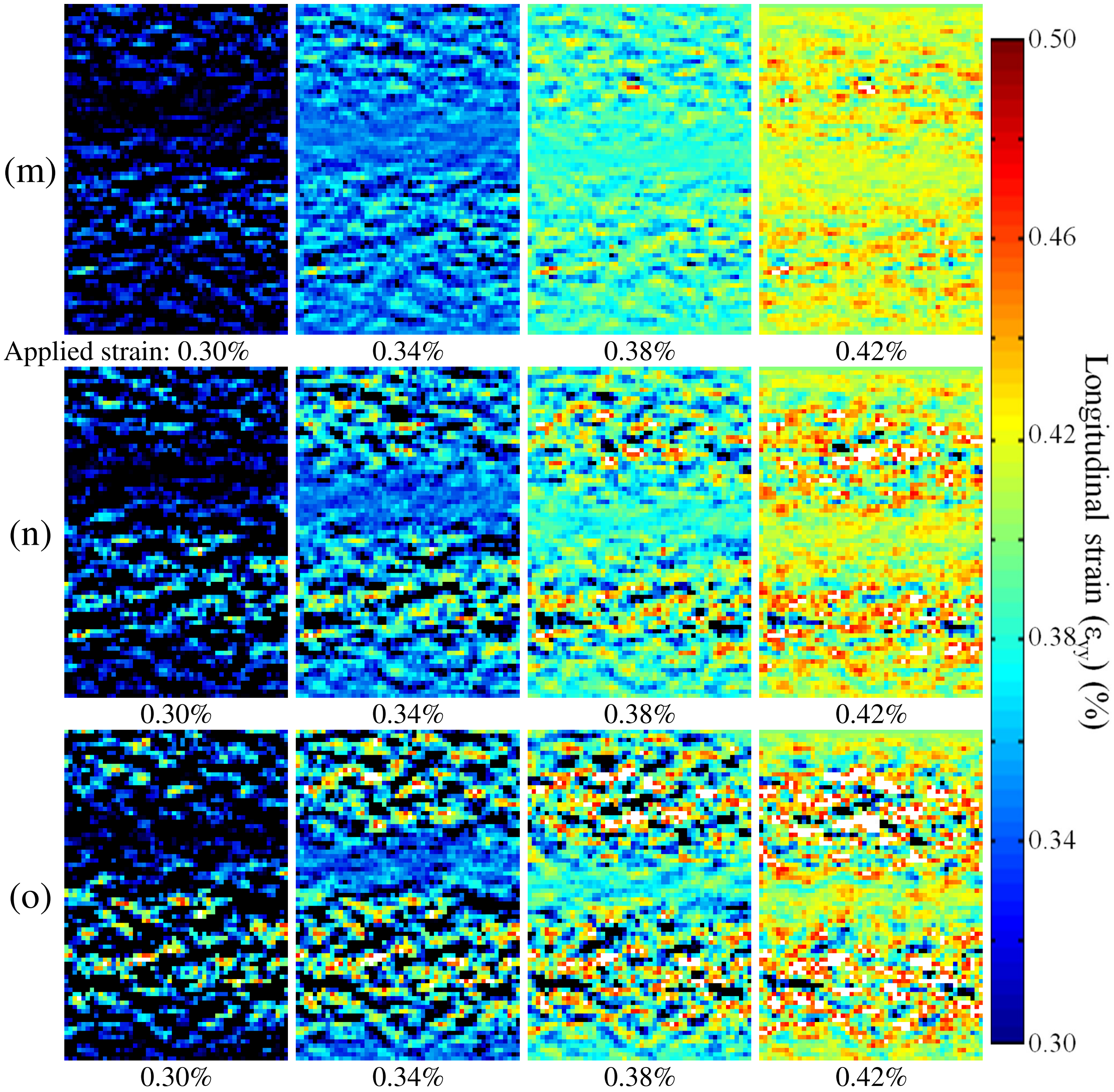

Figure 54: Selection of DIC Strain maps from artificially stretched images with fill factor simulation, showing the effect of speckle size and fill factor on systematic error behaviour.

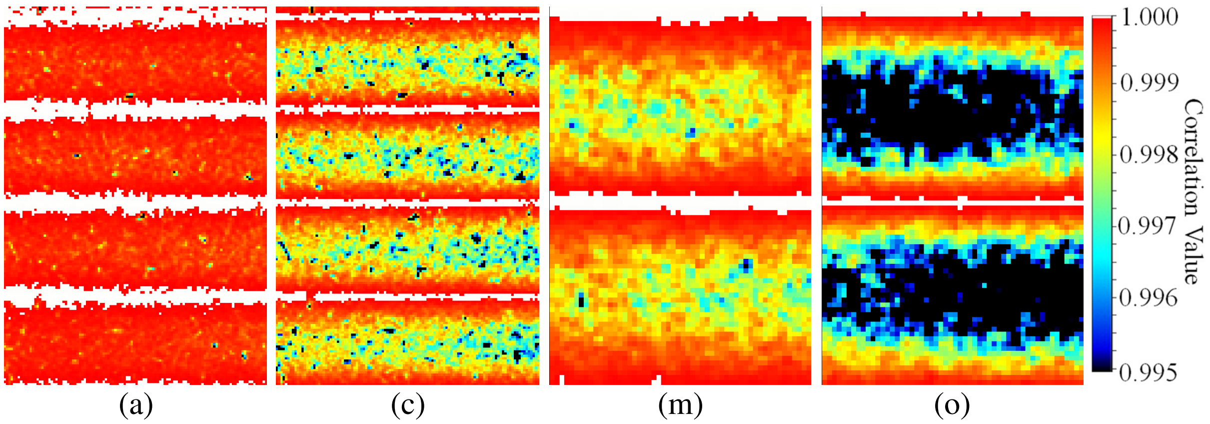

Figure 55: Maps of correlation value for the strain maps presented in Figure 53 and Figure 54 for an applied strain of 0.42%.

The strain maps at 0.5% of applied strain were analysed quantitatively using the following procedure. 0.5% strain was subtracted from the strain maps, so leaving the measurement error. The standard deviation of each row of strain data was then calculated, giving a measure of the strain precision as a function of vertical position. The mean strain of each row was not found to display any systematic behaviour. This procedure was applied to all fill factor simulations using regular active areas without Gaussian filtering, as shown in Figure 56. For all speckle sizes trialled, a lower fill factors result in decreased strain precision. The strain precision was expected to be inversely proportional to speckle size, as smaller speckles have fewer pixels and therefore carry less information. However, it was found that the full sized images displayed the highest strain errors, followed by the image sets downsampled to 50% of original size. The image sets downsampled to 75% of their original size show the lowest strain error, suggesting an optimum speckle size for these correlation settings. As subset size was kept constant across all tests, this finding is attributed to the greater number of speckles per subset in the downsampled images. Although more speckles are contained in each subset for the 50% downsampled image sets, it is believed that the speckles become too small, resulting in a decrease in strain precision.

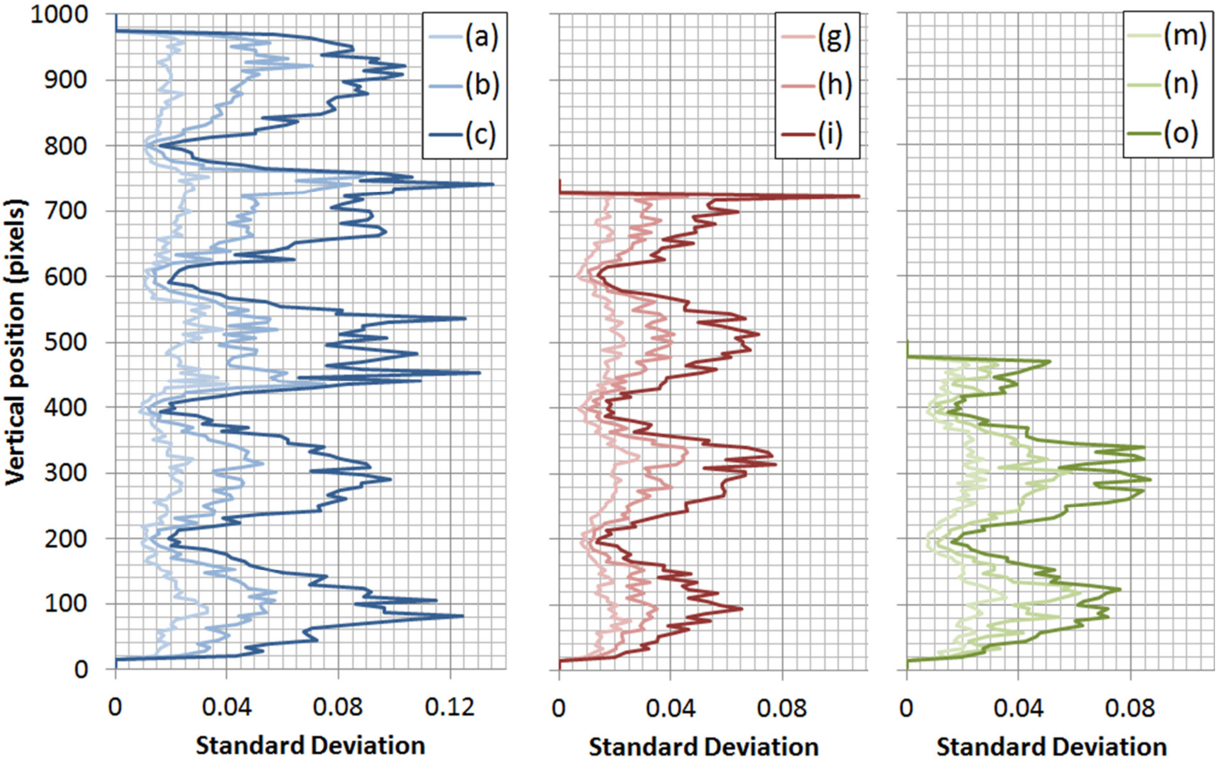

Figure 56: Strain precision as a function of vertical position for an applied strain of 0.5%. See Table 13 for description of test variables.

Further investigations were carried out by applying the same analysis to the fill factor simulations conducted with the use of the low pass filter. The results are shown in Figure 57 (please note the different scale compared to Figure 56). The use of the low pass filter eliminates the vast majority of strain error when full sizes images are used. The strain errors re-appear as greater downsampling is applied to images and lower fill factors are simulated. This proves that images must contain some high spatial frequency content for the banding effect to occur, but the problem is amplified by lower fill factors. Since high frequency content is inherent in all real images, the sensor fill factor will always have some effect on DIC strain measurements unless images are prefiltered.

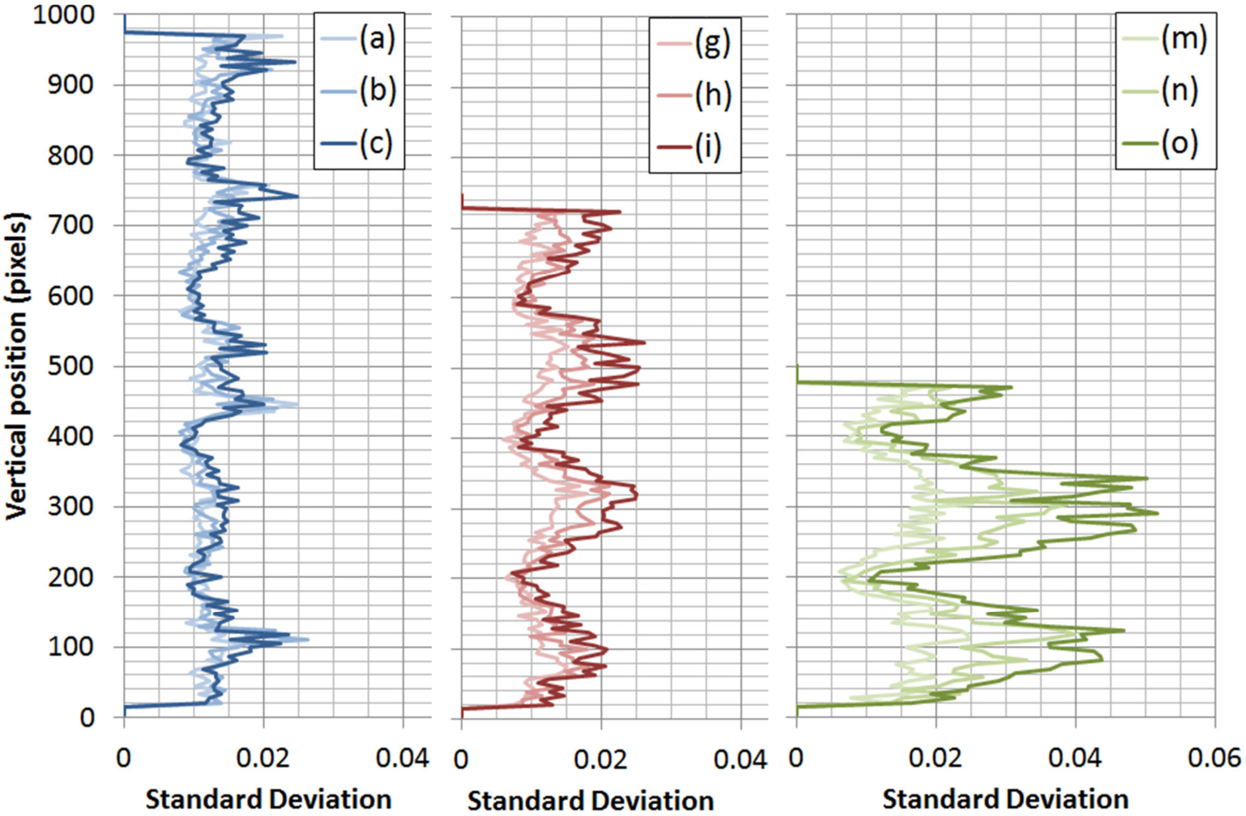

Figure 57: Strain precision as a function of vertical position for an applied strain of 0.5%, with low pass filter applied during artificial image straining. See Table 13 for a description of test variables.

The effect of non-regular active areas, as shown in Figure 52, was also investigated for their effect on the systematic errors. Selected strain maps from tests (d), (j) and (p) are presented in Figure 58. It was found that the use of non-regular active areas decreased the spatial frequency of the bands by a factor of two, i.e. two pixels of applied displacement were required for a single strain band to occur.

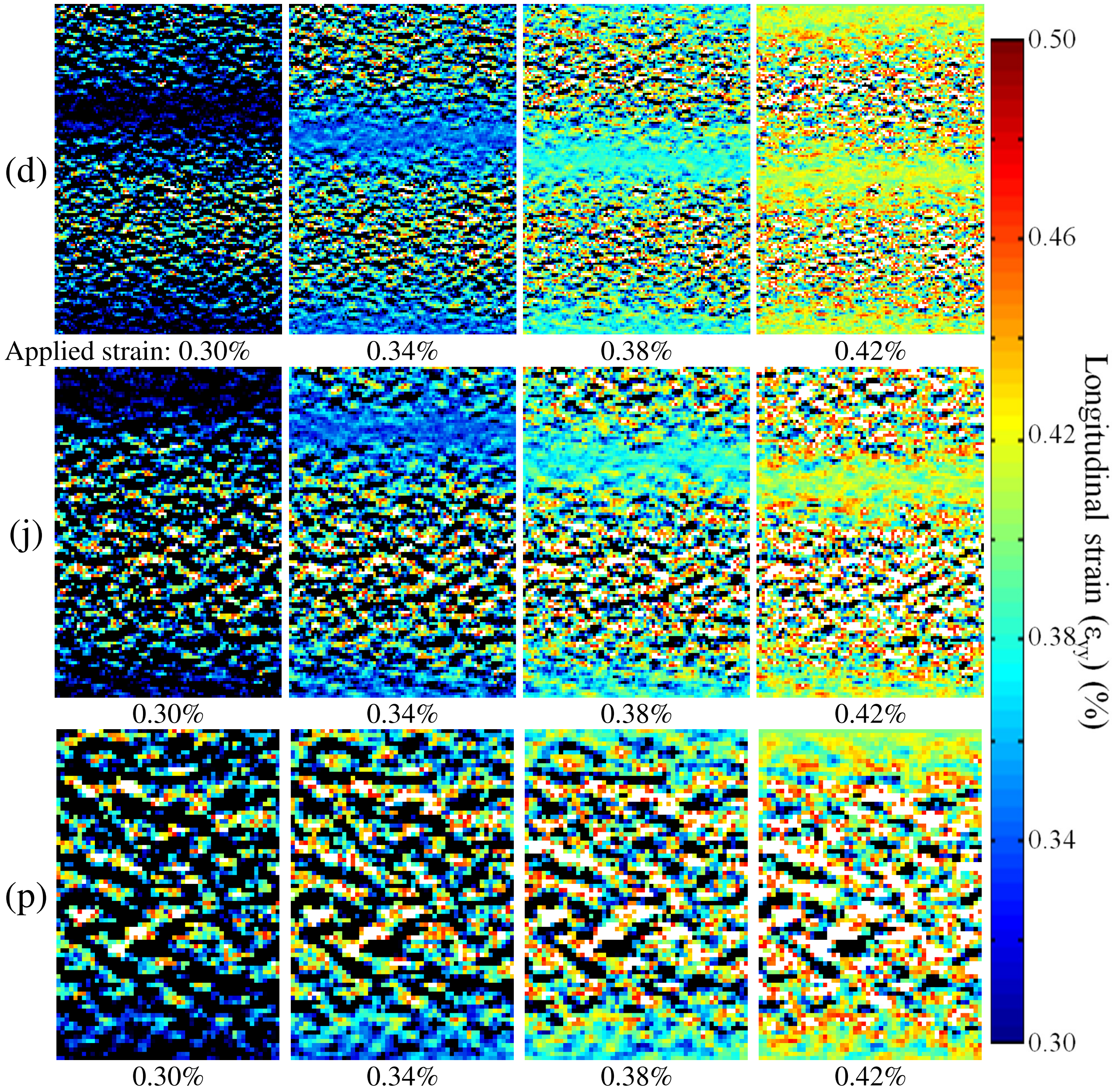

Figure 58: Selection of DIC Strain maps from artificially stretched images with fill factor simulation, showing the effect of active area location and speckle size on the systematic error behaviour.

In contrast to the tests conducted on simulations of regular active areas, the use of a low pass filter was not found to decrease the magnitude of the systematic error bands when non-regular active areas are used. Figure 59 shows a selection of strain maps produced after the application of the filter.

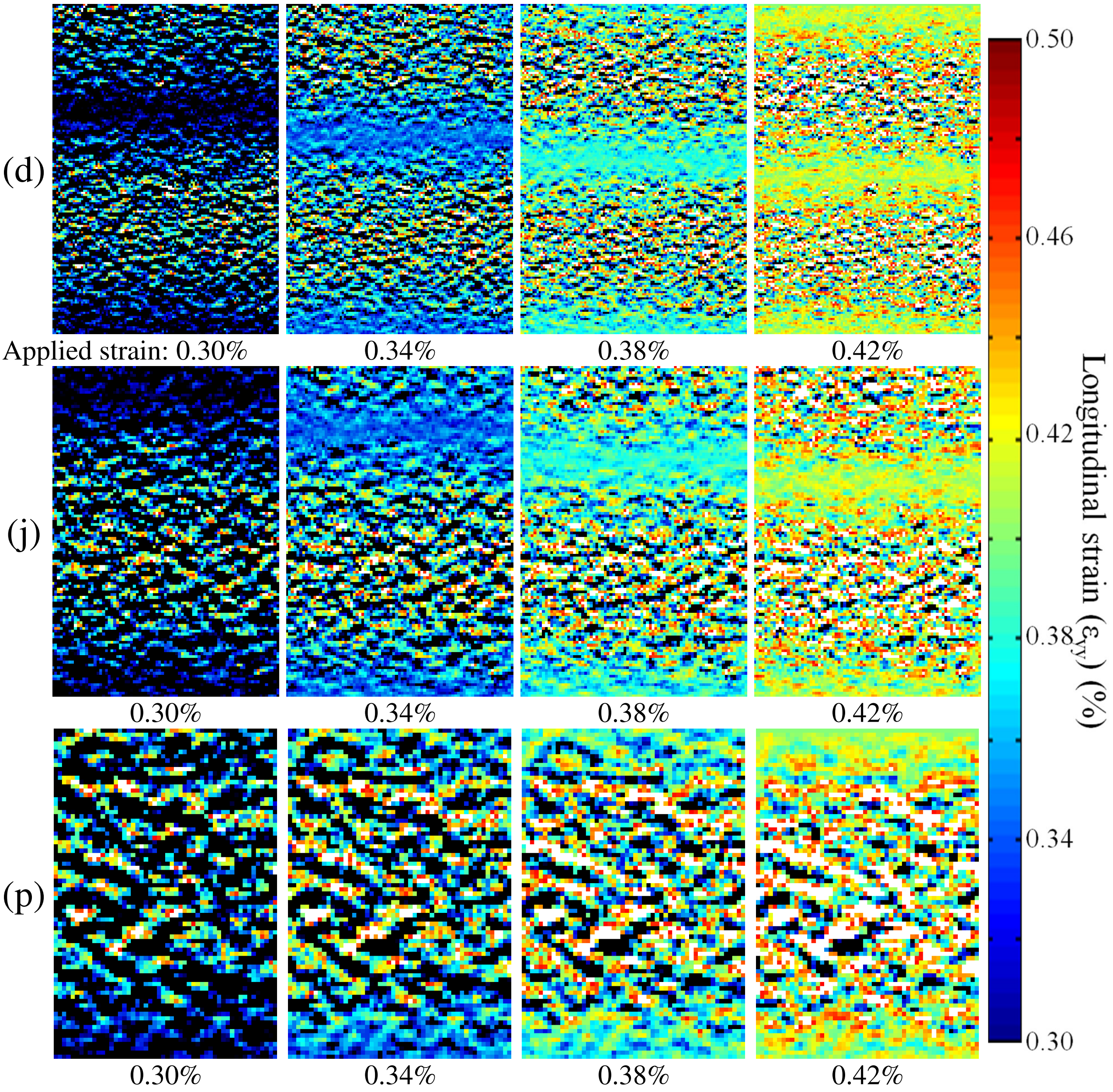

Figure 59: Selection of DIC Strain maps from artificially stretched images with a Gaussian low-pass filter and fill factor simulation, showing the effect of active area location and speckle size on the systematic error behaviour.

5.7 Discussion

The cause of the systematic banding in the images can be understood by considering the effect of the sensor fill factor and active area locations on the image produced. Figure 60 helps to visualise this by taking an idealised patterned surface, shown as an array of coloured dots, and then applying a displacement of one pixel. For the purposes of simplicity the white background of the speckle pattern is ignored. In the case of regular active areas, the correlation is at a minimum at 0.5 pixels displacement as entirely new areas of the specimen surface are imaged by the two pixels. These areas may bear no resemblance to the original reference image, resulting in a lower correlation value. As the surface is further displaced to 1 pixel, the original areas are sampled once again by adjacent pixels and the correlation value is at a maximum, resulting in maximum strain precision. When non-regular active areas are considered, the image only begins to sample the original areas again after 2 pixels displacement.

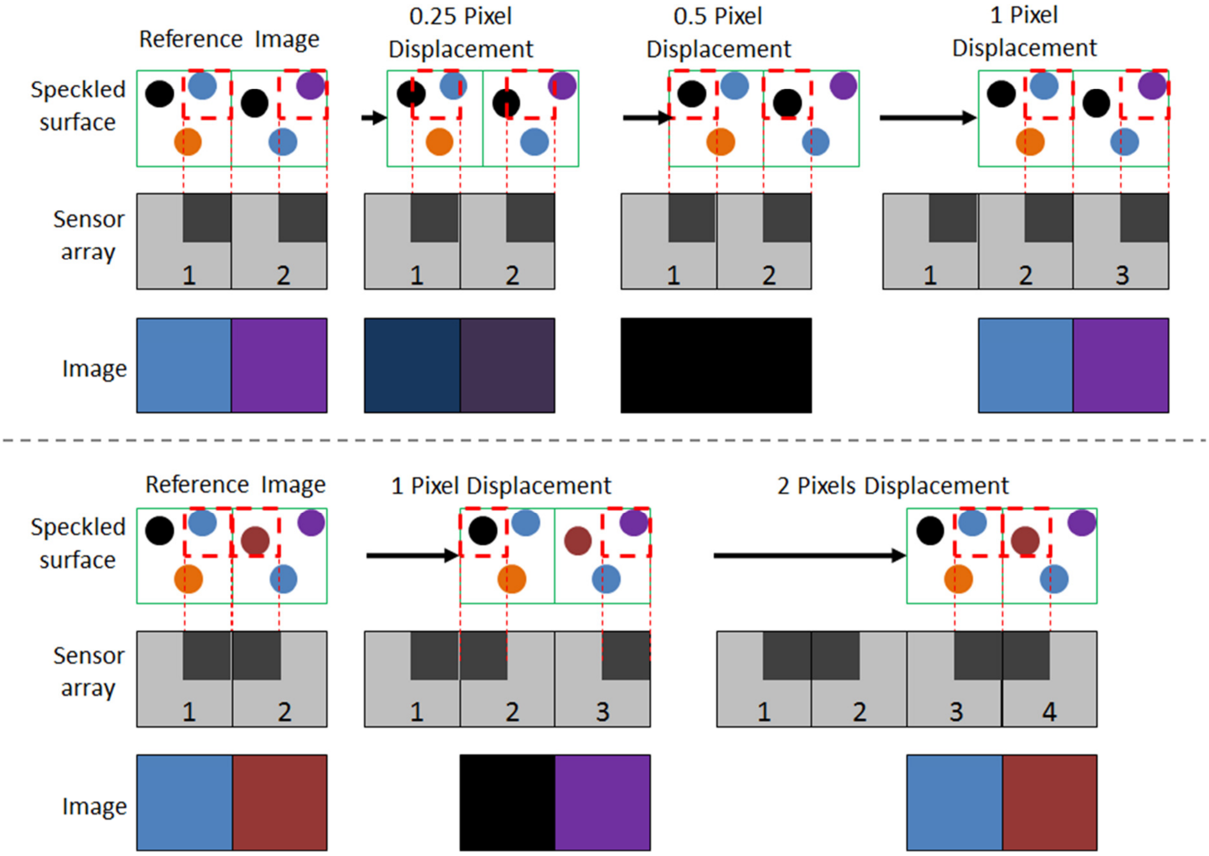

Figure 60: Schematic showing the effect of regular (upper) and non-regular (lower) active areas on the sampling behaviour of a camera sensor.

5.8 Conclusions

The application of DIC to images collected using high speed cameras has been investigated. A main aim of the PhD is to be able to identify damage occurring on FRP specimens during intermediate strain rate loading, so requiring the use of DIC with small subset sizes.

The use of a high accuracy 6th order spline subpixel interpolation method was found to be crucial to reduce systematic errors. As expected, the Photron SA5 and Redlake Motionpro X3-Plus high speed cameras were found to display a higher noise level than low frequency CCD cameras. However, the noise level was found to be much greater when using the Motionpro camera in a certain orientation.

Through the development of two separate numerical methods; a Fourier domain stretching algorithm and an algorithm to simulate sensor fill factor, it has been shown that there is a synergistic effect of speckle size and sensor fill factor on the systematic errors. Whilst use of a larger speckle pattern produces lower levels of systematic error, the error is not eliminated entirely and is amplified when cameras with low fill factors are used. Use of a low-pass filter in the frequency domain was found to decrease systematic errors to negligible levels. However, the error was found to reappear once smaller speckle sizes were created, proving that the effect is a function of both high frequency image content and sensor fill factor.

It has also been shown that sensors with non-regular active areas are incompatible with DIC. It is believed that such a sensor layout is used in the Motionpro-X3 Plus camera.

From the findings of this chapter, it is recommended that the Photron SA5 is to be used for future tests requiring the use of a high speed camera, whilst CCD cameras incorporating microlenses are used whenever high imaging frequencies are not required. A sixth order spline subpixel interpolation method is recommended to be used for all image correlations to minimise systematic errors.

Chapter 6

Quasi-Static Validation of Imaging Methodology

6.1 Introduction

The work discussed in the next three chapters aims to demonstrate an entire working methodology for the assessment of damage in FRP material during intermediate strain rate loading and in subsequent cyclic fatigue loading, with each chapter building upon the work of the previous. Firstly, in the present chapter, validation studies are conducted using DIC and IR-thermography to identify damage during quasi-static loading. The loading allows the use of low imaging frequencies, such that the CEDIP 480M IR camera can operate using its full window size and two AVT Manta G-504B 5-MPixel white-light cameras operating at 1 Hz framing rate can be used. This allows data of a finer resolution to be obtained, increasing the likelihood of successful damage identification. In Chapter 7 the methodology and test rig design to impart a purely tensile intermediate strain rate load, without fully failing FRP specimens is discussed. Included is a validation of the rig design along with a discussion of the design limitations. This interrupted loading methodology is used together with high speed imaging for the identification of surface damage during intermediate strain rate loading. Strain data is obtained after DIC analysis of the white light images and temperature evolution is obtained using IR thermography.

Chapter 8 describes the development of a camera triggering and data capture methodology for the assessment of damage propagation during cyclic fatigue loading. Timing validation studies and data post processing steps are also outlined. Chapter 8 uses this methodology to compare and contrast damage propagation behaviour in previously undamaged CFRP and GFRP specimens and in specimens previously loaded at an intermediate strain rate using the methodology outlined in Chapter 7. Confirmation of the optical measurements was obtained using X-ray CT scans of damaged specimens.

6.2 Experimental Methodology

The use of DIC and IR thermography allows two independent data types to be collected (surface strain and surface temperature), so giving greater certainty as to the identification of surface damage. Low strain rate loading allows the use of low imaging frame rates, permitting the use of larger window sizes and/or higher resolution cameras. Captured images consequently have a greater number of pixels, resulting in finer spatial resolution thermal and strain maps and a greater potential for identifying damage.

Sets of eight GFRP and CFRP specimens, previously described in Chapter 4, were loaded quasi-statically using an Instron 5569 electromechanical test machine. As inertial effects are small, specimen loading is easily stopped at pre-defined values. A summary of the loading conditions and specimens tested is presented in Table 14. Variability in the final applied stress level is due to tolerances in specimen width and thickness.

Material	Specimens tested	Cross section area (mm^2)	Applied strain rate (s^{-1})	Maximum applied load (kN)	Maximum applied stress (MPa)	Percentage of material UTS
GFRP	8	29.94 ± 0.58	3.33×10^{-5}	10.30 ± 0.01	344 ± 0.01	67.19 ± 1.4
CFRP	8	23.61 ± 0.27	3.33×10^{-5}	15.57 ± 0.03	659 ± 0.01	69.35 ± 0.8

Table 14: Loading conditions for quasi-static validation tests of imaging methodology (where ± signifies the standard deviation of all specimens tested).

The CEDIP Silver 480M IR camera was aligned by eye such that the sensor plane was nominally parallel to the specimen surface and situated at a stand-off distance of 200 mm. The camera aims to identify changes in the specimen temperature resulting from damage. Since such heating was expected to dissipate quickly, a high imaging frequency was required. The imaging frequency must be balanced against the time required to record images, which is limited by the available PC random access memory (RAM). An imaging frequency of 1 kHz was chosen to give a temporal resolution of 1 ms and a maximum recording time of approximately 140 seconds, sufficient for the duration of the quasi-static tests conducted. This frame rate requires the use of a sub-window of a quarter of the full sensor area (80 x 64 pixels), which allows the standard manufacturer temperature calibration procedure to be used.

White light images of the specimen surface were captured using a stereo pair of AVT Manta G-504B cameras fitted with Sigma FX 105 mm lenses. These cameras were positioned either side of the IR camera at an angle of approximately 15° from the IR camera optical axis, giving a combined angle of 30° between Manta cameras. The stereo calibration was carried out using a set of four images of a LaVision type 7 calibration plate, giving a satisfactory calibration root mean square (RMS) value of 1.13 pixels. The larger LED array was used to provide illumination, as described in Appendix C, allowing the use of the smallest aperture available for this type of lens, f/32. The use of a small aperture allows sufficient depth of field for the entire width of the specimen to be in focus simultaneously, despite the camera perspective. The white light cameras were positioned to match the field of view of the IR camera as closely as possible. A summary of the camera settings used for the validation tests is presented in Table 15.

Camera	Image size (pixels)	Imaging area (mm)	Spatial resolution (mm/pixel)	Imaging frequency (Hz)	Exposure/ integration time (µs)
2 x AVT Manta G-504B	2452 x 2056	26.31 x 22.06	0.011	1	18000
1 x CEDIP Silver 480M	80 x 64	30.87 x 24.70	0.386	1000	800

Table 15: Camera settings for quasi-static validation tests of imaging methodology

Figure 32 shows a white light image and an IR image of the same GFRP specimen prior to loading. An obvious artefact in the IR image is the large temperature gradient across the specimen of approximately 7 ºC. Figure 62 shows an IR image of another GFRP specimen prepared and imaged in the same manner without any LED illumination. A horizontal band of increased temperature at the bottom of the image can be attributed to a strip of aluminium foil placed on the specimen surface for alignment purposes. The variation of temperature across this specimen is approximately 1 °C and shows no evidence of the narcissus effect, arising from the cooled IR sensor reflecting on the specimen surface. The paint coating therefore has a sufficiently high emissivity that the temperature gradient found in Figure 32 must be as a result of surface heating arising from the LED illumination rather than surface reflections. No difference in emissivity can be noted between the applied black and white paint. Any difference in emissivity would be apparent as localised changes in surface temperature in Figure 62.

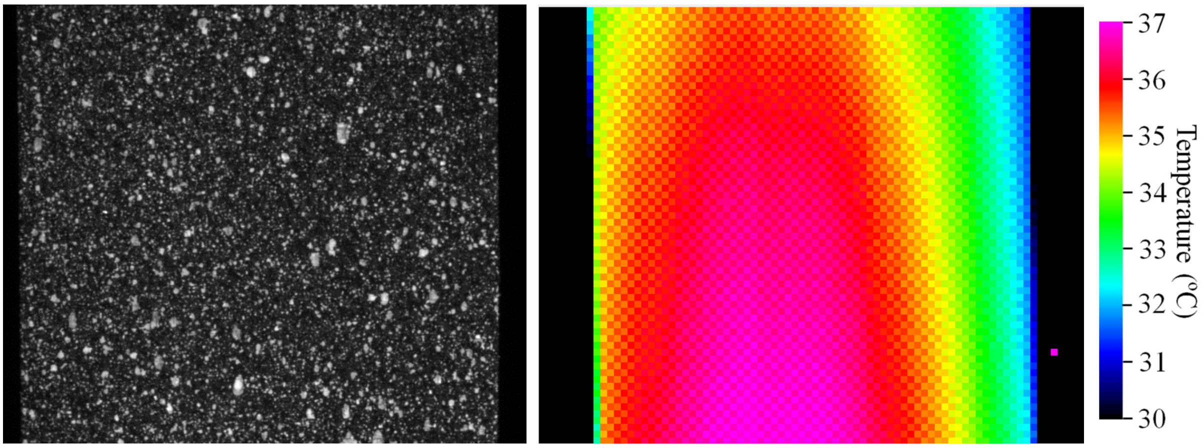

Figure 61: Example white-light image (left) and IR image (right) of a GFRP specimen prior to loading with LED illumination.

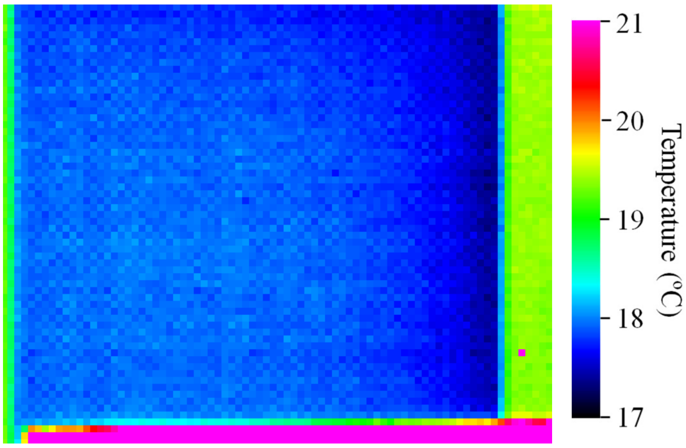

Figure 62: IR image of a GFRP specimen prior to loading without LED illumination.

Since loading was applied quasi-statically, the timing of image exposure was not as crucial in this application and the cameras were triggered directly in LabView without an external trigger circuit. To allow later synchronisation of white-light and IR images, the Manta cameras were set to output a 5V pulse at the start of each image exposure. This voltage was recorded alongside IR images using the

DAQ capability of the IR camera hardware, thus allowing the time of each white light image to be recorded.

As presented in Figure 63, a fine 0.05 mm diameter wire was temporarily attached to the surface of specimens prior to each test and white light and IR images captured. Being visible in the white light and IR spectrums, the wire tip allows a common datum point to be known between both image sets. This reference point allows the IR and DIC data to be post-processed and interpolated to match spatially, as discussed in further detail later in this section. Since the reference coordinates are determined through visual inspection, the location of the wire tip cannot be determined to greater accuracy than a single pixel.

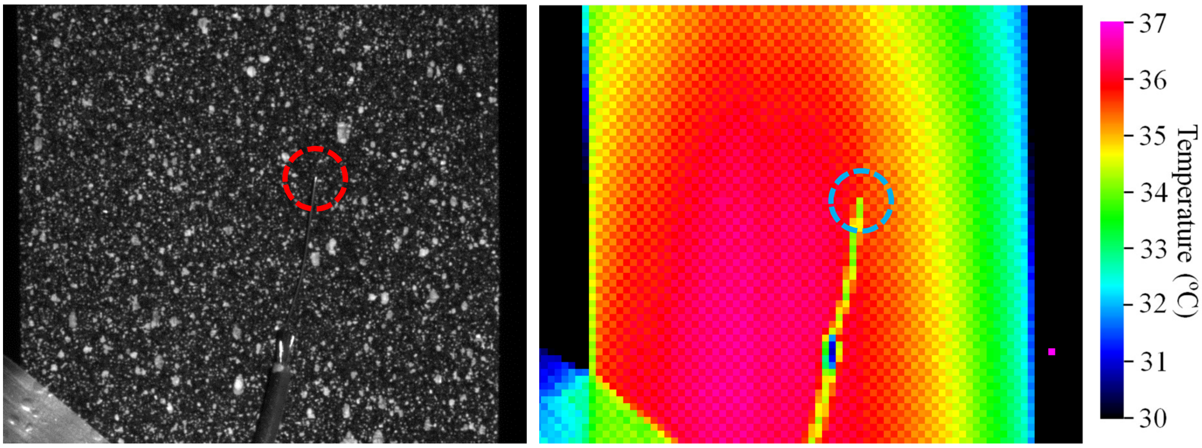

Figure 63: White-light image (left) and IR image (right) showing the 0.05 mm reference wire tip (highlighted by dashed circle) in both imaging spectrums.

In crossply specimens, surface cracks form in the transverse direction with a greater crack density as load level is increased, as previously reviewed in Chapter 3. Such cracks are expected to generate heat and cause a local temperature rise. As predicted, horizontal bands of heating were found to occur during the quasi-static loading of CFRP specimens, suggesting the formation of surface cracks. Conversely, none of the crossply GFRP specimens showed such temperature rises, suggesting that surface cracking did not occur. An example of surface heating on a CFRP specimen is presented in Figure 64. In this instance, the surface temperature of the specimen was found to have increased by approximately 0.53 ℃ in 2 ms. The majority of the temperature rise was found to have dissipated within 160 ms. This behaviour is in contrast to DIC based strain measurements, whereby surface cracks are highlighted as bands of increased strain and are a permanent feature on the specimen surface. As a result, DIC strain maps are not readily comparable to raw temperature data.

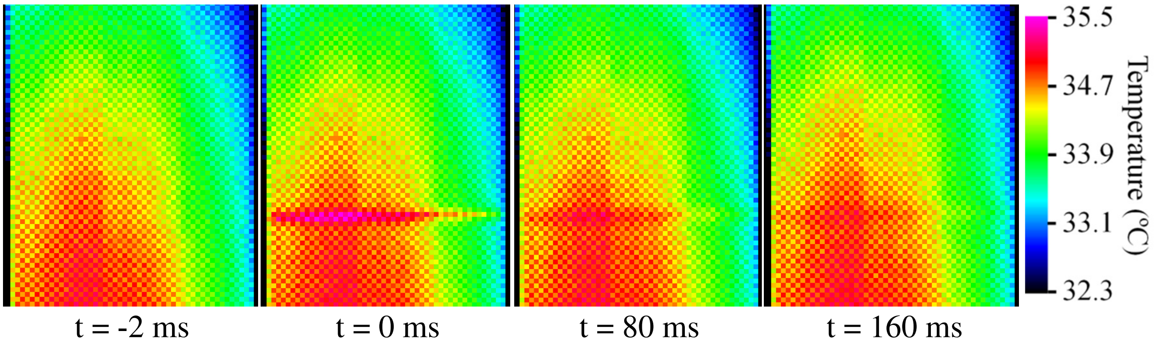

Figure 64: Selected IR images of a CFRP specimen loaded quasi-statically, showing the temperature progression of a single band of surface heating, where t = 0 ms at the first frame of significant heating.

6.2.1 IR Cumulative Thresholding Procedure

To enable the comparison of surface temperature and strain data, a time history of the surface temperature of the specimen was required. A thresholding procedure was adopted for this purpose to highlight any pixels which display a sudden increase in temperature. This method has the potential to highlight small increases in surface temperature that may not be detected by visual inspection, which might be the case for the GFRP specimens tested. The IR data was processed using the following procedure. Each IR image was subtracted from the previous image in the series to create a ΔT image. A threshold was then applied to the ΔT image such that only those pixels with a temperature change greater than the predefined threshold value remain. These pixels are then added to a separate array at the original pixel location. This is repeated for every IR image in the series, resulting in a cumulative ΔT image that highlights the location of any large changes in surface temperature.

A study was conducted to find an appropriate threshold value for the IR data collected. A value too low allows sensor noise to pass through to the final image, whilst a value too high may filter out real material heating. The camera is quoted as having a noise-equivalent temperature of 25 mK, i.e. the temperature that is equal to the noise of the detector. The threshold value therefore needs to be greater than this value otherwise sensor noise will not be filtered. In practice however, the variations in recorded temperature were found to be far greater and sensor noise was found to be highly variable between pixels. Several pixels were found to be faulty and highly overactive. The data from these pixels was eliminated. Figure 65 shows a section of IR data from a quasi-statically loading CFRP specimen processed using various threshold values. A value of 0.12 ℃ did not filter the sensor noise, whilst a value of 0.40 ℃ filtered out some of the specimen heating behaviour. A compromise value of 0.20 ℃ was used for subsequent analysis. A high temperature variation was found at the edges of all specimens. This may be either caused by random reflections from the surrounding environment or from slight horizontal movement of the specimen. At the left specimen edge, a subpixel translation of the specimen to the left will allow the specimen surface to fill a greater area of a pixel. Since the specimen is at a higher temperature than the background, the pixel will record a higher temperature, which may be great enough to pass through the 0.20 ℃ threshold.

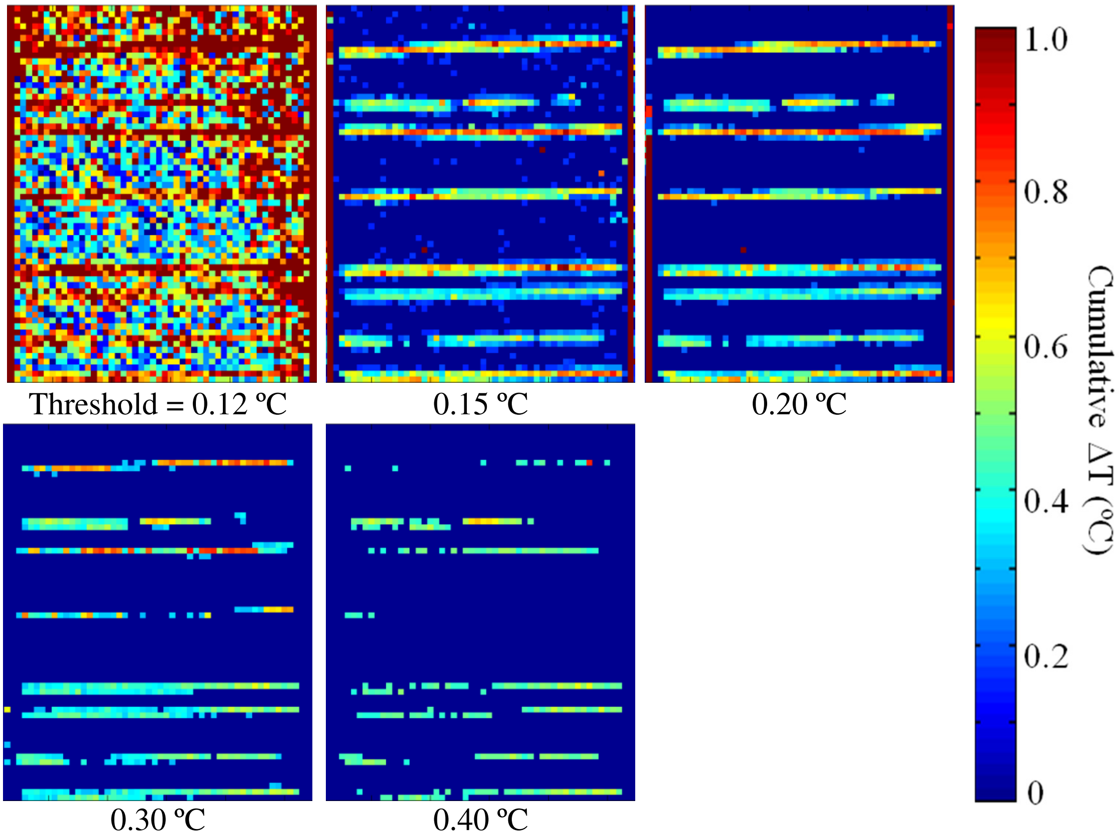

Figure 65: Effect of threshold value on the ability to resolve surface heat generation using the cumulative thresholding technique. Performed on a series of IR images obtained from a CFRP specimen loaded quasi-statically to 447 MPa.

6.2.2 IR Motion Compensation Procedure

A limitation of the cumulative thresholding procedure is that the recorded location of surface heating is only correct at the time of first initiation. This initiation location will move with the rigid body motion of the specimen as the applied strain increases. Further processing is necessary to take account of rigid body motion in the cumulative ΔT data. A Matlab algorithm was developed to move the cumulative ΔT data accordingly by applying the surface displacements obtained from DIC. The location of the wire tip was used as a datum point between the IR and white light images. Since the spatial resolutions and therefore the locations of the DIC and IR data types are different, a bilinear interpolation method was used to resample displacement data at the IR pixel locations. The displacements were then used to shift the previously recorded cumulative ΔT data to the new location in the window to subpixel accuracy. As the cumulative ΔT data is now no longer in exactly the same location, the next iteration of ΔT data cannot be directly added to the previous data. The previous ΔT data was therefore resampled at the original IR sensor pixel locations, again using bilinear interpolation, so allowing the next iteration of ΔT IR data to be added directly to the previous motion compensated cumulative ΔT data. Areas on the specimen surface that were not simultaneously imaged by both DIC and IR were omitted from any motion compensation procedure.

Figure 66 shows the effect of motion compensation on cumulative ΔT data and the effect of faulty pixels. Although the effect of motion compensation on this data set is slight, it is important to note that rigid body motion is likely to have a greater effect when the camera is situated closer to the specimen, as is likely to be the case in later tests performed at intermediate strain rates. The faulty pixel highlighted by a red arrow in Figure 66 was found to cause a large region of error, which is eliminated after discarding data from this pixel. A second overactive pixel is highlighted by a green arrow, causing a vertical line of thermal activity after motion compensation. An area of thermal activity can be noted to widen at the left specimen edge after motion compensation. This occurs due to the decreased accuracy of DIC at a free edge, causing erroneous displacement vectors to be calculated. Upon the application of motion compensation, the original single column of thermal activity is blurred over adjacent columns.

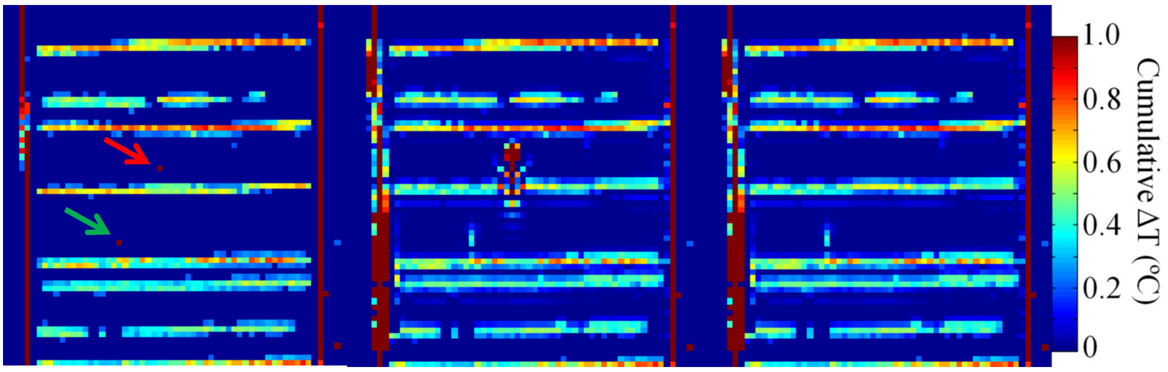

Original cumulative ΔT data Motion Compensated Motion Compensated with faulty pixel removed

Figure 66: Effect of motion compensation on cumulative ΔT data. Arrows indicate the location of faulty pixels.

6.2.3 Results from CFRP and GFRP specimens

The IR data collected during quasi-static loading of CFRP and GFRP specimens was processed using the previously described cumulative thresholding methodology and motion compensation. DIC was performed on the white light images in DaVis 8.1.3 using a variety of subset and step sizes. A high accuracy sixth order spline subpixel interpolation method was used, as recommended from the work conducted in Chapter 5. Use of a subset size of 31x31 pixels and a step size of 8 pixels was found to give an acceptable compromise between spatial resolution (2.73 mm) and noise. Static images collected from specimens prior to each test were processed using identical correlation settings. The standard deviation of the strain data produced was then calculated to give an indication of the measurement noise. The noise level for the CFRP sample presented in Figure 67 was found to be 0.053 % strain.

Figure 67 presents DIC longitudinal strain data and IR data obtained using the cumulative thresholding methodology of a CFRP specimen loaded quasi-statically. Such data was found to be typical of all the CFRP specimens tested. Strain data is plotted in the correct spatial location using the displacement vectors. Interpolation of the vectors was not required since each strain point has its own corresponding displacement vector. Coordinates are stated in units of mm, with the origin at centre of the first calibration plate image used for the stereo camera calibration. Some DIC data is lost at the top of the strain map with increasing strain due to the specimen surface moving out of view and equivalently at the bottom of the specimen where new areas of the specimen surface come into view.

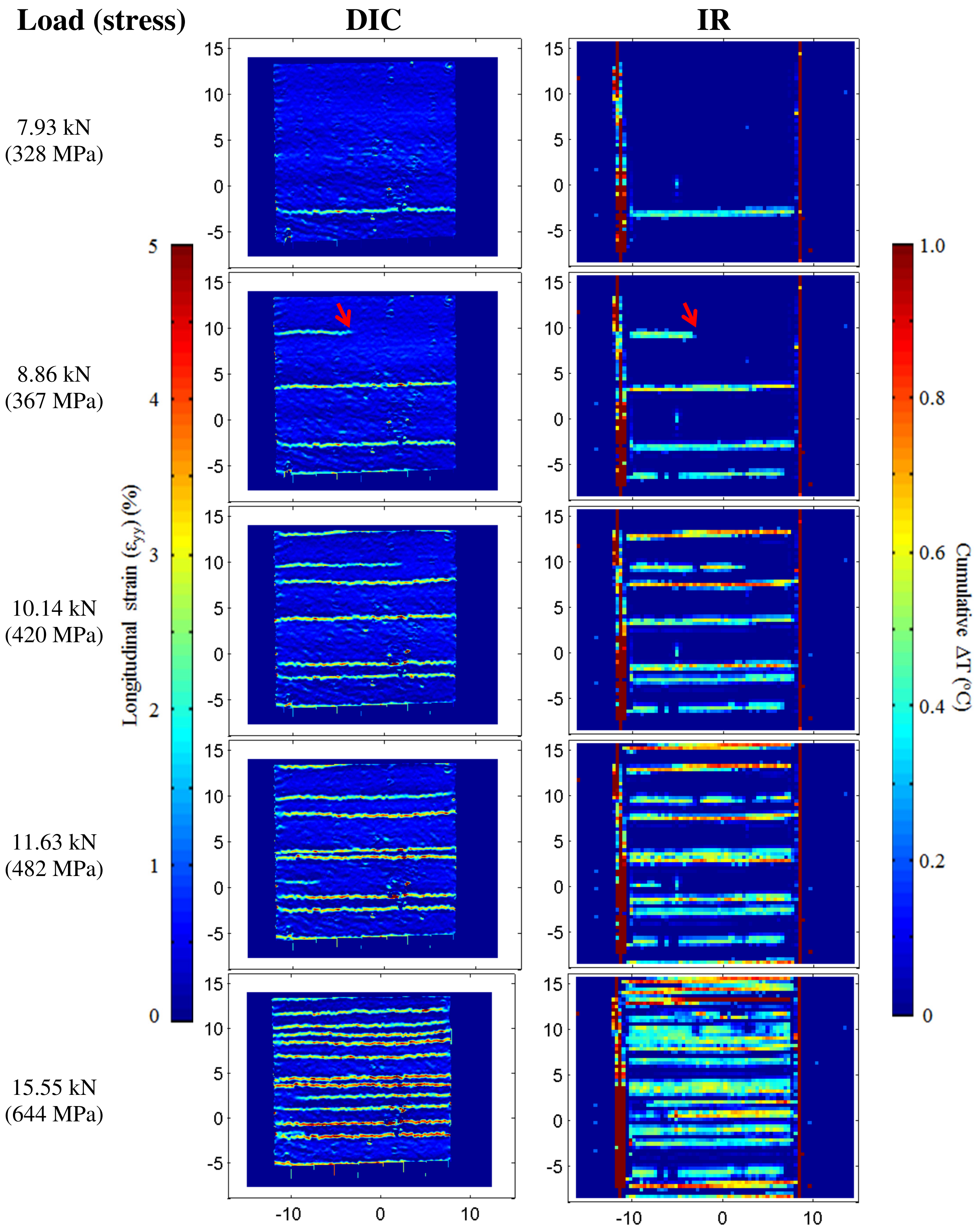

Figure 67: DIC strain data and cumulative ΔT IR data obtained from a CFRP specimen loaded quasi-statically to 68% of the material UTS.

It can be seen from Figure 67 that there is a strong correlation in the locations of bands of high strain and the locations of significant surface heating. As the bands are identifiable in both data types, the behaviour is highly indicative of transverse cracking in the surface lamina. The cracks were found to grow in number and density with increasing applied load, as expected for this material and laminate configuration. It is important to note that the strain measured by DIC at a crack is not the real strain experienced by the material and is simply used to highlight the onset of damage. Across a crack, each individual subset measures a combination of the crack opening displacement and the deformation within the subset as described by the subset shape function. This is then converted into a strain value using the central differencing method.

Due to the lower resolution of the IR data, the identification of individual surface cracks becomes more difficult with increasing crack density. The majority of cracks were found to extend across the entire specimen width within the period of one white-light frame (1 second), as is the case for the first crack identified at an applied stress of 328 MPa. Some cracks were found to progress more slowly across the width, an example of which is indicated by the arrow in Figure 67 and presented in greater detail in Figure 68.

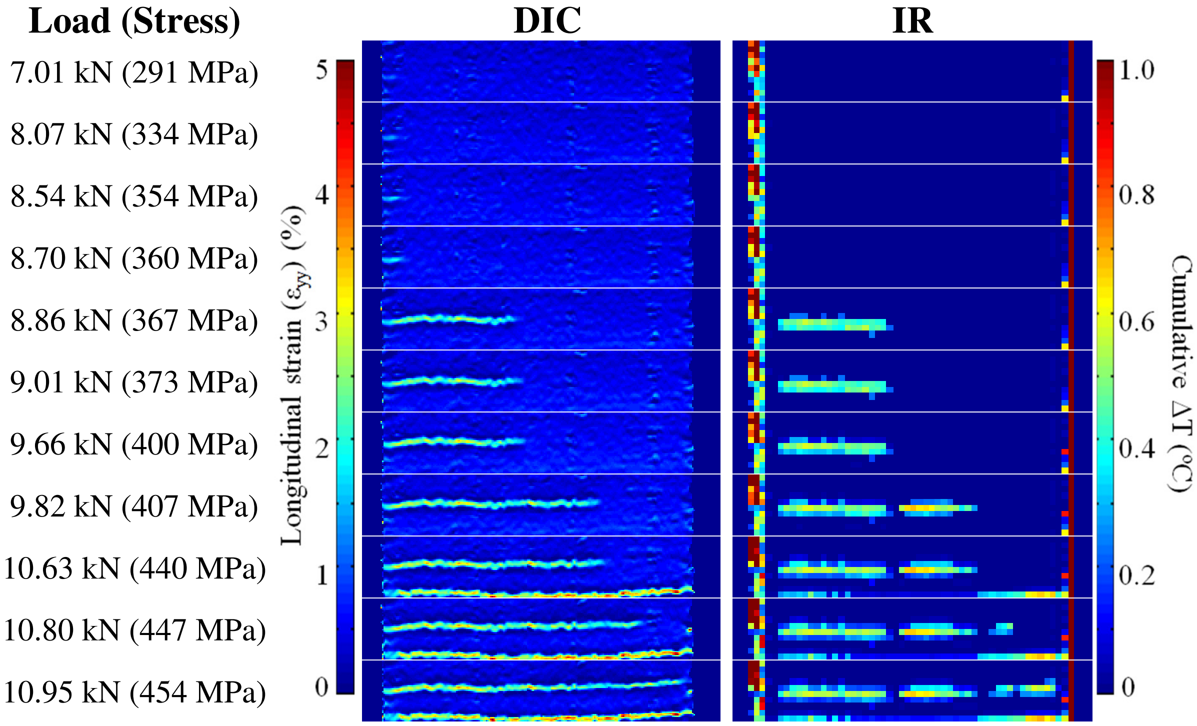

Figure 68: Cumulative IR and longitudinal strain data showing the development of a crack in a CFRP crossply specimen, the location of which is shown in Figure 67.

The strain maps presented in Figure 68 show that the crack initiated slowly from the left specimen edge between 291 and 360 MPa of applied stress. No corresponding temperature increase indicative of crack initiation could be noted in the IR data.

The crack was found to propagate quickly across approximately half the specimen width at 367 MPa of stress, with evidence seen in both the cumulative IR and strain data. A log of the mean temperature over this area of crack extension is shown in Figure 69 as Area 1. Between 367 and 400 MPa of applied stress, the crack propagates slowly by approximately 0.6 mm over 6 seconds, with no evidence being identified in the cumulative ΔT data or in the mean temperature over this area, as shown in Area 2 of Figure 69. At 407 MPa of applied stress the crack propagates by 5.0 mm. This area, denoted as Area 3 in Figure 69, can be resolved in both the cumulative ΔT map and also as a sharp temperature increase in the mean temperature plot. As expected, this finding shows that there is a minimum crack propagation rate needed to generate the required temperature change to pass through the cumulative thresholding technique. Due to sensor noise, it is not possible to further reduce the temperature threshold to identify the slowly propagating crack in Area 2.

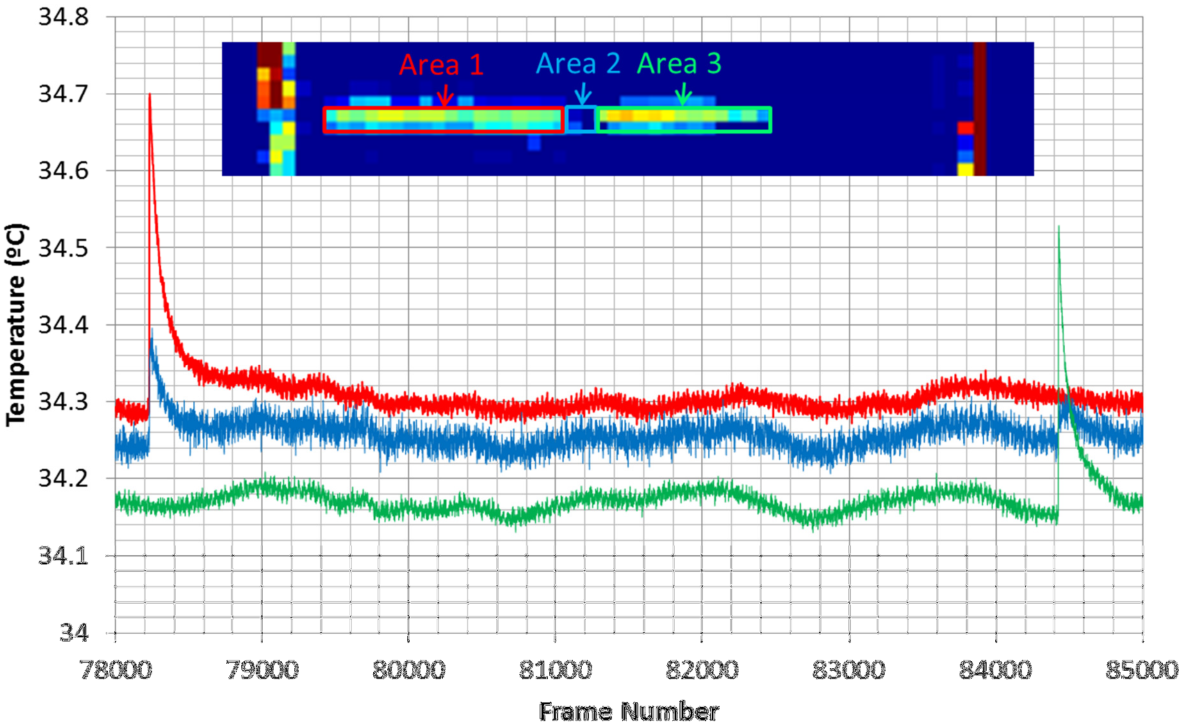

Figure 69: Log of the mean temperature during a seven second period over three areas on the specimen surface.

The minimum crack propagation rate required for damage identification using the cumulative thresholding technique is dependent upon many variables. In the case of a crack forming instantaneously, heat conduction and radiative effects can assumed to be zero. The temperature change of a volume of material is therefore dependent upon only the amount of heat released by a crack and the material specific heat capacity, as discussed in section 3.4. The heat release is in turn dependent on the material fracture toughness and the new surface area created [193]. Since all of these variables are constant for a given material, the released heat will be expected to be nominally identical between two cracks of the same length; i.e. as the crack extends through Area 2, the released heat per pixel area should be the same as the previous crack forming through Area 1. The time dependent effects of thermal conductivity and IR radiation must therefore be causing the local temperatures within Area 2 to remain below the 0.2 ºC threshold value throughout the 6 seconds of crack propagation. Estimations of the heat conduction and radiative cooling effects during this time period are presented in Appendix D. Whilst it was found that radiative cooling has a negligible effect, heat conduction effects are considerable and are the likely cause of the failure to resolve crack propagation inside Area 2. In contrast to DIC, the cumulative thresholding technique is therefore limited to the study of rapidly propagating cracks in FRP materials.

As can be seen in Figure 67, the majority of heating bands were found to stop at around 2 pixels from the free-edge of the specimen. There are two possibilities to explain this behaviour: the cracks are propagating more slowly as they reach the free edges, as was found to be the case for the crack shown in Figure 68, or edge cracks may have already formed, slowly and at a lower applied stress, resulting in no further heat generation as the transverse cracks coalesce with the edge cracks. In reality a combination of both is likely. Edge cracks will have formed at lower load levels and will be the preferential start and end path for a transverse crack. As there is likely to be high edge crack density by the time transverse cracking occurs, the driving force for a new crack path is lowered. Transverse cracks therefore propagate more slowly at the free edges if trying to form a new crack path rather than follow a pre-existing edge crack.

The combined IR and DIC methodology was next applied to six quasi-statically loaded GFRP specimens using the conditions stated in Table 14 and Table 15. White-light images were collected and processed using the same methodology previously described for CFRP specimens. IR data was processed using a slightly lower threshold value of 0.15 ℃ to highlight smaller temperature changes but at the cost of increased noise. Figure 70 presents the final longitudinal strain map and cumulative *ΔT* map for a typical GFRP specimen. The artefacts highlighted by green arrows in Figure 70 are caused by faulty pixels in the IR sensor as discussed previously in section 6.2.2. Similarly to the previous CFRP specimen, the large region of thermal activity at the left specimen edge is caused by erroneous DIC vectors. Such vectors cause the column of high thermal activity at the specimen edge to be moved inwards after the application of motion compensation. As the procedure retains pixels above a certain threshold, the error is not removed in the next iteration.

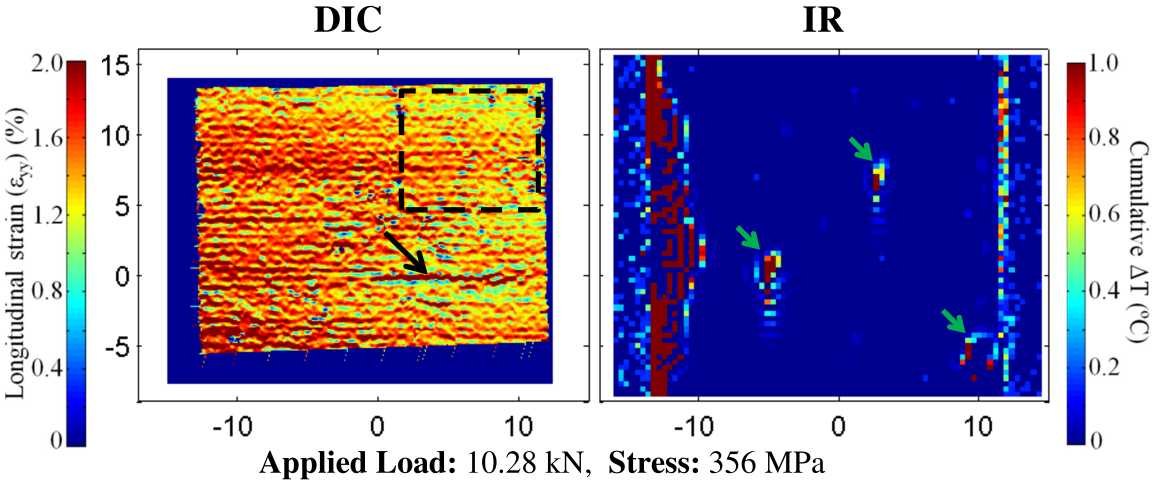

Figure 70: DIC strain data and cumulative ΔT IR data obtained from a GFRP specimen loaded quasi-statically to 70% of the material UTS. Highlighted area is further analysed in Figure 71.

The distinctive bands evident from CFRP samples are absent in both the strain and IR data collected from all of the GFRP specimens tested. Arguably, small horizontal bands of high strain can be seen to occur across the entire specimen surface as load is increased. This is believed to be transverse cracking occurring at a scale just resolvable by the DIC system. In contrast to the majority of CFRP cracks, these small bands appear slowly with increasing load. They cannot be seen in the horizontal strain maps, as would be expected by any system noise.

In a small number of samples a clearly identifiable horizontal band of high strain can be seen, one of which is highlighted by a black arrow in Figure 70. Such bands were found to also develop slowly over a period of around 30 seconds and to not extend across the entire specimen width. This band is not corroborated in the processed IR data, which is understandable given the previous analysis of heat conduction effects within a CFRP material. Although the thermal conduction of the GFRP material is likely to be lower, it is still likely to be within a similar order of magnitude. The crack surface area also plays a key role in the amount of heat released. The GFRP ply thickness is approximately half that of the CFRP, resulting in half the heat release for the same length crack. Also, the glass fibres are approximately twice the diameter of the carbon fibres so the same length crack in the GFRP material will create a much lower surface area than an equivalent crack in the CFRP material. Cracks in the surface of the GFRP material are therefore expected to generate far less heat. As the specific heat capacities of the two materials are nearly identical, a much lower temperature change will be produced in the GFRP material. Additional GFRP specimens were loaded to 87% of the material UTS but no overall difference in the material behaviour could be noted in the DIC data or the cumulative ΔT maps due to the increased load.

A CLT analysis carried out for the GFRP specimens using the eSuite software [173] found that the stress in the 90° plies at 70% UTS is estimated at 118 MPa. This is far above the expected transverse failure stress of glass-epoxy of 39 MPa [2]. Transverse cracking must therefore be occurring but at a scale smaller than that currently resolvable in the DIC data. The small cracks must also be causing temperature rises that are too small to be resolved within the cumulative ΔT IR data, the reasons of which are discussed previously.

The images were therefore recorrelated using a smaller step size of 6 pixels in an attempt to resolve smaller scale damage behaviour. The progression of longitudinal and horizontal strain over the area highlighted in Figure 70 is shown at a greater magnification in Figure 71. Upon closer inspection of the longitudinal strain data, an almost homogenous distribution of horizontal bands of higher strain can be seen to progressively form across the entire specimen surface above 3.34 kN of applied load. CLT predicts a stress of 38.5 MPa within 90° plies at this load level, close to the expected transverse ply failure load. These bands are not apparent in the horizontal strain maps and are not due to the fill factor effects described in Chapter 5 as they remain static on the specimen surface.

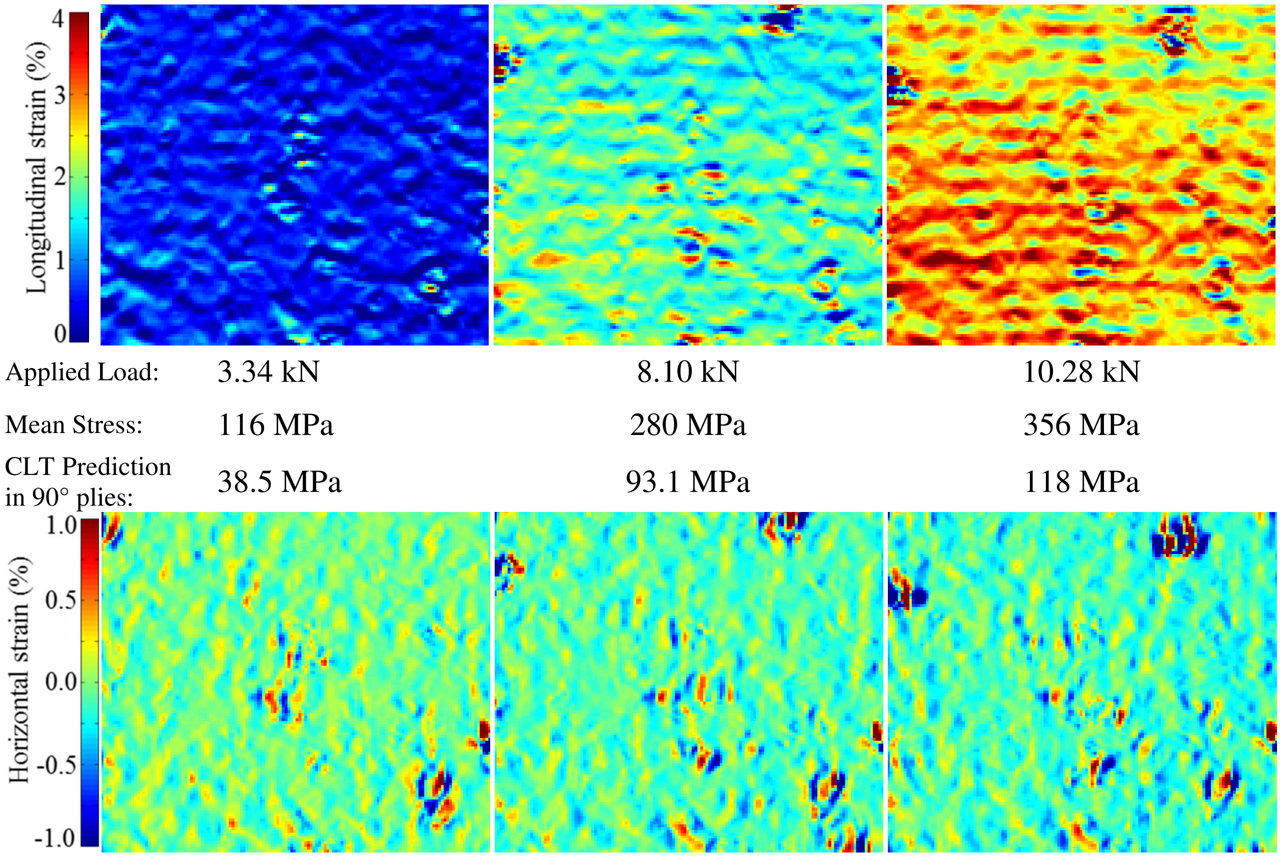

Figure 71: Longitudinal strain maps (upper) and horizontal strain maps (lower) for a GFRP specimen within the area highlighted in Figure 70

Based on the CLT analysis and the DIC studies conducted, it is considered that transverse cracking is occurring in the surface ply of the GFRP specimens tested but at a scale too small to be reliably identified using the white-light setup employed. This would ideally be confirmed using microscopic analysis of specimens. Higher spatial resolution white-light imaging would need to be used for future investigations into specimens of this material type and lay up.

6.3 Summary

The Chapter has successfully used low-frequency IR and white-light imaging to identify damage in FRP material during quasi-static loading. An IR cumulative thresholding technique has been developed to highlight areas of significant surface heating, indicative of damage. The technique was improved through the use of DIC assisted motion compensation, ensuring data remains spatially correct throughout a test and therefore comparable to DIC strain measurements. Faulty IR pixels have also been found to have a detrimental effect on the clarity of processed IR data.

The application of the methodology to crossply CFRP specimens has shown clear surface damage behaviour in the form of transverse cracks, matching both spatially and temporally. Due to heat conduction effects, the cumulative ΔT technique has been shown to be limited to the identification of rapidly propagating cracks. Data collected from GFRP specimens lack the spatial resolution to categorically identify transverse cracks within DIC strain data. No indication of transverse cracking could be noted within cumulative ΔT IR data for GFRP specimens. This is believed to be due to the slow crack formation, making conduction effects more important and the lower heat release of GFRP laminates due to lower crack surface area.

Having proven the methodology's capability of identifying damage in quasi-statically loaded specimens, the next step is to transfer the methodology to the use of high speed imaging for the identification of damage initiation at intermediate strain rates. This first requires adaptations to the VHS 80/20 machine to facilitate interrupted loading.

Chapter 7

Interrupted Intermediate Strain Rate Loading

7.1 Introduction

The work described in Chapter 6 has demonstrated the capability of the optical methodology for identifying surface damage in quasi-statically loaded specimens. The next step is to adapt the methodology to identify damage in FRP specimens during intermediate strain rate loading. A primary aim of the thesis is to subsequently study the damage propagation behaviour of specimens under cyclic loading after experiencing an intermediate strain rate load. For this reason, a methodology was required for applying an intermediate strain rate load without reaching final specimen failure. Adaptations to the standard loading methodology previously described in Chapter 4 were required. The chapter first outlines the operation of the interrupted loading methodology developed and validation studies conducted. The optical methodology developed in Chapter 6 is next transferred to high speed imaging and combined with the interrupted loading methodology, enabling the study of damage in GFRP and CFRP specimens during intermediate strain rate loading. Finally, validation of the optical measurements is conducted using X-ray CT and optical microscopy analysis.

7.2 Interrupted Loading Methodology

As previously discussed in Chapter 4, the Instron VHS operates in an 'open loop' mode during high speed testing, such that there is no feedback control between the actuator and the load or position transducers. As a result, the actuator cannot be stopped at a predefined load or position using the standard machine setup resulting in the specimen being completely destroyed. To investigate the damage propagation behaviour of FRP specimens after the application of an intermediate strain rate load, an alternative loading methodology is therefore required to avoid complete specimen failure.

Very few previous studies have attempted to adapt open-loop servohydraulic test machines for interrupted loading. The work by Fitoussi *et al* [108] is one such attempt where a mechanical fuse was placed in the load path of a test on an FRP specimen. The fuse consists of a double edge notched tensile (DENT) poly(methylmethacrylate) (PMMA) coupon, which was designed based on a dynamic finite-element analysis (FEA) of the fuse, allowing the failure load to be pre-determined. The study highlights several complicating aspects of high strain rate testing, the most challenging of which is the introduction of uniform stress and strain into FRP specimens. This is difficult to achieve in practice due to stress-wave propagation effects caused by the transient loading known as 'ringing' in the load cell. This creates a non-uniform stress and strain field in the specimen both spatially and temporally which subsequently causes a non-uniform strain-rate, making material characterisation difficult when using point or global measurement techniques. Fitoussi *et al* [108] minimised stress wave effects through the use of a dogbone shaped FRP specimen to give a smooth load transmission path and through the introduction of a rubber damping joint at the point of contact in the slack adaptor. Although it is important to minimise the effects of load cell ringing, it was deemed that obtaining a perfectly homogenous strain field would not be hugely beneficial to the study of FRP damage. Also, the collection of full-field DIC data negates such a reliance on a perfectly uniform strain field, since the strain and strain rate can be quantified both spatially and temporally across the specimen for each test.

The study by Fitoussi *et al* [108] found clear differences in the distribution and level of damage in FRP coupons when loaded at intermediate and quasi-static strain rates. The author drew these conclusions based on scanning electron microscope (SEM) images of the damaged coupons. However, it is clear from the strain gauge data presented that the specimen enters into a vertical oscillation after the PMMA fuse fails. This occurs due to the release of elastic strain energy in the specimen causing the intermediate grip to return and pass its starting position, so loading the specimen under compression. The author comments that the compressive loading did not cause any additional damage as the compression stress after fuse failure was limited to 80% of the initial tensile stress. Since FRP composites are often more susceptible to damage under compression due to microbuckling and fibre kinking, this analysis is questionable. Unidirectional E-glass epoxy has been found to have a longitudinal compressive strength 43% lower than its tensile strength, whilst unidirectional carbon-epoxy has been found to have a longitudinal compressive strength 34% lower that its tensile strength [2]. Since the author has no means of observing the onset of damage during loading, the exact cause of damage cannot be determined. Although the work in this chapter uses high speed imaging techniques to allow the observation of damage during loading, it is preferential to eliminate any compression loading of FRP specimens to be certain of the exact cause of damage.

Due to the complexity of the approach used by Fittousi *et al* [108], simpler alternative methodologies for achieving interrupted loading were evaluated. Early trials aimed to weaken a section of specimen, thus eliminating the need for a separate fuse and an intermediate set of grips. A schematic of this procedure is outlined in Figure 72.

Edge notches approximately 2 mm long were cut into one side of 12 mm wide crossply *[0,90]s* CFRP specimens using a fine saw blade. Upon loading at quasi-static strain rates it was found that the failure occurs at the notched location at lower load levels than the unnotched specimens, as required. However, notch length was highly variable result in inconsistent failure loads. In addition, the notching of specimens was found to affect the load transfer to the rest of the specimen, as shown in the DIC strain maps presented in Figure 73, where the material directly above and below the notch has no load carrying capacity and hence experiences far lower strain than the rest of the specimen.

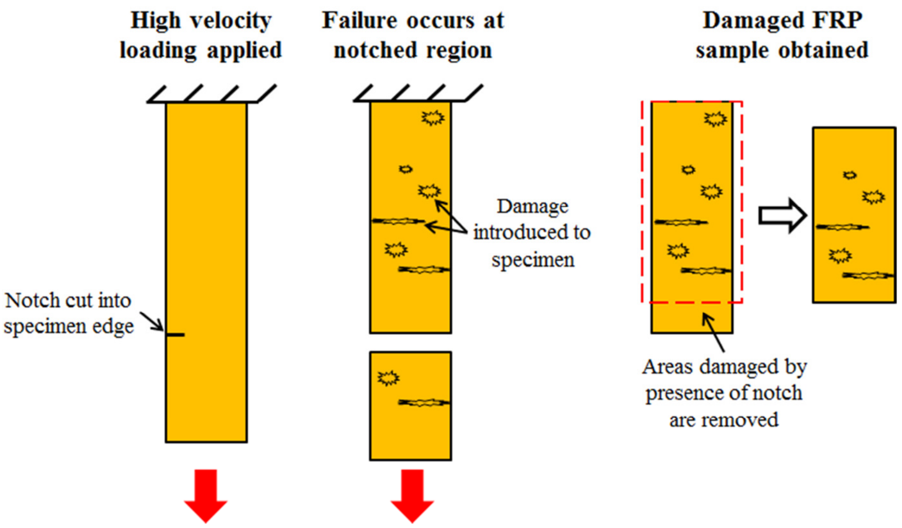

Figure 72: Proposed edge notching methodology for the loading of FRP material at an intermediate strain rate.

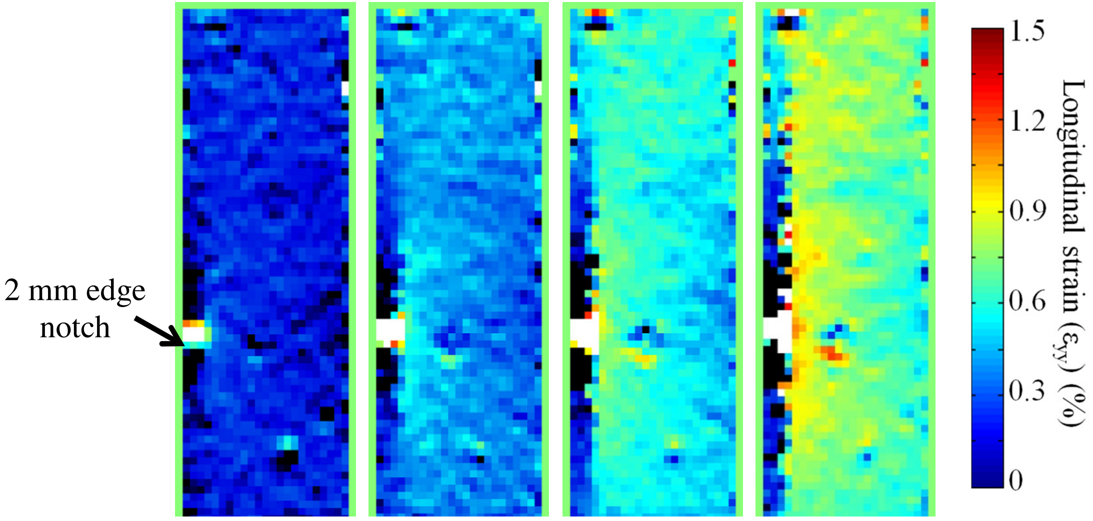

Figure 73: Longitudinal strain maps (ε_{yy}) of a notched crossply CFRP specimen loaded quasi-statically.

The presence of the notch was also found to affect the damage behaviour of the material. In the majority of specimens, longitudinal splitting was found to emanate from the notch root, along the strain discontinuity shown in Figure 73. Such damage was found to extend significantly into the portion of the specimen used to form the subsequent final sample. For the above reasons, notched specimens cannot be used to impart an interrupted load into FRP specimens. Other similar methods were also considered, such as cutting a single ply during laminate manufacture or waisting a section of the gauge length to a dogbone shape. These approaches were also deemed to affect the load transfer to the rest of the specimen and change the damage initiation behaviour and were not investigated further.

It was therefore decided to adapt the methodology proposed by Fittousi *et al* [108]. The DENT fuse design was deemed to be too time consuming and expensive to manufacture for each interrupted test. The fuse also requires an extra set of grips in series with the FRP specimen. This increases both mass and inertia of the moving parts and raises the possibility of slippage due to the additional grip surfaces. Directly adhering fuses to FRP specimens may solve these issues but could raise further complications in achieving sufficient adhesion strength. A simpler design not reliant on extra gripping surfaces was therefore preferred for providing interrupted loading to FRP specimens.

Load level and strain rate can be tightly controlled using a standard servo-mechanical test machine. When using the Instron VHS 80/20, with no such control, the task becomes significantly more complex. The variables that are of the most importance during an interrupted test at an intermediate strain rate test are as follows:

i. *Strain rate of applied load*

   The strain rate can be roughly adjusted by changing the intended actuator velocity prior to a test. The machine then uses a different velocity calibration file, as previously discussed in Chapter 4. The exact strain rate can be measured more accurately on the specimen surface through the manipulation of DIC data or through analysis of strain data from an attached strain gauge.

ii. *Maximum applied load level*

   The failure load of the fuse needs to be adjustable so that the effect of differing load level on the damage initiation can be studied across a range of materials.

iii. *Rig and specimen behaviour after fuse failure*

   For simplicity, the thesis is concerned with developing a methodology for applying purely tensile intermediate strain rate loads. The behaviour of the loading rig after fuse failure is therefore an important aspect to avoid any potential for compressive loads.

The chosen design relies on the use of fuses in the form of shear pins which are notched at two locations using a 1 mm radius tool. A schematic of a shear pin is shown in Figure 74 (c). The load level imparted by the shear pin is varied according to FRP specimen size and material by altering the depth of the notches. Use of a cylindrical shear pin allows a lathe to be utilised, giving faster manufacture times and typically tighter tolerances than a DENT fuse coupon manufactured by milling. The use of simple machining techniques also allows fuses to be manufactured by a relatively unskilled worker, so allowing shear pins to be manufactured on demand.

The shear pin loading system developed is shown in Figure 74 (a full set of engineering drawings is available in Appendix B). Shear pin loading was achieved through a redesign of the slack adaptor rod into two separate parts with a shear pin providing the load transfer path in between. Two circlips are attached to the shear pin prior to each test to avoid lateral movement, ensuring that the correct notched areas are loaded under shear.

Shear pins were originally intended to be manufactured from PMMA to give a brittle failure and a repeatable failure load, in a similar manner to the DENT fuses used by Fitoussi *et al* [108]. Since the material should behave without plasticity and an analytical solution of stress concentration factor is available for this shear pin geometry [194], it was considered that the failure loads could be predicted with reasonable accuracy. PMMA pins of the same geometry shown in Figure 74 (c) were loaded under shear using an early rig design similar to that shown in Figure 74 (a) with a crossply GFRP specimen in-situ. Failure loads were found to be highly variable and not as predicted by the analytical solutions. Plots of load against actuator position for several PMMA shear pins loaded quasi-statically are shown in Figure 75, showing a high degree of variability. It was also found that due to the cutting force applied during turning and the low stiffness of PMMA, the desired notch depth tolerances of +/-0.05 mm were difficult to achieve.

Due to these complications, shear pins manufactured from aluminium alloy 6082-T6 were trialled. The shear pins were again loaded under shear, using the earlier rig design with a crossply GFRP specimen in-situ. A schematic of the shear pin loading process is shown in Figure 78. The aluminium alloy shear pins were found to give highly repeatable load traces and final failure loads, as shown in Figure 76 and Figure 77. An additional benefit of using aluminium shear pins was the tighter manufacturing tolerances achievable of ± 0.05 mm.

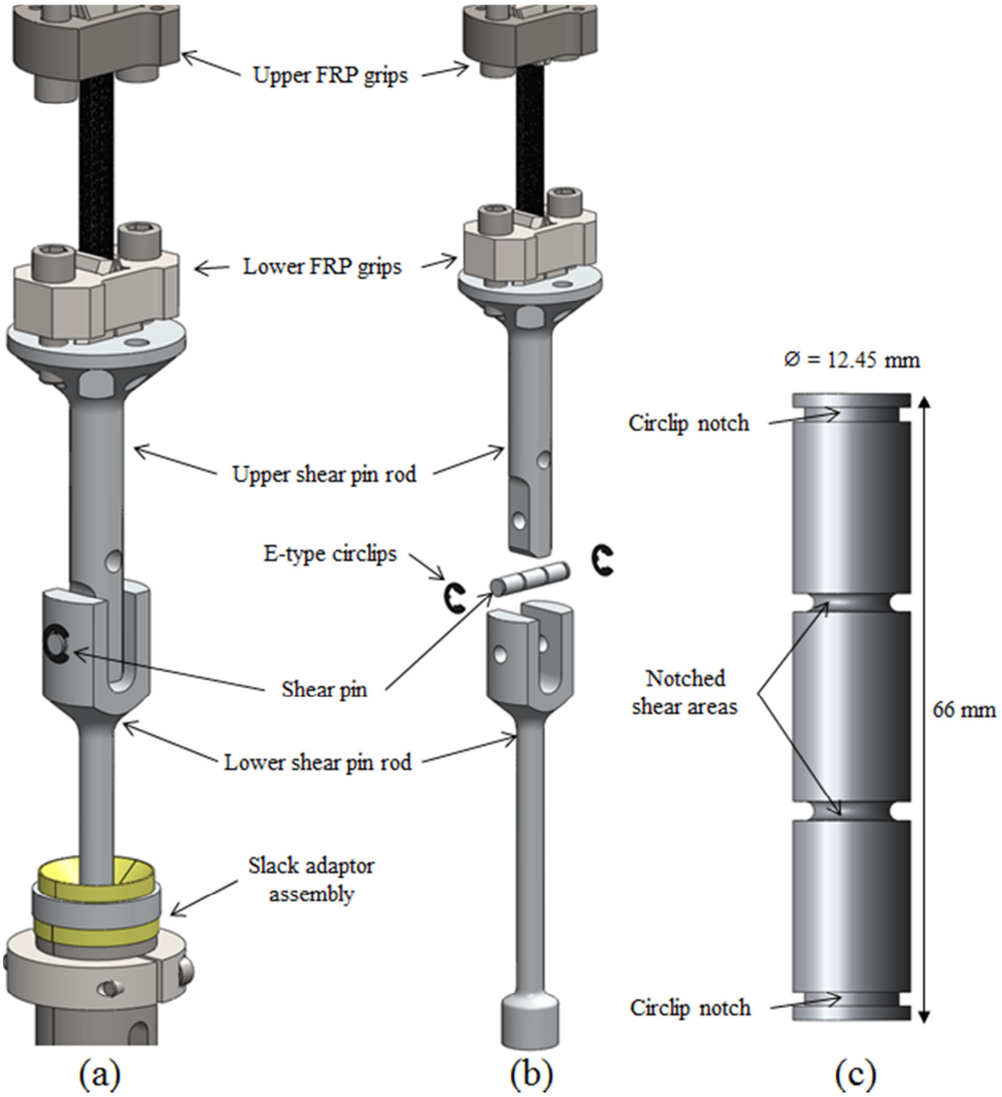

Figure 74: Interrupted loading rig in a conventional layout (a) and an exploded view (b) with a close up of a shear pin (c)

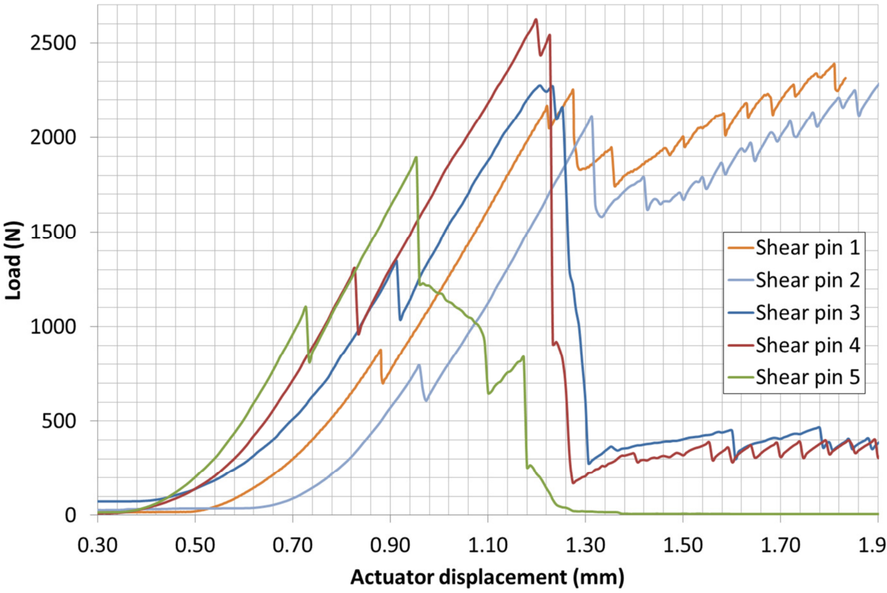

Figure 75: Plots of load vs. actuator position for 6.45 ± 0.15 mm notched diameter PMMA shear pins loaded quasi-statically showing considerable variability in failure load.

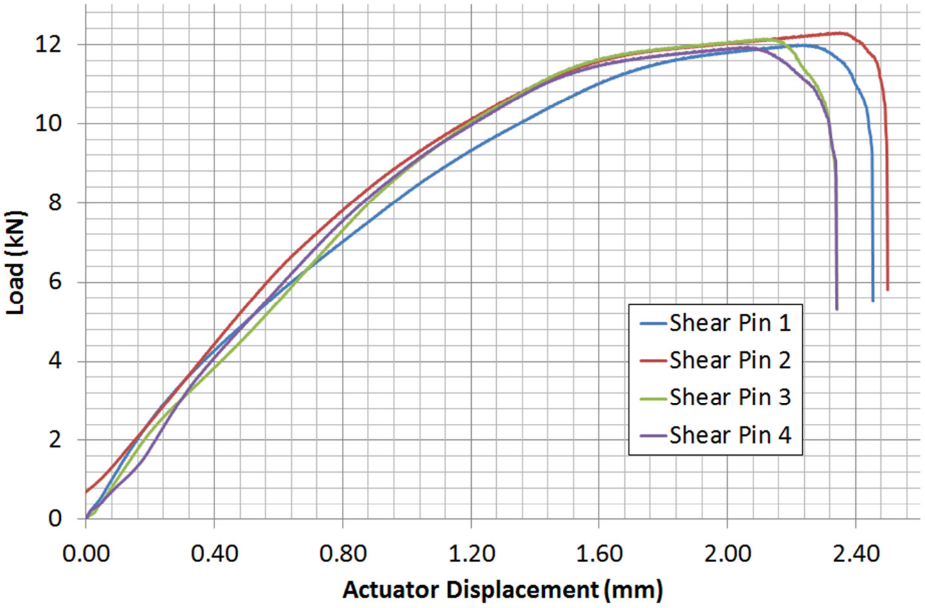

Figure 76: Plots of load vs. actuator position for 6.25 ± 0.10 mm notched diameter aluminium 6085-T6 shear pins loaded quasi-statically in a servo-mechanical test machine.

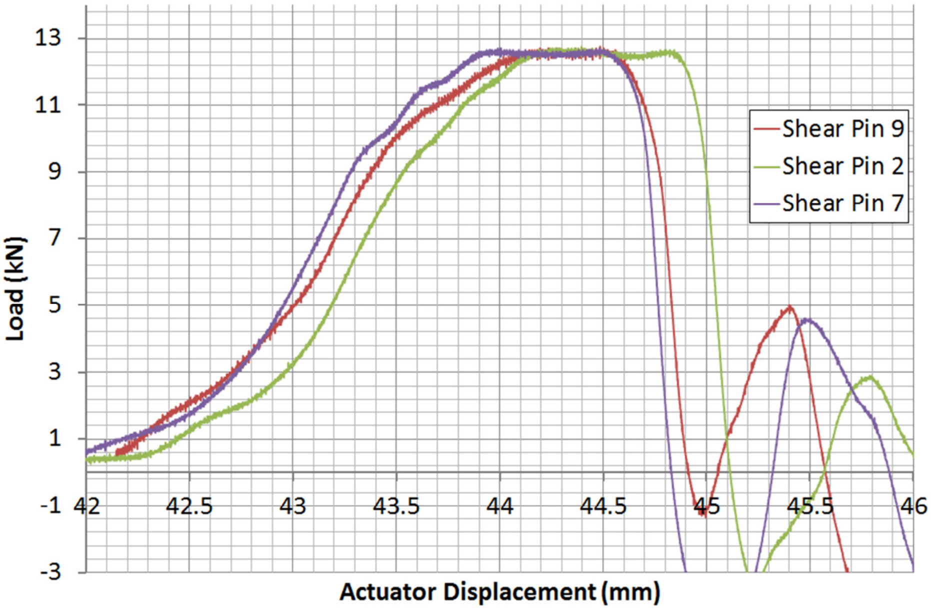

Figure 77: Plots of load vs. actuator position for 6.25 ± 0.10 mm notched diameter aluminium 6082-T6 shear pins loaded at 1 m/s actuator velocity in the Instron VHS.

Due to the onset of plasticity, the failure loads of aluminium alloy shear pins cannot be easily estimated analytically. Shear pin failure loads were therefore determined empirically. A further complication in the use of aluminium alloy shear pins is a change in response found at higher actuator velocities. Whilst the peak loads of nominally identical shear pins were found to be very similar when loaded at quasi-static and 1 m/s actuator velocities, it was found that an actuator velocity of 2.7 m/s resulted in a consistent 50% increase in the peak load. This is contrary to previous work studying the strain rate response of aluminium alloy 6082-T6 which found a much lower strain rate dependency [195, 196]. This behaviour can be explained by considering the failure process of the shear pin, as presented in Figure 78. The central part of the shear pin elongates during failure due to plasticity, but remains constrained laterally by the fork of the lower shear pin rod as it descends. This causes friction between the central part of the shear pin and fork after pin failure, causing an overall increase in the applied load to FRP specimens. Further evidence for this behaviour is gained by visual inspection of the inner fork surfaces after loading, where shear pin material has transferred onto the inner fork surfaces.

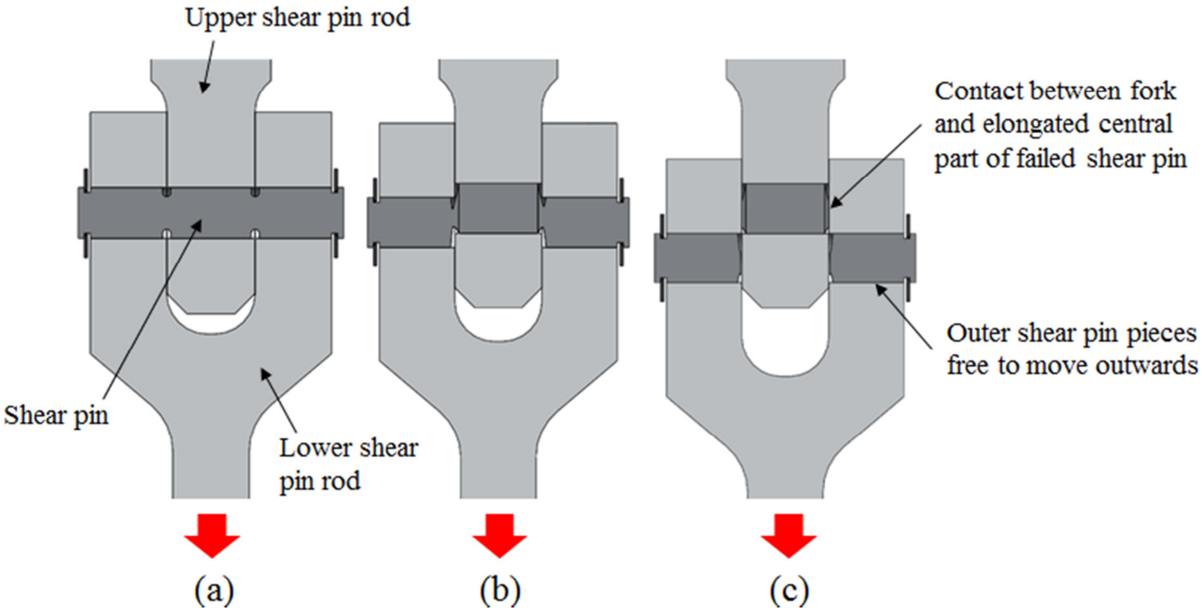

Figure 78: Process of shear pin failure and cause of increased failure load at high velocities

Having described the interrupted loading methodology developed, further adaptions and considerations of the methodology are now discussed.

7.2.1 Inertial Effects

Further complications from dynamic loading arise when the inertia of the various rig parts is considered. The shear pin must transmit sufficient force to accelerate the mass of all rig parts above the shear pin to the required velocity, such that the FRP specimen above is loaded at the required strain rate. However, the shear pin cannot have a failure load greater than that of the specimen itself. Under quasi-static conditions the inertia effects are small, whilst at very high velocities the shear pin is likely to break due to the shock loading before the force can be transmitted effectively to the FRP specimen. There will therefore be a maximum permissible actuator velocity for a given strength shear pin.

Initial predictions were calculated using Newton's second law to estimate the force required to overcome rig inertia. The calculations were based on the total mass of the rig parts above the shear pin (2.14 kg) and the estimated distance over which the acceleration takes place (0.5 mm). The acceleration distance was estimated based on the expected compression of the 1 mm thick polyethylene washer located at the point of contact in the slack adaptor. It was calculated that an actuator velocity of 5, 4, 3, 2 and 1 m/s, would create respective inertial loads of 54, 34, 19, 8.6 and 2.1 kN. To load specimens at a velocity of 5 m/s, a shear pin with a failure load of at least 54 kN would be required. Since the failure load of the GFRP specimens was measured to be 20.7 kN, this would limit the applied velocity to just over 2 m/s. This simple analysis does not take into account elasticity of the rig parts or the additional resistance caused by the FRP specimen in the loading chain. A further experimental study was therefore carried out to determine the velocity limits of the shear pin loading system.

Nominally identical shear pins of 5.90 ± 0.10 mm were loaded at actuator velocities between 1.5 and 5 m/s using the rig design presented in Figure 74. The study also used the anti-compression methodology discussed in section 7.2.2 to prevent compressive loading. Crossply GFRP specimens, as previously described in Chapter 4, were situated in the loading path for this study. A plot showing how the peak load changes with increasing actuator velocity is presented in Figure 79. Initially peak load increases with actuator velocity due to frictional effects between the remnant shear pin and rig parts. After approximately 3.2 m/s, a sharp decrease in peak load occurs due to the inability of the shear pin to transfer sufficient load to overcome the inertial effects of the lower grip. This therefore limits the methodology to a maximum actuator velocity of 3.2 m/s (32 s^{-1}) for the crossply GFRP specimens used in the thesis. The use of stronger specimens allows correspondingly stronger shear pins to be used, raising the maximum allowable actuator velocity.

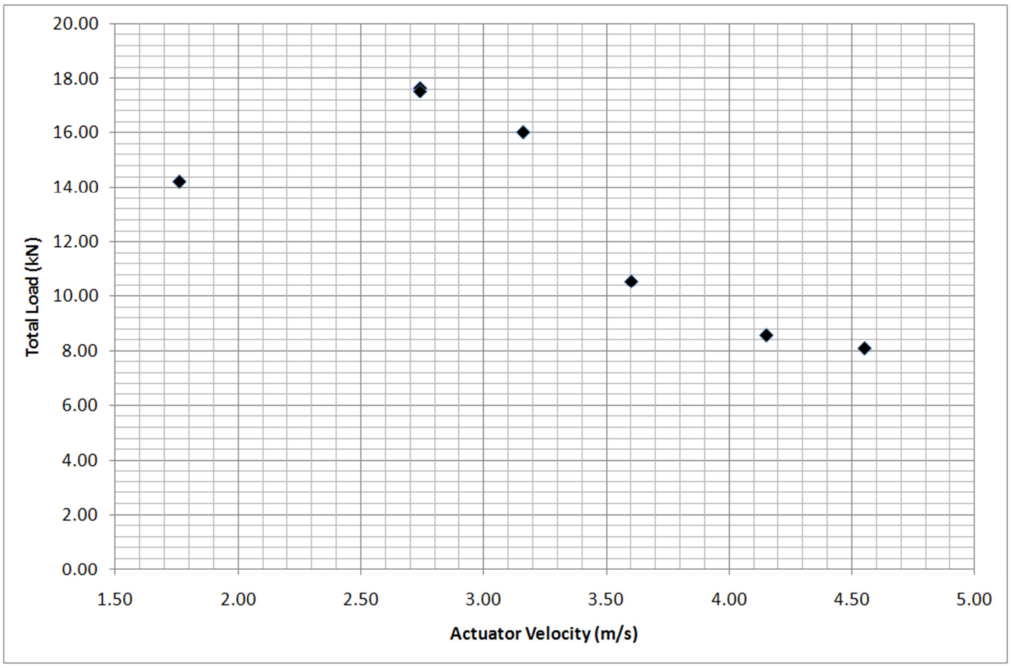

Figure 79: Peak loads of 5.90 ± 0.10 mm notched diameter shear pins across a range of actuator velocities showing the maximum permissible loading velocity for GFRP specimens.

Having discussed the rig behaviour up to shear pin failure, it must now be considered how the rig behaves after the failure event.

7.2.2 Anti-Compression Rig

After shear pin failure, the lower grip will recoil because of the strain energy stored in the specimen from the initial shear pin loading. The inertia of this mass has the potential to cause the FRP specimen to be loaded in compression and to create additional damage; such behaviour was not accounted for by Fitoussi *et al* [108]. As FRP materials are more susceptible to damage when subjected to compressive loads, the behaviour of the rig was investigated further. High speed white light images were collected of the side of FRP specimens during shear pin loading, a selection of which are shown in Figure 80. It is clear that the specimen undergoes significant compression and bending after pin failure. This springback needs to be avoided if tensile damage is to be differentiated from damage caused by compression or bending. A further device was therefore developed to prevent the specimen entering into compression pin failure.

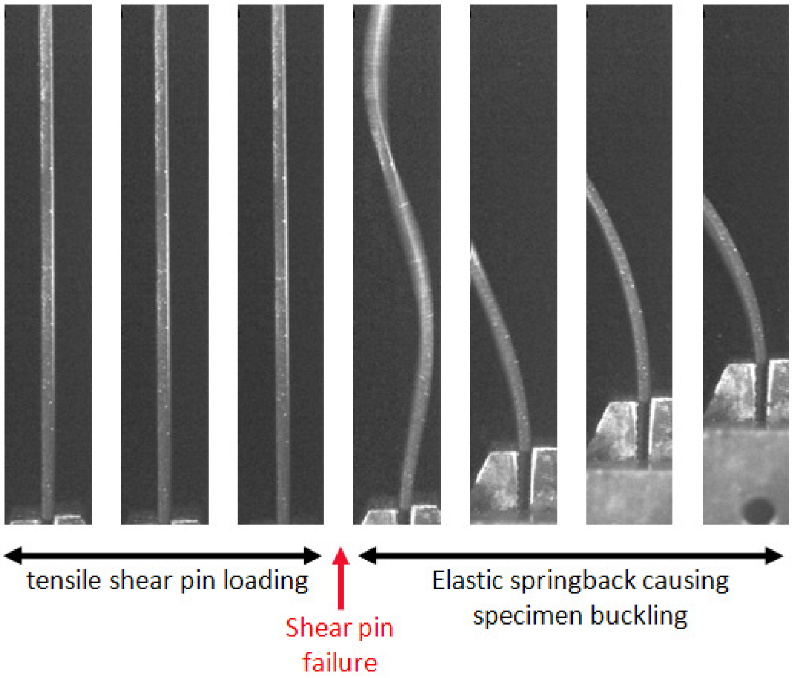

Figure 80: High speed images of the side of an FRP specimen showing buckling caused by specimen springback

The anti-compression rig developed relies on a crossbar consisting of a rigid box-section beam that prevents the lower grip from returning past its original position. A small preload is applied to the specimen before a test by adjusting four M10 bolts to account for any compliance in the crossbar. Two ZEDEX-100EL55 polymer dampers are situated at the point of contact between the crossbar and the shear pin rod to help minimise the introduction of ringing to the loading. A schematic of the Instron VHS with the interrupted loading rig and anti-compression rig in place is shown in Figure 81.

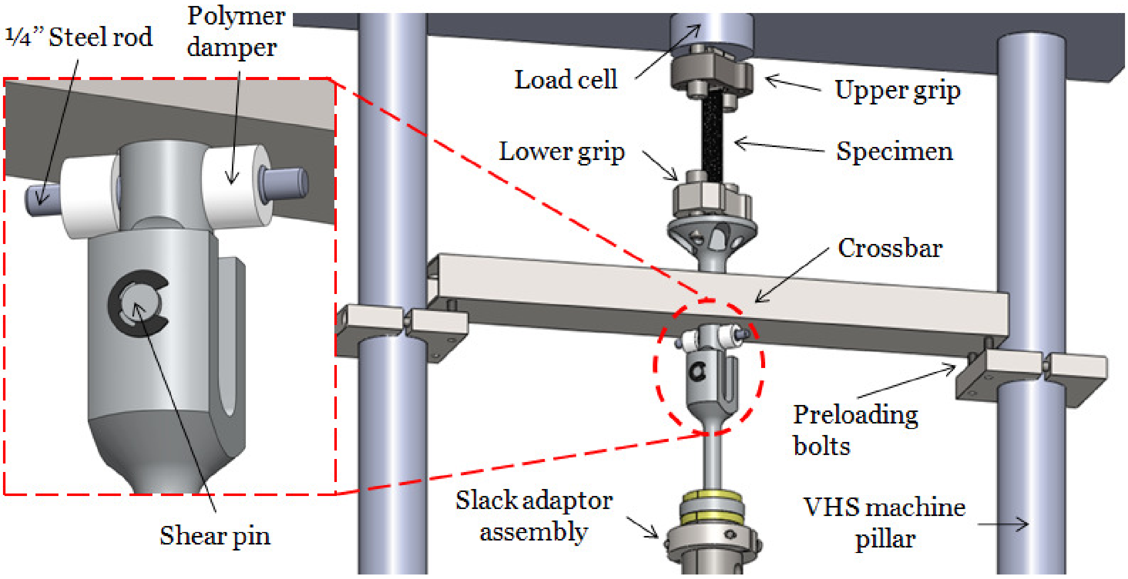

Figure 81: Schematic of anti-compression rig and interrupted loading rig in-situ on the Instron VHS machine

An important note is that piezoelectric load cells are highly susceptible to drift. For this reason, the charge amplifier is programmed to reset the load output to zero immediately before a test, so cancelling any preload applied to the FRP specimen. The preload was established prior to each test using a strain gauge attached to the specimen combined and the Young's modulus of the material obtained experimentally under quasi-static loading. Example data from a crossply GFRP specimen preloaded to 0.34% strain loaded at 5 m/s using the interrupted loading and anti-compression methodology is shown in Figure 82.

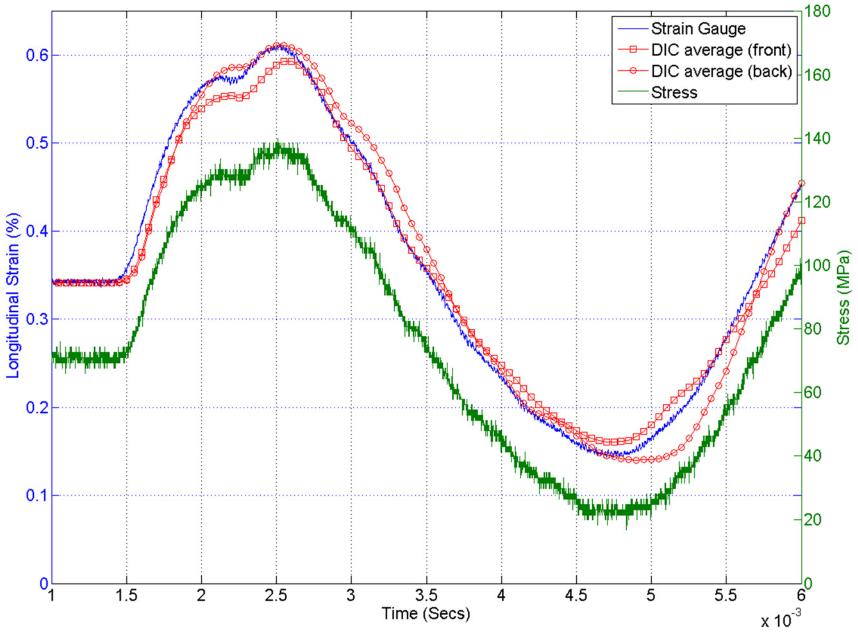

Figure 82: Plots of stress and strain data obtained from a GFRP crossply specimen loaded at 5 m/s actuator velocity using the interrupted loading and anti-compression methodologies.

It can be seen that neither the specimen stress, as calculated from the load cell data, nor the strain gauge reading, passes into compression. Further confirmation was provided through the DIC analysis of images taken from two Photron SA1 high speed cameras positioned perpendicular to the front and back specimen surfaces, also given in Figure 82. By taking an average of the entire specimen area, it can again be seen that the specimen does not experience compression during the test and purely tensile loading is achieved.

Having developed a repeatable methodology for imparting purely tensile interruptible loads to FRP specimens and investigated the operational limits of the design, the methodology was applied to the study of GFRP and CFRP samples in conjunction with the previously validated optical methodology.

7.3 Damage Initiation in CFRP and GFRP at Intermediate Strain Rates

The interrupted loading and anti-compression rigs were employed for the intermediate strain rate loading of a set of five crossply $[90,0]_S$ CFRP and five $[90,0,90,0]_S$ GFRP specimens in the Instron VHS test machine. The specimen geometry is previously described in Chapter 4. The tests were conducted for two main purposes: the first being to investigate the potential of using high speed imaging for full-field damage assessment in FRP materials and the second being to investigate the effect of applied strain rate on the damage initiation behaviour through comparison to the results in Chapter 6. As discussed in section 7.2.1, the maximum actuator velocity possible for shear pins of 5.90 mm notch diameter was found to be approximately 3.2 m/s, beyond which, inertial effects cause shear pin failure before the specimen can be accelerated to the correct velocity.

Five CFRP and six GFRP specimens were loaded at an intermediate strain rate using nominally identical shear pins using the interrupted loading methodology. A summary of all tests conducted is presented in Table 16. Actuator velocity from the actuator LVDT was 3.23 ± 0.037 m/s, so giving a nominal applied strain rate of 32.3 s^{-1} for the 100 mm gauge length specimens. In reality, the actual strain rate experienced by the material will be much lower due to rig compliance. Strain rate was therefore calculated according to equation 4.1 using strain data sourced from DIC and strain gauges. DIC longitudinal strain data was averaged over the entire specimen area for each image, whilst strain gauge data was processed using a 40 point moving average to reduce measurement noise. Typical plots of strain rate during intermediate strain rate tests on GFRP and CFRP specimens are shown in Figure 83 and Figure 84 respectively. The calculated strain rate was found to match closely between the two data sources, with typical maximums of 11 s^{-1} for CFRP specimens and 15.2 s^{-1} for GFRP specimens, much lower than nominal strain rate predicted by actuator velocity. This is believed to be due to elasticity of the rig components and ductility of the shear pin material reducing the applied strain rate.

Test No.	Specimen		Shear pin notched area (mm^2)	Actuator Velocity (m/s)	Load			Stress (MPa)	Fraction of failure stress	Strain rate	
	Materia l	Cross-Section area (mm^2)			Preload (kN)	Dynamic (kN)	Total (kN)			DIC (s^{-1})	Strain gauge (s^{-1})
1	CFRP	22.57	55.24	3.199	6.29	10.69	16.99	753	70 %	10.8	10.3
2	CFRP	22.25	55.14	3.210	6.30	10.79	17.09	768	72 %	11.3	11.1
3	CFRP	22.55	55.61	3.216	6.56	11.04	17.60	780	73 %	10.6	11.5
4	CFRP	22.21	55.24	3.217	6.79	10.25	17.05	767	72 %	11.8	12.6
5	CFRP	22.30	55.70	3.204	6.88	10.45	17.32	777	72 %	10.9	12.0
Mean ± s.d		22.38 ± 0.17	55.39 ± 0.25	3.209 ± 0.008	6.57 ± 0.27	10.64 ± 0.30	17.21 ± 0.25	769 ± 10.8	72 ± 0.01	11.1 ± 0.5	11.5 ± 0.9
6	GFRP	30.27	55.80	3.237	4.95	10.35	15.31	506	69 %	16.1	14.9
7	GFRP	29.37	55.80	3.194	5.00	10.16	15.16	516	71 %	16.3	15.2
8	GFRP	30.83	55.80	3.236	5.20	9.72	14.92	484	66 %	15.5	14.7
9	GFRP	30.03	55.15	3.286	5.26	9.08	14.35	478	66 %	15.4	15.0
10	GFRP	30.62	55.80	3.309	5.28	9.86	15.14	494	68 %	15.6	15.6
11	GFRP	29.10	55.52	3.208	4.84	10.16	15.00	516	71 %	17.6	15.7
Mean ± s.d		30.04 ± 0.69	55.64 ± 0.27	3.245 ± 0.045	5.09 ± 0.18	9.89 ± 0.46	14.98 ± 0.34	499 ± 16.2	69 ± 0.02	16.1 ± 0.8	15.2 ± 0.4

Table 16: Summary of intermediate strain rate tests conducted using the interrupted loading methodology

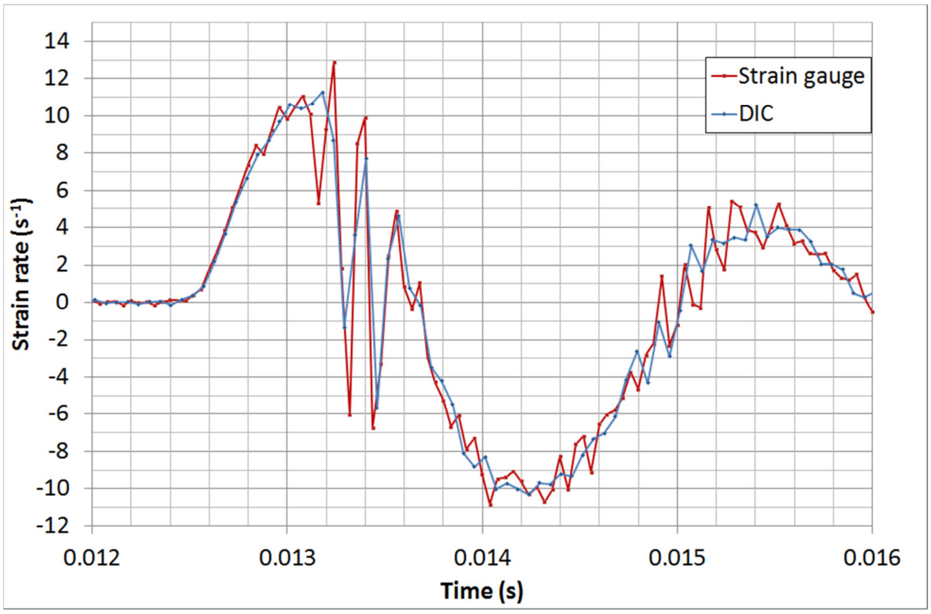

Figure 83: Strain rate during an interrupted loading test on a CFRP specimen, calculated from DIC data and strain gauge data.

A preload of approximately 6.55 kN was applied to CFRP specimens whilst a nominal preload of 5.14 kN was applied to GFRP specimens. Shear pins of 5.95 mm nominal notch diameter were used to provide dynamic loads of approximately 10.64 kN and 9.83 kN to CFRP and GFRP specimens respectively. In earlier trials, this combination of preload and shear pin geometry was found to successfully prevent specimens experiencing compression after shear pin failure. These loading ranges give a total stress equivalent of 72% and 69% of the material UTS for the CFRP and GFRP specimens respectively. The results are therefore comparable to the quasi-static tests presented in Chapter 6, in which specimens were loaded to 70% of their quasi-static failure stress. A plot of total load (preload plus dynamic load) and strain against time for a typical CFRP specimen is shown in Figure 85. It is again shown that the preloading methodology was able to successfully prevent the specimen from entering into compression with a minimum strain gauge reading of 0.06% strain and a minimum total load of 1.31 kN. Such behaviour was typical across all tests.

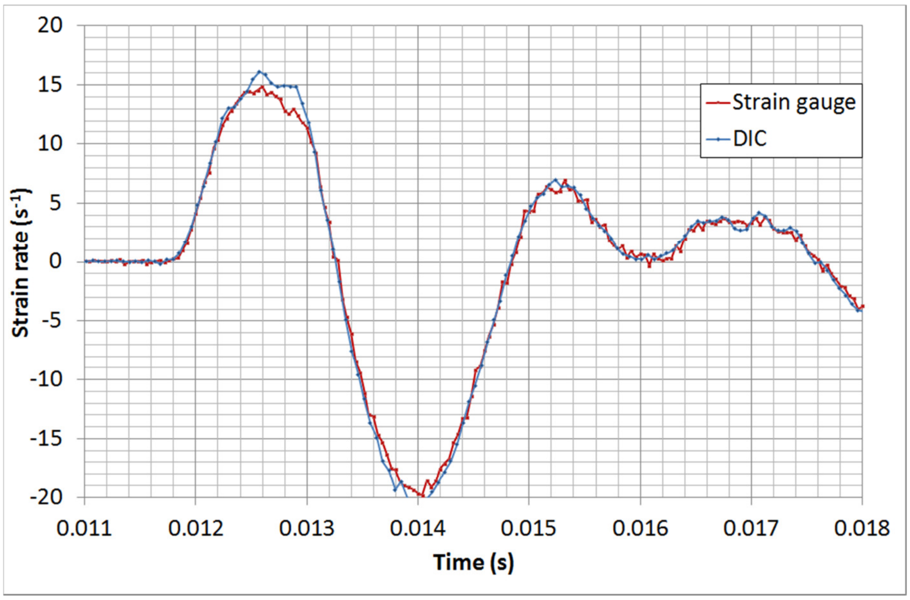

Figure 84: Strain rate during an interrupted loading test on a GFRP specimen, calculated from DIC data and physical strain gauge data.

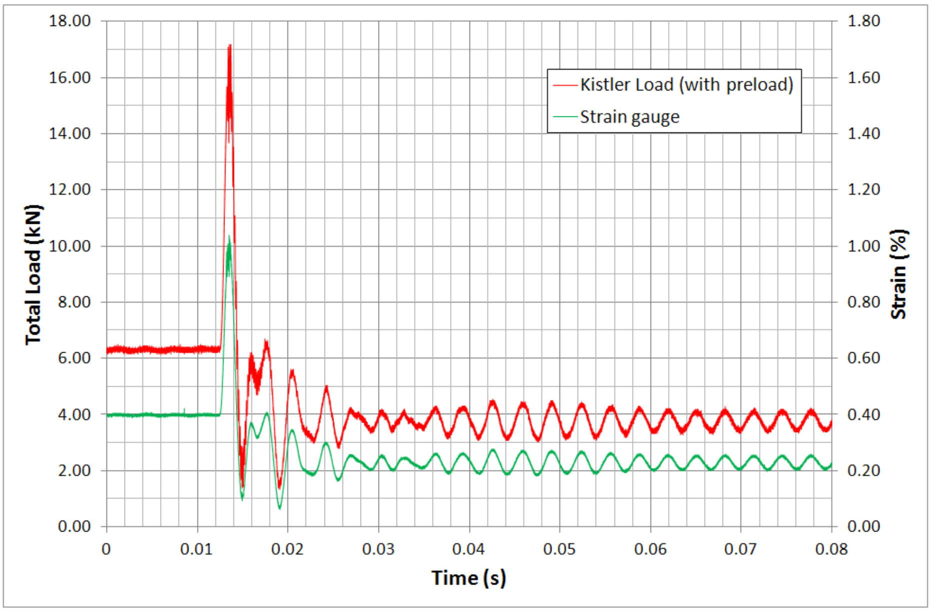

Figure 85: Plots of load and strain against time for a typical CFRP crossply specimen loaded at an actuator velocity of 3.23 m/s.

A plot of the same data focussing on the shear pin loading phase is shown in Figure 86. The shear pin load can be seen to begin at 0.0127 s and to end at approximately 0.0139 s. Two types of oscillatory behaviour can be seen in the load trace; a high frequency oscillation of approximately 12.8 kHz originating at 0.0134 s and a lower frequency oscillation of approximately 400 Hz induced after shear pin failure. The high frequency oscillation is likely to be a result of specimen damage occurring, releasing strain energy and causing a longitudinal vibration in the specimen. The low frequency oscillation is likely to be caused by specimen spring back resulting in the lower grip hitting the anti-compression rig crossbar and causing the entire rig to enter into a low frequency vertical oscillation. This vibration causes the specimen to be cyclically loaded for two cycles at approximately ± 2 kN, before rapidly decaying to a cyclic load of approximately ± 0.75 kN. It is not considered that such cyclic loading contributed to any additional surface damage. This conclusion was based upon the inspection of DIC strain maps, derived from white-light images of the specimen surface which continued to be collected for approximately 12 ms after shear pin failure, the period in which the highest amplitude cyclic loading occurs.

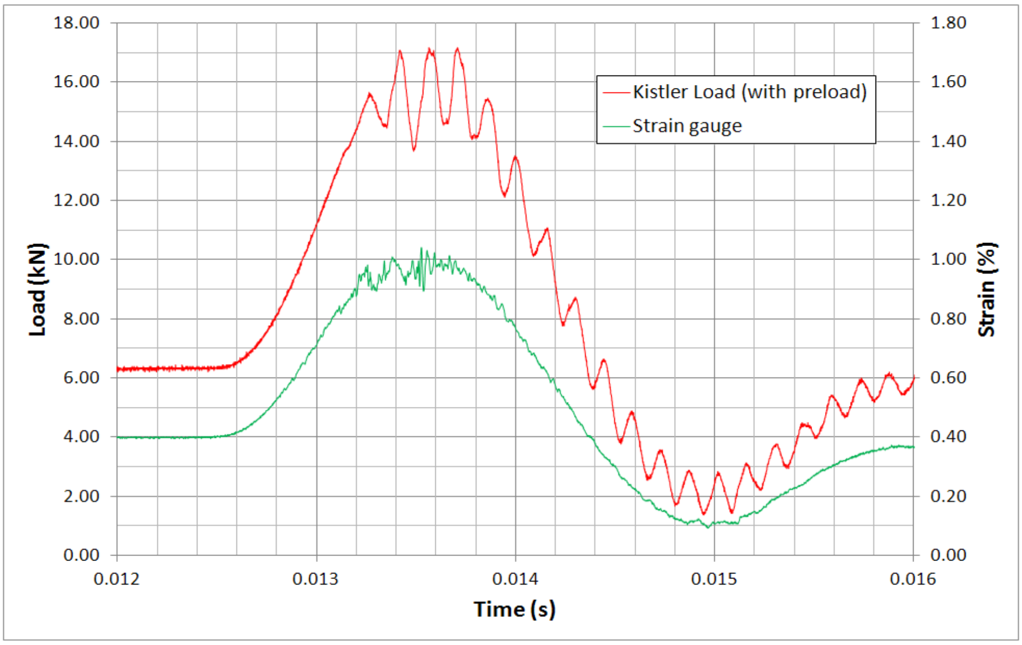

Figure 86: Plot of load and strain against time for a typical CFRP crossply specimen loaded at an actuator velocity of 3.23 m/s focussing on the shear pin loading phase.

Specimens were imaged during loading using a CEDIP Silver 480M IR camera and two Photron SA1 high speed white-light cameras. Details of the camera systems and settings used are described in Table 17.

Camera	Image Size (pixels)	Imaging Size (mm)	Spatial Resolution (mm/pixel)	Imaging Frequency (Hz)	Exposure/ Integration time (µs)
CEDIP Silver 480M	64 x 24	21.12 x 7.92	0.33	9372	80
2 x Photron SA1	624 x 448	20.33 x 14.60	0.033	18000	55.6

Table 17: Imaging settings for intermediate strain rate tests

The IR camera was positioned perpendicularly to the specimen surface with an SA1 camera located on either side. To maximise the spatial resolution in both the IR and white light images, the cameras were positioned as close to the specimen as possible with an approximate standoff distance of 150 mm for the SA1 cameras and 200 mm for the IR camera. A photograph of the camera setup is shown in Figure 87. The minimum standoff distance possible was determined by the physical size of the camera housings and the increasing angle between the SA1 cameras at smaller standoff distances. An angle greater than 60° was found to result in a deterioration of the stereo camera calibration. A compromise was reached with the SA1 cameras having an angle of 50° between cameras axes giving a calibration RMS value of 0.31 pixels. The SA1 cameras were equipped with 105 mm sigma lenses set to an aperture of f/16. Illumination was provided by both of the custom LED units, further details on which are presented in Appendix C. As discussed in section 4.5, the LED lighting produces far lower levels of IR radiation when compared to halogen lighting and so minimises image distortions caused by air density changes.

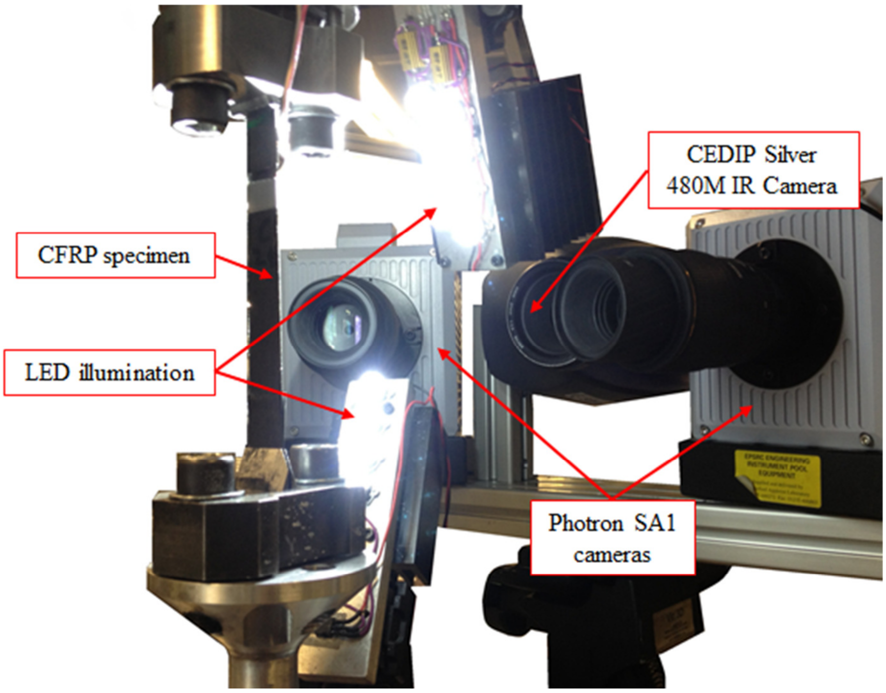

Figure 87: Camera and lighting setup for intermediate strain rate testing

The CEDIP Silver 480M IR camera must use a sub-window to image at frequencies above 383 Hz. Since any cracking on the specimen surface is expected to form in the transverse direction, a tall and narrow sub-window was chosen to increase the likelihood of capturing multiple instances of crack initiation. The sub-windowing on this model of IR camera only allows certain image sizes to be selected and has a preference for sub-windows which are wider than they are high. For this reason the IR camera was rotated and mounted at 90°.

Figure 88 shows a full-frame 320 x 256 IR image of a CFRP specimen along with the sub-windowing area used during the intermediate strain rate tests. Also shown is the white-light imaging area of the SA1 cameras. Due to slight camera misalignment, only half of the IR sub window was found to coincide with the white-light image area for the CFRP tests conducted. The error was rectified for later tests conducted on GFRP specimens, as shown in Figure 89. A fine wire was temporarily attached to the surface of specimens prior to a test and white light and IR images captured. The wire, being visible in both the white light and IR spectrums, allows a common datum point to be known between both image sets. This reference point allows the post-processing of IR and DIC data to match spatially. As previously discussed in section 4.5, the high specimen surface temperature and vertical temperature gradient were found to be caused by the LED illumination despite their relatively low IR output.

Approximately 18 white light and 9 IR images were collected during the shear pin loading sequence. Cameras were triggered using the methodology outlined in section 4.4. As previously discussed, the Photron SA1 cameras were set to start recording upon receiving the trigger signal but were not programmed to reset the internal clock, such that the start of the first image exposure occurs up to one frame period earlier than the trigger pulse. The IR camera operated using a circular pre-buffer of 500 frames to be certain of capturing the loading event. The trigger pulse was also recorded onto one of the data channels of the IR camera allowing the trigger to be synchronised with the correct IR image. The start of exposure of the 500th IR image may therefore occur up to one frame earlier than the trigger signal. Figure 90 shows a typical load plot for a CFRP specimen loaded using the shear pin methodology and the temporal location of white light and IR images. The letters a to d designate the images used in subsequent figures.

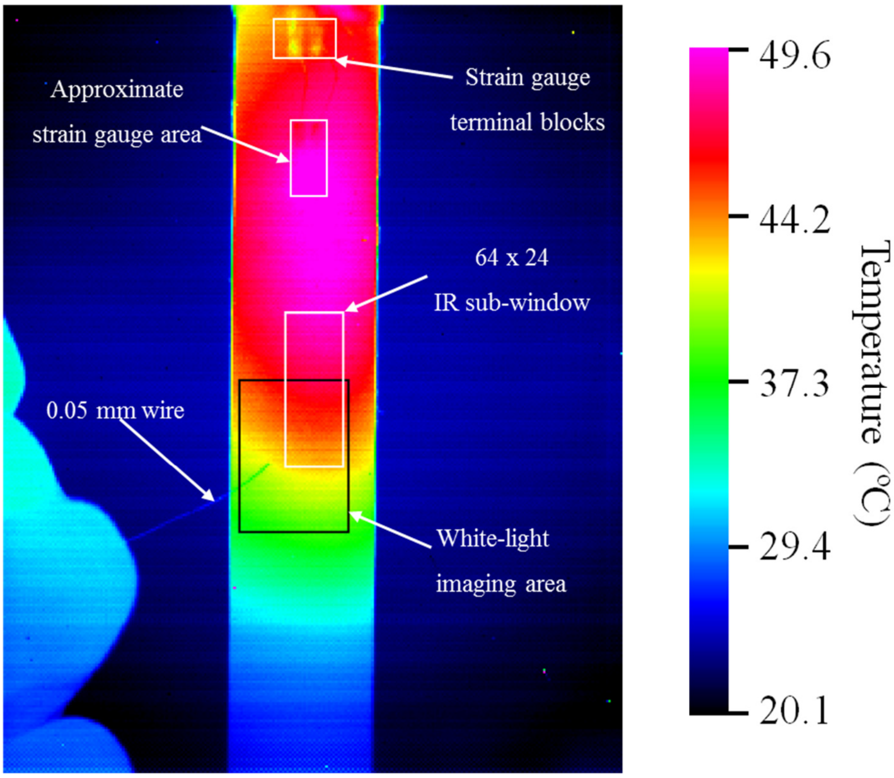

Figure 88: Full-frame IR image of a CFRP specimen showing sub-window area, white-light imaging area and strain gauge location

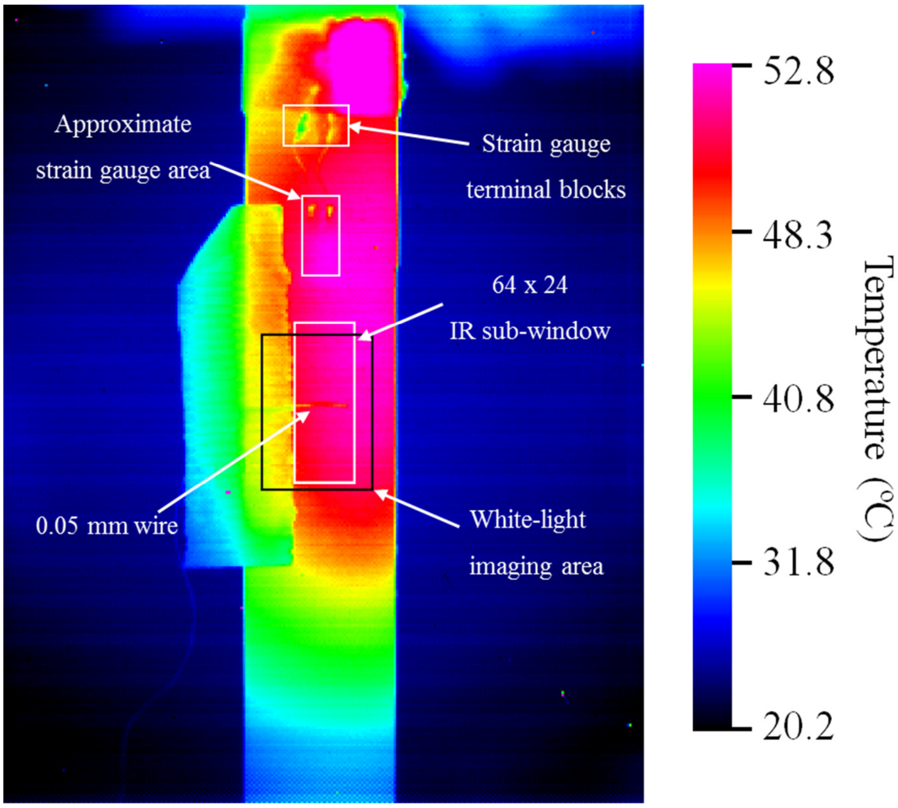

Figure 89: Full-frame IR image of a GFRP specimen showing sub-window area, white-light imaging area and strain gauge location

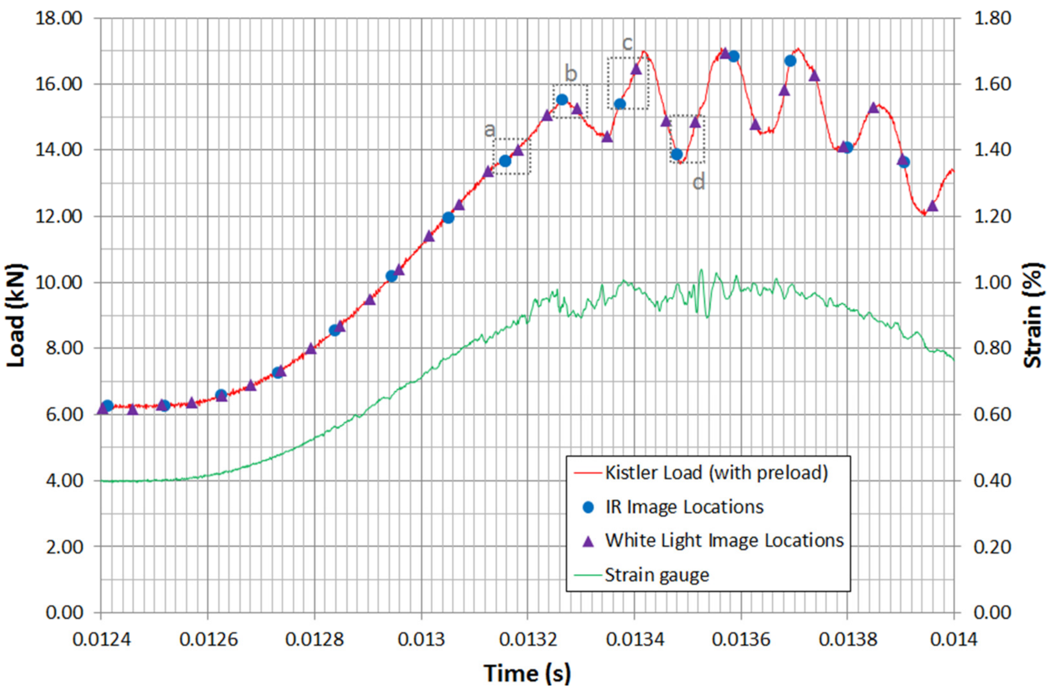

Figure 90: Plot of load and strain against time during shear pin loading of a CFRP specimen showing locations in time of white light and IR images.

White light images were processed in DaVis 8.1.3 using a subset size of 21x21 pixels and a step size of 6 pixels giving a spatial resolution of 4.16 mm. A high accuracy sixth order spline subpixel interpolation method was used, as recommended from the work conducted in Chapter 5. Static images collected from specimens before each test were processed using the same correlation settings to determine the noise level of the DIC measurements. The standard deviation of the strain data was found to be between 0.087 and 0.119 % strain across all samples tested.

IR images were calibrated using the methodology established by Fruehmann *et al* [47]. Examples of uncalibrated and calibrated IR images recorded during loading of a CFRP specimen are shown in Figure 91. After calibration, a vertical temperature gradient of approximately 8 K can be noted. This behaviour was found to be common across all samples with the centre of the specimen being significantly warmer. This is caused by heating from the LED illumination which is focused on the centre of the specimen. After calibration, horizontal bands of heating can be noted in the IR images of approximately 2 K for the CFRP specimens. No such behaviour could be noted in the data collected from GFRP specimens. To more easily distinguish damage induced heating from sensor noise, the calibrated IR data was processed using the thresholding algorithm previously described in section 6.2.1.

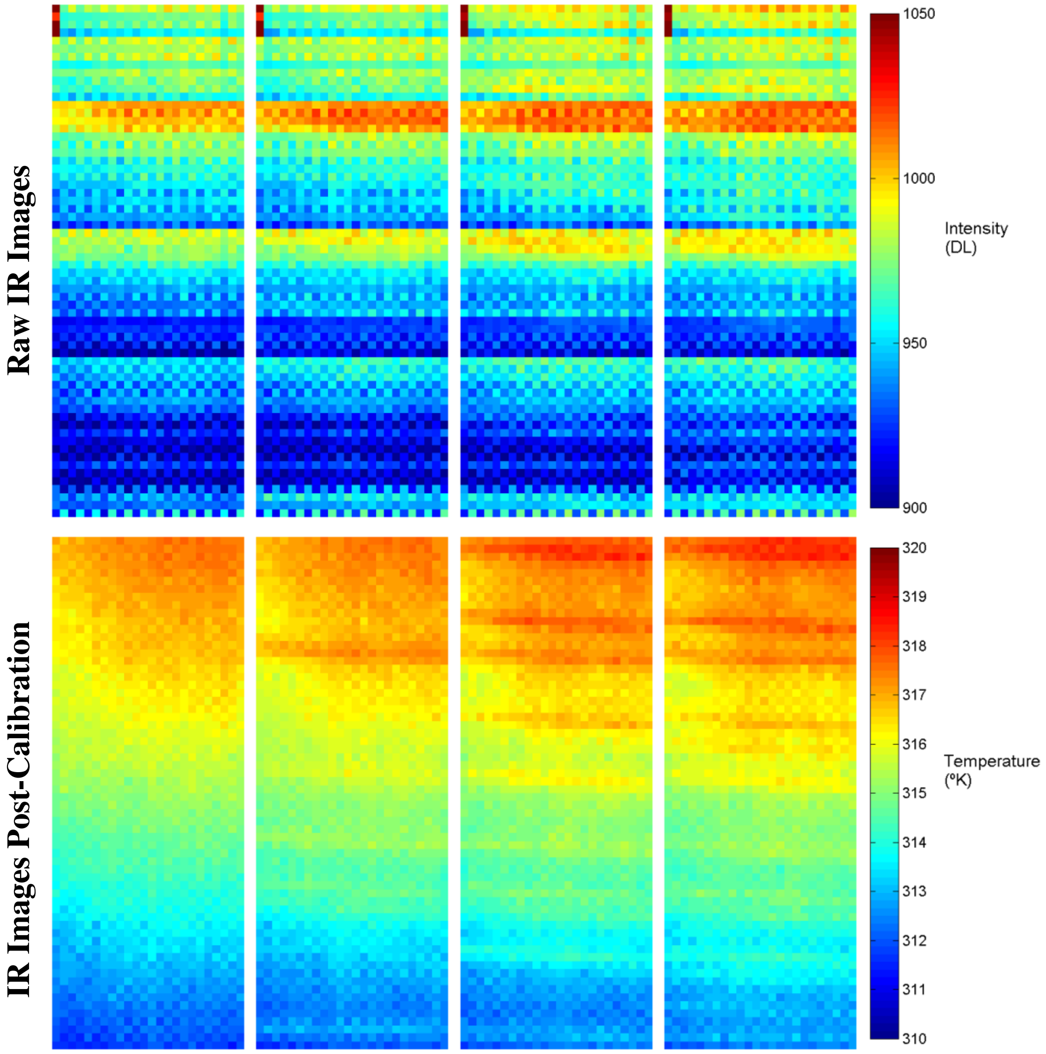

Figure 91: Example of raw IR images in digital levels (upper) and thermally calibrated IR images (lower) recorded at 9.372 kHz of a CFRP specimen during shear pin loading.

A further study was conducted to find an appropriate threshold value for the IR data collected from the intermediate strain rate tests. Figure 92 shows a set of processed IR data showing the effect of different threshold values. A threshold value of 0.20°C allows much of the sensor noise to pass to the final image with any potential damage being unresolvable as a result. A higher value of 0.80°C was found to filter out the majority of heat generation in the material. A compromise threshold value of 0.50 °C was used for subsequent IR analysis. Sensor noise was found to be non-uniform across the sub window area, with four pixels found to be faulty, displaying highly random temperature outputs above all threshold values trialled, prior to any loading being applied. A threshold value of 0.5 °C was found to yield the best compromise and was used for subsequent analysis.

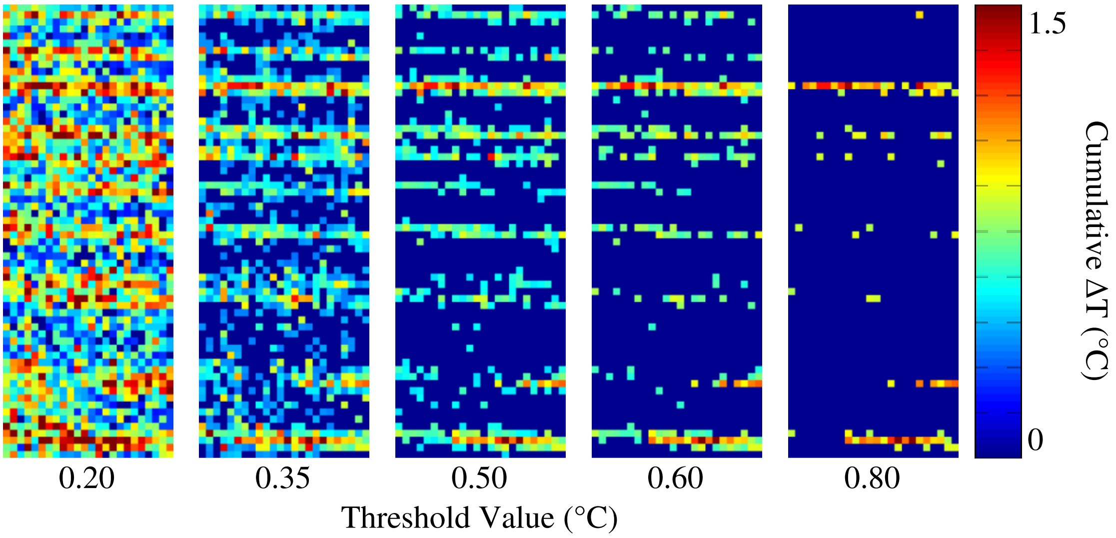

Figure 92: Cumulative ΔT IR plots during the shear pin loading of a CFRP specimen to 71% of its failure stress showing the effect of threshold value

To take into account the rigid body motion of the specimen during loading, the motion compensation procedure developed in section 6.2.2 was applied to the *ΔT* IR data. Any areas of IR subwindow that do not overlap the DIC data were omitted from motion compensation. Figure 93 to Figure 96 show full-field DIC longitudinal strain data and cumulative IR data collected from the same CFRP specimen used to plot Figure 90, which was loaded to 70% of its UTS using the interrupted loading methodology. Figure 93 to Figure 96 show DIC strain and cumulative *ΔT* IR maps obtained from images collected at points a, b, c and d respectively, as shown in Figure 90. The DIC plots were calculated from the white-light image immediately preceding the IR image shown. The areas highlighted in red show the overlapping imaging areas of the white light and IR cameras. Due to rigid body motion of the specimen some DIC data is lost at the top of the plot as new areas of the specimen surface move into view and also at the bottom of the data, where previously visible subsets move out of the field of view.

An area of decorrelation can be noted in the bottom left of the DIC data as highlighted within Figure 93. This is as a result of contamination on the specimen surface occurring after taking the reference image but before the intermediate strain rate test.

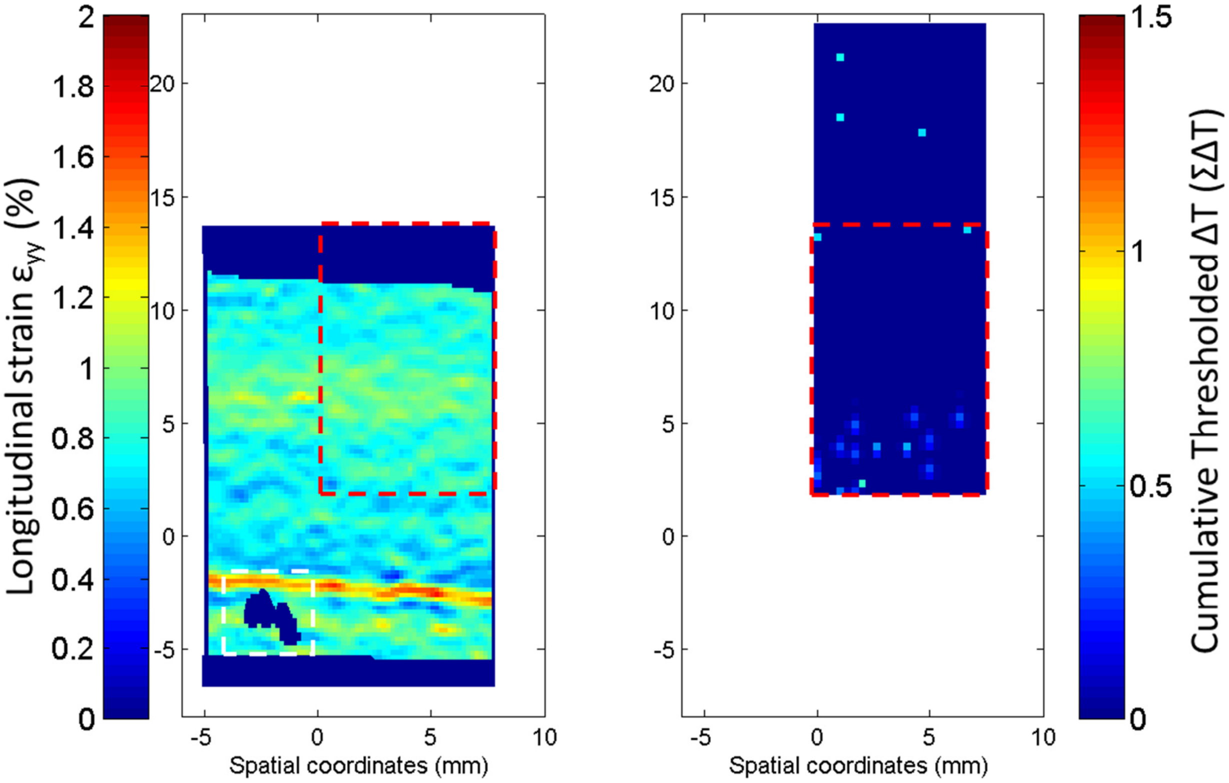

Figure 93: (a) Spatially corrected plots of DIC strain data and cumulative ΔT IR data for a CFRP specimen loaded at an intermediate strain rate. Red boxes denote the overlapping imaging areas and a white box shows an area of decorrelation.

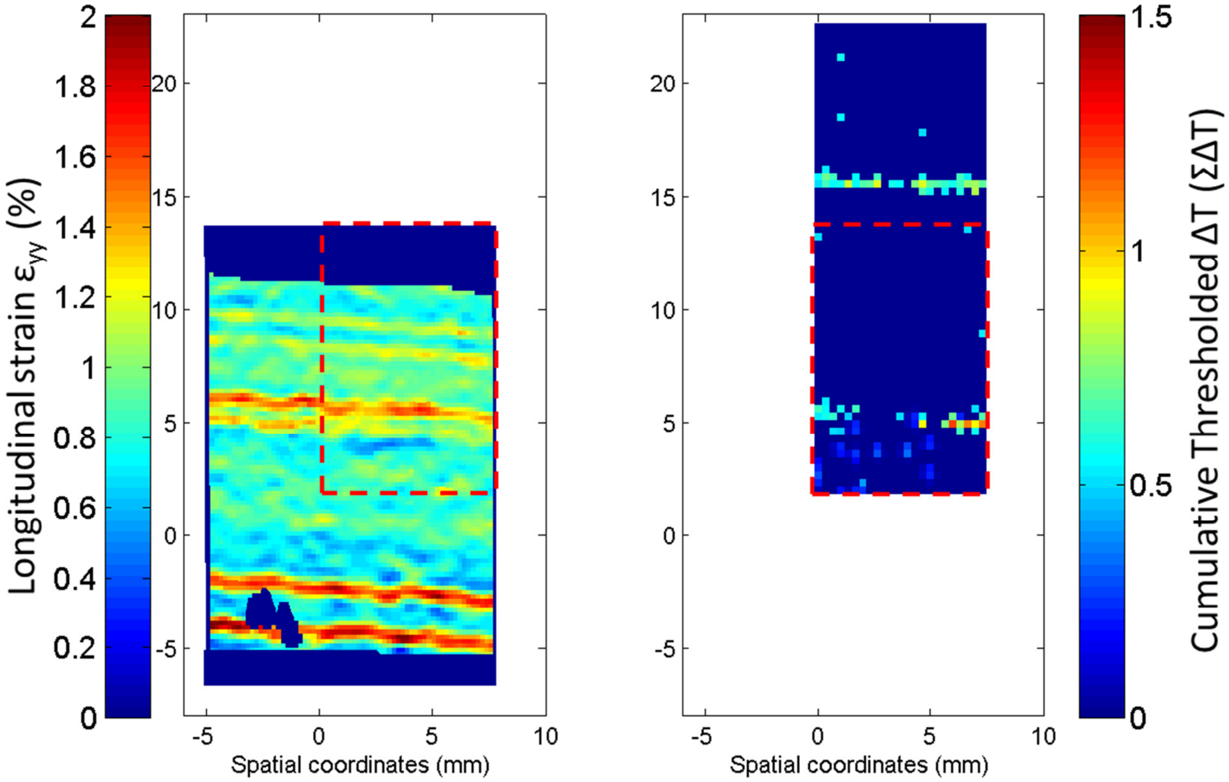

Figure 94: (b) Spatially corrected plots of DIC strain data and cumulative ΔT IR data for a CFRP specimen loaded at an intermediate strain rate

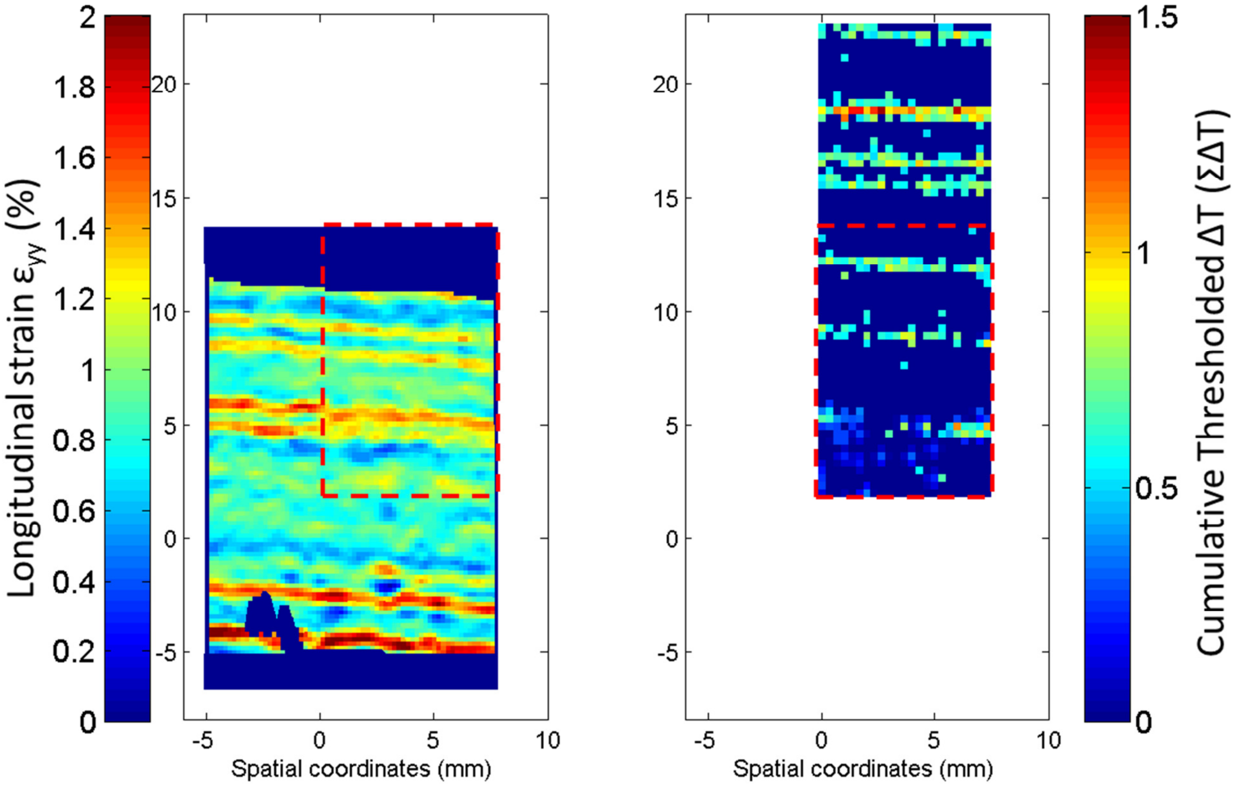

Figure 95: (c) Spatially corrected plots of DIC strain data and cumulative ΔT IR data for a CFRP specimen loaded at an intermediate strain rate

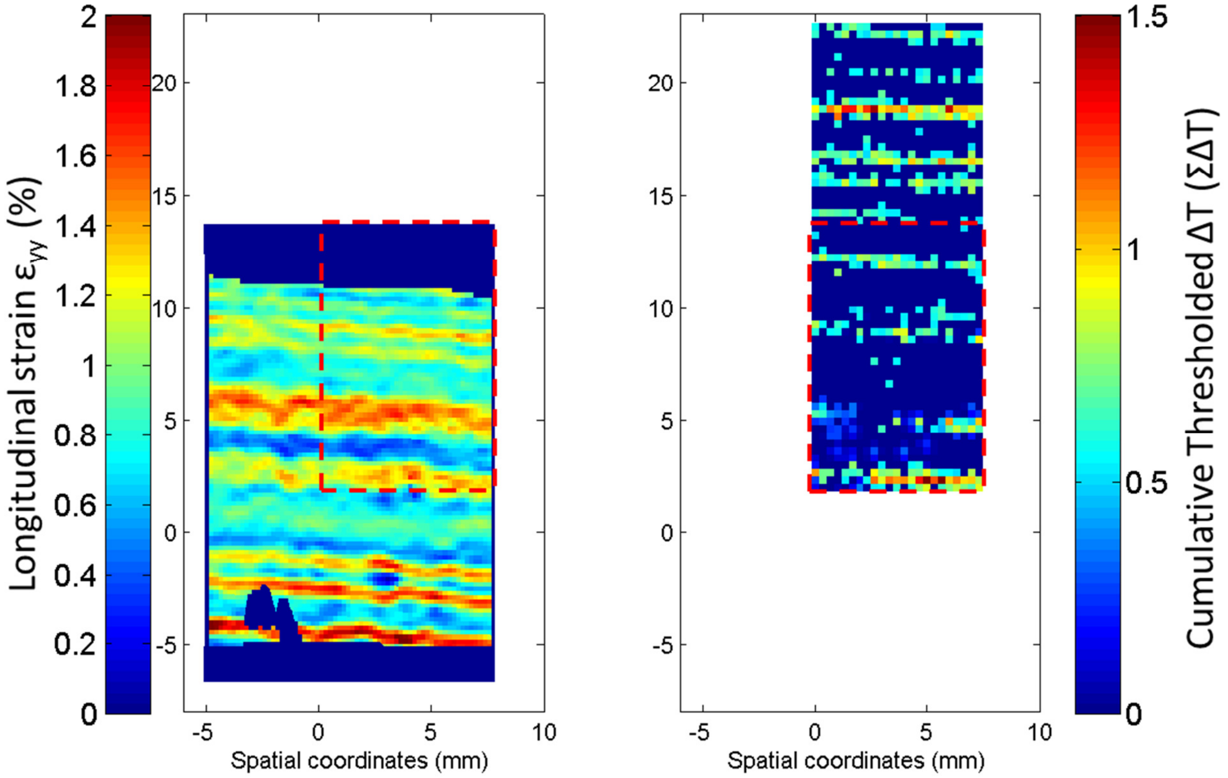

Figure 96: (d) Spatially corrected plots of DIC strain data and cumulative ΔT IR data for a CFRP specimen loaded at an intermediate strain rate

Since the DIC data and the cumulative ΔT IR data are plotted in the correct spatial location, a direct comparison can be made to confirm the onset of damage with greater confidence. Although bands of heating and high strain can be seen to generally occur at the same location on the specimen surface, the behaviour is not as distinct as data collected at quasi-static strain rates, previously discussed in section 6.2.3. This can be attributed to the lower spatial resolution of the raw images collected during the intermediate strain rate loading, and the lower spatial resolution of the strain and IR data subsequently produced. A band of high strain and a band of heating appear within the overlapping imaging areas in Figure 94 at approximately the same height in both data sets. The DIC data shows one band of high strain with a band of lower strain magnitude immediately below. The IR data, however, shows one single horizontal band of increased temperature at this location. The most likely reason is that the smaller strain band signifies a smaller crack which did not generate sufficient heat at the surface to pass the thresholding procedure. Another possibility is that the smaller crack occurred on the back surface of the specimen resulting in a small increase in strain that was resolvable by DIC on the front surface. Any heat generated by such a crack would take time to diffuse through the specimen thickness to the front surface, whilst also diffusing in the plane of the specimen. The heating from such a crack would therefore be filtered by the threshold procedure. Another possibility is that the crack only occurs in the applied paint layer, resulting in a temperature change that is small and filtered by the thresholding procedure. The notion of the paint cracking versus actual cracks occurring is studied further in the microscopic analysis conducted on a different CFRP specimen in section 7.4. A further band of high strain and surface heating forms in the images in Figure 96 at the bottom of the IR sub window. Again, this occurs at approximately the same location in both data sets.

Some bands were found to initiate a frame earlier in the strain data than in the IR data. As previously discussed in Chapter 4, the IR and white-light cameras were not programmed to reset their internal clocks upon receipt of a trigger signal. The temporal synchronisation of IR and white-light images is therefore only accurate to within one white-light frame period and is believed to be the cause of the anomalous behaviour between DIC and IR data.

A large increase in noise was found in a single DIC strain map which corresponded to the point of maximum strain rate. When the raw images were studied it was apparent that the images from which this strain map was derived had significantly more blurring than other images in the data set. This meant that only one strain map was affected as the correlation software was still able to track the surface correctly in subsequent images. To avoid blurring, a shorter exposure time would be necessary, so requiring the use of more powerful lighting or a camera system with greater light sensitivity.

Other CFRP specimens tested were processed using the same image analysis procedure. Similar behaviour was found to that of the previously discussed dataset.

The data collected from GFRP specimens loaded at an intermediate strain rate were processed using the same procedure. A selection of non-consecutive DIC strain and cumulative ΔT maps from one such specimen is shown in Figure 97. Red boxes denote the overlapping imaging areas of the IR and white-light cameras. In contrast to the findings from Chapter 6 of quasi-statically loaded GFRP specimens, clear bands of high surface strain and surface heating can be noted. The first sign of potential damage is highlighted within dashed ovals shown in Figure 97 (i). A single horizontal band of high strain can be noted in the DIC strain map whilst a corresponding area of thermal activity in the cumulative ΔT map can be noted at the same position. Several other individual pixels of activity can be noted in this cumulative ΔT map away from the highlighted area. These pixels are faulty and were found to display a high variability in pixel intensity regardless of applied load.

The locations of further strain banding, shown in Figure 97 (ii) and (iii) can be seen to generally match well with the cumulative ΔT data. However, some strain bands were found to occur earlier in time than found in the cumulative ΔT data. One such strain band, highlighted in Figure 97 (ii) can be seen to initiate without a corresponding increase in surface temperature. A corresponding band of heating is not found on the specimen surface until the next IR image is processed, as highlighted in Figure 97 (iii). This behaviour is attributable to the poor image synchronisation. It was found that the DIC and IR data from other GFRP samples showed similar results with spatially matching banding in each image set.

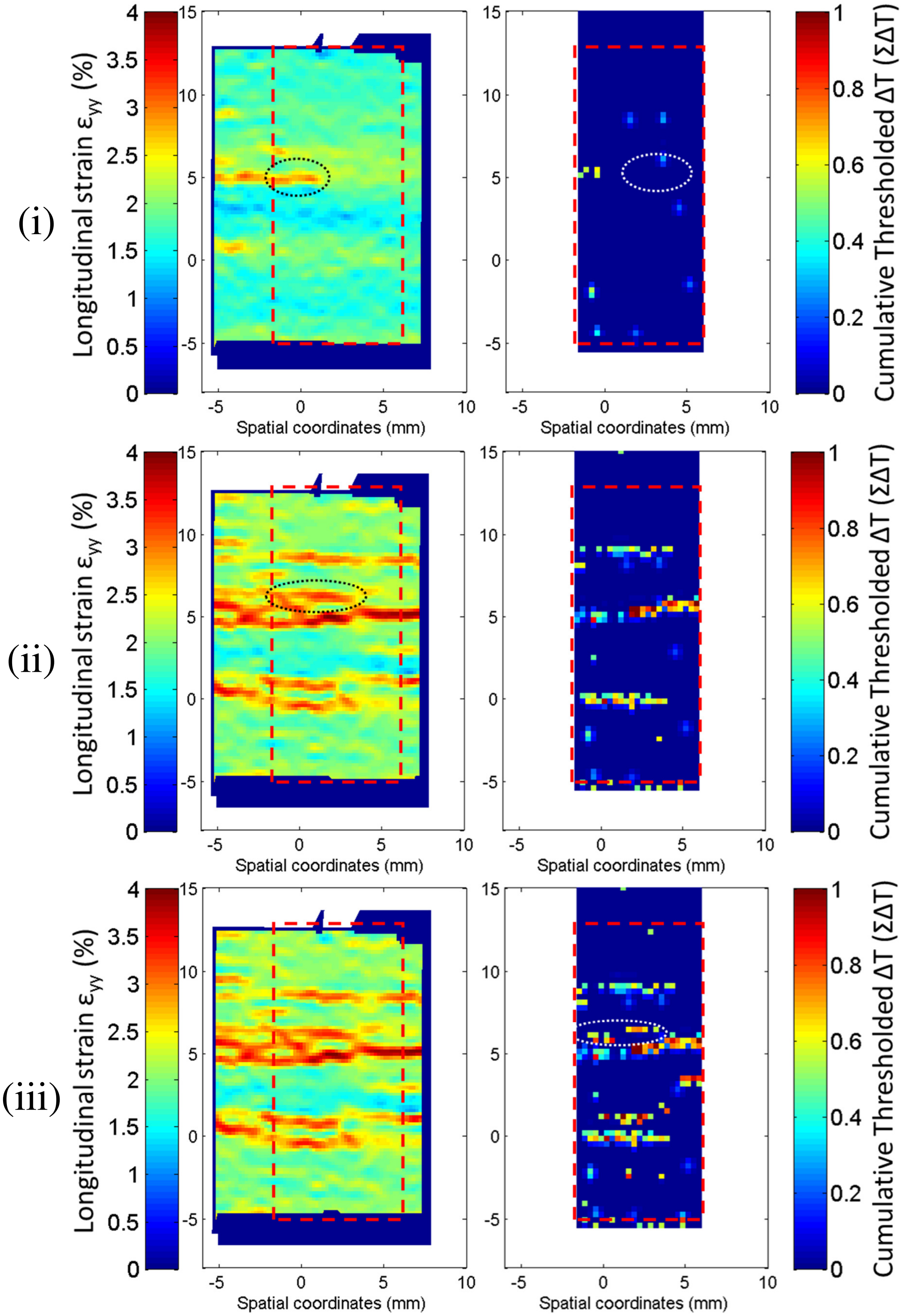

Figure 97: Spatially correct plots of DIC strain data and cumulative ΔT IR data for a GFRP specimen loaded at an intermediate strain rate. Red boxes denote the overlapping imaging areas and dotted ovals denote areas of interest.

As discussed in section 6.2.3, surface damage in quasi-statically loaded GFRP specimens could not be accurately identified using DIC or the cumulative thresholding process. Based upon CLT analysis, transverse cracking must have occurred and it was therefore concluded that the transverse cracks were too small to be accurately identified with the white-light imaging setup used. The cracks were also found to form extremely slowly, so allowing the heat release from crack formation to conduct to surrounding areas without a significant rise in surface temperature. The results from GFRP specimens loaded at an intermediate strain rate contrast greatly with these findings. Clearly identifiable bands of high strain and thermal response can be noted across all specimens tested. Since the spatial resolution of the strain data collected at intermediate strain rates is much lower than that collected at quasi-static strain rates, the damage must have become more pronounced and localised due to the increase in strain rate. This agrees well with previous work on FRP materials, as discussed in section 3.3. The ability to identify damage from the IR data using the cumulative thresholding technique is believed to be due to the rapid crack initiation and consequently the rapid release of heat. Thermal conductivity effects, found to dominate at quasi-static strain rates, are much less of an issue and surface temperature rises at the crack location are much higher. The result is that even when using the higher ΔT threshold of 0.5°C, crack induced heating can be identified in the intermediate strain rate tests.

The results gathered from CFRP and GFRP specimens are highly indicative of surface damage. To fully prove the existence of damage, further confirmation studies were carried out using microscopic and computed tomography (CT) analysis.

7.4 Microscopic and Computed Tomography Validation

In the previous section it was proposed that surface damage was resolvable from the DIC and IR data collected. It is clear from the response of these specimens that the strain values recorded across a crack are an order of magnitude greater than the strain errors previously found due to low fill-factor. To validate the results, a microscopic investigation was conducted on a CFRP specimen previously loaded using the interrupted loading methodology. Figure 98 shows a

DIC longitudinal strain plot closest to the point of maximum load. A red line denotes the location at which the specimen cross section was examined. The overlaid speckle pattern has been corrected for camera perspective, as per the procedure discussed in section 2.4.3. Also shown is a plot of vertical displacement and longitudinal strain along the cross section cut.

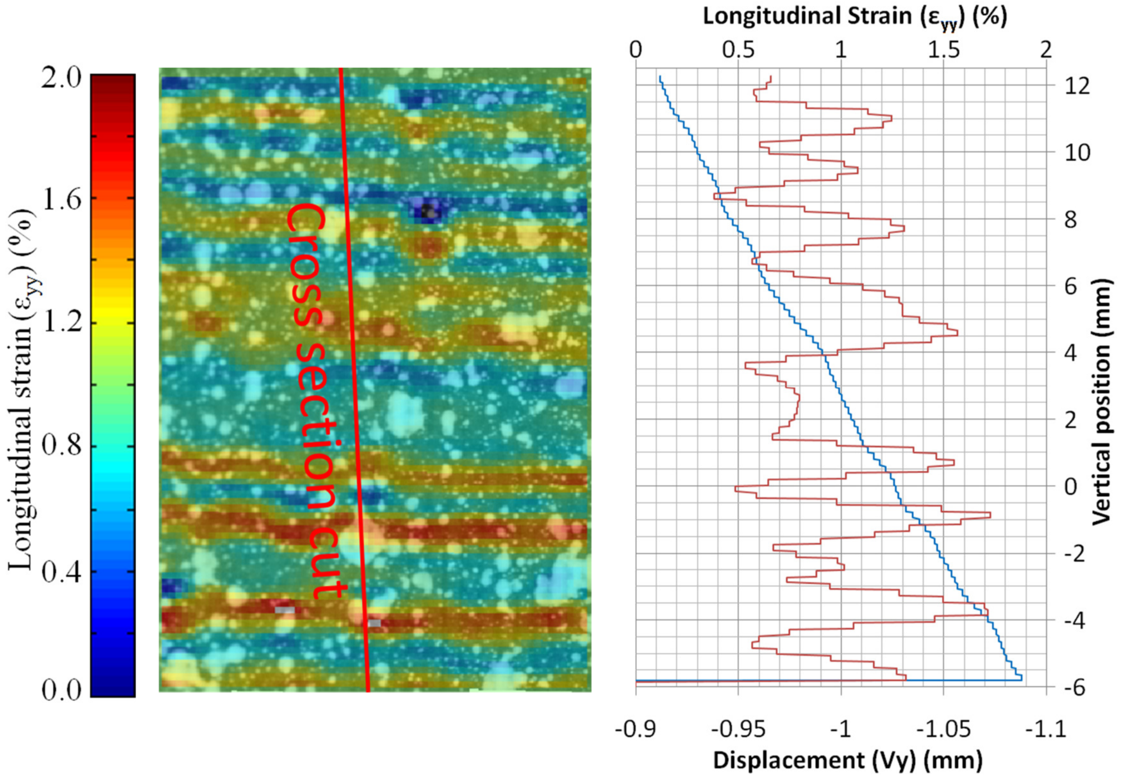

DIC ε_{yy} strain with corrected image overlaid

Plot of displacement and strain along cross section

Figure 98: Plot of longitudinal strain with overlaid raw image (left) of a CFRP specimen loaded at an intermediate strain rate to 70% of UTS showing location of cross sectional cut. Plot of DIC strain (red) and displacement (blue) along cross section line (right).

The displacement data shown in Figure 98 does not show obvious discontinuities that would be indicative of surface cracking. This is believed to be due to low spatial resolution of the strain data.

Prior to cutting the specimen, the surface speckle pattern was examined under an optical microscope. An overview of the specimen area studied is shown in the left hand image presented in Figure 99. Areas highlighted in green are shown magnified further in Figure 100. Figure 99 also shows a plot of the longitudinal strain corresponding to the area under examination, showing the bands of high strain. The specimen was cut using a fine wafering saw and ground to the line shown in Figure 99. The cross section was polished and examined under an optical microscope. An overview of the specimen cross section is shown in the right hand image in Figure 99 with areas highlighted in green shown at greater magnification in Figure 101.

Although difficult to distinguish in areas covered only by matt black paint, surface cracks could be noted when crossing a white speckle. Surface cracks were found at each of the highlighted areas shown in Figure 100. The locations of the surface cracks were found to match well with the regions of high strain in the DIC data. To confirm that the surface cracks are not just present in the paint layer and continue into the composite material itself, the specimen cross section was analysed. Where each band of high strain was located, a transverse crack was found which penetrated fully through the surface 90° layer and terminated at the first 0° layer. The images in Figure 101 show two examples of such cracks at two different magnifications. An interesting finding is that the crack in the area marked E was found to penetrate through the 90° layer and also the paint coating, whereas the crack in image G was found to form in the 90° layer but not continue through the paint coating. Regardless of this, both cracks were clearly resolvable through the use of DIC, proving that the optical methodology used at intermediate strain rates is correctly identifying damage in the surface lamina of FRP material.

To further validate the optical measurements, an X-ray CT scan was carried out on a CFRP specimen loaded to 72% of its UTS using the interrupted loading methodology.

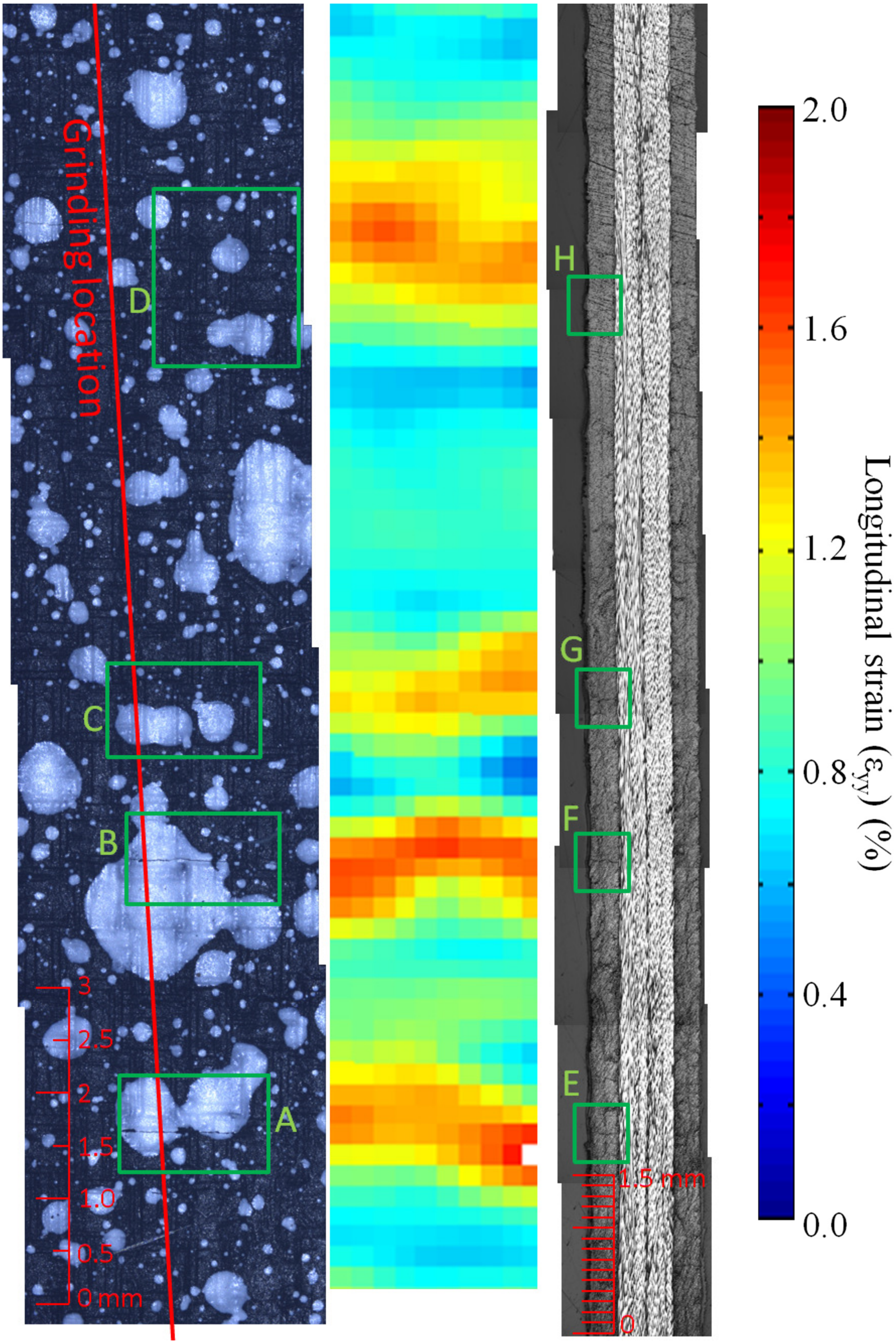

Specimen surface DIC ε_{yy} strain Polished cross section

Figure 99: Overview of the microscopic analysis conducted on a CFRP specimen loaded to 70% of its failure stress at an intermediate strain rate.

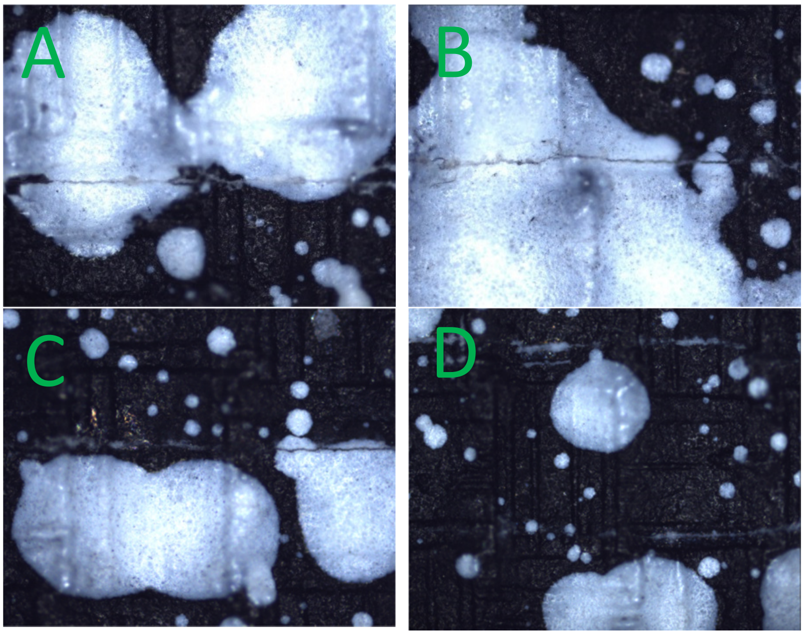

Figure 100: Microscopic images of the surface of a CFRP specimen prior to cutting for cross section analysis (341 µm/pixel). See Figure 99 for image locations.

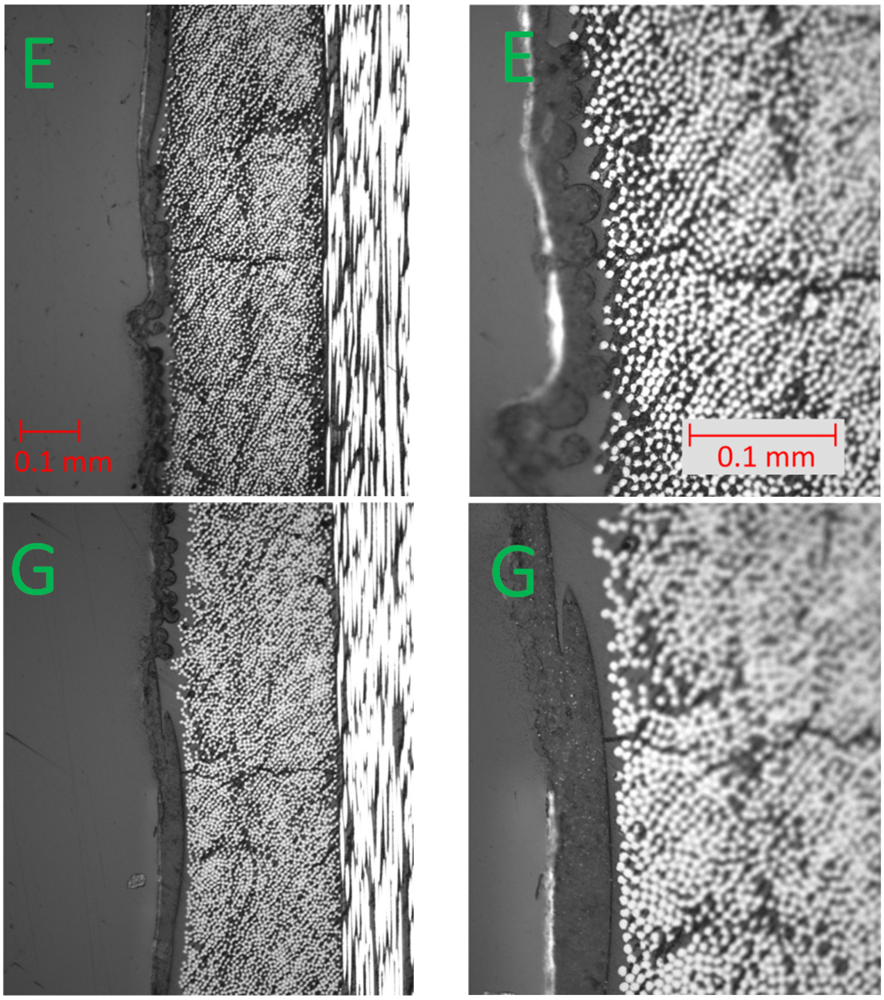

Figure 101: Microscopic images of the cross-section of a CFRP specimen showing the presence of transverse cracks. 0.340 µm/pixel (left images) and 0.138 µm/pixel (right images) See Figure 99 for cross-section location and individual image locations.

The CT scan was conducted using a custom 225 kV Nikon/Metris HMX ST machine operating at 60 kV. 3143 radiographs of 2000 x 2000 pixels were taken at 0.115° angular steps. After 3D reconstruction, voxel sizes of 10.1 μm were obtained. Figure 102 shows a vertical section of DIC longitudinal strain data at the time of maximum load and a CT scan image through the specimen thickness at the cross section location shown. Strain data has been plotted at the initial subset location, i.e. the strain map does not deform with applied loading. This allows the data to be compared to the unloaded specimen in the CT scan image. Any residual deformation due to the onset of damage will still exist in the specimen.

Due to the relatively low spatial resolution of the CT data compared to the previous microscopic analysis, cracks were more difficult to identify. Cracks highlighted in red at areas a, c and d in Figure 102 were found to match well with the locations of high strain. However, a possible crack highlighted in blue within area d was also found which does not correspond to an increase in strain. Similarly, multiple cracks inside area b are apparent in the CT data but not in the DIC strain data. Higher spatial resolution CT data is therefore required to be confident of the identification of transverse cracking in this specimen.

Despite the CT data not being able to fully confirm the presence and location of damage to validate the DIC and IR measurements, the optical microscopy conducted has been able to accurately confirm the existence of damage at the locations predicted. The combined white-light and IR methodology can therefore be considered as a validated methodology for identifying damage during intermediate strain rate loading.

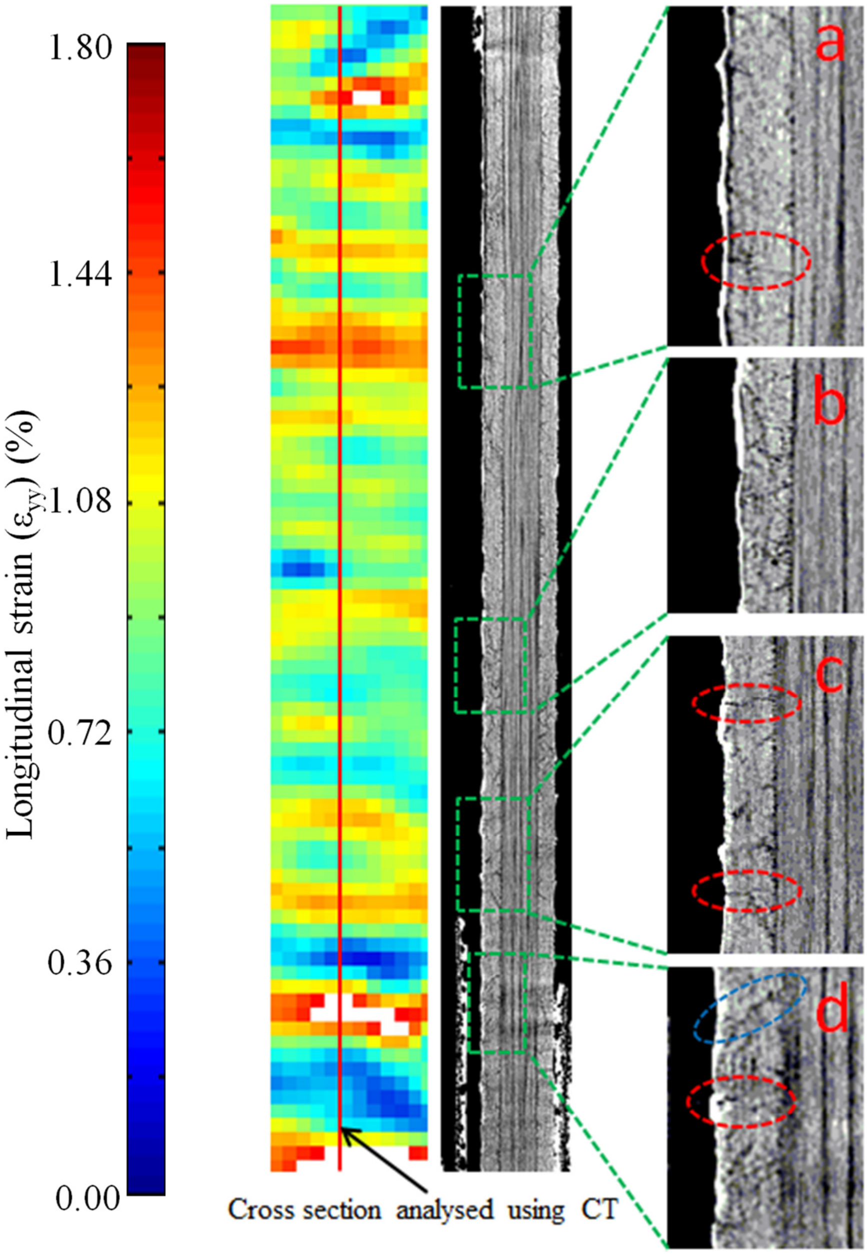

Figure 102: Comparison of DIC strain (at point of maximum applied load) to a CT scan image taken at the cross section location shown for a CFRP specimen loaded using the interrupted loading methodology. Regions of interest are highlighted in red.

7.5 Summary

The chapter has described the development and validation of an experimental methodology for applying a purely tensile intermediate strain rate load to FRP specimens. The imaging methodology established in Chapter 6 is successfully transferred to use with high speed cameras, enabling the identification of surface damage in FRP materials during intermediate strain rate interrupted loading. Whilst the damage response of CFRP specimens were found to be relatively unchanged by an increase in strain rate, GFRP specimens exhibited a more localised damage response at higher strain rates. Such damage was proven using optical microscopy and X-ray CT analysis. As expected, it was found that the IR thresholding procedure is better suited to the identification of damage at higher strain rates, due to thermal conductivity effects.

Chapter 8

Combined TSA and DIC for Assessment of Damage Propagation

8.1 Introduction

The development of an experimental methodology combining the techniques of DIC and TSA for the identification of damage propagation in FRP material under cyclic loading is described. The use of the two techniques allows the collection of surface strain and stress sum data, so giving greater insight into how damage propagates in FRP. Unlike point measurement methods, the full-field techniques allow damage to be identified across an entire surface without prior knowledge of the material behaviour, as demonstrated successfully in Chapter 6. The chapter focuses on establishing the experimental methodology and includes example data collected from GFRP and CFRP specimens. It is envisaged that the methodology will provide a new approach to investigating the damage behaviour of FRP components under fatigue loading, enabling the production of damage tolerant and more efficient structures.

As discussed in section 2.7, TSA requires the application of a cyclic load and so is inherently suited to the study of materials under fatigue loading. For adiabatic conditions, the FRP material must be cyclically loaded at around 5 – 10 Hz. The CEDIP Silver 480M camera is capable of imaging full-frame at a frequency of 383 Hz, more than sufficient for sampling at this loading frequency. Capturing white-light images during a fatigue load requires considerably more effort. A simple and data-efficient solution is to pause the fatigue loading at the peak load and collect a single white-light image. This approach is labour intensive and may cause greater damage due to the extended dwell time at high load. It was therefore deemed crucial to establish an automated means of capturing IR and white-light image data, suitable for DIC, without pausing the fatigue test and without any user interaction.

A potential solution is to use high speed white-light cameras to collect a series of images throughout a loading cycle. Post-processing is then required to identify the image at the peak load. Given that the exposure time is maximised and that a specimen is loaded at 10 Hz, an imaging frequency of at least 200 Hz would be required to be certain of capturing a full image exposure above 95% of the peak load. As only the image at the peak load point is of interest, the vast majority of images are collected unnecessarily, wasting computer resources. Also, since the spatial resolution and quality of DIC data relies heavily on the size and quality of the images used, it is highly advantageous to use higher resolution CCD cameras where possible. The use of CCD based cameras with a high fill factor also eliminates the majority of the DIC systematic errors previously discussed in Chapter 5, if the correct interpolation algorithm is used. Since high resolution CCD cameras generally have a low frame rate, accurate timing is necessary to capture images at exactly the peak load in a cycle. A further benefit of using a methodology based around low-frame rate CCD cameras rather than high speed cameras is the decreased cost, allowing the methodology developed to be more accessible to future users.

8.2 Automating Image Capture

Where out of plane motion is negligible, the use of a single white-light camera and 2D DIC is preferred due to the increased in-plane displacement vector accuracy [17]. A methodology was therefore investigated using the CEDIP 480M IR camera in conjunction with a single white-light camera. However, since both the IR and white-light sensors need to be parallel with the specimen surface it would be necessary to use a mirror/beam splitter. Trials used a similar set-up to Bodelot *et al* [197], employing a mirror/filter to allow the majority of IR wavelength light to pass but reflecting visible wavelengths. The methodology was not adopted due to tolerances in mirror flatness causing large image distortions, which could not be removed using the DIC calibration procedure. Therefore it was decided to use a calibrated stereo camera system to obtain images for DIC, whilst the IR camera remained nominally perpendicular to the specimen surface.

A system is required that can automatically and repeatedly capture a set of IR images and a set of white-light images at the point of maximum load during fatigue loading. National Instruments LabView 9.0 was used to develop the automated system in conjunction with a National Instruments USB-6211 data acquisition input/output device and a set of two Manta G-504B 5 MPixel white-light cameras manufactured by Allied Vision Technologies. LabView was used as it is compatible with this camera type and features a variety of Virtual Instruments (VI's) specifically for the control of digital cameras. The addition of the USB-6211 device allows test machine voltage data to be collected and trigger signals to be sent to cameras as required. An overview of the USB-6211 and Manta camera specifications are presented in Table 18 and Table 19 respectively.

Device Model	Differential Analogue Inputs	Analogue Outputs	Output Slew Rate	Max Sampling Rate	Resolution	Digital Inputs/Outputs
USB-6211	8	2	5 V/µs	250 kS/S	16 bit	4

Table 18: Overview of National Instrument USB-6211 device specifications [198]

Camera Model	Pixel Size	Sensor Type	Image Size	ADC	Maximum Frame rate	Exposure time range
Manta G-504B	3.45 x 3.45 µm	SONY IT CCD ICX655AL/AQ with microlenses	2452 x 2056 pixels	14 bit	9 Hz	38 µs to 60 s

Table 19: Overview of Allied Vision Technologies Manta G-504B camera specifications [199]

The test machine was set to operate in load control such that the load range and mean load remain nominally constant throughout, regardless of damage onset in the FRP specimen. The code was implemented by first defining in LabView the cycle numbers where the data collection section of code is executed. A simpler code implementation could use test time as the trigger, but this is dependent on the accuracy of the test machine loading frequency. Hence, loading cycles were counted by offsetting the mean load signal to give a sinusoidal voltage signal about zero. This signal was then sampled using one of the analogue inputs of the

USB-6211 device, smoothed and when a change in gradient is detected a loading cycle is recorded.

Upon execution of the camera trigger code, the USB-6211 device outputs a 5V TTL pulse to the IR camera to begin the recording of an IR video for later TSA analysis. At this point, test machine data is also collected across a variety of channels and recorded as a text file. Next, the code triggers the stereo set of Manta cameras. Accurate triggering of the Manta cameras was found to be the most challenging aspect of the combined TSA/DIC methodology.

Execution of the standard LabView camera triggering VI was found to operate using the process timing of the Windows operating system. Image timing was therefore found to be highly unpredictable. An alternative methodology was therefore explored to ensure images are captured at the maximum load point.

A simple zero-crossing detector circuit was developed to produce square pulses whenever the load signal rises above 0 V. A circuit diagram of the zero crossing detector is shown in Figure 103. The circuit uses simple solid state electronics and as a result has an extremely fast response time of the order of several microseconds.

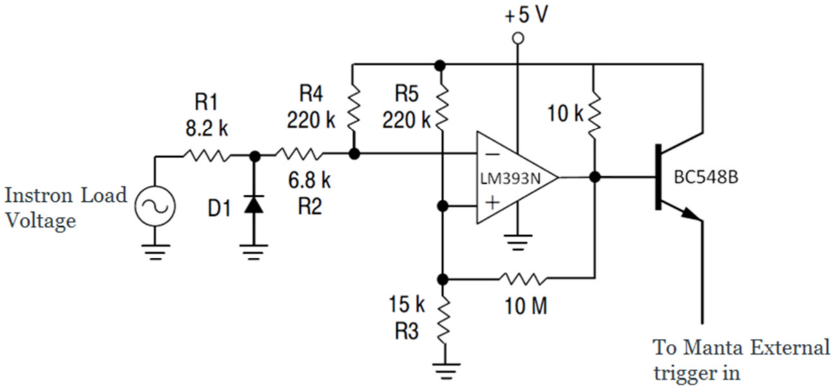

Figure 103: Circuit diagram of zero crossing detector

Although the circuit continues to send trigger pulses to the cameras throughout the test, the LabView code instructs the camera to only become receptive once the desired cycle number is reached and after the IR camera has been triggered. Each time the data collection code is executed, the cameras capture two images, the first at the minimum load point and the second at the maximum load point. For each image, the Manta cameras wait in two stages; the cameras initially wait for the next rising edge from the zero-crossing detector and once received, the camera waits an additional time of approximately of 0.25 or 0.75 cycles before image exposure to collect minimum and maximum load images respectively. The exact wait time of the second stage is pre-calculated by the LabView code based on loading frequency and exposure time, such that the centre of the image exposure occurs at exactly the max load point. As the execution time of the LabView code is variable the exact cycle number at which the minimum and maximum load is unknown but typically occur within 8 and 26 cycles respectively after the triggering of the IR camera. Figure 104 shows the successfully working methodology with the centre of the image exposure occurring at the point of maximum load. It should be noted that short exposure times are still required to minimise image blurring, the value of which is dependent upon the loading frequency.

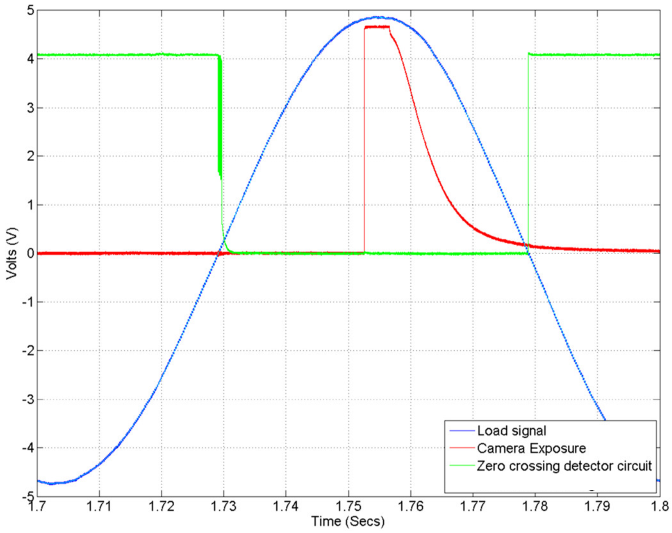

Figure 104: Example data showing image exposure at the point of maximum load

The image timing was validated by cyclically loading a specimen using an Instron 8802 servo-hydraulic test machine at a frequency of 5 Hz. The machine was set to operate in load control with amplitude control set to off, thus ensuring maximum accuracy in applied frequency. Load and camera exposure voltages were sampled using a Picoscope 4424 oscilloscope operating at 6 MHz sampling rate. Load data was smoothed using a 1000 point moving average. The time difference between maximum load and the centre of exposure was then calculated. The results are given in Table 20. The timing of the images was found to be more than satisfactory with the worst error case of +0.773 ms equating to 99.8% of the maximum load. The methodology can therefore be applied to tests conducted at much greater loading frequencies. It should be noted that greater timing errors were found when using badly auto-tuned or cold test machines. This is due to the inability of the test machine to apply an accurate sinusoidal load. A similar timing study was conducted to assess the variation of image timing between Manta cameras. As both cameras are triggered from the same zero-crossing detector, the image timing errors with respect to one another were found to be below 1 μs.

Trial Number	Image Timing Error (ms)		Trial Number	Image Timing Error (ms)	
	Min Load	Max Load		Min Load	Max Load
1	0.06400	-0.28900	11	0.16700	0.31500
2	0.09600	0.77300	12	-0.00800	0.26700
3	-0.11700	-0.18800	13	0.13900	-0.18600
4	0.39100	0.58900	14	-0.20900	-0.09200
5	0.30200	-0.32600	15	0.39600	-0.07400
6	-0.03100	-0.67900	16	-0.11300	-0.23500
7	-0.09700	-0.38300	17	-0.10200	-0.11900
8	0.19400	0.39200	18	0.31400	-0.23800
9	-0.11700	0.24300	19	-0.10000	0.20400
10	-0.11200	-0.09800	20	-0.10000	-0.42100

	Image Timing Error (ms)	
	Min Load	Max Load
Mean error	0.056	-0.007
Error range	0.605	1.452
Standard deviation	0.192	0.364

Table 20: Manta Camera triggering timing validation trials

8.3 Development of TSA Methodology

Whilst epoxy based composite materials have a sufficiently high emissivity to not require a paint coating for TSA analysis, the DIC technique still requires use of a paint coating to give sufficient surface contrast. An extensive analysis of the effect of paint coating type and thickness on TSA measurements was conducted by Robinson *et al* on aluminium and steel specimens [16]. The study found that RS matt black paint gave the most consistent thermoelastic signal and that two to three passes (equivalent to 15 to 25 μm coating thickness) combined with a loading frequency of between 5 and 15 Hz was optimum for TSA analysis. These recommendations are only applicable to metallic materials and their use on FRP materials requires further verification.

As previously discussed in section 2.7, the TSA relationship shown in equation 2.28 assumes that temperature changes occur adiabatically, i.e. no heat conduction occurs. This is most commonly achieved by cyclically loading a material at a frequency between 10 and 30 Hz, although other factors may also influence the loading frequency required for adiabatic conditions [19].

A study was therefore conducted into the required loading frequency to achieve adiabatic conditions for the GFRP and CFRP crossply specimens previously discussed in Chapter 4. Specimens were coated in two passes of RS matt black paint followed by a light coat of Ambersil matt white paint to create a DIC speckle pattern. A specimen prepared in a similar manner and examined under an optical microscope was found to have a paint coating thickness varying between 15 and 40 µm. The large variation of paint thickness is due to the high surface roughness of the FRP material; an artefact of the peel-ply fabric required during manufacture. A GFRP and a CFRP specimen were cyclically loaded at 87 ± 69.6 MPa and 109 ± 87.7 MPa respectively over a range of frequencies. The specimens were imaged using a CEDIP Silver 480M IR camera operating at 383 Hz and 1300 µs integration time. IR videos were processed in the TSA software Altair LI 5.90 produced by CEDIP. The mean thermoelastic temperature rise (*ΔT*) over the specimen area is plotted against loading frequency in Figure 105. The CFRP specimen tends towards a *ΔT* value of 0.162 ºC at frequencies above approximately 4 Hz, whilst the GFRP specimen tends towards a *ΔT* value of 0.31 ºC above 4 Hz. The GFRP specimen exhibits a slight decrease with greater loading frequencies. This is believed to be caused by damage occurring homogenously over the outer 90º ply, decreasing the thermoelastic response. It is recommended that any future work repeat this frequency analysis on the GFRP specimens at lower stress levels. Based on these trials, cyclic loading was kept at or above 5 Hz for all tests conducted.

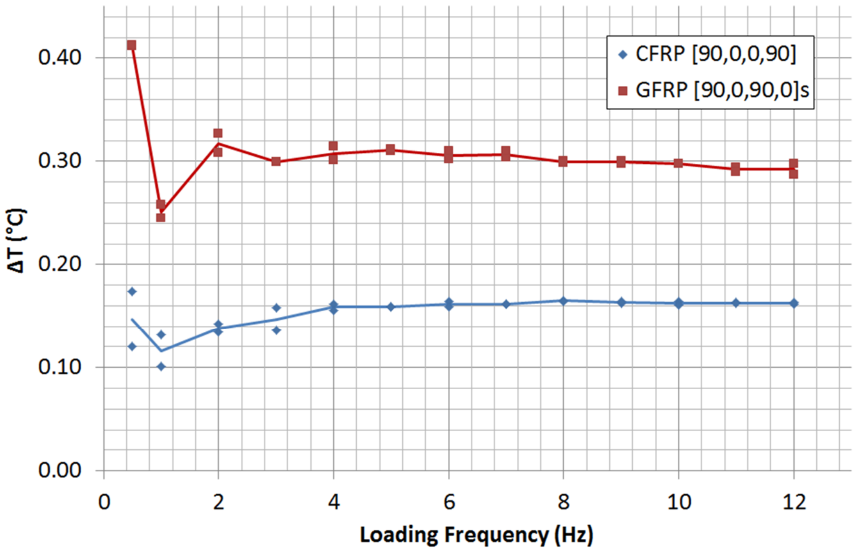

Figure 105: Effect of loading frequency on the thermoelastic response of speckle patterned CFRP and GFRP specimens

8.3.1 Motion Compensation Procedure

A consequence of applying a strain to a material is that any given area on the material surface will undergo rigid body motion. Rigid body motion during the recording of an IR video is detrimental to TSA analysis as the incident IR radiation of individual pixels becomes a combination of the original sampling area and surrounding areas. The motion effect only becomes apparent when the spatial resolution is sufficiently high, and according to Fruehmann [52] needs only be applied when a high magnification G1 lens is used.

A minimum stand-off distance of 200 mm was required for the IR camera to avoid blocking the optical path of the white-light cameras. As a result, only the 27 mm lens could be used. Despite use of a lower magnification lens, it was found that motion compensation was still required due to the large cyclic deformations applied and the relatively high spatial resolution.

Motion compensation was performed using the ‘Random Motion’ 5.90 software by CEDIP. The software is able to compensate for translation, rotation and deformations in an IR video [52]. The algorithm requires that two markers of high IR contrast are located on the material surface, ideally at the top and bottom of the image. The translation and rotation of these points is then tracked in all images in the movie sequence. The software uses this information to interpolate the translation, displacement and rotation of all pixels in the image and for every image in the sequence. This data is used to move and distort the image sequence to subpixel accuracy such that the surface appears stationary with respect to the first image in the sequence. The exact interpolation algorithm used is not documented.

When using the triggering methodology developed in 8.2, the IR camera begins recording at an arbitrary time within a loading cycle. As the motion compensation is with reference to the first image in the sequence, any two motion compensated IR videos are likely to be with reference to different load values. For this reason, all IR videos collected were cropped to start at the image closest to the first maximum load point by study of the load cell voltage recorded with IR images.

As the quality of the motion compensation procedure is highly dependent on the sharpness of the tracking points used, the most suitable method for producing tracking marks was investigated [52]. Pencil, Tippex, ball-point pen and self-adhesive aluminium foil markings were trialled on a cyclically loaded specimen, as shown in Figure 106. Whilst the small size of the Tippex, pencil and pen markings gave a small marking and less wasted image area, it was found that the greater emissivity difference of the aluminium foil markings gave the most stable video after motion compensation and was subsequently used for all future tests. The self-adhesive aluminium foil, most commonly used for electrical and thermal shielding, was found to remain well adhered to the specimen surface even after the application of in excess of one million loading cycles.

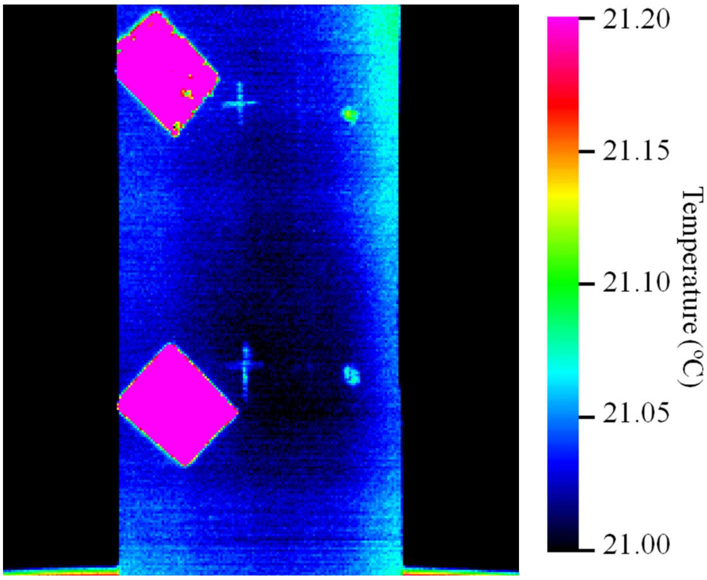

Figure 106: IR image of motion compensation reference mark trial, showing aluminium foil (left), pencil lead (centre left), ballpoint pen (centre right) and Tippex (right) markers.

Motion compensation can have a large effect on the ΔT maps after TSA has been applied even when using the 27 mm lens, as shown in Figure 107. Cracks that were previously unresolvable in the lower portion of the specimen where there is the most displacement become well defined and overall noise is much reduced.

As the motion compensated TSA data is with reference to the point of maximum load, the data is directly comparable to DIC strain data which is also taken at the point of maximum load. Further motion compensation using the DIC displacement data, as outlined in the method developed in section 6.2.2, is therefore not required.

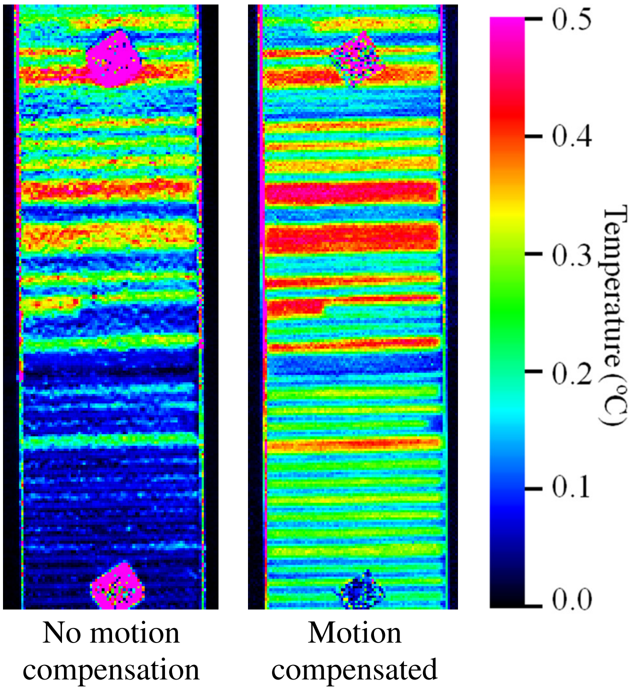

Figure 107: TSA processed ΔT maps of a damaged CFRP specimen, showing the effect of motion compensation.

8.4 Damage Propagation in Previously Undamaged Crossply CFRP Specimens

Having established a methodology for collecting TSA and DIC data during cyclic loading, the procedure was applied to the fatigue loading of previously undamaged CFRP specimens with the aim of capturing the full-field evolution of surface damage. It should be noted that the primary aim of the thesis is to establish the experimental methodology rather than the collection of extensive material data on damage propagation behaviour. As such, tests are primarily aimed at proving a working methodology.

CFRP specimens, previously described in Chapter 4, were cyclically loaded under tension-tension fatigue in an Instron 8802 servo-hydraulic test machine operating in load control. The tests were conducted overnight and ran for approximately 14 hours. The specimens were undamaged prior to application of the cyclic load. A summary of loading conditions and data collection intervals is presented in Table 21. Damage was expected to occur more rapidly during the initial stages of fatigue life, as discussed in Chapter 3, hence data was collected more frequently during the initial 10000 cycles. The applied cyclic load gives a peak stress of 570

MPa, equivalent to 53% of the material UTS. Illumination was provided by the larger LED array, as discussed in more detail in Appendix C. A summary of the camera settings used is presented in Table 22.

Specimen	Mean Stress	Cyclic Stress Amplitude	Frequency	Loading Cycles	Data collection intervals	
					< 10000 cycles	> 10000 cycles
$[90,0]_S$ CFRP	300 MPa	270 MPa	5 Hz	250000	Every 500 cycles	Every 5000 cycles

Table 21: Test summary for previously undamaged CFRP specimens

Camera	Image size (pixels)	Imaging area on specimen (mm)	Spatial resolution (mm/pixel)	Imaging frequency (Hz)	Images captured	Exposure/ integration time (μs)
2 x AVT Manta G-504B	2452 x 2056	19.96 x 28.92	0.014	N/A	1 at min load 1 at max load	900
1 x CEDIP Silver 480M	320 x 256	19.96 x 67.23	0.261	383	600	1300

Table 22: Camera settings for tests conducted on undamaged CFRP specimens

Prior to each test, two sets of reference images were taken of the specimen at zero load. In addition to the markers used for motion compensation, a piece of self-adhesive aluminium foil was attached to the centre of the specimen. IR and white-light images were subsequently taken to give a known datum point in both sets of data, allowing the two datasets to be aligned during post processing. The foil was then removed and another set of white-light images taken. These images were used as the reference images for later DIC analysis. A set of IR and white-light reference images are shown in Figure 108 showing the overlapping imaging areas. The IR camera was situated as close to the specimen as possible to remain in focus using the 27 mm lens.

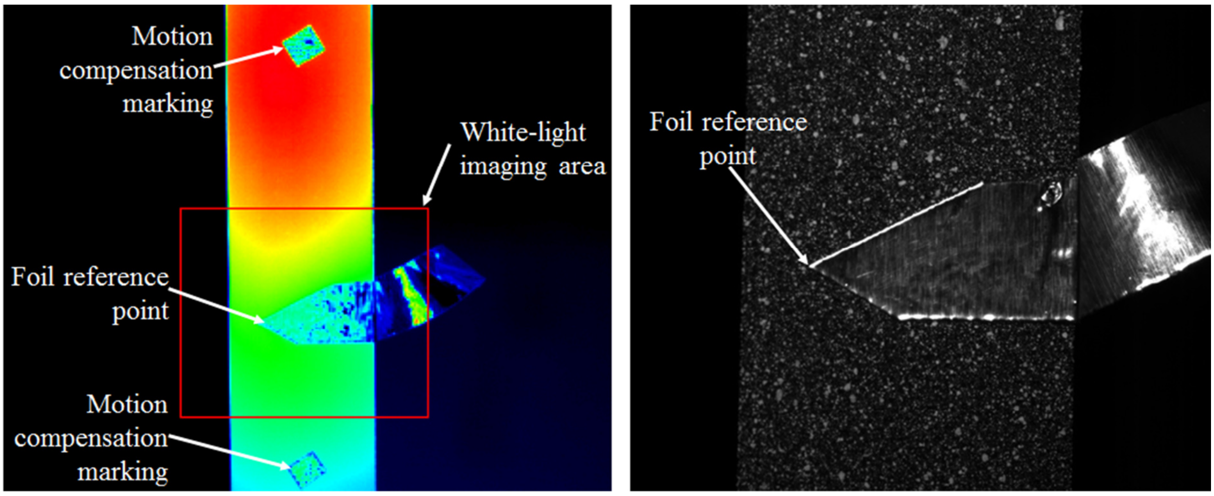

IR reference image

White-light reference image

Figure 108: White-light and IR reference images taken prior to loading of a CFRP specimen

White-light images were processed in DaVis 8.1 using a cell size of 31 x 31 pixels, a step size of 6 pixels and a 6th order spline subpixel interpolation method. IR videos were motion compensated using the procedure discussed in 8.3.1 and TSA processed using Altair LI 5.90. A Matlab code was developed to plot DIC and TSA data at the correct spatial locations. Any strain data exported from DaVis is plotted at the reference cell locations, making the strain data appear static throughout a test. The code developed therefore uses the DIC vertical and horizontal displacement vectors to shift the DIC strain data to their correct spatial location for each image. Using the foil as a point of reference, a 2D grid of IR pixel locations is next calculated using the same coordinate system as the DIC data, so allowing the TSA and DIC data to be overlaid.

Maps of longitudinal (ε_{yy}), horizontal (ε_{xx}) and shear strain (ε_{xy}) were calculated via DIC analysis for each of the data sets collected. Maps of thermoelastic temperature change (ΔT), mean temperature (T_m) and phase were calculated via TSA analysis for each of the sets of data collected during the fatigue test. ΔT data was divided by the mean temperature T_m at each pixel location to give a normalised thermoelastic response ($\Delta T/T_m$). This procedure compensates for changes in absolute temperature on the specimen surface that may occur due to changes in room temperature or local heating arising from damage [18]. It should be noted that the thermoelastic constants K_1 and K_2 were not evaluated and as such, the $\Delta T/T_m$ data is proportional to the sum of the principal stresses, as given by equation 2.28. The normalised thermoelastic data maps were further processed to investigate how the thermoelastic response of each pixel changes with time using the formula:

$$\Delta\left(\frac{\Delta \mathrm{T}}{T}\right) = \left(\frac{\Delta T}{T}\right)_n - \left(\frac{\Delta T}{T}\right)_{n-1} \qquad 8.1$$

where ΔT is the thermoelastic temperature change, T_m is the mean temperature and n is the data set number.

Selected full field data from all data types are presented in Figure 109 across the entire fatigue test. The normalised thermoelastic response ($\Delta T/T_m$) and longitudinal strain maps (ε_{yy}) from the first, second and sixth data sets collected are shown at higher magnification in Figure 110. Despite the first data set being collected after just 10 loading cycles, it is obvious that significant damage has already occurred to the surface *90º* layer. Multiple horizontal lines of high strain, evident in the longitudinal strain map, were found to match spatially with horizontal lines of reduced thermoelastic response. Such behaviour is expected to occur as DIC records the crack opening displacement as an increase in longitudinal strain whilst TSA measures a decreased thermoelastic response as the cracked surface layer has a reduced load-bearing capability and therefore carried less stress.

Most cracks formed across the entire specimen width within the 500 loading cycle interval between data collection. Examples of slowly propagating transverse cracks are highlighted inside the boxes shown in Figure 110. Between 500 and 3000 cycles a crack initiates from the left edge, whilst a pre-existing crack propagates by approximately 1.8 mm. In subsequent images the two cracks are shown to coalesce.

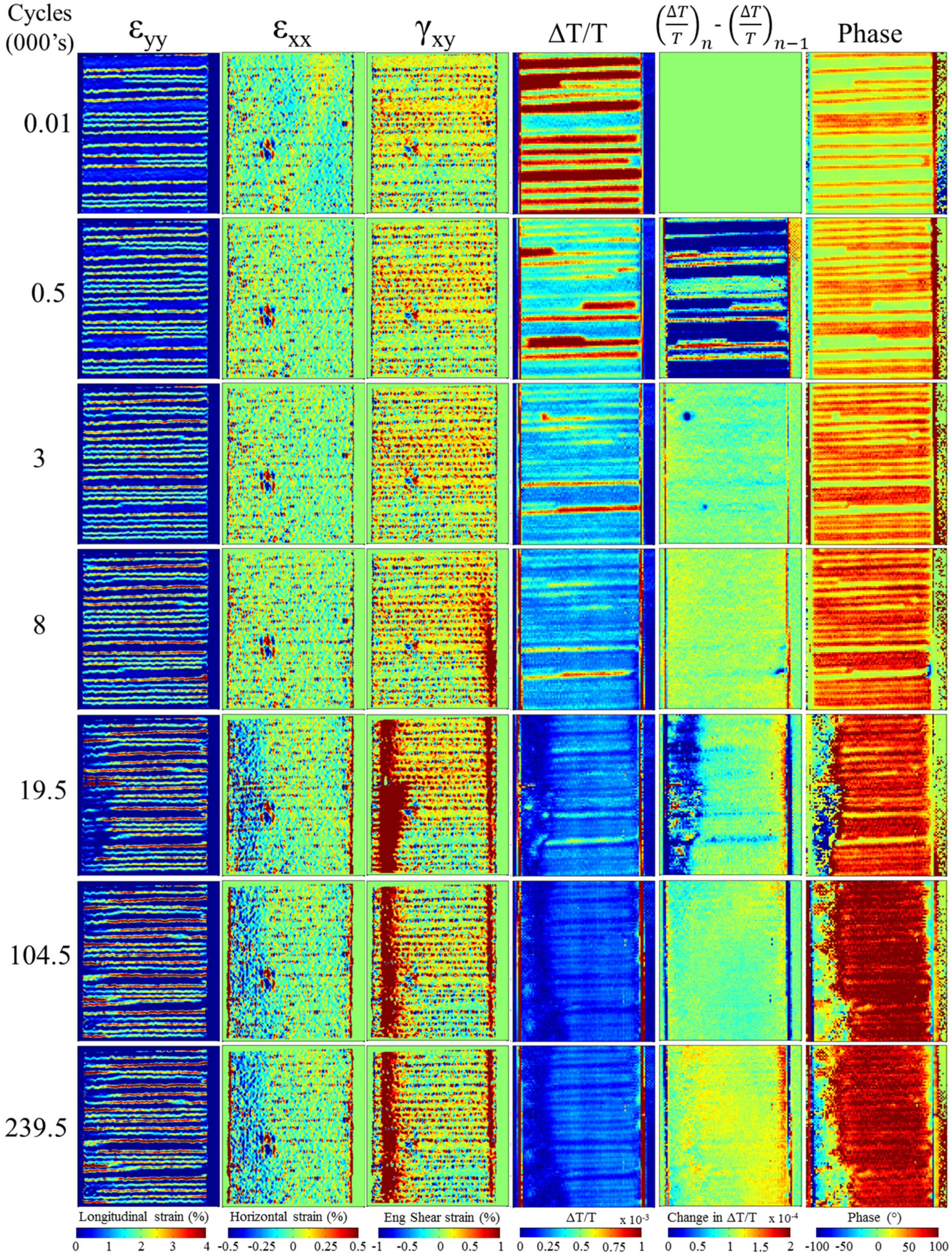

Figure 109: Full-field data collected during the fatigue loading of a previously undamaged crossply CFRP specimen

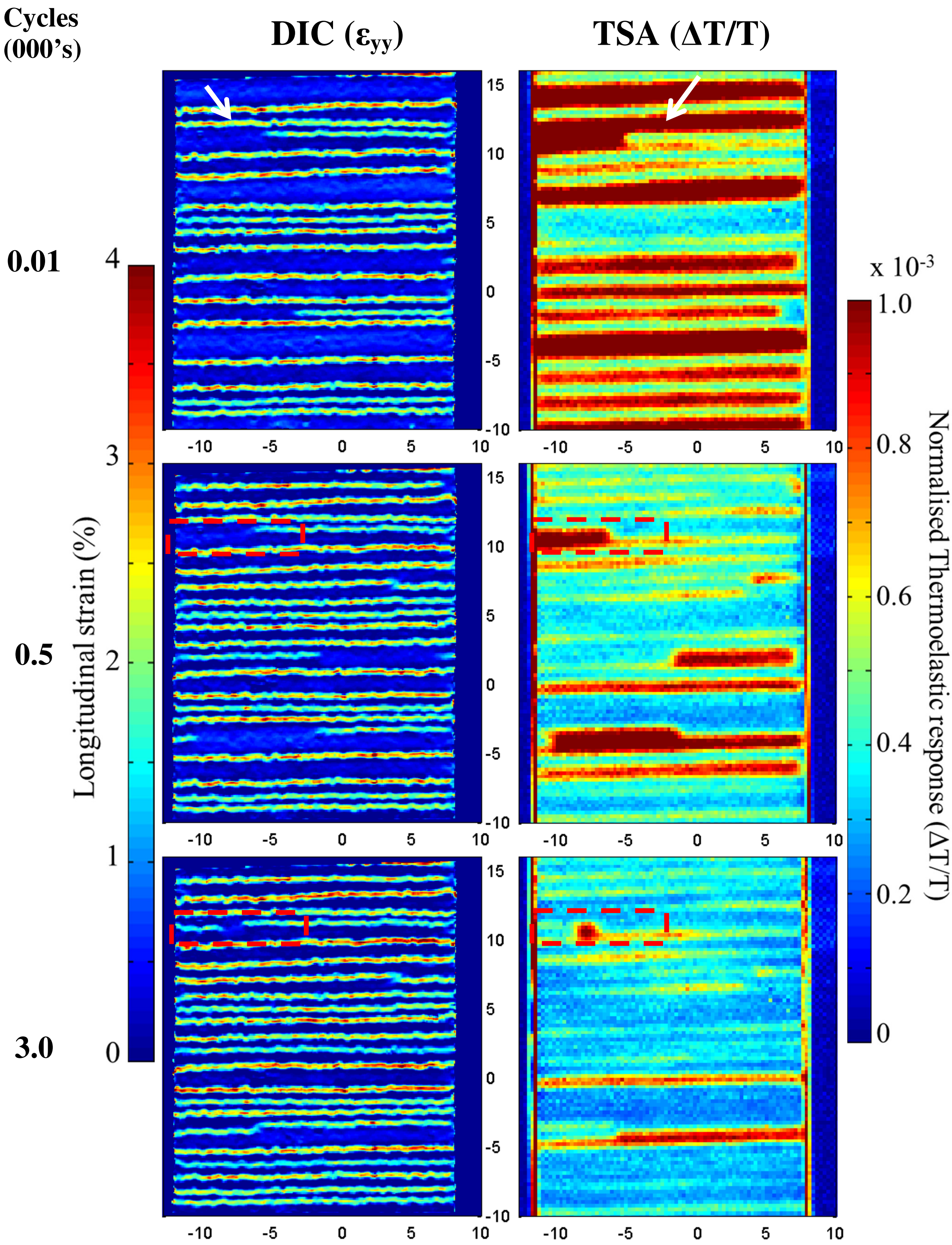

Figure 110: Development of longitudinal strain (ε_{yy}) and normalised thermoelastic response ($\Delta T/T$) during the early fatigue life of a previously undamaged crossply CFRP specimen.

Although such damage evolution was found to generally agree well between the DIC and TSA data, there were some exceptions. One such instance is highlighted by the set of white arrows in the first data set collected in Figure 110, whereby a crack evident in the strain data occurs at a band of high thermoelastic response. In the next data set the crack is evident in both data sets. This erroneous behaviour can be explained by consideration of the image timing.

The IR camera is triggered first and continues to record images over approximately 8 loading cycles. The triggering methodology next collects a set of white light images at the minimum load point followed by a set of white light images at the maximum load point. Whilst the minimum load images are captured within the time period of the IR video, the maximum load images are captured approximately 15 cycles later. This delay allows time for further damage to occur, so causing an apparent difference in surface response. Transverse crack saturation is reached at around 6000 cycles. After which, a region of low thermoelastic response can be noted to form at the bottom of the data map at the right specimen edge. Between 6000 and 9500 cycles this region spreads upwards. Between 14500 and 19500 cycles a similar behaviour can be noted at the left specimen edge. The TSA phase and DIC shear strain (ε_{xy}) maps were studied for further information on this behaviour, a selection of which are presented in Figure 111.

Under adiabatic conditions the phase map will display either 0º or 180º, indicating areas of compression or tension. Non-adiabatic conditions, such as at locations of damage cause a shift in the phase angle of the IR signal. Phase maps were initially shifted by 180º such that areas experiencing an applied tensile load appear as 0º phase, as is expected from areas of undamaged material. Undamaged areas of specimen in the first data set were found to be approximately 20º out of phase with the load signal. This offset remains constant throughout the test and is due to a combination of delays arising from the test machine, load cell and IR camera [52]. Unlike other TSA systems, this offset is not calibrated for before a test and was therefore corrected for in Matlab by shifting all phase values by -20º. In FRP specimens, frictional heating between damaged layers or crack surfaces takes a finite time to conduct to the surface, causing a phase change in the recorded IR signal.

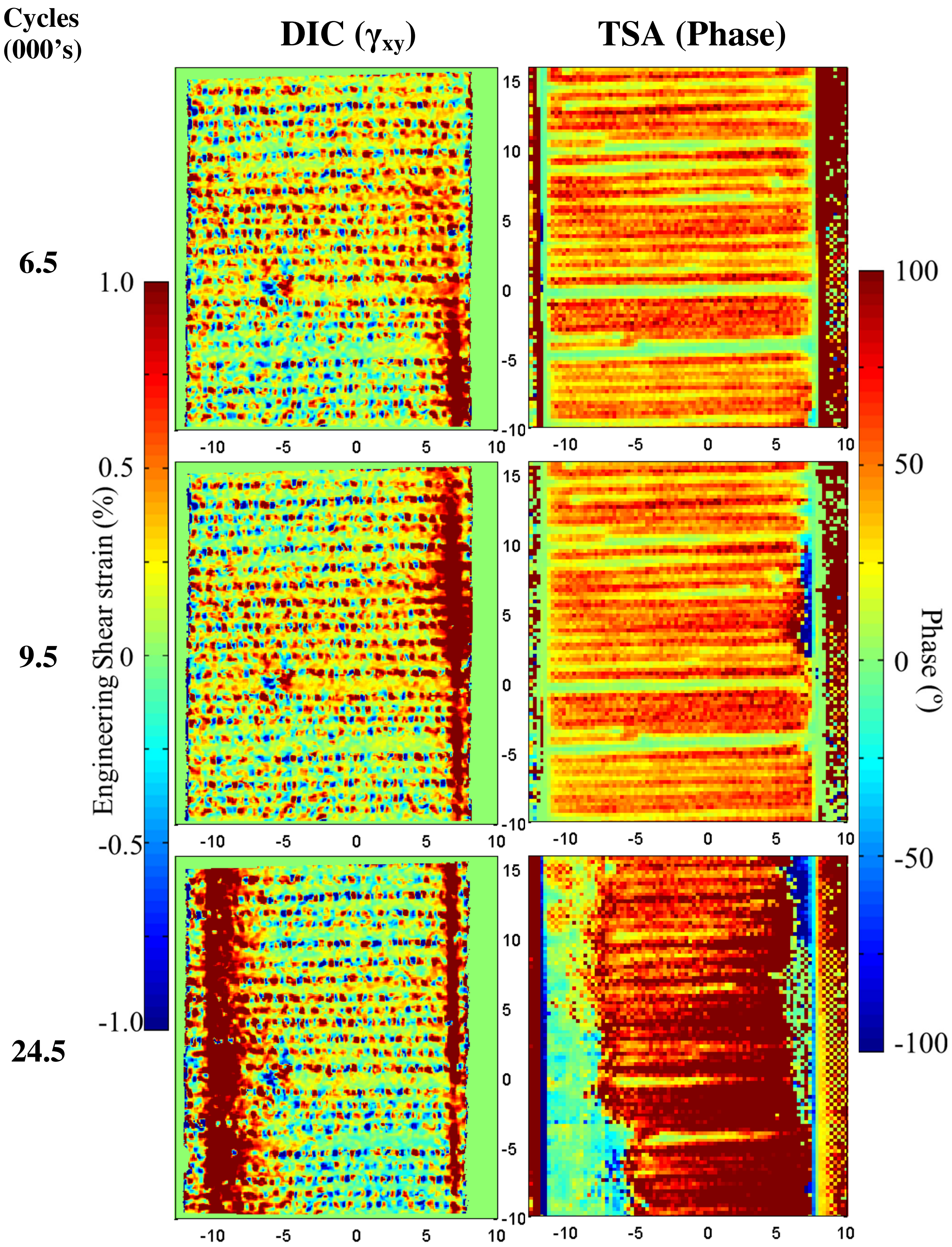

Figure 111: Development of shear strain (ε_{xy}) and TSA phase during the fatigue of a previously undamaged crossply CFRP specimen.

Whilst some undamaged patches of material remain at 0° phase at 6500 cycles, the majority of the specimen surface is out of phase, indicating widespread surface damage. From 6500 cycles onwards, a change in in the response occurs. Between 6000 and 9500 cycles, an area of negative phase propagates vertically from the bottom of the image at the right edge of the specimen. This behaviour coincides with regions of high shear strain shown by the DIC. Between 14500 and 19500 cycles a similar response occurs at the left specimen edge. The change in response is consistent with delamination damage propagating from the free edge of the specimen, which is a dominant failure mode in cross ply laminates caused by the free edge effect as discussed in detail in section 3.2.4. Further evidence of delamination was found in the DIC out of plane displacement measurements. Figure 112 presents the change in out of plane displacement (ΔV_z) between 9500 and 24500 cycles. A region at the left specimen edge shows an increase in displacement, as would be expected from a delamination. To confirm if delamination is taking place in these regions a CT examination was carried out, as described in section 8.4.1.

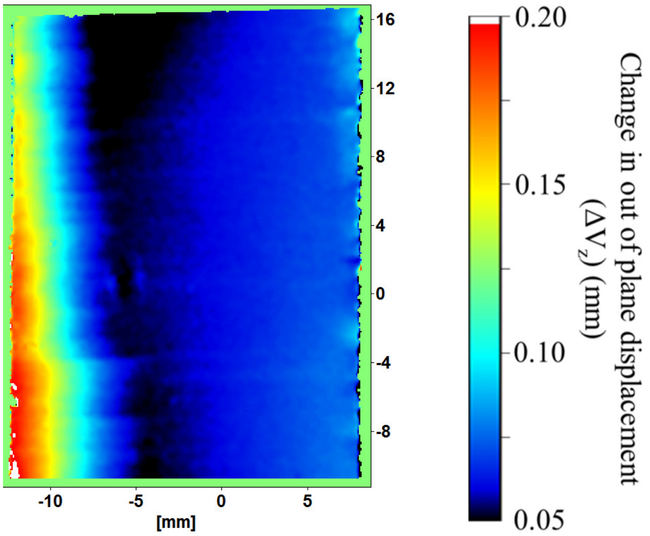

Figure 112: Change in out of plane displacement between 9.5 and 24.5 thousand cycles.

An interesting finding throughout this test and many later tests is that the entire specimen appears to move as the test progresses in both the white light and IR data. The more sudden changes in specimen position are caused by the onset of damage, but the gradual movement of the specimen to the lower right is considered to be caused by a change in laboratory temperature overnight, causing deformation of the camera stand and an apparent movement of the specimen.

8.4.1 Computed Tomography Inspection

CT scans were conducted using a custom 225kV Nikon/Metris HMX ST machine operating at 60 kV. 3143 radiographs of 2000 x 2000 pixels were taken at 0.115° angular steps. After 3D reconstruction, voxel sizes of 10.1 µm were obtained. Figure 113 shows the final shear and longitudinal strain maps for the previously discussed specimen and the locations at which CT cross sectional images were extracted. Strain data is plotted at the initial reference subset location, i.e. the strain map does not deform with applied loading, so allowing the data to be representative of the unloaded specimen in the CT scan. Any residual deformation due to damage will still exist in the specimen.

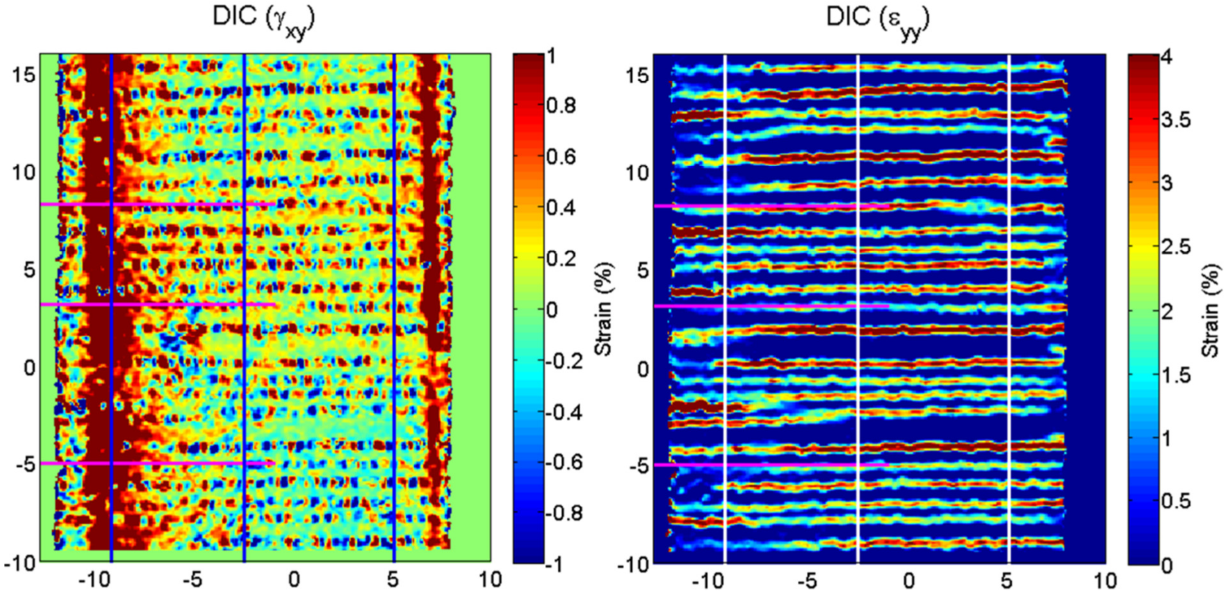

Figure 113: DIC strain data at 2.5 x 10^5 cycles showing the locations of vertical (blue/white) and horizontal (magenta) CT scan cross sections, as presented in Figure 115 and Figure 116.

Unfortunately, the CT scan area did not extend fully to the right specimen edge and as a result, the damage behaviour at this location could not be verified. Cross sectional CT images at the locations highlighted in magenta are shown in Figure 115 whilst locations highlighted in blue/white are shown in Figure 116. As previously hypothesised, a large area of delamination can be seen in Figure 115 between the outer *90º* and inner *0º* layers as highlighted within the green boxes. By visual inspection of the CT data, the edge delamination was found to have penetrated approximately 5.2 mm into the specimen width at the top and middle locations, whilst at the bottom location the delamination was found to have penetrated approximately 8.3 mm. This finding matches well with the extent of the out of phase regions present in Figure 114, so confirming the identification of delamination in Figure 111.

Longitudinal splitting in the central *0º* layers is also evident in the CT data, as highlighted inside the blue areas shown in Figure 115. The split extends the full height of the CT scan area at approximately 1.3 mm from the left specimen edge. The regions of increased shear strain, shown in Figure 113, starts at 1.4 mm from the specimen free edge. It is therefore believed that the longitudinal split in the central 0° layers is the cause of the increased shear strain measured on the surface.

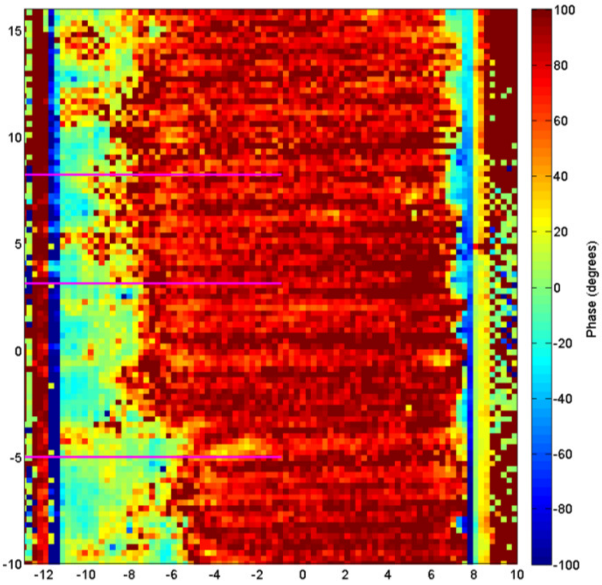

Figure 114: Final TSA phase plot of CFRP specimen after 250 thousand loading cycles. Magenta lines show the location of CT cross section images presented in Figure 115

Vertical CT cross-sections at the locations shown in Figure 113 are presented in Figure 116, with two areas shown at a greater magnification. For comparison, sections of longitudinal strain data are shown aligned vertically. In the vast majority of cases, regions of high strain were found to clearly coincide with a surface ply crack in the CT data, some examples of which are highlighted in red. In a small number of cases cracks in the CT data cannot be clearly resolved, or multiple cracks were identified. One such case is highlighted in green. The use of a higher resolution CT scan would likely clarify such data. The use of CT scanning has successfully validated the damage behaviour previously identified using TSA and DIC.

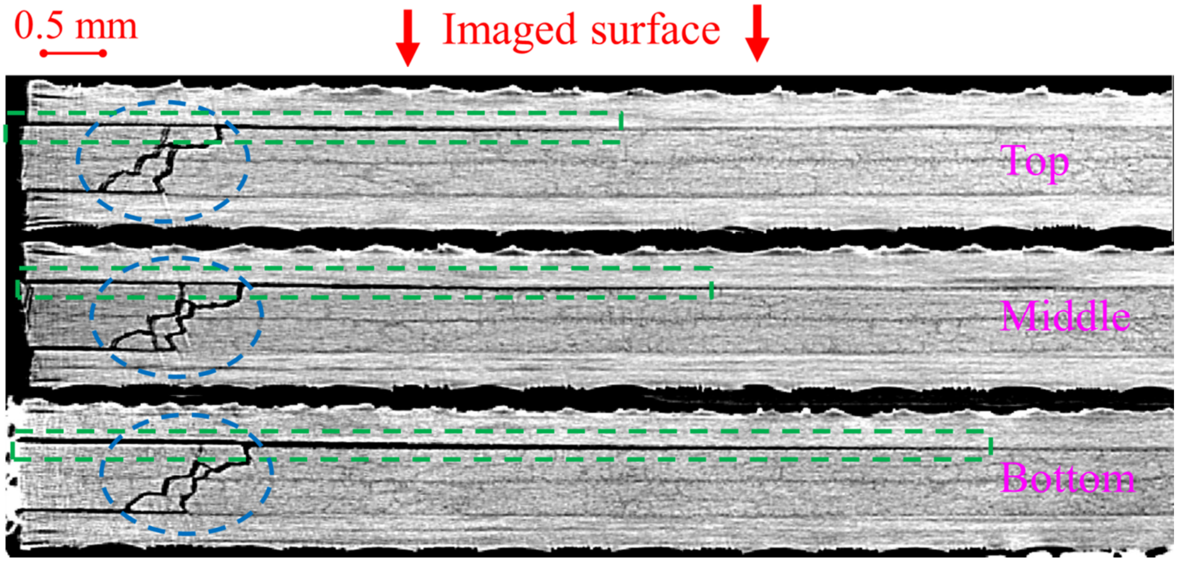

Figure 115: CT width-wise cross sectional images of a fatigued CFRP specimen at the locations shown in Figure 113. Delaminations and longitudinal splitting is highlighted in green and blue respectively.

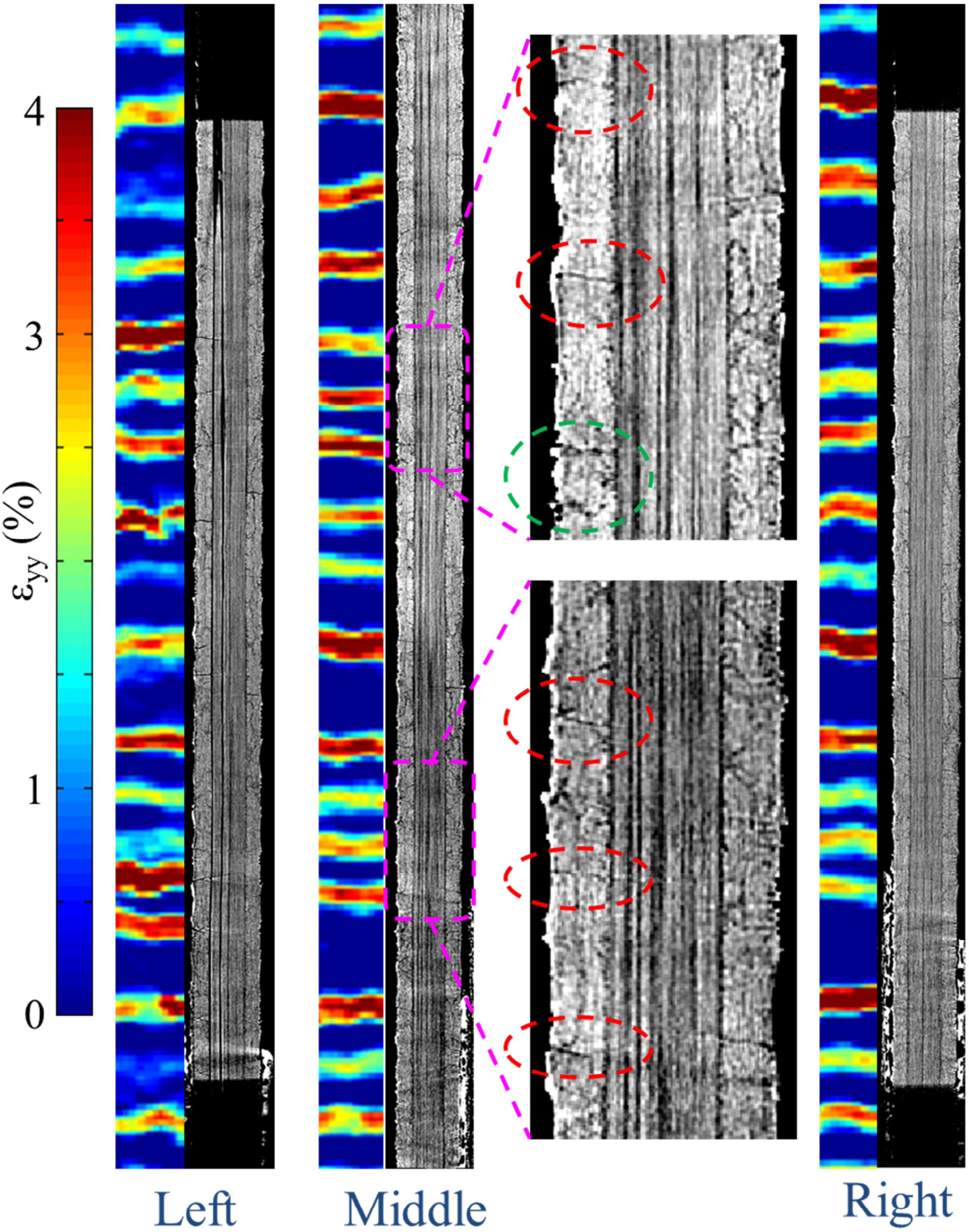

Figure 116: Comparison of DIC longitudinal strain data and CT cross sectional images of a fatigued CFRP specimen at the locations shown in Figure 113.

8.5 Damage Propagation in Previously Damaged Crossply CFRP Specimens

An identical loading methodology to that used in section 8.4 was applied to two of the specimens previously damaged at an intermediate strain rate using the methodology discussed in Chapter 7. The speckle pattern previously applied for high-speed imaging was removed using acetone and a new finer pattern applied. Images of the surface before and after were used to determine a constant reference point on the specimen surface, allowing the comparison of data collected at intermediate strain rate and during fatigue loading. A selection of full-field data collected during the fatigue loading of a previously damaged specimen is presented in Figure 117.

A greater level of transverse cracking can be noted in the first longitudinal strain map than was found in the specimen previously presented in Figure 109. This result is expected as significant transverse cracking was identified in the IR and DIC data collected during intermediate rate loading.

It was originally envisaged that damage originally identified during intermediate strain rate loading would be identifiable during the initial stages of fatigue loading and the propagation from these initial points of damage monitored. Although the methodology is capable of doing so, the transverse cracks found during intermediate strain rate loading could not be identified in the initial data sets collected during fatigue loading. This is due to the rapid onset of further transverse cracking in the initial few cycles, resulting in the original damage becoming unresolvable. In future tests it is recommended to use a lower cyclic load initially to enable the identification of prior damage.

Upon inspection of the longitudinal strain and normalised ΔT data, transverse crack density was found to increase within the first 10000 cycles, similar to the behaviour previously found. After 3500 cycles, activity in the shear strain data was found to occur close to the right free edge. This behaviour is believed to be caused by a combination of two longitudinal splits, highlighted in Figure 118, and was found to occur earlier than in the previously presented specimen.

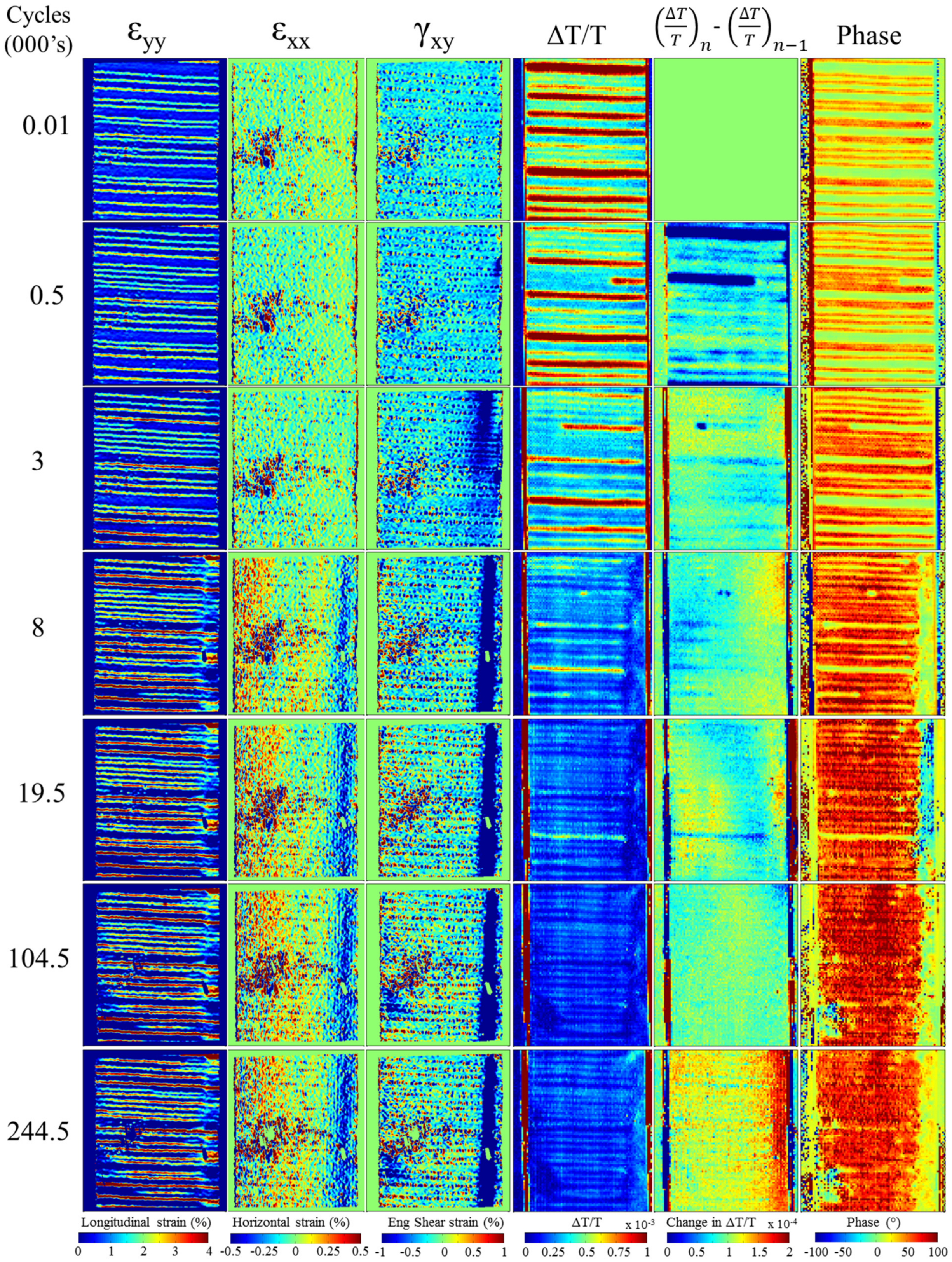

Figure 117: Full-field data collected during the fatigue loading of a crossply CFRP specimen previously loaded at an intermediate strain rate to 70% UTS

It is likely that the intermediate strain rate loading caused damage to occur in the central *0°* plies, leading to an increased tendency for longitudinal splitting under fatigue loading. Further testing of a greater number of samples would be required to fully validate this claim combined with optical/ X-ray CT validation. A further point of interest in Figure 118 is that the area of low shear strain is not apparent in the phase data until several thousand cycles later. This may highlight two different damage types, with a longitudinal split occurring first, generating the change in shear strain, followed by delamination as identified in the phase data. Without pausing the test at this moment and inspecting the specimen it is difficult to verify this claim however.

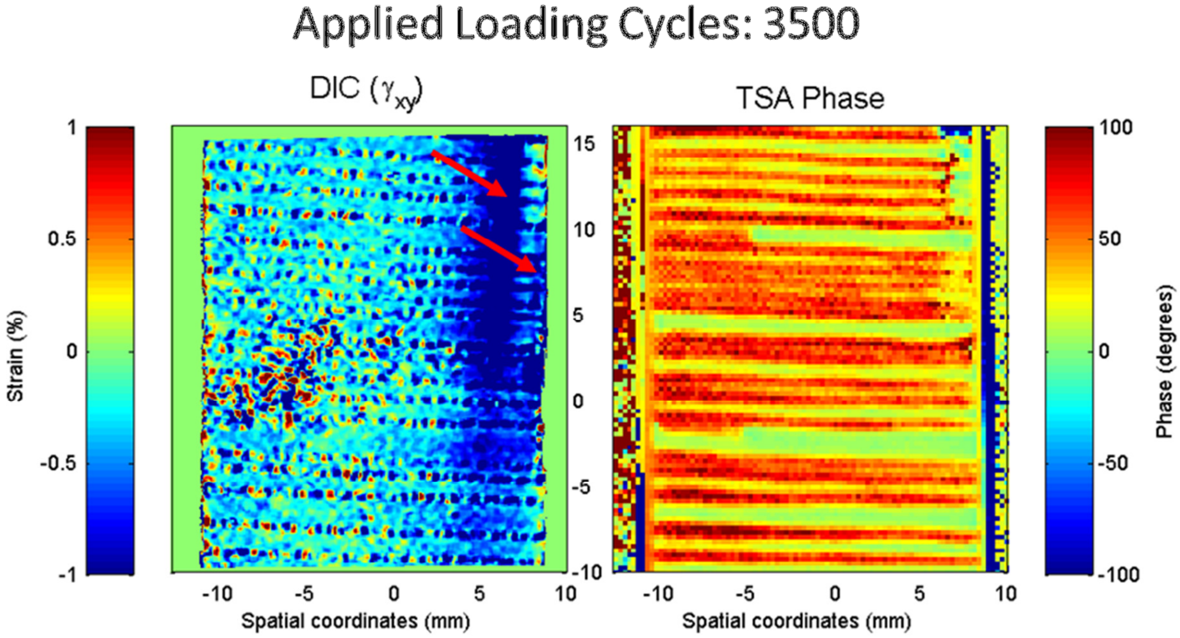

Figure 118: Engineering shear strain and TSA phase data collected during the fatigue loading of a specimen previously loaded at an intermediate strain rate, showing the formation of two longitudinal splits at the areas highlighted.

After 29500 cycles, an area of reduced shear strain was found to appear close to the left specimen edge, as indicated by the lower red arrow. Over the next 10000 cycles a second area of low shear strain formed, as highlighted in Figure 119 by the upper red arrow. These two areas coincide with areas of phase change in the TSA data and therefore may indicate delaminations.

The specimen was scanned using X-ray CT to confirm or deny the TSA and DIC findings.

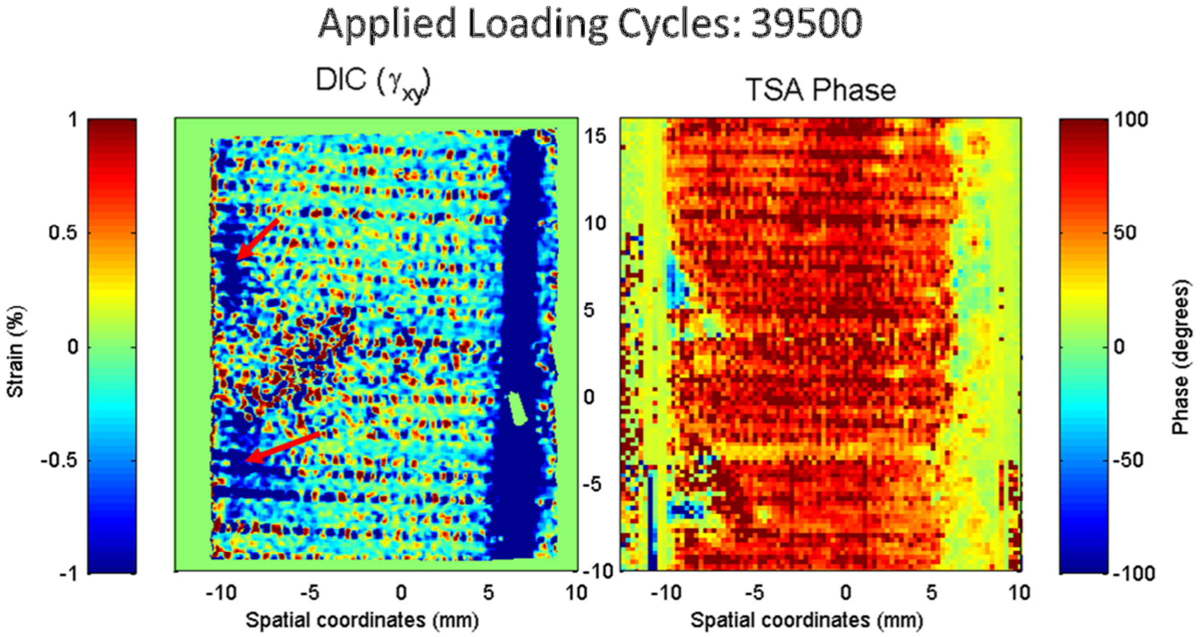

Figure 119: Engineering shear strain and TSA phase data collected during the fatigue loading of a specimen previously loaded at an intermediate strain rate, showing the formation of two areas of delamination at the areas highlighted.

8.5.1 Computed Tomography Inspection

The damaged specimen was investigated using X-ray CT with the same settings and voxel resolution as the scan previously presented in section 8.4.1. The final TSA phase and engineering shear strain maps are shown in Figure 120, along with vertical white lines and horizontal magenta lines showing the locations of CT cross section images. The horizontal and vertical CT cross section images are presented in Figure 121 and Figure 123 respectively.

From both CT and visual inspection, a much greater level of damage was found in the specimen previously damaged by intermediate strain rate loading than the specimen previously presented in section 8.4. Interestingly, a much greater level of damage could be noted on the reverse specimen surface, as shown within the area highlighted in red in Figure 123. Transverse cracks of much greater opening displacement and delaminations across the majority of the 0/90 interface can be noted on the back surface. The front surface shows smaller cracks and much less delaminated area. The paint layer on the front surface may be providing extra reinforcement resulting in lessened damage. Alternatively, a through thickness temperature gradient may be arising from the LED illumination, causing a cooler back surface. Thermal expansion effects may therefore result in the back surface carrying a disproportionate amount of load, resulting in greater damage. It is unclear why only the specimens that had been previously loaded at an intermediate strain rate displayed this behaviour since all specimens were illuminated with the same power lighting at the same distance. Further tests would need to be conducted to fully investigate this behaviour.

Similarly to the specimen previously discussed in 8.4.1, longitudinal splits in the 0° plies and delaminations were found to occur close the free edges, as shown in Figure 121. It was hypothesised that two longitudinal splits could be identified within the shear strain map presented in Figure 118. Unfortunately this could not be validated as the CT scan area was found to only extend to the top magenta line shown in Figure 120.

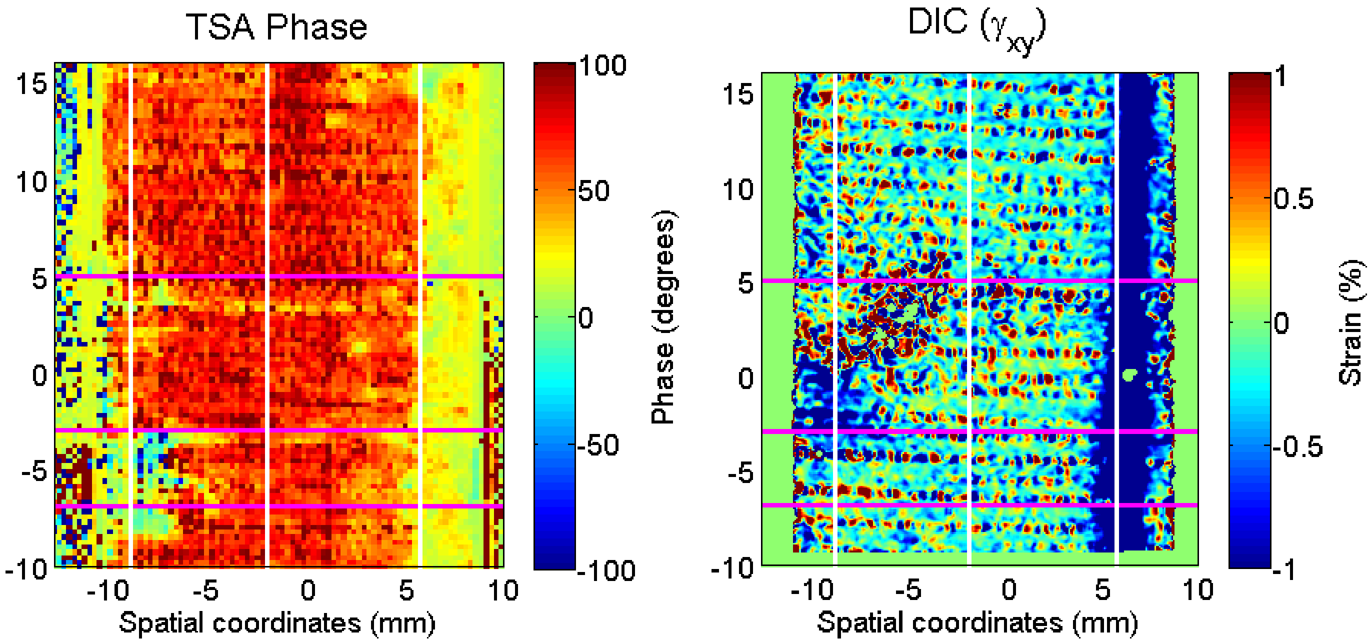

Figure 120: DIC shear strain and TSA phase data after 2.5 x 10^5 cycles showing the locations of vertical (white) and horizontal (magenta) CT scan cross sections, as presented in Figure 121 and Figure 123.

The delaminations highlighted in green in Figure 121 correspond to the right specimen edge in Figure 120. The width of the box corresponds to the approximate extent of the delamination into the specimen width. Due to the low spatial resolution of the CT data, only approximate lengths could be determined. It was found that the delamination penetrated further into the width at the middle and bottom cross sections locations, matching with the findings of the optical data.

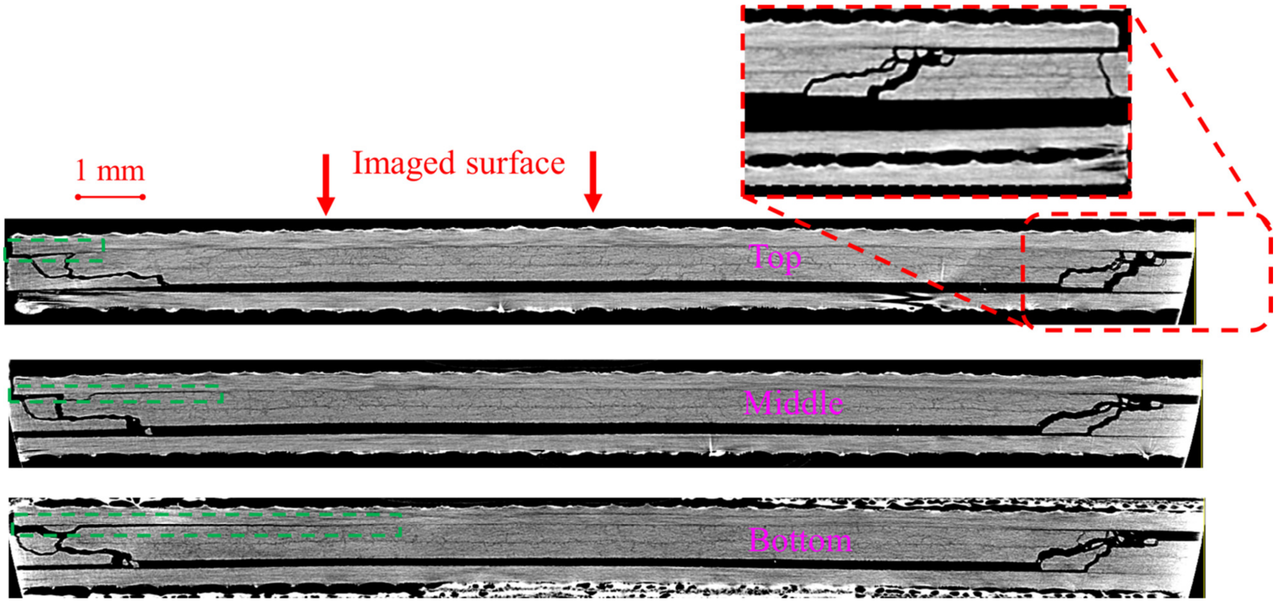

Figure 121: Width-wise cross sectional X-ray CT images of a fatigued CFRP specimen after 2.5 x 10^5 cycles. Cross section locations are shown in Figure 120.

The cause of the high negative shear strain at the right specimen edge is believed to be caused by the longitudinal split at the specimen edge. Visual inspection of the specimen revealed that the split extended to the top of the specimen, leading to a bundle of 0° fibres becoming detached and non-load bearing, as shown in Figure 122.

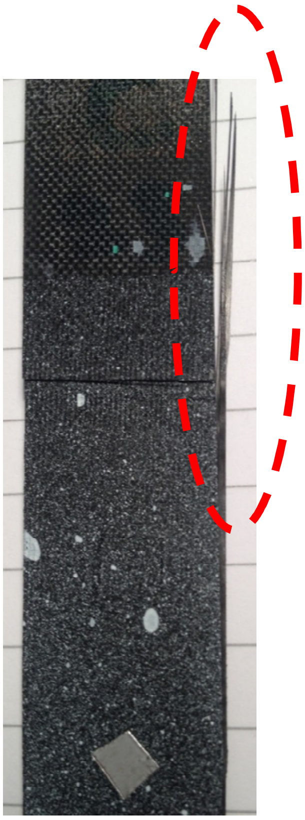

Figure 122: Longitudinal splitting of fatigued CFRP specimen at right specimen edge.

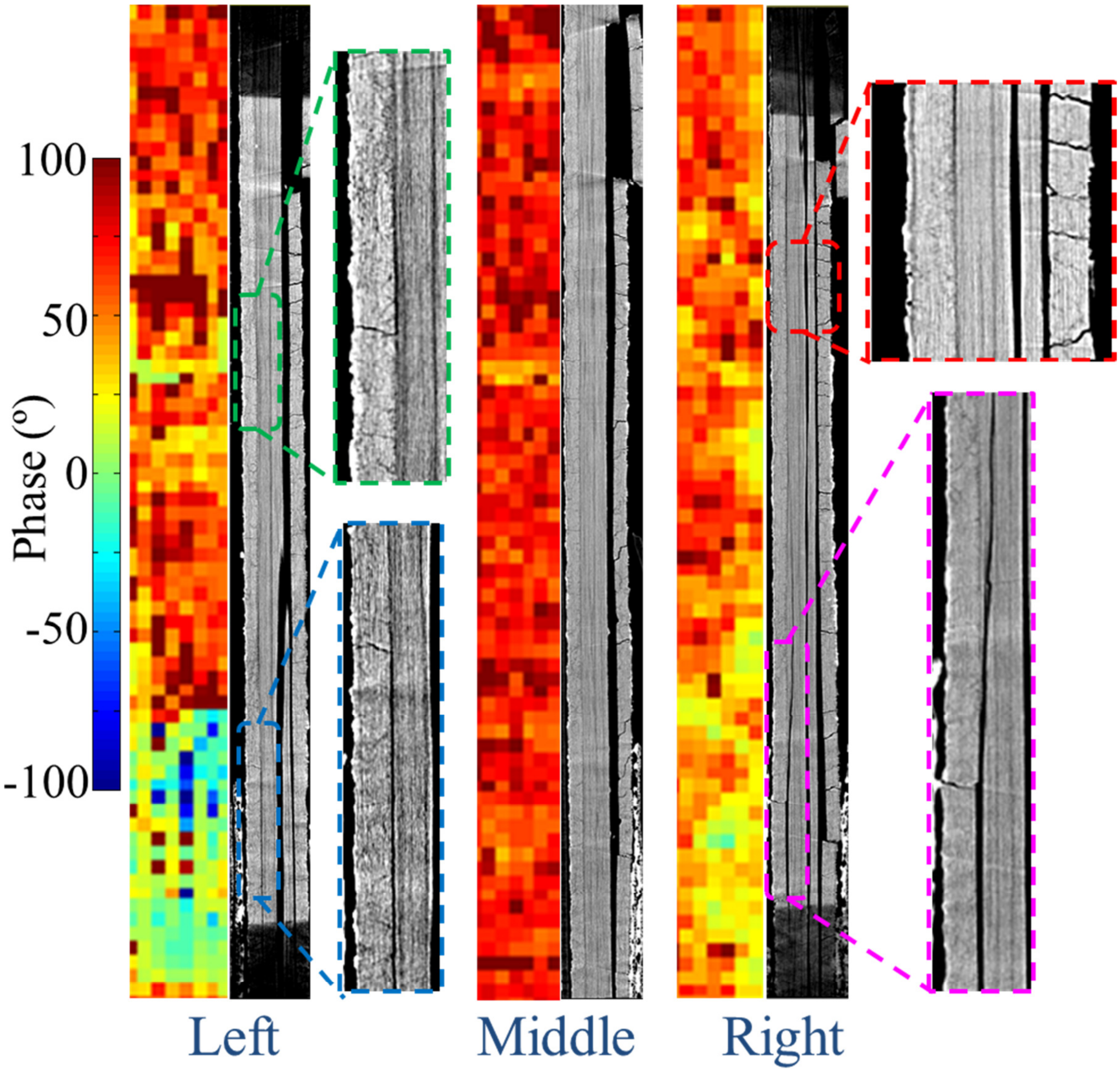

Figure 123: Comparison of TSA phase data and CT cross sectional images of a fatigued CFRP specimen at the locations shown in Figure 120.

The left vertical CT cross section shown in Figure 123 highlights two areas of delamination in green and blue. These areas coincide with two areas of phase change which can be identified more clearly in Figure 120. Another delamination close to the right specimen edge is highlighted in magenta and also coincides with an area of phase change.

8.6 Damage Propagation in Previously Undamaged Crossply GFRP Specimens

GFRP specimens, previously described in section 4.6, were cyclically loaded under tension-tension fatigue using the same image capture and data processing methodology as previously used for the CFRP specimens in section 8.4 and 8.5. Initial trials were conducted to final specimen failure using the loading conditions stated in Table 23 and the camera settings stated in Table 24. The number of cycles to failure was found to be highly unpredictable, ranging from between 20 to 440 thousand cycles. The locations of failure were also unpredictable, with some specimens failing at the end tab suggesting a stress concentration arising from end tab geometry. Most others specimens were found to fail approximately 10 mm from the top end tab, suggesting a manufacturing defect in the prepreg material, common across all specimens.

Specimen	Mean Stress	Cyclic Stress Amplitude	Frequency	Loading Cycles	Data collection intervals
$[90,0,90,0]_S$ GFRP	85 MPa	75 MPa	10 Hz	240000	Every 5000 cycles

Table 23: Test summary for previously undamaged GFRP specimens

Camera	Image size (pixels)	Imaging area on specimen (mm)	Spatial resolution (mm/pixel)	Imaging frequency (Hz)	Images captured	Exposure/ integration time (µs)
2 x AVT Manta G-504B	2452 x 2056	24.99 x 26.81	0.014	N/A	1 at min load 1 at max load	900
1 x CEDIP Silver 480M	320 x 256	24.99 x 67.23	0.261	383	600	1300

Table 24: Camera settings for tests conducted on undamaged GFRP specimens

The requirement for high resolution white-light images limits the imaging area to approximately one third of the specimen gauge length. As a result, the failure locations were not imaged in the majority of data sets. However, after the loading of a GFRP specimen to 240 thousand loading cycles, inspection of IR data revealed an area of localised heating at the border of the IR imaging area. Example DIC and TSA data of the first and last data sets are presented in Figure 124. A steady decrease in the thermoelastic response and a phase shift can be noted across the majority of the specimen surface, suggesting the onset of micro-cracking in the surface *90º* layer as previously suggested in section 6.2.3. The DIC longitudinal strain data shows many small bands of increased strain, further supporting this claim.

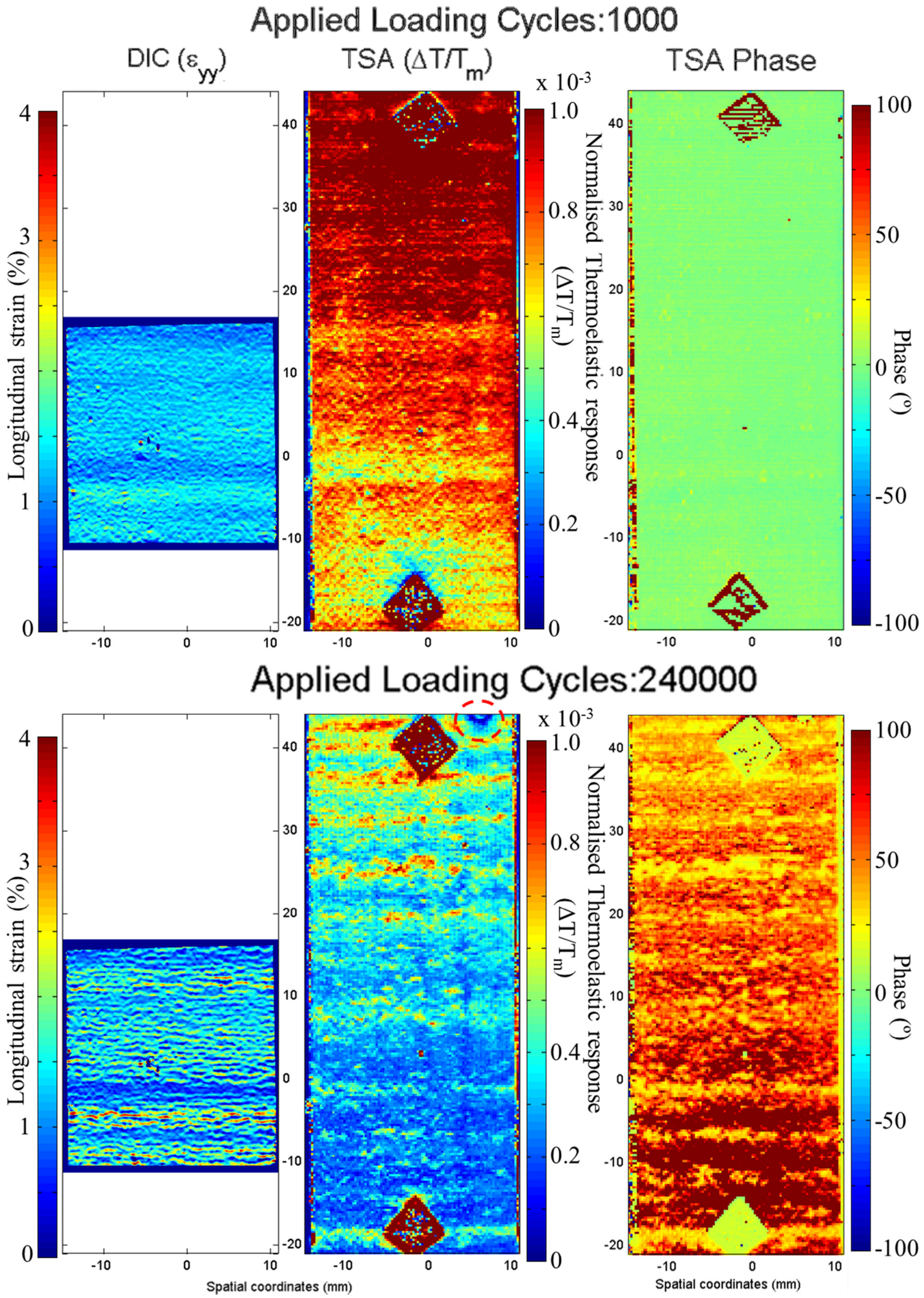

Figure 124: Longitudinal strain and normalised thermoelastic data for a GFRP specimen loaded to 240000 cycles.

A sharp decrease in the thermoelastic response can be identified at the area of localised heating, as circled in red in Figure 124. This area corresponds to a change in the TSA phase map and so is highly indicative of damage. The test was therefore paused at 240000 cycles so that the cameras could be moved to focus on the damage region. New reference images were taken at zero load and the fatigue test resumed. Data collection intervals were shortened to every 2000 cycles. Selected plots of longitudinal strain (ε_{yy}) and normalised thermoelastic response ($\Delta T/T_m$) are presented in Figure 125, whilst selected plots of shear strain and TSA phase are presented in Figure 126.

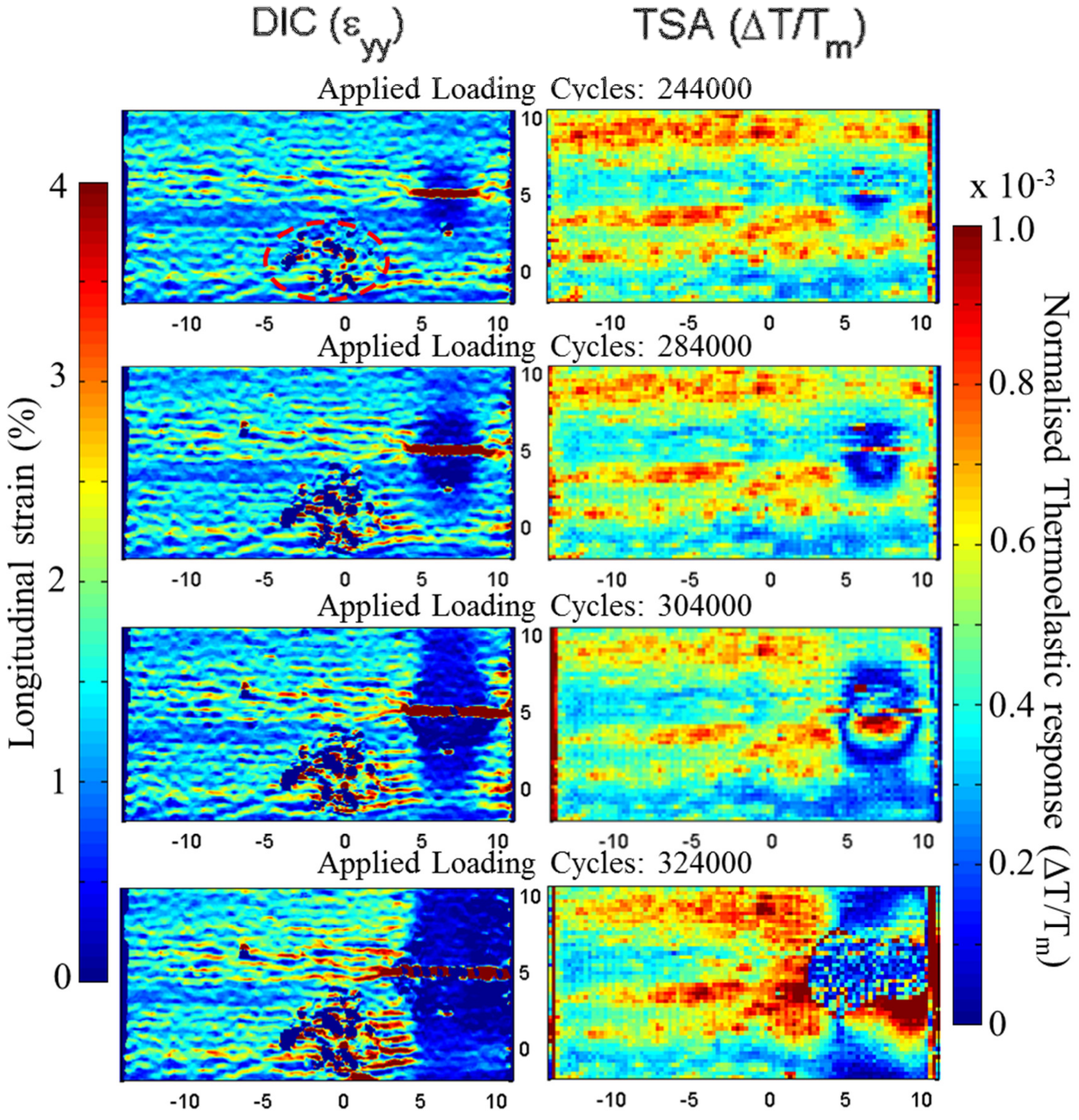

Figure 125: Development of longitudinal strain (ε_{yy}) and normalised thermoelastic response ($\Delta T/T_m$) during the late fatigue life of a crossply GFRP specimen.

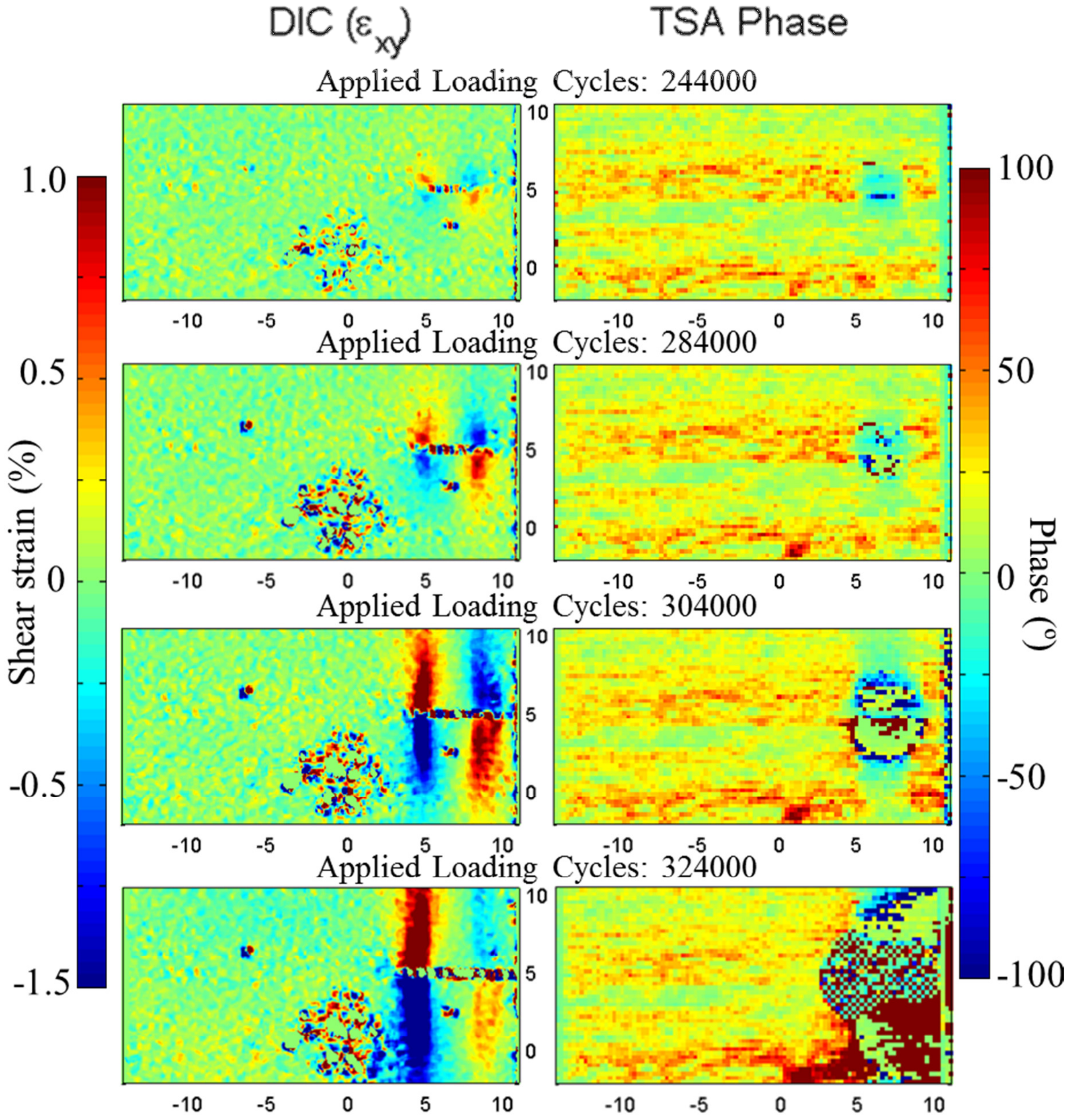

Figure 126: Development of shear strain (ε_{xy}) and TSA phase during the late fatigue life of a previously undamaged crossply GFRP specimen.

A region of decorrelation highlighted in red in Figure 125 is caused by the detaching of small areas of paint from the specimen surface. This is likely caused by surface contamination prior to paint application. As the paint has a very similar emissivity to the specimen material, the TSA data was not affected.

A clear region of damage close to the specimen right edge can be seen to grow in size throughout the various maps shown in Figure 125 and Figure 126. Although a significant crack in the outer *90º* layer can be seen in both the longitudinal strain maps and by visual inspection of the raw images, it is the fibre failure in one or more of the *0º* layers at this location which may be causing the majority of the damage behaviour shown and ultimately, final failure. Both longitudinal strain and normalised thermoelastic response can be seen to decrease directly above and below the damaged area. This is to be expected as fibre breaks in the *0º* layers reduce the load bearing capability across the damage site, causing load transfer to adjacent, undamaged 0º fibres. As the outer *90º* layer is effectively acting as a strain witness of the underlying *0º* layer, the stress sum experienced by the outer *90º* is also reduced by this event, causing the reduction in thermoelastic response.

The maps of shear strain and phase give more information to the damage types occurring. As previously discussed in section 8.4, a change in the phase around the damage site is highly indicative of delaminations. The shear strain maps indicate how the strain is being redistributed due to the presence of the propagating *0º* layer crack. As the normal stress in the *0º* fibres at the crack tip increases, the normal stress in the *0º* fibres above and below the crack decreases, creating a shearing deformation along the fibres. This behaviour is carried through to the outer *90º* layer allowing measurement by DIC. As a shear stress causes no change in the principle stresses, the thermoelastic response remains unchanged.

As this specimen was taken to final failure, no microscopic or CT analysis could be conducted. Due to the unpredictability of the GFRP specimens, further fatigue analysis was concentrated on the CFRP specimens.

8.7 Future Improvements

There were found to be several areas of the damage propagation methodology which require future improvement.

- The cycle counter should be changed to operate directly from the output of the zero-crossing detector circuit to give a more robust solution.
- At the moment, loading cycles are not counted during the execution of the camera trigger part of the LabView code. Small cumulative errors are therefore introduced into the number of loading cycles counted. This should be changed, either by continuing to sample load data during the trigger

sequence or by estimating the number of cycles missed based on the time taken to execute the trigger sequence.

- It is recommended that future uses of the methodology adapt the LabView code to also use the zero-crossing detector to trigger the IR camera, thus ensuring that videos start at the exact point of maximum load.
- For the work conducted in the thesis, an IR lens with a magnification between that of the 27 mm lens and the G1 lens would ideally be used to give IR and white light imaging areas of a more similar imaging area. The G1 lens was the only other IR lens available and can only be used at stand-off distances of a few mm.
- As the images collected at the maximum load point are generally of greater importance, future users of the methodology are recommended to collect the maximum load image first to ensure better temporal synchronisation between the TSA and DIC data. A possible alternative is to use the limited on-board RAM of the Manta cameras to store both the minimum and maximum images for later data transfer to the PC, so allowing the minimum 0.11 seconds interframe period, governed by the camera maximum frame rate and thus ensuring that both image captures occur within the IR video time period.
- Throughout the entire test, the overall magnitude of the $\Delta T/T$ maps and the phase maps can be seen to fluctuate even when no further damage is created, as is the case towards the end of the fatigue test. This behaviour is believed to be caused by small errors in the motion compensation procedure between data sets, either as a result of error introduced from the cropping of the IR video to the first maximum load point, or as a result of tracking inaccuracy. Although the Random Motion software was found to perform best when using the aluminium foil markers, the highly reflective surface causes IR intensity changes that are primarily from the surrounding environment. As a result, the recorded intensities are liable to change based on the marker position during cyclic loading, which may introduce errors to the motion compensation. It is recommended that future users of the methodology investigate other types of adhesive tapes to use as motion compensation markers or to use the DIC data to apply motion compensation.

8.8 Conclusions

The chapter has successfully established and validated a semi-automated combined white-light and IR imaging methodology for the study of FRP specimens during un-interrupted fatigue tests. The approach has used simple electronics, intense LED lighting and a LabView based methodology to achieve accurate camera timing to within 0.77 ms, so allowing the use of low frequency, high resolution white light cameras during dynamic loading. The use of high resolution cameras has subsequently given high spatial resolution strain maps, allowing the imaging of small scale damage in CFRP and GFRP specimens.

The use of a combined TSA and DIC methodology has allowed various damage types to be identified in the two types of specimen tested. Transverse cracking in CFRP laminates has been clearly identified in longitudinal strain and normalised thermoelastic data, whilst delaminations have been identified in shear strain and TSA phase data. Longitudinal splitting was also identified in one CFRP specimen as a result of fibre pull-out, causing a significant surface shear response.

Large-scale fibre breaks were imaged in a GFRP specimen which would not be possible with one technique alone. The damage behaviour of the CFRP specimen discussed has been successfully validated using CT analysis. Due to the unpredictability of the GFRP specimens, further fatigue work concentrated on the study of CFRP specimens.

Chapter 9

Conclusions and Future Work

9.1 Conclusions

The primary aim of this research has been to establish experimental methodologies based on optical techniques to study damage initiation and evolution in FRP materials, both during intermediate strain rate loading and during subsequent cyclic loading. The motivation for the work has arisen from the current lack of material data on the damage behaviour of FRP materials during high strain rate loading due to the lack of viable measurement techniques.

The work in the thesis can be divided into 4 main parts:

1. The application of DIC to high speed imaging.
2. The development of an interrupted loading methodology for the application of purely tensile loads at intermediate strain rates to FRP specimens without causing final failure.
3. The development and use of a combined DIC and TSA methodology for the study of damage propagation in FRP during fatigue loading.
4. The development and use of a combined DIC and IR-thermography methodology for the identification of damage in FRP during interrupted, intermediate strain rate loading.

The main findings in each area are summarised in the following sections.

9.1.1 The application of DIC to high speed imaging

The work conducted has fulfilled the first objective defined in chapter 1; to understand the characteristics of high speed cameras, their limitations and to identify methods for reducing sources of error. The use of high speed cameras for high spatial resolution DIC measurements has highlighted several important findings and recommendations for future users:

- The use of high accuracy subpixel interpolation algorithms for DIC is essential to be able to distinguish between small scale heterogenous behaviour and systematic errors.
- The magnitude of systematic DIC errors has been shown to vary substantially between high speed cameras and can be dependent on camera rotation.
- Low fill-factor sensors have been proven through numerical simulation to be detrimental to the accuracy of DIC measurements. A link has been shown between speckle size and sensor fill-factor that increases the strength of the pixel locking effect.
- The layout of pixel active areas has been shown to affect the spatial frequency of systematic errors.

9.1.2 The development of an interrupted loading rig

Due to the open loop control system used by the Instron VHS 80/20 a methodology was required to stop the loading of an FRP specimen at a known load so that specimens can be subsequent tested for damage propagation behaviour. The development of this methodology has attributed to fulfilling the second objective defined for the thesis; to establish a methodology for the study of FRP damage during elevated strain rate loading.

- A loading rig has been designed and validated that incorporates a simple shear pin fuse, which allows a variable load to be imparted to ASTM standard size FRP specimens up to an actuator velocity of 3.2 m/s, equivalent to a strain rate of approximately 15 s^{-1}.

- In contrast to previous studies, purely tensile intermediate strain-rate loading was achieved through the use of an anti-compression device, giving greater confidence to the true cause of any damage.

9.1.3 The development and use of a combined DIC-TSA methodology for the study of FRP damage propagation

The extended time period of a typical fatigue test and the preference for high resolution white-light cameras for DIC has required the development of an automated methodology based around LabView to accurately trigger cameras and collect data. The methodology has been applied to crossply GFRP and CFRP specimens successfully identifying damage propagation, thus fulfilling the final objective stated in chapter 1; to establish an optical methodology for the study of damage in FRP materials.

- An automated methodology has been developed for the collection of test machine and image data.
- The methodology uses simple electronics to trigger white-light cameras to within 99.8% of the maximum load point during a 5 Hz cyclic load.
- Transverse cracking has been identified for CFRP crossply laminates using DIC longitudinal strain maps and confirmed using TSA thermoelastic data. Validation has been provided using X-ray CT.
- Delaminations and longitudinal splitting have been identified in crossply CFRP laminates from DIC shear strain data and TSA phase data. Validation is provided using X-ray CT analysis.

9.1.4 A combined DIC-IR thermography methodology for FRP damage identification during intermediate strain rate loading

To enable the identification of damage initiation in FRP materials during intermediate strain rate loading a combined DIC and IR-thermography methodology was devised using high speed imaging. The application of this methodology to FRP specimens and the successful identification of damage fulfils the second objective stated in chapter 1.

- A high intensity illumination solution was designed, allowing white-light imaging frequencies of beyond 60 kHz to be realised. The unit outputs less heat than the previously used halogen lighting, such that materials under investigation with high speed cameras are less influenced by temperature changes. DIC errors due to air distortion were minimised to negligible levels.
- Transverse cracking has been identified in both GFRP and CFRP laminates using a thresholding procedure applied to high speed thermal images and confirmed through DIC analysis of high speed white-light images. Validation of full-field data has been carried out using optical microscopy and X-ray CT studies.
- A new motion compensation procedure has been designed for thresholded IR data using DIC displacement data, thus enabling the direct comparison of DIC strain and thermal data throughout an intermediate strain rate test.

9.2 Recommendations for Future Work

- Redesign of the interrupted loading rig to minimise inertia of the rig parts, thus enabling a higher maximum applied strain rate to FRP specimens.
- An extension of the FRP intermediate strain rate loading regimes to include compression and bending.
- Improvements to the temporal synchronisation of the white-light and IR high speed cameras as discussed in section 4.4.
- To undertake the improvements to the automated camera triggering methodology, as outlined in section 8.7.
- To apply the full-field methodologies developed to the study of a range of laminate configurations and material types. It is envisaged that the generation of such data can lead to the development of future guidelines and recommendations on the best design of FRP components for increased damage tolerance.

References

[1] A. B. Strong, *Fundamentals of Composites Manufacturing: Materials, Methods and Applications*, Second ed.: Society of Manufacturing Engineers, (2008).

[2] I. M. Daniel and O. Ishai, *Engineering Mechanics of Composite Materials*. New York, (1994).

[3] B. Roeseler, B. Sahr, and M. Kismarton, "Composite stuctures: the first 100 years," in *Proceedings of the 16th International Conference on Composite Materials*, Kyoto, Japan, (2007).

[4] G. L. Dillingham, "Status of FAA's Actions to Oversee the Safety of Composite Airplanes," United States Government Accountabilty Office, (2011), p. 50.

[5] A. M. S. Hamouda and M. S. J. Hashmi, "Testing of composite materials at high rates of strain: advances and challenges," *Journal of Materials Processing Technology,* vol. 77, pp. 327-336, (1998).

[6] I. M. Daniel, B. T. Werner, and J. S. Fenner, "Strain-rate-dependent failure criteria for composites," *Composites Science and Technology,* vol. 71, pp. 357-364, (2011).

[7] Aerospace: Red Ink at Rolls-Royce. *Time Magazine*. (1970).

[8] S. Hooker, *Not Much of an Engineer*: Crowood Press Ltd., (1985).

[9] D. A. Crump and J. M. Dulieu-Barton, "Synchronised imaging to establish thermomechanical behaviour of material subjected to high strain rate loading," *Experimental Mechanics,* vol. (in preparation), (2013).

[10] F. Pierron, B. Green, and M. R. Wisnom, "Full-field assessment of the damage process of laminated composite open-hole tensile specimens. Part I: Methodology," *Composites Part A: Applied Science and Manufacturing,* vol. 38, pp. 2307-2320, (2007).

[11] G. Crammond, "Development of optical techniques for the experimental analysis of local stress and strain distributions in adhesively bonded composite joints," Doctoral Thesis, Faculty of Engineering and the Environment, University of Southampton, (2013).

[12] M. Grédiac, "The use of full-field measurement methods in composite material characterization: interest and limitations," *Composites Part A: Applied Science and Manufacturing,* vol. 35, pp. 751-761, (2004).

[13] J. E. Field, W. G. Proud, and S. M. Walley, "Review of optical and X-ray techniques used at the Cavendish Laboratory," *Imaging Science Journal, The,* vol. 57, pp. 317-325, (2009).

[14] E. A. Patterson, "Digital Photoelasticity: Principles, Practice and Potential," *Strain,* vol. 38, pp. 27-39, (2002).

[15] J. L. Piro and M. Grédiac, "Producing and transferring low-spatial frequency grids for measuring displacement fields with moiré and grid methods," *Experimental Techniques,* vol. 28, pp. 23-26, (2004).

[16] A. F. Robinson and et al., "Paint coating characterization for thermoelastic stress analysis of metallic materials," *Measurement Science and Technology,* vol. 21, p. 085502, (2010).

[17] B. Pan, K. Qian, H. Xie, and A. Asundi, "Two-dimensional digital image correlation for in-plane displacement and strain measurement: a review," *Measurement Science and Technology,* vol. 20, p. 062001, (2009).

[18] T. R. Emery and J. M. Dulieu-Barton, "Thermoelastic Stress Analysis of damage mechanisms in composite materials," *Composites Part A: Applied Science and Manufacturing,* vol. 41, pp. 1729-1742, (2010).

[19] J. Dulieu-Barton and P. Stanley, "Development and applications of thermoelastic stress analysis," *The Journal of Strain Analysis for Engineering Design,* vol. 33, pp. 93-104, (1998).

[20] B. Mahoney, "Experimental Validation of a Methodology to Quantify Distributed Damage in Laminated Composites Using the Thermoelastic Effect," *Experimental Techniques,* p. 4, (1996).

[21] L. Krstulovic-Opara, B. Klarin, P. Neves, and Z. Domazet, "Thermal imaging and Thermoelastic Stress Analysis of impact damage of composite materials," *Engineering Failure Analysis,* vol. 18, pp. 713-719, (2011).

[22] R. K. Fruehmann, J. M. Dulieu-Barton, and S. Quinn, "Assessment of fatigue damage evolution in woven composite materials using infra-red techniques," *Composites Science and Technology,* vol. 70, pp. 937-946, (2010).

[23] S. Sambasivam, "The Surface Resin Layer for Strain Analysis of Laminated Composites," in *SEM XI International Congress and Exposition on Experimental and Applied Mechanics*, Orlando, Florida USA, (2008).

[24] D. Litwiller, "CCD vs. CMOS: Facts and Fiction," Dalsa Corporation, (2001).

[25] M. Bigas, E. Cabruja, J. Forest, and J. Salvi, "Review of CMOS image sensors," *Microelectronics Journal,* vol. 37, pp. 433-451, (2006).

[26] V. Tiwari, M. Sutton, and S. McNeill, "Assessment of High Speed Imaging Systems for 2D and 3D Deformation Measurements: Methodology Development and Validation," *Experimental Mechanics,* vol. 47, pp. 561-579, (2007).

[27] M. A. Sutton, J.-J. Orteu, and H. W. Schreier, *Image Correlation for Shape, Motion and Deformation Measurements*, (2009).

[28] B. Pan, "Recent Progress in Digital Image Correlation," *Experimental Mechanics,* vol. 51, pp. 1223-1235, (2011).

[29] P. Lava, S. Cooreman, S. Coppieters, M. De Strycker, and D. Debruyne, "Assessment of measuring errors in DIC using deformation fields generated by plastic FEA," *Optics and Lasers in Engineering,* vol. 47, pp. 747-753, (2009).

[30] LaVision GmbH, Göttingen, "Product-Manual for DaVis 8.1 (Strainmaster)," (2012).

[31] LaVision GmbH, Göttingen, "Product-Manual for DaVis 7.4 (Strainmaster)," (2012).

[32] D. Khennouf, "Assessing the Feasibility of Using Digital Image Correlation to Monitor Deformation in Historical Tapestries," Doctoral Thesis, Faculty of Engineering, Science and Mathematics, University of Southampton, (2010).

[33] M. A. Sutton, J. H. Yan, V. Tiwari, H. W. Schreier, and J. J. Orteu, "The effect of out-of-plane motion on 2D and 3D digital image correlation measurements," *Optics and Lasers in Engineering,* vol. 46, pp. 746-757, (2008).

[34] J. D. Helm and J. R. Deaner, "Off-Axis Two-Dimensional Digital Image Correlation," presented at the SEM X International Congress & Exposition on Experimental & Applied Mechanics, (2004).

[35] Meng L B, Jin G C, and Y. X. F, "Errors caused by misalignment of the optical camera axis and the object surface in the DSCM," *J. Tsinghua Univ,* (2006).

[36] D. Lecompte, A. Smits, S. Bossuyt, H. Sol, J. Vantomme, D. Van Hemelrijck*, et al.*, "Quality assessment of speckle patterns for digital image correlation," *Optics and Lasers in Engineering,* vol. 44, pp. 1132-1145, (2006).

[37] S. Yaofeng and J. H. L. Pang, "Study of optimal subset size in digital image correlation of speckle pattern images," *Optics and Lasers in Engineering,* vol. 45, pp. 967-974, (2007).

[38] T. Hua, H. Xie, S. Wang, Z. Hu, P. Chen, and Q. Zhang, "Evaluation of the quality of a speckle pattern in the digital image correlation method by mean subset fluctuation," *Optics & Laser Technology,* vol. 43, pp. 9-13, (2011).

[39] G. Crammond, S. W. Boyd, and J. M. Dulieu-Barton, "Speckle pattern quality assessment for digital image correlation," *Optics and Lasers in Engineering,* vol. 51, pp. 1368-1378, (2013).

[40] E. F. J. Overmars, N. G. W. Warncke, C. Poelma, and J. Westerweel, "Bias errors in PIV: the pixel locking effect revisited," presented at the 15th Int Symp on Applications of Laser Techniques to Fluid Mechanics, Lisbon, Portugal, (2010).

[41] H. W. Schreier, J. R. Braasch, and M. A. Sutton, "Systematic errors in digital image correlation caused by intensity interpolation," *Optical Engineering,* vol. 39, pp. 2915-2921, (2000).

[42] R. K. Fruehmann, J. M. Dulieu-Barton, and S. Quinn, "On the thermoelastic response of woven composite materials," *The Journal of Strain Analysis for Engineering Design,* vol. 43, pp. 435-450, (2008).

[43] R. K. Fruehmann, D. A. Crump, and J. M. Dulieu-Barton, "The use of Infrared Thermography at High Frame Rates," presented at the SEM Annual Conference & Exposition on Experimental & Applied Mechanics, Mohegan Sun, Connecticut, USA, (2011).

[44] G. Pitarresi and E. Patterson, "A review of the general theory of thermoelastic stress analysis," *The Journal of Strain Analysis for Engineering Design,* vol. 38, pp. 405-417, (2003).

[45] "Product Manual- Silver 480M," Cedip Infrared Systems, (2007).

[46] "Product Datasheet - Orion SC7000 Series," FLIR Systems Inc., (2013).

[47] R. K. Fruehmann, D. A. Crump, and J. M. Dulieu-Barton, "Characterization of an infrared detector for high frame rate thermography," *Measurement Science and Technology,* vol. 24, p. 105403, (2013).

[48] W. L. K. Thomson, "On the dynamical theory of heat.," *Transactions of the Royal Society of Edinburgh,* pp. 261-283, (1853).

[49] A. F. Robinson, "Assessment of residual stress using thermoelastic stress analysis," Doctoral, School of Engineering Sciences, University of Southampton, (2011).

[50] S. Sambasivam, "Thermoelastic stress analysis of laminated composite materials," Faculty of Engineering, Science and Mathematics, University of Southampton.

[51] D. A. Crump, "Reducing the Cost of Manufacturing Composite Aircraft Secondary Structure," University of Southampton, (2009).

[52] R. K. Fruehmann, "Stress and Damage Assessment in Woven Composite Materials by means of Thermoelastic Stress Analysis," Faculty of Engineering, Science and Mathematics, University of Southampton, (2009).

[53] S. Offermann, J. L. Beaudoin, C. Bissieux, and H. Frick, "Thermoelastic stress analysis under nonadiabatic conditions," *Experimental Mechanics,* vol. 37, pp. 409-413, (1997).

[54] A. K. Wong, "A non-adiabatic thermoelastic theory for composite laminates," *Journal of Physics and Chemistry of Solids,* vol. 52, pp. 483-494, (1991).

[55] S. Quinn and J. M. Dulieu-Barton, "Identification of the sources of non-adiabatic behaviour for practical thermoelastic stress analysis," *The Journal of Strain Analysis for Engineering Design,* vol. 37, pp. 59-71, January 1, 2002 (2002).

[56] A. K. Wong, R. Jones, and J. G. Sparrow, "Thermoelastic constant or thermoelastic parameter," *Journal of Physics and Chemistry of Solids,* vol. 48, pp. 749-753, (1987).

[57] J. M. Dulieu-Barton, "Introduction to thermoelastic stress analysis," *Strain,* vol. 35, pp. 35-39, (1999).

[58] D. Zhang, N. F. Enke, and B. I. Sandor, "Thermographic stress analysis of composite materials," *Experimental Mechanics,* vol. 30, pp. 68-73, (1990).

[59] D. Zhang and B. I. Sandor, "Advances in Thermographic Stress Analysis and Evaluation of Damage in Composites," in *Composite Materials: Testing and Design*, (1992), pp. 428-443.

[60] T. R. Emery, J. M. Dulieu-Barton, J. S. Earl, and P. R. Cunningham, "A generalised approach to the calibration of orthotropic materials for thermoelastic stress analysis," *Composites Science and Technology,* vol. 68, pp. 743-752, (2008).

[61] P. K. Mallick, *Composites Engineering Handbook*, 1 ed.: CRC Press, (1997).

[62] E. Starovoitov and F. B. O. Naghiyev, *Foundations of the Theory of Elasticity, Plasticity, and Viscoelasticity*: Apple Academic Press, (2012).

[63] R. W. Hertzberg, *Deformation and Fracture Mechanics of Engineering Materials*, Fourth ed., (1996).

[64] F. Tanaka, T. Okabe, H. Okuda, I. A. Kinloch, and R. J. Young, "Factors controlling the strength of carbon fibres in tension," *Composites Part A: Applied Science and Manufacturing,* vol. 57, pp. 88-94, (2014).

[65] J. R. Vinson and R. L. Sierakowski, *Behavior of Structures Composed of Composite Materials (2nd Edition)*. Secaucus, NJ, USA, (2002).

[66] J. López-Puente and S. Li, "Analysis of strain rate sensitivity of carbon/epoxy woven composites," *International Journal of Impact Engineering,* vol. 48, pp. 54-64, (2012).

[67] A. A. Doughett, Peder, *Composite Laminates: Properties, Performance and Applications*. Hauppage, NY, USA: Nova Science Publishers Inc., (2010).

[68] T. E. Tay, G. Liu, V. B. C. Tan, X. S. Sun, and D. C. Pham, "Progressive Failure Analysis of Composites," *Journal of Composite Materials,* vol. 42, pp. 1921-1966, September 1, 2008 (2008).

[69] W. J. Cantwell and J. Morton, "The significance of damage and defects and their detection in composite materials - a review," *Journal of Strain Analysis for Engineering Design,* vol. 27, pp. 29-42, (1992).

[70] A. E. Scott, I. Sinclair, S. M. Spearing, M. N. Mavrogordato, and W. Hepples, "Influence of voids on damage mechanisms in carbon/epoxy composites determined via high resolution computed tomography," *Composites Science and Technology,* vol. 90, pp. 147-153, (2014).

[71] G. Foray, A. Descamps-Mandine, M. R'Mili, and J. Lamon, "Statistical flaw strength distributions for glass fibres: Correlation between bundle test and AFM-derived flaw size density functions," *Acta Materialia,* vol. 60, pp. 3711-3718, (2012).

[72] J. L. Thomason, "The interface region in glass fibre-reinforced epoxy resin composites: 3. Characterization of fibre surface coatings and the interphase," *Composites,* vol. 26, pp. 487-498, (1995).

[73] R. Talreja, "Damage analysis for structural integrity and durability of composite materials," *Fatigue & Fracture of Engineering Materials & Structures,* vol. 29, pp. 481-506, (2006).

[74] S. L. Phoenix and L. J. Tierney, "A statistical model for the time dependent failure of unidirectional composite materials under local elastic load-sharing among fibers," *Engineering Fracture Mechanics,* vol. 18, pp. 193-215, (1983).

[75] K. Hoiseth and J. Qu, "Cracking paths at the ply interface in a cross-ply laminate," *Composites Part B: Engineering,* vol. 34, pp. 437-445, (2003).

[76] M. L. Accorsi, A. Pegoretti, and A. T. Dibenedetto, "Dynamic analysis of fibre breakage in single-and multiple-fibre composites," *Journal of Materials Science,* vol. 31, pp. 4181-4187, 1996/01/01 (1996).

[77] A. E. Scott, M. Mavrogordato, P. Wright, I. Sinclair, and S. M. Spearing, "In situ fibre fracture measurement in carbon–epoxy laminates using high resolution computed tomography," *Composites Science and Technology,* vol. 71, pp. 1471-1477, (2011).

[78] J. Aveston and G. A. K. Cooper, A., "Single and multiple fracture. The Properties of Fibre Composites," in *Properties of Fibre Composites*, National Physical Laboratory, (1971), pp. 15-26.

[79] V. Cecen, I. H. Tavman, M. Kok, and Y. Aydogdu, "Epoxy- and polyester-based composites reinforced with glass, carbon and aramid fabrics: Measurement of heat capacity and thermal conductivity of composites by differential scanning calorimetry," *Polymer Composites,* vol. 30, pp. 1299-1311, (2009).

[80] L. E. Asp, L. A. Berglund, and P. Gudmundson, "Effects of a composite-like stress state on the fracture of epoxies," *Composites Science and Technology,* vol. 53, pp. 27-37, (1995).

[81] J. E. Bailey, P. T. Curtis, and A. Parvizi, "On the Transverse Cracking and Longitudinal Splitting Behaviour of Glass and Carbon Fibre Reinforced Epoxy Cross Ply Laminates and the Effect of Poisson and Thermally Generated Strain," *Proceedings of the Royal Society of London. Series A, Mathematical and Physical Sciences,* vol. 366, pp. 599-623, (1979).

[82] P. D. Soden, M. J. Hinton, and A. S. Kaddour, "Lamina Properties, Lay-Up Configurations and Loading Conditions for a Range of Fibre-Reinfiorced Composite Laminates " *Composites Science and Technology,* vol. 58, pp. 1011-1022, (1998).

[83] M. J. Hinton, A. S. Kaddour, and P. D. Soden, *Failure criteria in fibre reinforced polymer composites: The World-Wide Failure Exercise*, Elsevier, (2004).

[84] R. M. Christensen, "The World Wide Failure Exercise II Examination of Results," *Journal of Reinforced Plastics and Composites,* vol. 32, pp. 1668-1672, (2013).

[85] A. Kaddour, M. Hinton, P. Smith, and S. Li, "The background to the third world-wide failure exercise," *Journal of Composite Materials,* vol. 47, pp. 2417-2426, (2013).

[86] R. Talreja and K. Gamstedt, *Damage and Failure of Composite Materials*: Cambridge University Press, (2012).

[87] S. Kravchenko, O. Kravchenko, M. Wortmann, M. Pietrek, P. Horst, and R. B. Pipes, "Composite toughness enhancement with interlaminar reinforcement," *Composites Part A: Applied Science and Manufacturing,* vol. 54, pp. 98-106, (2013).

[88] J. M. Berthelot, A. E. Mahi, and J. F. Le Corre, "Development of transverse cracking in cross-ply laminates during fatigue tests," *Composites Science and Technology,* vol. 61, pp. 1711-1721, (2001).

[89] T. Yokozeki, T. Aoki, and T. Ishikawa, "Fatigue growth of matrix cracks in the transverse direction of CFRP laminates," *Composites Science and Technology,* vol. 62, pp. 1223-1229, (2002).

[90] S. Ogihara and N. Takeda, "Interaction between transverse cracks and delamination during damage progress in CFRP cross-ply laminates," *Composites Science and Technology,* vol. 54, pp. 395-404, (1995).

[91] C. Mittelstedt and W. Becker, "Free-Edge Effects in Composite Laminates," *Applied Mechanics Reviews,* vol. 60, pp. 217-245, (2007).

[92] J. S. Dustin and R. Byron Pipes, "Free-edge singularities meet the microstructure: Important considerations," *Composites Science and Technology,* vol. 72, pp. 933-937, (2012).

[93] P. Lecomte-Grosbras, B. Paluch, and M. Brieu, "Characterization of free edge effects: influence of mechanical properties, microstructure and structure effects," *Journal of Composite Materials,* vol. 47, pp. 2823-2834, (2013).

[94] P. Lecomte-Grosbras, B. Paluch, M. Brieu, G. D. Saxcé, and L. Sabatier, "Interlaminar shear strain measurement on angle-ply laminate free edge using digital image correlation," *Composites Part A: Applied Science and Manufacturing,* vol. 40, pp. 1911-1920, (2009).

[95] M. Tahani and A. Nosier, "Free edge stress analysis of general cross-ply composite laminates under extension and thermal loading," *Composite Structures,* vol. 60, pp. 91-103, (2003).

[96] Z. Tian, F. Zhao, and Q. Yang, "Straight free-edge effects in laminated composites," *Finite Elements in Analysis and Design,* vol. 41, pp. 1-14, (2004).

[97] C. T. Herakovich, "On the relationship between engineering properties and delamination of composite materials," *Journal of Composite Materials,* vol. 15, (1981).

[98] T. R. Emery, "Identification of Damage in Composite Materials using Thermoelastic Stress Analysis," Doctoral Thesis, Faculty of Engineering, Science and Mathematics, University of Southampton, (2007).

[99] E. Adolfsson and P. Gudmundson, "Matrix crack induced stiffness reductions in $[(O_m/90_n/+[\theta]_p/-[\theta]_q)_s]_M$ composite laminates," *Composites Engineering,* vol. 5, pp. 107-123, (1995).

[100] M. Tahani and A. Nosier, "Three-dimensional interlaminar stress analysis at free edges of general cross-ply composite laminates," *Materials & Design,* vol. 24, pp. 121-130, (2003).

[101] A. S. D. Wang and F. W. Crossman, "Some New Results on Edge Effect in Symmetric Composite Laminates," *Journal of Composite Materials,* vol. 11, pp. 92-106, (1977).

[102] N. Takeda and S. Ogihara, "Initiation and growth of delamination from the tips of transverse cracks in CFRP cross-ply laminates," *Composites Science and Technology,* vol. 52, pp. 309-318, (1994).

[103] R. Talreja, "Transverse Cracking and Stiffness Reduction in Composite Laminates," *Journal of Composite Materials,* vol. 19, pp. 355-375, (1985).

[104] L.-Y. Xu, "Interaction between matrix cracking and edge delamination in composite laminates," *Composites Science and Technology,* vol. 50, pp. 469-478, (1994).

[105] A. Gilat, R. K. Goldberg, and G. D. Roberts, "Experimental study of strain-rate-dependent behavior of carbon/epoxy composite," *Composites Science and Technology,* vol. 62, pp. 1469-1476, (2002).

[106] I. Daniel, R. LaBedz, and T. Liber, "New method for testing composites at very high strain rates," *Experimental Mechanics,* vol. 21, pp. 71-77, (1981).

[107] A. C. Johnson, S. A. Hayes, and F. R. Jones, "The role of matrix cracks and fibre/matrix debonding on the stress transfer between fibre and matrix in a single fibre fragmentation test," *Composites Part A: Applied Science and Manufacturing,* vol. 43, pp. 65-72, (2012).

[108] J. Fitoussi, F. Meraghni, Z. Jendli, G. Hug, and D. Baptiste, "Experimental methodology for high strain-rates tensile behaviour analysis of polymer matrix composites," *Composites Science and Technology,* vol. 65, pp. 2174-2188, (2005).

[109] S. Pardo, D. Baptiste, F. Décobert, J. Fitoussi, and R. Joannic, "Tensile dynamic behaviour of a quasi-unidirectonal E-glass/polyester composite," *Composites Science and Technology,* vol. 62, pp. 579-584, (2002).

[110] H. Y. Chou, A. R. Bunsell, G. Mair, and A. Thionnet, "Effect of the loading rate on ultimate strength of composites. Application: Pressure vessel slow burst test," *Composite Structures,* vol. 104, pp. 144-153, (2013).

[111] R. Steinberger, T. I. Valadas Leitão, E. Ladstätter, G. Pinter, W. Billinger, and R. W. Lang, "Infrared thermographic techniques for non-destructive damage characterization of carbon fibre reinforced polymers during tensile fatigue testing," *International Journal of Fatigue,* vol. 28, pp. 1340-1347, (2006).

[112] J. W. Holmes and S. F. Shuler, "Temperature rise during fatigue of fibre-reinforced ceramics," *Journal of materials science letters,* vol. 9, pp. 1290-1291, (1990).

[113] R. Weichert and K. Schönert, "Heat Generation at the Tip of a Moving Crack," *Journal of Physical Solids,* vol. 26, pp. 151-161, (1977).

[114] T. Lisle, C. Bouvet, M. L. Pastor, P. Margueres, and R. Prieto Corral, "Damage analysis and fracture toughness evaluation in a thin woven composite laminate under static tension using infrared thermography," *Composites Part A: Applied Science and Manufacturing,* vol. 53, pp. 75-87, (2013).

[115] Y. A. Çengel and M. A. Boles, *Thermodynamics: An Engineering Approach*: McGraw-Hill Professional Publishing, (2004).

[116] T. Tian, "Anisotropic Thermal Property Measurement of Carbon-fiber/Epoxy Composite Materials," Univeristy of Nebraska - Lincoln, (2011).

[117] M. Grédiac, "The use of heterogeneous strain fields for the characterization of composite materials," *Composites Science and Technology,* vol. 56, pp. 841-846, (1996).

[118] M. S. Loukil, Z. Ayadi, and J. Varna, "ESPI analysis of crack face displacements in damaged laminates," *Composites Science and Technology*, vol. 94, p. 80 - 88, (2014).

[119] D. Francis and et al., "Shearography technology and applications: a review," *Measurement Science and Technology,* vol. 21, p. 102001, (2010).

[120] J. Lambert, A. R. Chambers, I. Sinclair, and S. M. Spearing, "3D damage characterisation and the role of voids in the fatigue of wind turbine blade materials," *Composites Science and Technology,* vol. 72, pp. 337-343, (2012).

[121] F. Sket, A. Enfedaque, C. Alton, C. González, J. M. Molina-Aldareguia, and J. Llorca, "Automatic quantification of matrix cracking and fiber rotation by X-ray computed tomography in shear-deformed carbon fiber-reinforced laminates," *Composites Science and Technology*, vol. 90, p. 129 - 138, (2014).

[122] A. E. Scott, I. Sinclair, S. M. Spearing, A. Thionnet, and A. R. Bunsell, "Damage accumulation in a carbon/epoxy composite: Comparison between a multiscale model and computed tomography experimental results," *Composites Part A: Applied Science and Manufacturing,* vol. 43, pp. 1514-1522, (2012).

[123] S. Fidan, T. Sınmazçelik, and E. Avcu, "Internal damage investigation of the impacted glass/glass+aramid fiber reinforced composites by micro-computerized tomography," *NDT & E International,* vol. 51, pp. 1-7, (2012).

[124] D. J. Bull, S. M. Spearing, I. Sinclair, and L. Helfen, "Three-dimensional assessment of low velocity impact damage in particle toughened composite laminates using micro-focus X-ray computed tomography and synchrotron

radiation laminography," *Composites Part A: Applied Science and Manufacturing,* vol. 52, pp. 62-69, (2013).

[125] F. Cosmi and A. Bernasconi, "Micro-CT investigation on fatigue damage evolution in short fibre reinforced polymers," *Composites Science and Technology,* vol. 79, pp. 70-76, (2013).

[126] D. J. Bull, L. Helfen, I. Sinclair, S. M. Spearing, and T. Baumbach, "A comparison of multi-scale 3D X-ray tomographic inspection techniques for assessing carbon fibre composite impact damage," *Composites Science and Technology,* vol. 75, pp. 55-61, (2013).

[127] A. P. Mouritz, C. Townsend, and M. Z. Shah Khan, "Non-destructive detection of fatigue damage in thick composites by pulse-echo ultrasonics," *Composites Science and Technology,* vol. 60, pp. 23-32, (2000).

[128] P. Marguères and F. Meraghni, "Damage induced anisotropy and stiffness reduction evaluation in composite materials using ultrasonic wave transmission," *Composites Part A: Applied Science and Manufacturing,* vol. 45, pp. 134-144, (2013).

[129] B. Vieille, V. M. Casado, and C. Bouvet, "About the impact behavior of woven-ply carbon fiber-reinforced thermoplastic- and thermosetting-composites: A comparative study," *Composite Structures,* vol. 101, pp. 9-21, (2013).

[130] F. Pierron, B. Green, M. R. Wisnom, and S. R. Hallett, "Full-field assessment of the damage process of laminated composite open-hole tensile specimens. Part II: Experimental results," *Composites Part A: Applied Science and Manufacturing,* vol. 38, pp. 2321-2332, (2007).

[131] F. Meraghni, H. Nouri, N. Bourgeois, C. Czarnota, and P. Lory, "Parameters identification of fatigue damage model for short glass fiber reinforced polyamide (PA6-GF30) using digital image correlation," *Procedia Engineering,* vol. 10, pp. 2110-2116, (2011).

[132] S. Giancane, F. W. Panella, R. Nobile, and V. Dattoma, "Fatigue damage evolution of fiber reinforced composites with digital image correlation analysis," *Procedia Engineering,* vol. 2, pp. 1307-1315, (2010).

[133] M. Colin de Verdiere, A. K. Pickett, A. A. Skordos, and V. Witzel, "Evaluation of the mechanical and damage behaviour of tufted non crimped fabric composites using full field measurements," *Composites Science and Technology,* vol. 69, pp. 131-138, (2009).

[134] M. Torres Arellano, L. Crouzeix, B. Douchin, F. Collombet, H. Hernández Moreno, and J. González Velázquez, "Strain field measurement of filament-wound composites at ±55° using digital image correlation: An approach for unit cells employing flat specimens," *Composite Structures,* vol. 92, pp. 2457-2464, (2010).

[135] G. Belingardi, E. G. Koricho, and A. T. Beyene, "Characterization and damage analysis of notched cross-ply and angle-ply fabric GFRP composite material," *Composite Structures,* vol. 102, pp. 237-249, (2013).

[136] M. A. Caminero, M. Lopez-Pedrosa, C. Pinna, and C. Soutis, "Damage monitoring and analysis of composite laminates with an open hole and adhesively bonded repairs using digital image correlation," *Composites Part B: Engineering,* vol. 53, pp. 76-91, (2013).

[137] L. P. Canal, C. González, J. M. Molina-Aldareguía, J. Segurado, and J. Llorca, "Application of digital image correlation at the microscale in fiber-reinforced composites," *Composites Part A: Applied Science and Manufacturing,* vol. 43, pp. 1630-1638, (2012).

[138] L. P. Canal, C. González, J. M. Molina-Aldareguía, J. Segurado, and J. Llorca, "Application of digital image correlation at the microscale in fiber-reinforced composites," *Composites Part A: Applied Science and Manufacturing*, vol. 43, pp. 1630 - 1638, (2012).

[139] S. Giancane, F. W. Panella, and V. Dattoma, "Characterization of fatigue damage in long fiber epoxy composite laminates," *International Journal of Fatigue,* vol. 32, pp. 46-53, (2010).

[140] M. L. Silva and G. Ravichandran, "Combined thermoelastic stress analysis and digital image correlation with a single infrared camera," *The Journal of Strain Analysis for Engineering Design,* vol. 46, pp. 783-793, (2011).

[141] M. Naderi, A. Kahirdeh, and M. M. Khonsari, "Dissipated thermal energy and damage evolution of Glass/Epoxy using infrared thermography and acoustic emission," *Composites Part B: Engineering,* vol. 43, pp. 1613-1620, (2012).

[142] W. R. Broughton, M. R. L. Gower, M. J. Lodeiro, G. D. Pilkington, and R. M. Shaw, "An experimental assessment of open-hole tension-tension fatigue behaviour of a GFRP laminate," *Composites Part A: Applied Science and Manufacturing,* vol. 42, pp. 1310-1320, (2011).

[143] J. Montesano, Z. Fawaz, and H. Bougherara, "Use of infrared thermography to investigate the fatigue behavior of a carbon fiber reinforced polymer composite," *Composite Structures,* vol. 97, pp. 76-83, (2013).

[144] T. R. Emery, "Identification of damage in composite materials using thermoelastic stress analysis," Doctoral thesis, Faculty of Engineering, Science and Mathematics, University of Southampton, (2007).

[145] J. M. Dulieu-Barton and T. R. Emery, "Prediction of fatigue life in composite materials using thermoelastic stress analysis," presented at the 17th European Congress on Fracture (ECF17), (2008).

[146] R. K. Fruehmann, J. M. Dulieu-Barton, and S. Quinn, "Thermoelastic stress and damage analysis using transient loading," *Experimental Mechnanics,* vol. 50, pp. 1075-1086, (2010).

[147] C. Goidescu, H. Welemane, C. Garnier, M. Fazzini, R. Brault, E. Péronnet*, et al.*, "Damage investigation in CFRP composites using full-field measurement techniques: Combination of digital image stereo-correlation, infrared thermography and X-ray tomography," *Composites Part B: Engineering,* vol. 48, pp. 95-105, (2013).

[148] J. LeBlanc and A. Shukla, "Response of E-glass/vinyl ester composite panels to underwater explosive loading: Effects of laminate modifications," *International Journal of Impact Engineering,* vol. 38, pp. 796-803, (2011).

[149] P. L. Reu and T. J. Miller, "The application of high-speed digital image correlation," *The Journal of Strain Analysis for Engineering Design,* vol. 43, pp. 673-688, (2008).

[150] V. Tiwari, M. A. Sutton, S. R. McNeill, S. Xu, X. Deng, W. L. Fourney*, et al.*, "Application of 3D image correlation for full-field transient plate deformation measurements during blast loading," *International Journal of Impact Engineering,* vol. 36, pp. 862-874, (2009).

[151] H. Koerber, J. Xavier, and P. P. Camanho, "High strain rate characterisation of unidirectional carbon-epoxy IM7-8552 in transverse compression and in-plane shear using digital image correlation," *Mechanics of Materials,* vol. 42, pp. 1004-1019, (2010).

[152] D. Lee, H. Tippur, and P. Bogert, "Quasi-static and dynamic fracture of graphite/epoxy composites: An optical study of loading-rate effects," *Composites Part B: Engineering,* vol. 41, pp. 462-474, (2010).

[153] ASTM, "D 3039/D 3039M-95a," in *Standard Test Method for Tensile Properties of Polymer Matrix Composite Materials*, ed, (2000).

[154] M. R. Wisnom, "Size effects in the testing of fibre-composite materials," *Composites Science and Technology,* vol. 59, pp. 1937-1957, (1999).

[155] T. K. O'Brien, "Characterisation of delamination onset and growth in a composite laminate," in *Damage in Composite Materials*. vol. ASTM STP 775, K. L. Reifsnider, Ed., ed: American Society for Testing and Materials, (1982), pp. 140 - 167.

[156] H. M. Hsiao and I. M. Daniel, "Strain rate behavior of composite materials," *Composites Part B: Engineering,* vol. 29, pp. 521-533, (1998).

[157] S. Li, "Studying Dynamic Elastic Behavior of Materials by Using SHPB," in *SEM XI International Congress and Exposition on Experimental and Applied Mechanics*, Orlando, Florida USA, (2008).

[158] D. M. Ştefănescu and M. A. Anghel, "Electrical methods for force measurement – A brief survey," *Measurement,* vol. 46, pp. 949-959, (2013).

[159] R. Eriksson, "High speed characterization of composite materials," Master thesis, Department of Mechanical Engineering, Technical University of Denmark, (2010).

[160] X. Xiao, "Dynamic tensile testing of plastic materials," *Polymer Testing,* vol. 27, pp. 164-178, (2008).

[161] F. d. A. Silva, D. Zhu, B. Mobasher, C. Soranakom, and R. D. Toledo Filho, "High speed tensile behavior of sisal fiber cement composites," *Materials Science and Engineering: A,* vol. 527, pp. 544-552, (2010).

[162] M. Borsutzki, D. Cornette, Y. Kuriyama, A. Uenishi, B. Yan, and E. Opbroek, "Recommendations for Dynamic Tensile Testing of Sheet Steels " International Iron and Steel Institute, (2005).

[163] X. S. Xiao, "Analysis of Dynamic Tensile Testing," in *SEM XI International Congress and Exposition on Experimental and Applied Mechanics*, Orlando, Florida USA, (2008).

[164] (16/09/2013). *Matweb material property database - Aluminium 7075 - T651.* Available: http://www.matweb.com/search/DataSheet.aspx?MatGUID=4f19a42be94546b686bbf43f79c51b7d&ckck=1

[165] Personal communication: Russell Brown, Photron Europe Ltd., "Photron Camera trigger mode and expected delay information," (2013).

[166] "FASTCAM SA1.1 Hardware Manual," Photron Europe. Ltd., (2007).

[167] "Model 2311 Signal Conditioning Amplifier Instruction Manual," Vishay Measurement Group, (1993).

[168] Vishay Precision Group - Micro-Measurements, "Shunt Calibration of Strain Gage Instrumentation - Tech Note TN-514."

[169] P. W. W. Fuller, "An introduction to high speed photography and photonics," *Imaging Science Journal, The,* vol. 57, pp. 293-302, (2009).

[170] Umeco Composites: Advanced Composites Group, "ACG MTM28 Series Component Prepregs Datasheet," (2009).

[171] Gurit, "SP High Modulus Marine Product Catalogue," (2012).

[172] Gurit, "SE 84LV Low Temperature Cure Epoxy Prepreg System Datasheet," (2012).

[173] *eSuite 1.0 Beta*. Available: http://www.espcomposites.com/software/software.html

[174] M. L. Longana, J. M. Dulieu-Barton, and F. Pierron, "Identification of constitutive properties of composite materials under high strain rate loading using optical strain measurement technique," presented at the 15th European Conference on Composite Materials, Venice, (2012).

[175] Vishay Precision Group.-. Micro-Measurements, "Application Note VMM-19: Surface Preparation of Composites," (2005).

[176] P. Reu, "Introduction to Digital Image Correlation: Best Practices and Applications," *Experimental Techniques,* vol. 36, pp. 3-4, (2012).

[177] B. Vieille, J. Aucher, and L. Taleb, "Overstress accommodation in notched woven-ply thermoplastic laminates at high-temperature: Numerical modeling and validation by Digital Image Correlation," *Composites Part B: Engineering,* vol. 45, pp. 290-302, (2013).

[178] M. R. Arthington, C. R. Siviour, and N. Petrinic, "Improved materials characterisation through the application of geometry reconstruction to quasi-static and high-strain-rate tension tests," *International Journal of Impact Engineering,* vol. 46, pp. 86-96, (2012).

[179] J. E. Field, S. M. Walley, W. G. Proud, H. T. Goldrein, and C. R. Siviour, "Review of experimental techniques for high rate deformation and shock studies," *International Journal of Impact Engineering,* vol. 30, pp. 725-775, (2004).

[180] P. Kumar, J. LeBlanc, D. S. Stargel, and A. Shukla, "Effect of plate curvature on blast response of aluminum panels," *International Journal of Impact Engineering,* vol. 46, pp. 74-85, (2012).

[181] F. Pierron, M. Sutton, and V. Tiwari, "Ultra High Speed DIC and Virtual Fields Method Analysis of a Three Point Bending Impact Test on an Aluminium Bar," *Experimental Mechanics,* vol. 51, pp. 537-563, (2011).

[182] F. Pierron, R. Cheriguene, P. Forquin, R. Moulart, M. Rossi, and M. Sutton, "Performances and Limitations of Three Ultra High-Speed Imaging Cameras for Full-Field Deformation Measurements," presented at the Advances in Experimental Mechanics VIII, (2011).

[183] H. Helmers and M. Schellenberg, "CMOS vs. CCD sensors in speckle interferometry," *Optics & Laser Technology,* vol. 35, pp. 587-595, (2003).

[184] Personal communication: T. Nicholls, Photron Europe Ltd., "Fill factor of SA1 and SA5 cameras," (2013).

[185] Personal communication: D. Hollis, LaVision UK Ltd. "LaVision Imager E-Lite 5M fill factor," (2011).

[186] "Product Manual - Imager E-Lite," LaVision UK Ltd, (2009).

[187] "Fastcam SA5 Datasheet," Photron Europe Ltd., (2013).

[188] "MotionPro X3-Plus Datasheet," Redlake Inc., (2013).

[189] B. Pan and et al., "Performance of sub-pixel registration algorithms in digital image correlation," *Measurement Science and Technology,* vol. 17, p. 1615, (2006).

[190] P. Lava. *Match ID 2D*. Available: http://www.matchid.org/

[191] S. W. Smith, *The Scientist and Engineer's Guide to Digital Signal Processing*: California Technical Pub, (1997).

[192] R. G. Lyons. (1999, 5/12/2013). *How to Interpolate in the Time-Domain by Zero-Padding in the Frequency Domain*. Available: http://www.dspguru.com/dsp/howtos/how-to-interpolate-in-time-domain-by-zero-padding-in-frequency-domain

[193] W. Wang, J. M. Dulieu-Barton, O. T. Thomsen, and R. K. Fruehmann, "Characterization of Interfacial Fracture Toughness of Sandwich Structures using High Speed Infrared Thermography," presented at the High Speed Imaging for Dynamic Testing of Materials and Structures (DYMAT), London, (2013).

[194] W. D. Pilkey and D. F. Pilkey, *Peterson's Stress Concentration Factors*, Third ed. Hoboken: John Wiley, (2008).

[195] L. Djapic Oosterkamp, A. Ivankovic, and G. Venizelos, "High strain rate properties of selected aluminium alloys," *Materials Science and Engineering: A,* vol. 278, pp. 225-235, (2000).

[196] J. J. Harrigan, J. C. F. Millett, and N. K. Bourne, "Strength of the aluminium alloy 6082-T6 under high strain-rate conditions," *AIP Conference Proceedings,* vol. 955, pp. 657-660, (2007).

[197] L. Bodelot, L. Sabatier, E. Charkaluk, and P. Dufrénoy, "Optical and infrared coupled full-field measurements at a mesoscopic scale," presented at the 9th International Conference on Quantitative InfraRed Thermography, Krakow - Poland, (2008).

[198] National Instruments PLC., "NI USB-621x User Manual," (2013).

[199] "Technical Manual - AVT GigE Vision Cameras V7.0.1," Allied Vision Technologies, (2013).

[200] "Datasheet: Oslon1 PowerStar Whites, ILH-ON01-XXXX-SC201-XX Series," Intelligent LED Solutions.

[201] "Datasheet: Tina-Pin-OSL lenses for Osram Oslon SSL LEDs," Ledil Oy.

Appendices

Appendix A

List of Publications

- **Evaluation of Edge Cracks in Cross-Ply Laminates Using Image Correlation and Thermoelastic Stress Analysis,**
  G. P Battams, J. M. Dulieu-Barton, S. W. Boyd,
  Applied Mechanics and Materials ***24-25****, Advances in Experimental Mechanics VII*, Liverpool, 2010,
  doi:10.4028/www.scientific.net/AMM.24-25.91

- **Methodology Development for High Strain Rate Damage in Laminated Composite Materials,**
  G. P Battams, J. M. Dulieu-Barton, S. W. Boyd,
  15th European Conference on Composite Materials, Venice, 2012,

- **Combining Optical Techniques to Assess the Damage Tolerance of Composite Materials,**
  G. P Battams, J. M. Dulieu-Barton, S. W. Boyd,
  9th International Conference on Advances in Experimental Mechanics, Cardiff, 2013,

- **Systematic Errors in the Use of High Speed Cameras for Digital Image Correlation,**
  G. P Battams, D. A. Crump, S. W. Boyd, J. M. Dulieu-Barton,
  High Speed Imaging for Dynamic Testing of Materials and Structures, London, 2013

Appendix B: Technical Drawings

Slack Adaptor: Overview

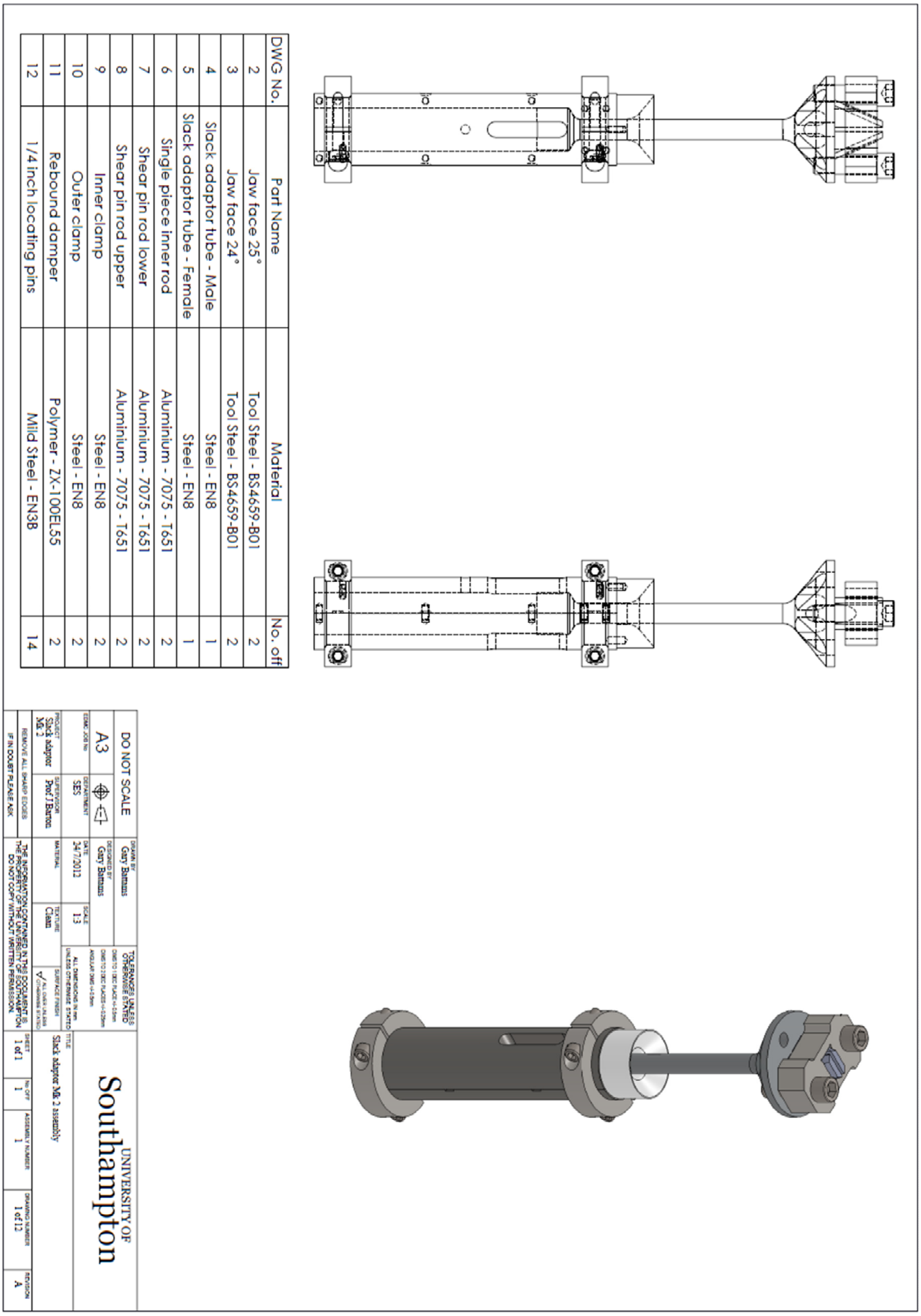

DWG No.	Part Name	Material	No. off
2	Jaw face 25°	Tool Steel - BS4659-B01	2
3	Jaw face 24°	Tool Steel - BS4659-B01	2
4	Slack adaptor tube - Male	Steel - EN8	1
5	Slack adaptor tube - Female	Steel - EN8	1
6	Single piece inner rod	Aluminium - 7075 - T651	2
7	Shear pin rod lower	Aluminium - 7075 - T651	2
8	Shear pin rod upper	Aluminium - 7075 - T651	2
9	Inner clamp	Steel - EN8	2
10	Outer clamp	Steel - EN8	2
11	Rebound damper	Polymer - ZX-100EL55	2
12	1/4 inch locating pins	Mild Steel - EN3B	14

Slack Adaptor Tube (Male)

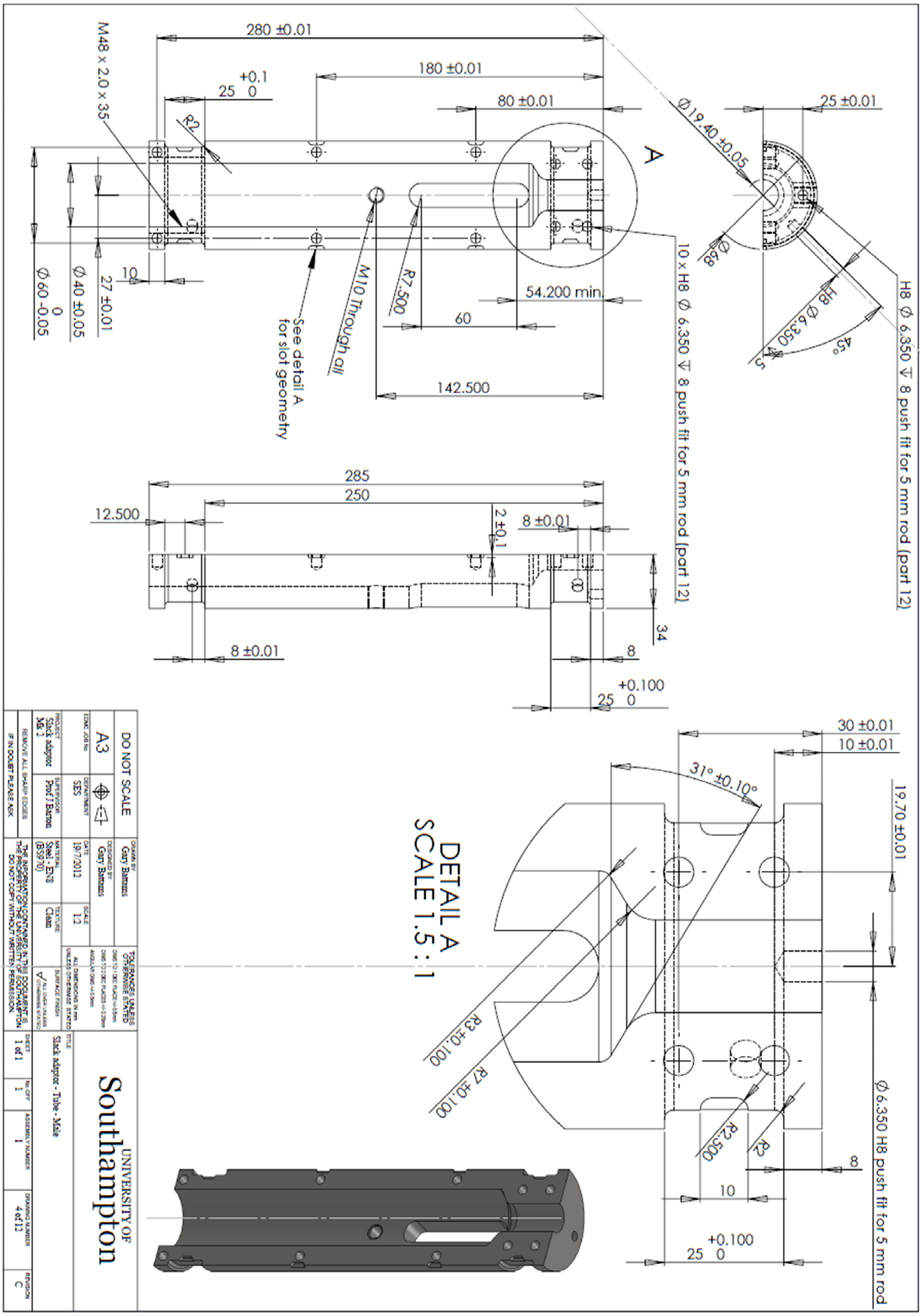

Slack Adaptor Tube (Female)

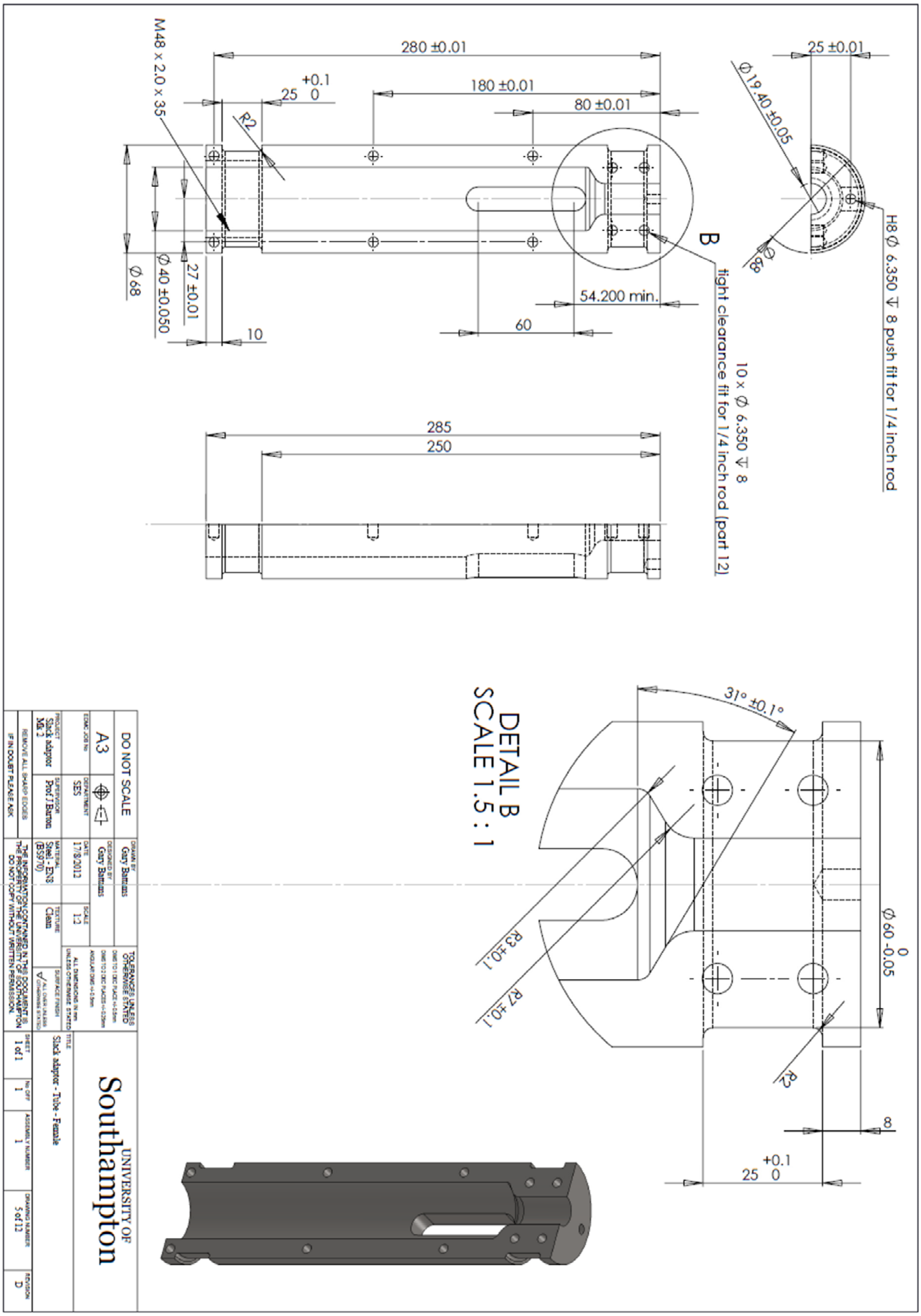

Single-Piece Inner Rod

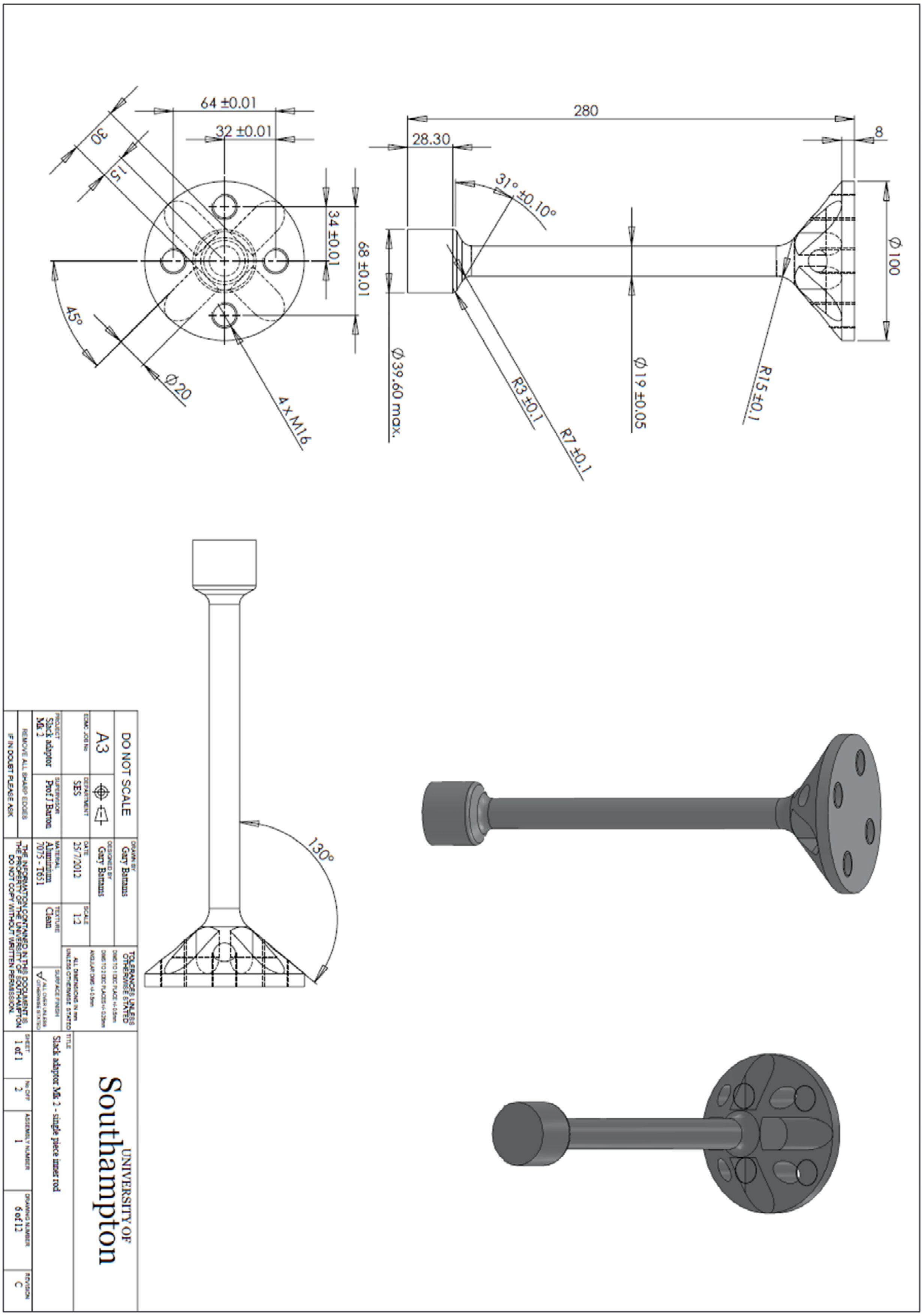

Shear Pin Rod (Lower)

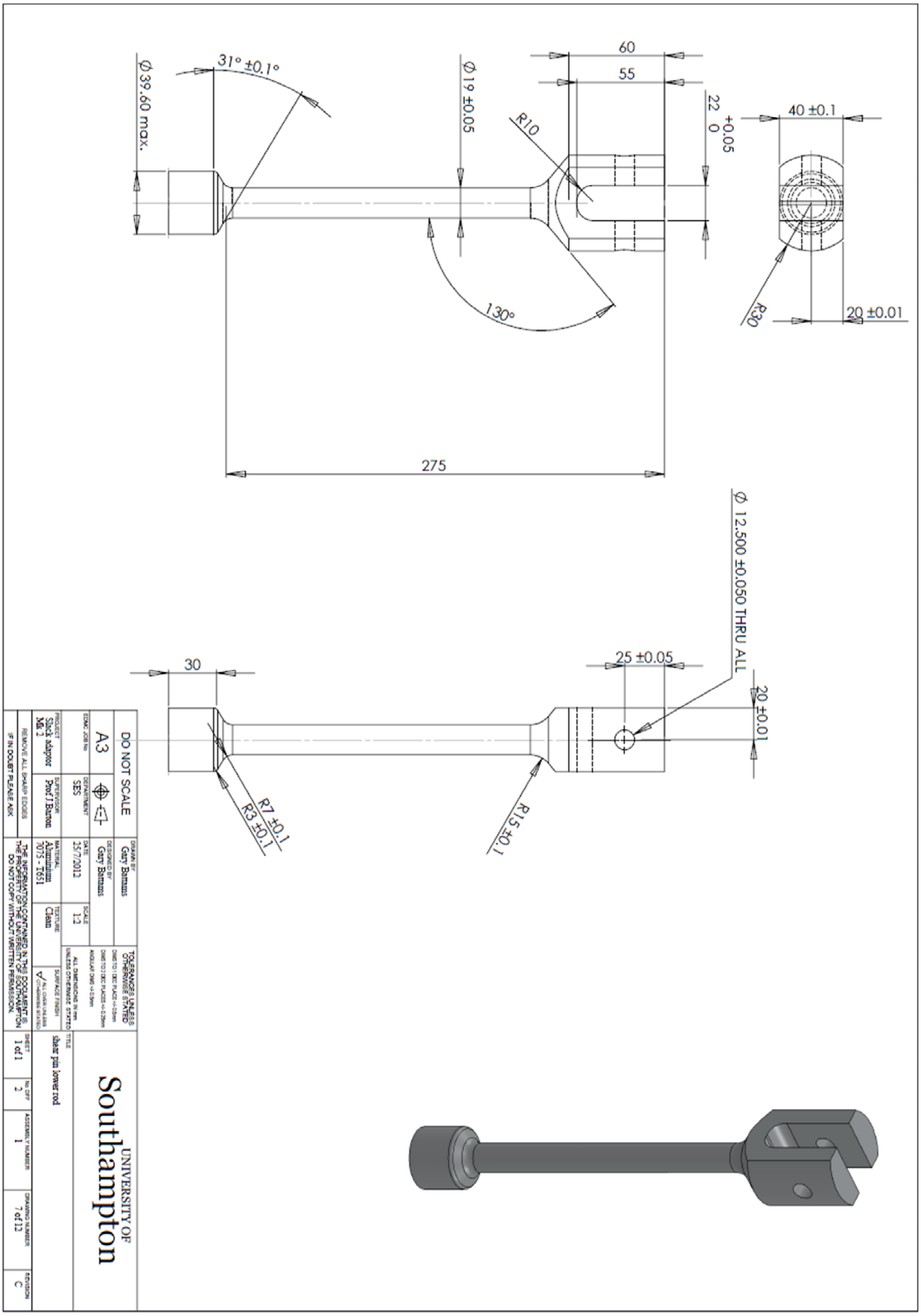

Shear Pin Rod (Upper)

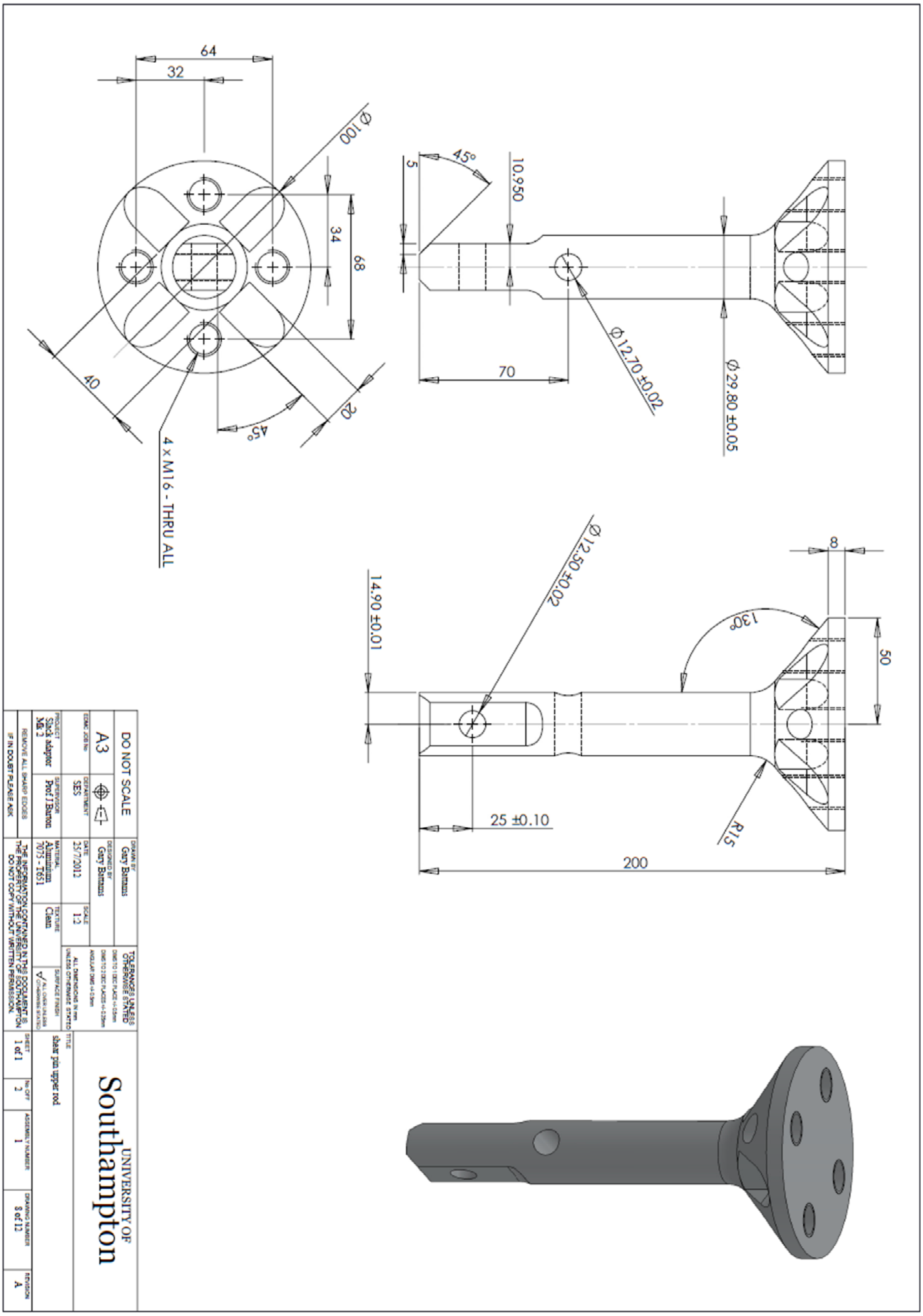

Clamp Inner

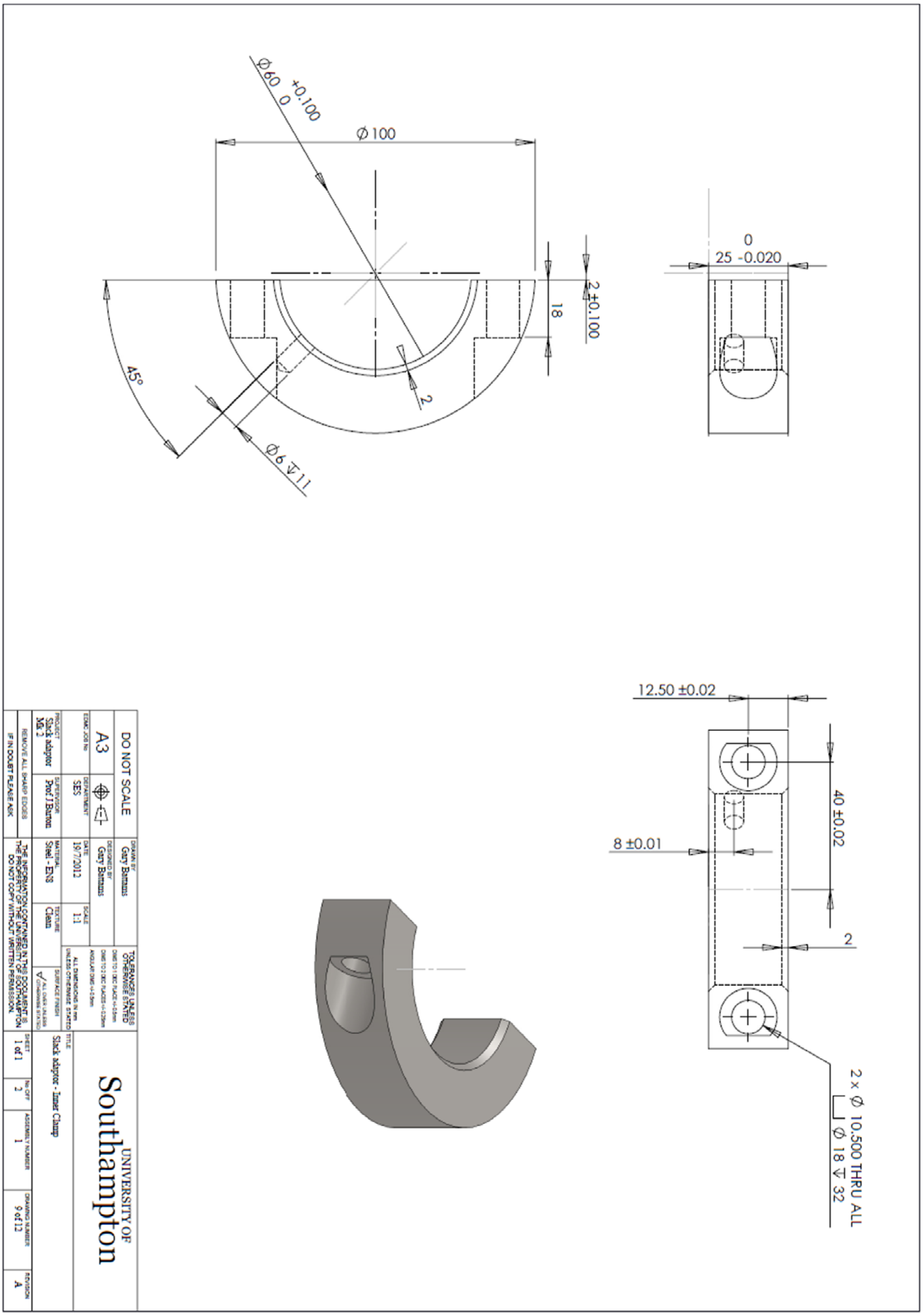

Ø60 +0.100 0
Ø100
2 ±0.100
18
45°
2
Ø6 ⊽ 11
0
25 -0.020
12.50 ±0.02
40 ±0.02
8 ±0.01
2
2 × Ø 10.500 THRU ALL
⌴ Ø 18 ⊽ 32
DO NOT SCALE
A3
EDMC JOB No
DEPARTMENT
SES
PROJECT
Slack adaptor Mk 2
SUPERVISOR
Prof J Barton
REMOVE ALL SHARP EDGES
IF IN DOUBT PLEASE ASK
DRAWN BY
Gary Bannans
DESIGNED BY
Gary Bannans
DATE
19/7/2012
SCALE
1:1
MATERIAL
Steel - EN8
TEXTURE
Clean
TOLERANCES UNLESS OTHERWISE STATED
ALL DIMENSIONS IN mm UNLESS OTHERWISE STATED
SURFACE FINISH
THE INFORMATION CONTAINED IN THIS DOCUMENT IS THE PROPERTY OF THE UNIVERSITY OF SOUTHAMPTON DO NOT COPY WITHOUT WRITTEN PERMISSION.
UNIVERSITY OF
Southampton
TITLE
Slack adaptor - Inner Clamp
SHEET
1 of 1
No OFF
2
ASSEMBLY NUMBER
1
DRAWING NUMBER
9 of 12
REVISION
A

Clamp Outer

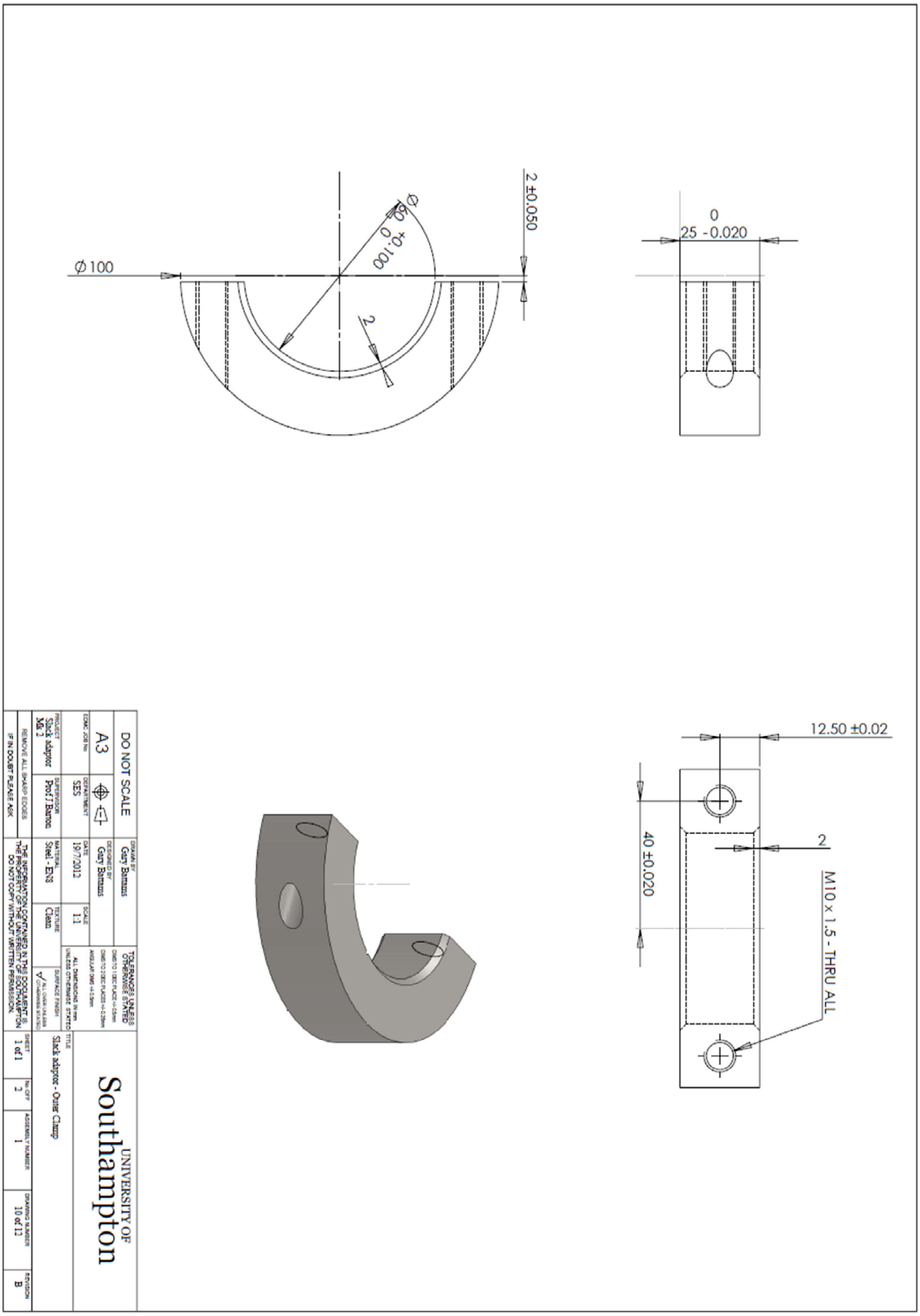
⌀100
⌀60 +0.100 0
2 ±0.050
2
25 0 -0.020
12.50 ±0.02
40 ±0.020
2
M10 x 1.5 - THRU ALL
DO NOT SCALE
A3
EDMC JOB No
PROJECT Slack adaptor Mk 2
DEPARTMENT SES
SUPERVISOR Prof J Barton
REMOVE ALL SHARP EDGES
IF IN DOUBT PLEASE ASK
DRAWN BY Gary Batmans
DESIGNED BY Gary Batmans
DATE 19/7/2012
SCALE 1:1
MATERIAL Steel - EN8
TEXTURE Clean
TOLERANCES UNLESS OTHERWISE STATED
DIMS TO 1 DEC PLACE +/-0.5mm
DIMS TO 2 DEC PLACES +/-0.25mm
ANGULAR DIMS +/-0.5mm
ALL DIMENSIONS IN mm UNLESS OTHERWISE STATED
SURFACE FINISH
ALL OVER UNLESS OTHERWISE STATED
THE INFORMATION CONTAINED IN THIS DOCUMENT IS THE PROPERTY OF THE UNIVERSITY OF SOUTHAMPTON DO NOT COPY WITHOUT WRITTEN PERMISSION.
UNIVERSITY OF Southampton
TITLE Slack adaptor - Outer Clamp
SHEET 1 of 1
No OFF 2
ASSEMBLY NUMBER 1
DRAWING NUMBER 10 of 12
REVISION B

Rebound Damper

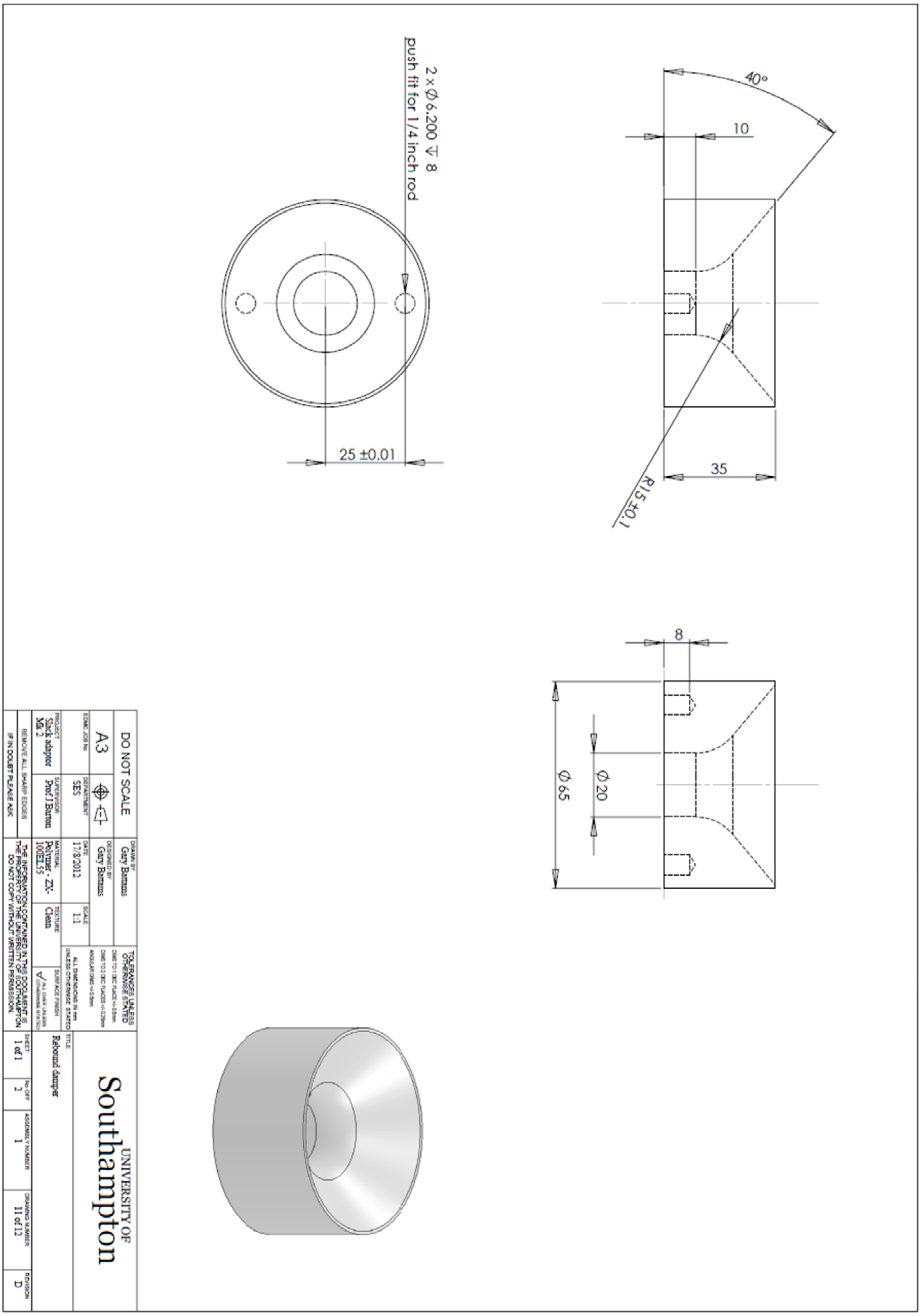

Alignment Pin

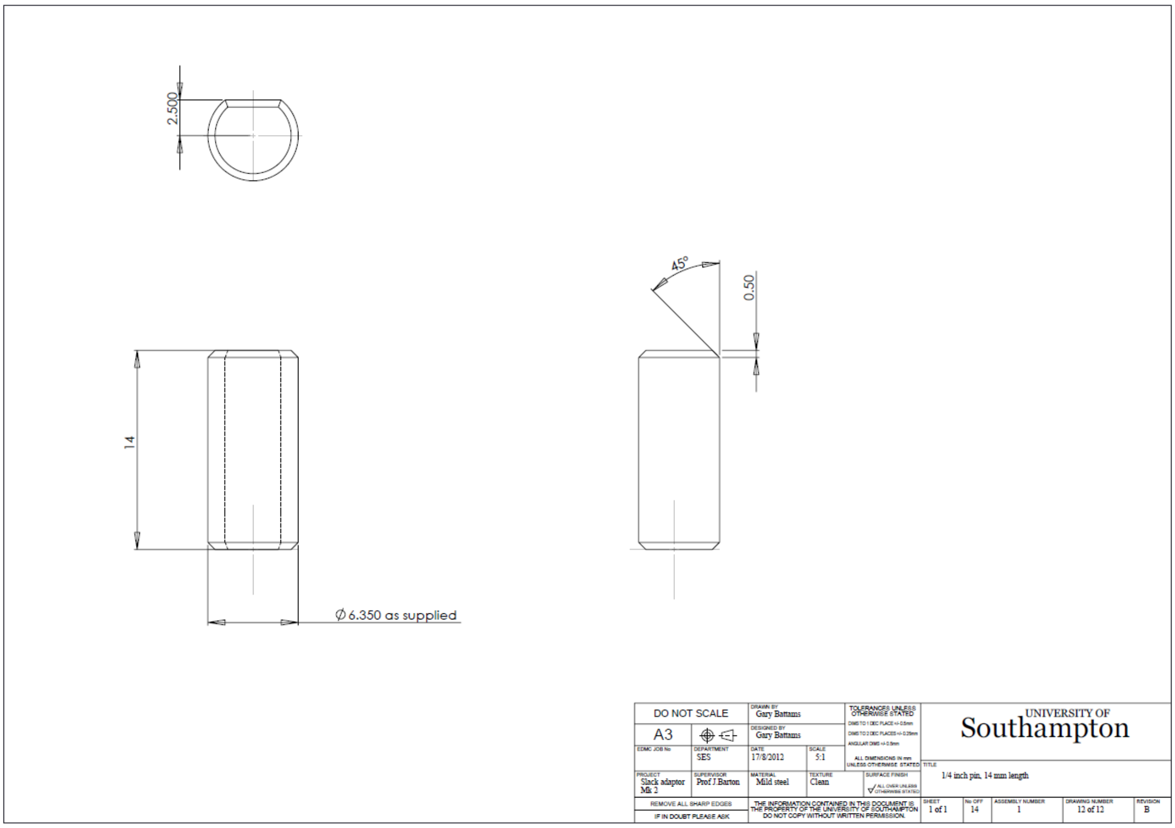

DO NOT SCALE
A3
DRAWN BY Gary Battams
DESIGNED BY Gary Battams
TOLERANCES UNLESS OTHERWISE STATED
DIMS TO 1 DEC PLACE +/- 0.5mm
DIMS TO 2 DEC PLACES +/- 0.25mm
ANGULAR DIMS +/- 0.5mm
ALL DIMENSIONS IN mm UNLESS OTHERWISE STATED
UNIVERSITY OF Southampton
EDMC JOB No
DEPARTMENT SES
DATE 17/8/2012
SCALE 5:1
TITLE 1/4 inch pin, 14 mm length
PROJECT Slack adaptor Mk 2
SUPERVISOR Prof J.Barton
MATERIAL Mild steel
TEXTURE Clean
SURFACE FINISH ✓ ALL OVER UNLESS OTHERWISE STATED
REMOVE ALL SHARP EDGES
IF IN DOUBT PLEASE ASK
THE INFORMATION CONTAINED IN THIS DOCUMENT IS THE PROPERTY OF THE UNIVERSITY OF SOUTHAMPTON DO NOT COPY WITHOUT WRITTEN PERMISSION.
SHEET 1 of 1
No OFF 14
ASSEMBLY NUMBER 1
DRAWING NUMBER 12 of 12
REVISION B

Anti-Compression Rig: Overview

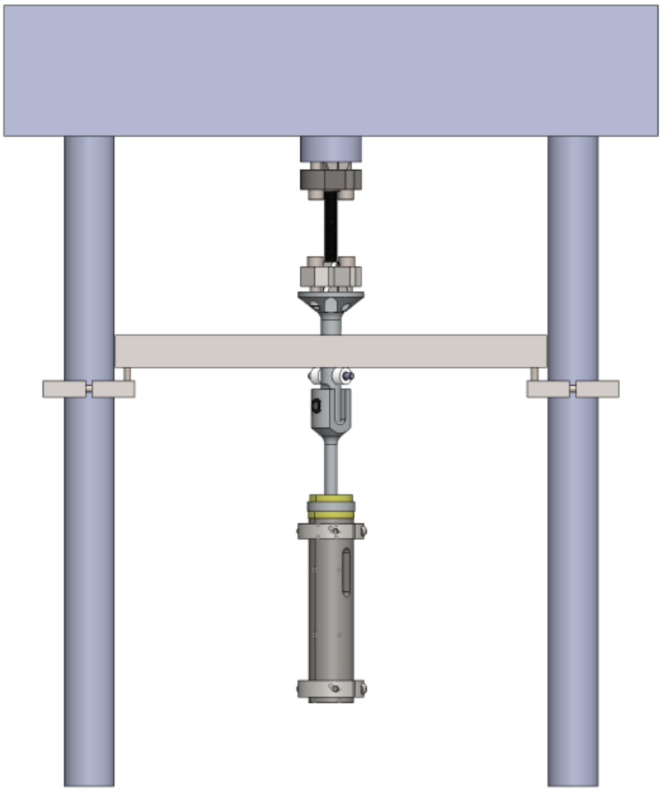

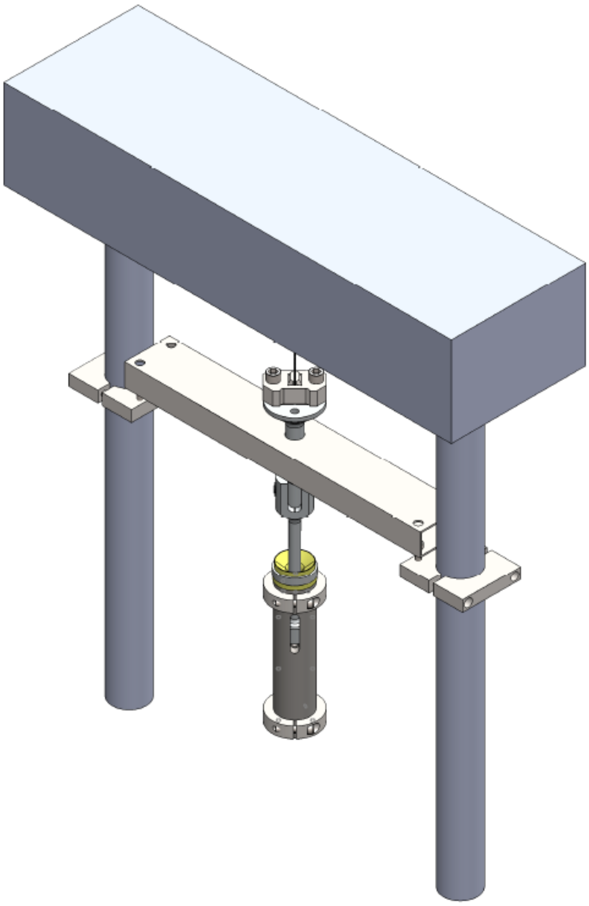

Crossbar

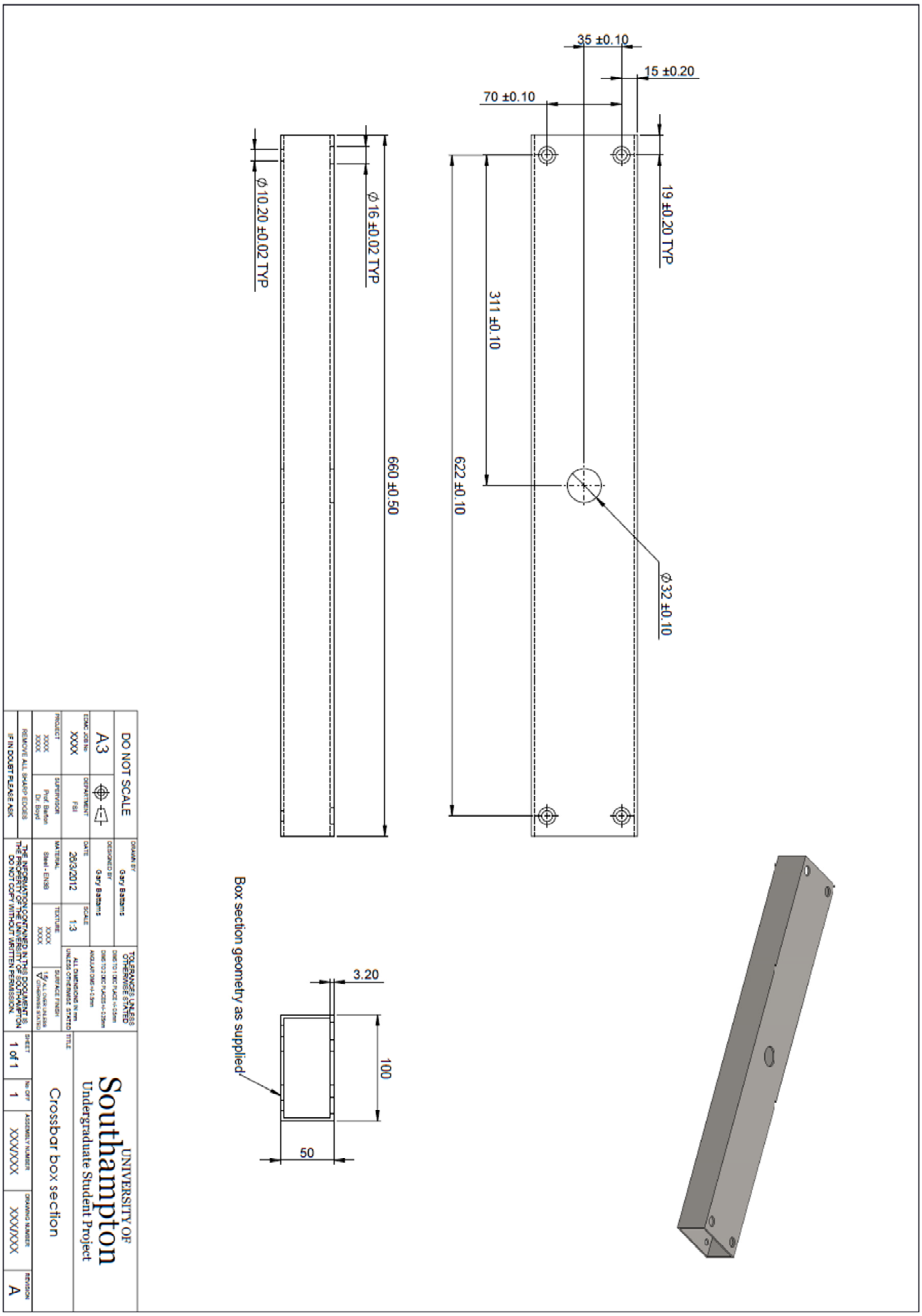
35 ±0.10
15 ±0.20
70 ±0.10
19 ±0.20 TYP
Ø 10.20 ±0.02 TYP
Ø 16 ±0.02 TYP
311 ±0.10
660 ±0.50
622 ±0.10
Ø 32 ±0.10
3.20
100
50
Box section geometry as supplied
DO NOT SCALE
A3
EDMC JOB No
XXXX
DEPARTMENT
FSI
PROJECT
XXXX
XXXX
SUPERVISOR
Prof. Barton
Dr. Boyd
REMOVE ALL SHARP EDGES
IF IN DOUBT PLEASE ASK
DRAWN BY
Gary Battams
DESIGNED BY
Gary Battams
DATE
26/3/2012
SCALE
1:3
MATERIAL
Steel - EN3B
TEXTURE
XXXX
XXXX
TOLERANCES UNLESS OTHERWISE STATED
DIMS TO 1 DEC PLACE +/- 0.5mm
DIMS TO 2 DEC PLACES +/- 0.25mm
ANGULAR DIMS +/- 0.5 deg
ALL DIMENSIONS IN mm UNLESS OTHERWISE STATED
SURFACE FINISH
ALL OVER UNLESS OTHERWISE STATED
THE INFORMATION CONTAINED IN THIS DOCUMENT IS THE PROPERTY OF THE UNIVERSITY OF SOUTHAMPTON DO NOT COPY WITHOUT WRITTEN PERMISSION.
UNIVERSITY OF
Southampton
Undergraduate Student Project
TITLE
Crossbar box section
SHEET
1 of 1
No OFF
1
ASSEMBLY NUMBER
XXX/XXX
DRAWING NUMBER
XXX/XXX
REVISION
A

Inner Grip

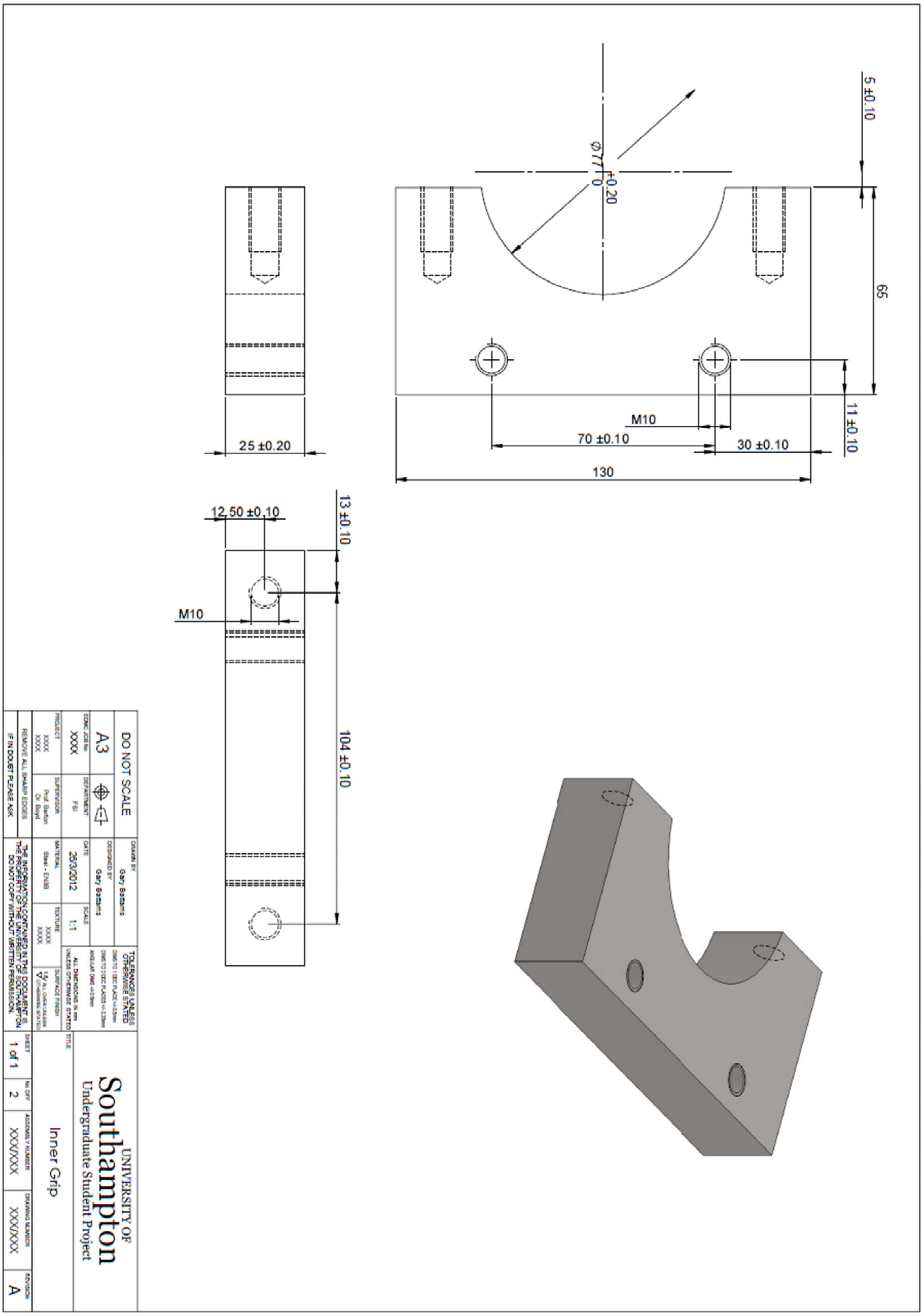
Ø77 +0.20 0
5 ±0.10
65
11 ±0.10
M10
70 ±0.10
30 ±0.10
130
25 ±0.20
12.50 ±0.10
13 ±0.10
M10
104 ±0.10
DO NOT SCALE
A3
EDMC JOB No
XXXX
DEPARTMENT
FSI
PROJECT
XXXX
XXXX
SUPERVISOR
Prof. Barton
Dr. Boyd
REMOVE ALL SHARP EDGES
IF IN DOUBT PLEASE ASK
DRAWN BY
Gary Bastams
DESIGNED BY
Gary Bastams
DATE
28/3/2012
SCALE
1:1
MATERIAL
Steel - EN8B
TEXTURE
XXXX
XXXX
TOLERANCES UNLESS OTHERWISE STATED
ALL DIMENSIONS IN mm UNLESS OTHERWISE STATED
SURFACE FINISH
THE INFORMATION CONTAINED IN THIS DOCUMENT IS THE PROPERTY OF THE UNIVERSITY OF SOUTHAMPTON DO NOT COPY WITHOUT WRITTEN PERMISSION.
UNIVERSITY OF
Southampton
Undergraduate Student Project
TITLE
Inner Grip
SHEET
1 of 1
No OFF
2
ASSEMBLY NUMBER
XXX/XXX
DRAWING NUMBER
XXX/XXX
REVISION
A

Outer Grip

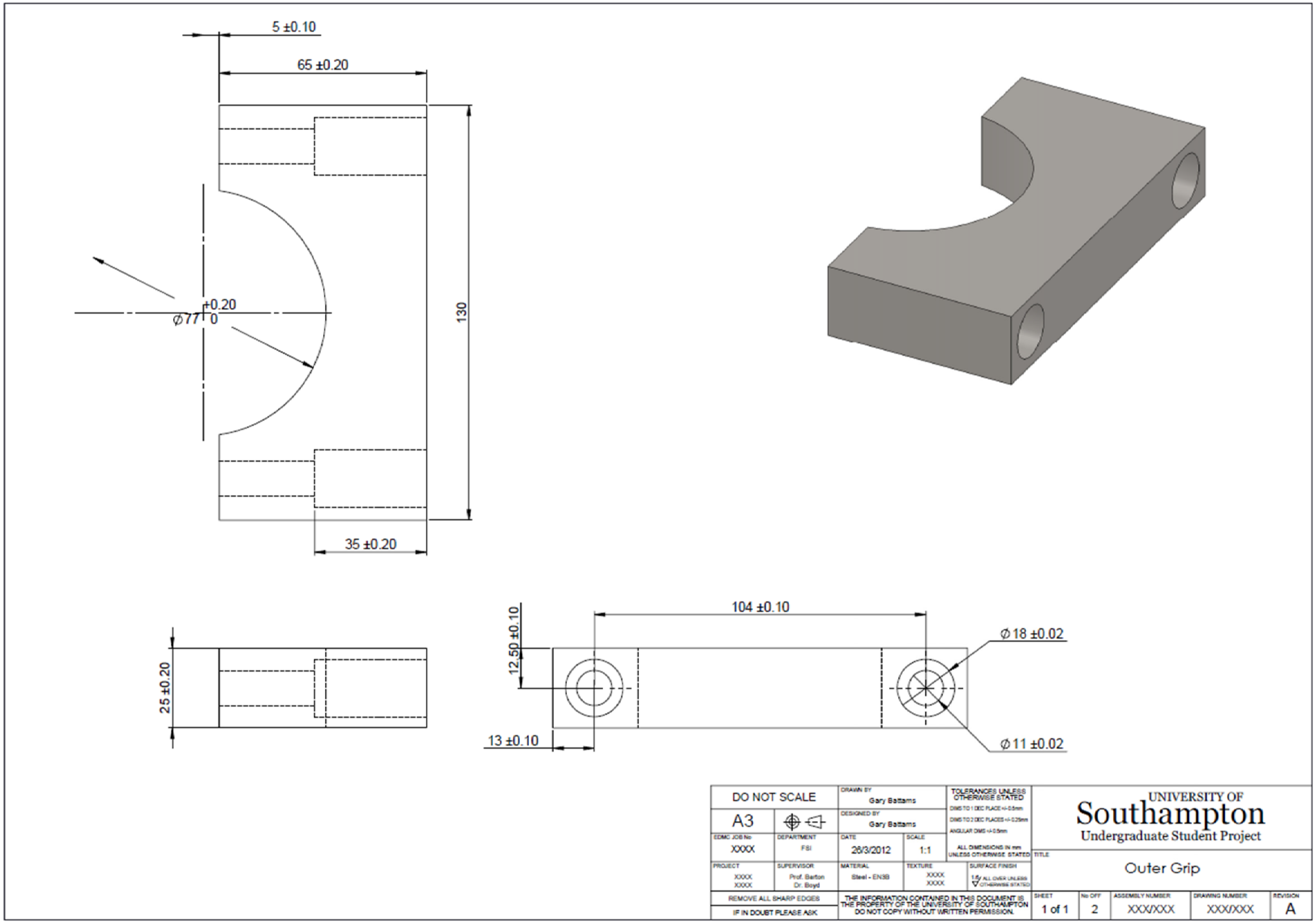
5 ±0.10
65 ±0.20
Ø77 +0.20 0
130
35 ±0.20
25 ±0.20
12.50 ±0.10
104 ±0.10
Ø18 ±0.02
13 ±0.10
Ø11 ±0.02
DO NOT SCALE
A3
EDMC JOB No
XXXX
DEPARTMENT
FSI
PROJECT
XXXX
XXXX
SUPERVISOR
Prof. Barton
Dr. Boyd
DRAWN BY
Gary Battams
DESIGNED BY
Gary Battams
DATE
26/3/2012
SCALE
1:1
MATERIAL
Steel - EN3B
TEXTURE
XXXX
XXXX
TOLERANCES UNLESS OTHERWISE STATED
DIMS TO 1 DEC PLACE +/-0.5mm
DIMS TO 2 DEC PLACES +/-0.25mm
ANGULAR DIMS +/-0.5mm
ALL DIMENSIONS IN mm UNLESS OTHERWISE STATED
SURFACE FINISH
1.6 ALL OVER UNLESS OTHERWISE STATED
REMOVE ALL SHARP EDGES
IF IN DOUBT PLEASE ASK
THE INFORMATION CONTAINED IN THIS DOCUMENT IS THE PROPERTY OF THE UNIVERSITY OF SOUTHAMPTON DO NOT COPY WITHOUT WRITTEN PERMISSION.
UNIVERSITY OF
Southampton
Undergraduate Student Project
TITLE
Outer Grip
SHEET
1 of 1
No OFF
2
ASSEMBLY NUMBER
XXX/XXX
DRAWING NUMBER
XXX/XXX
REVISION
A

Damper

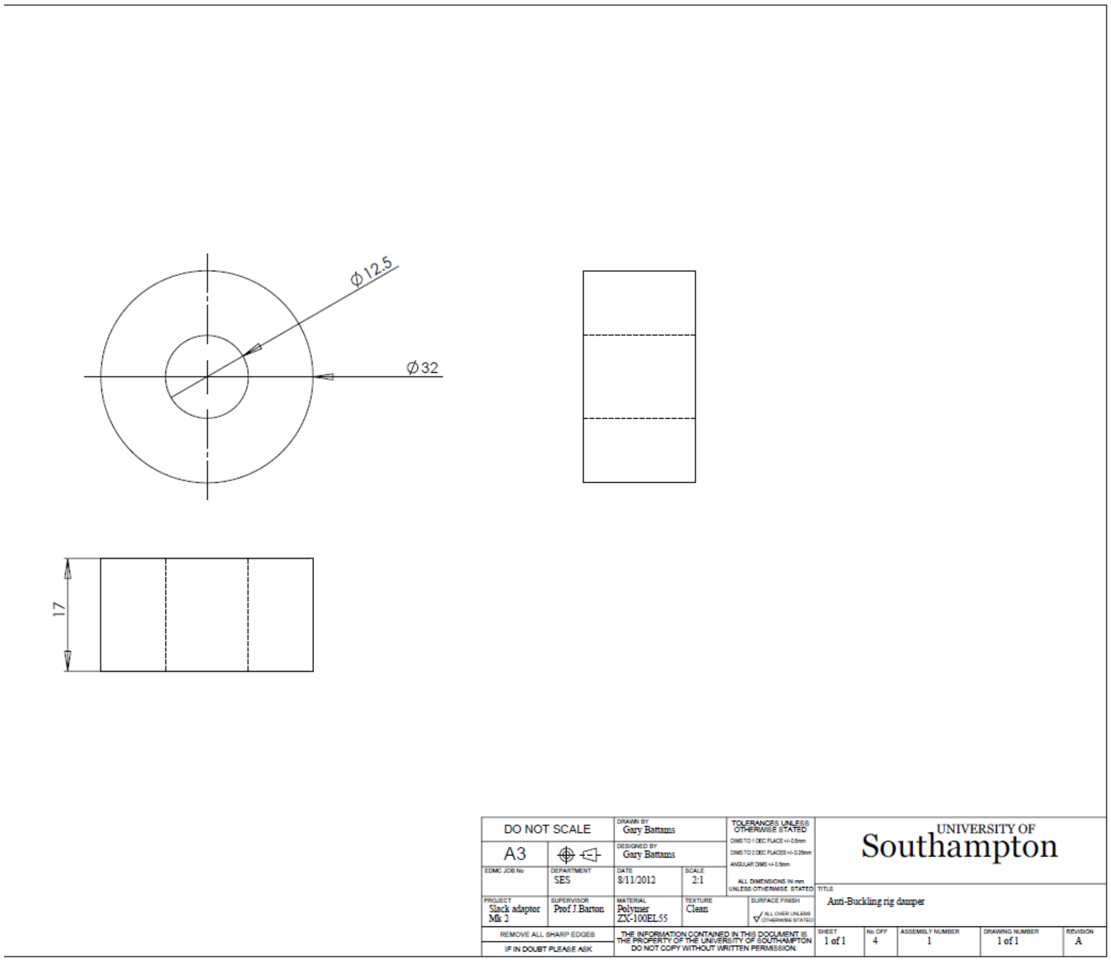

Ø12.5
Ø32
17
DO NOT SCALE
A3
DRAWN BY
Gary Battams
DESIGNED BY
Gary Battams
TOLERANCES UNLESS OTHERWISE STATED
DIMS TO 1 DEC PLACE +/- 0.5mm
DIMS TO 2 DEC PLACES +/- 0.25mm
ANGULAR DIMS +/- 0.5mm
ALL DIMENSIONS IN mm UNLESS OTHERWISE STATED
UNIVERSITY OF Southampton
EDMC JOB No
DEPARTMENT
SES
DATE
8/11/2012
SCALE
2:1
TITLE
Anti-Buckling rig damper
PROJECT
Slack adaptor Mk 2
SUPERVISOR
Prof J.Barton
MATERIAL
Polymer ZX-100EL55
TEXTURE
Clean
SURFACE FINISH
ALL OVER UNLESS OTHERWISE STATED
REMOVE ALL SHARP EDGES
IF IN DOUBT PLEASE ASK
THE INFORMATION CONTAINED IN THIS DOCUMENT IS THE PROPERTY OF THE UNIVERSITY OF SOUTHAMPTON DO NOT COPY WITHOUT WRITTEN PERMISSION.
SHEET
1 of 1
No OFF
4
ASSEMBLY NUMBER
1
DRAWING NUMBER
1 of 1
REVISION
A

Appendix C

LED Light Unit Design

Two lighting units were developed during the thesis. The first, lower powered unit consists of a set of 4 LED modules and the second larger unit uses a set of 8 identical LED modules. The smaller unit consist of a single column of LED modules mounted on an aluminium base, whilst the larger unit consists of a column of 2 x 4 LED modules on an aluminium base. Modules are located in columns to better suit the aspect ratio of the specimens tested. Polycarbonate lenses are situated on each module to focus the light into a narrow beam.

LED module:

Intelligent LED Solutions:
ILH-ON01-ULWH-SC201
Cool white
(6000K to 6500K colour temperature).

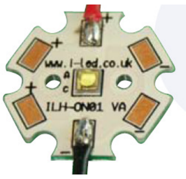

[200]

Lens:

Tina-Pin-OSL Real Spot:
FWHM Angle of 4.5 degrees.

[201]

Luminous flux output is estimated to ~250 lumens per LED module, equating to 1000 and 2000 lumens for the two LED lighting units.

As the LED units are to be used with high speed cameras, it is required that the LED modules are not controlled using the normal method of digital current pulsing. Such control results in pulses of light at a similar frequency to that used by the high speed cameras. The modules were therefore wired in series and powered directly using a DC mains power source or appropriate voltage and power. Finally, the aluminium base is cooled through use of a passive Fischer Elektronik Heatsink SK89 100 mm IGBT.

Appendix D

Analysis of Heat Conduction in Crossply CFRP

Given that an area of 1 IR pixel in the top surface ply remains at a temperature 0.2°C hotter than the surrounding material, the following analysis calculates an estimate of the expected temperature drop due to conduction to the surrounding material over a period of 3.2 seconds. This is the estimated time for the crack to propagate by 1 pixel within Area 2 in Figure 69. This is carried out to determine if conduction effects are significant enough over this time period to keep the temperature below the 0.2 °C threshold.

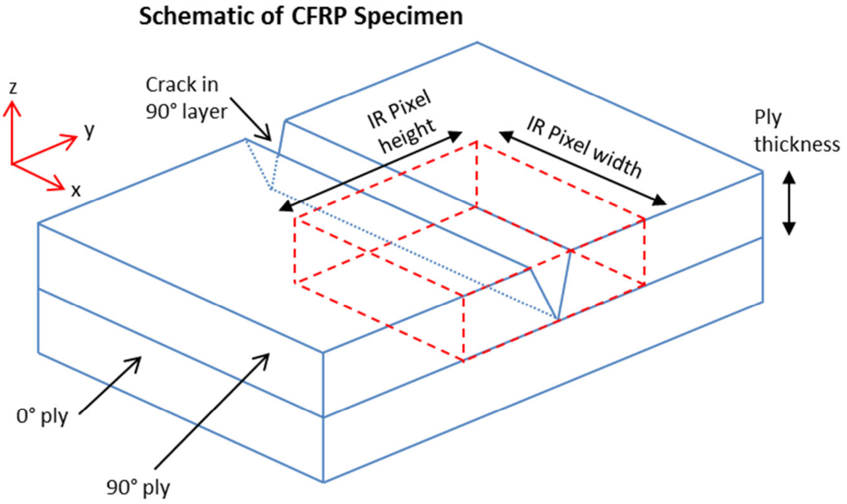

Fourier's heat conduction law in one dimension:

$$\dot{Q} = \frac{\Delta Q}{\Delta t} = -kA\frac{\Delta T}{\Delta x}$$

$$\Delta Q = -kA\frac{\Delta T}{\Delta x}\Delta t$$

where $\dot{Q}$ is the rate of heat conduction, Q is heat, Δt is time interval, k is thermal conductivity of the material, A is the surface area normal to the flow of heat, ΔT is the temperature difference between two points at Δx distance apart.

For information purposes:

$$\alpha = \frac{k}{C_p\rho}$$

where α is the thermal diffusivity, ρ is the material density and C_p is the specific heat capacity.

Due to the orthotropic properties of the FRP material, the thermal conductivity is not constant in all directions. Tian [116] found the following properties for unidirectional CFRP:

Table 5. 3 Thermal conductivity of carbon-fiber/epoxy composite from literature

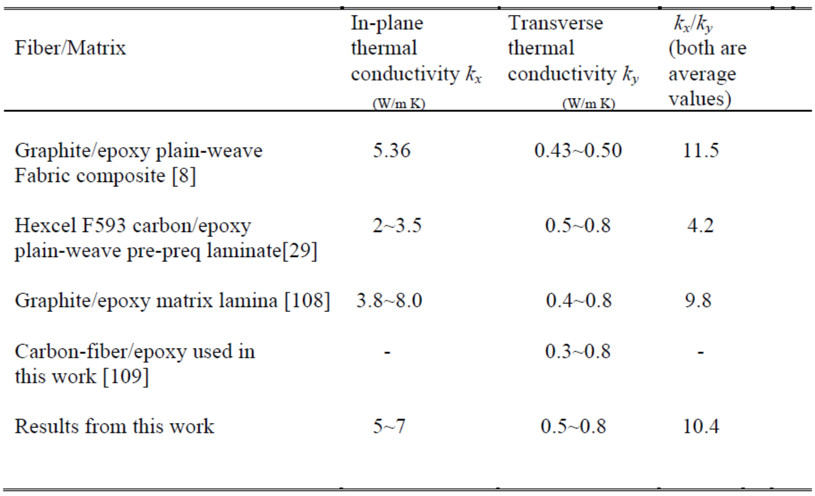

Fiber/Matrix	In-plane thermal conductivity k_x (W/m K)	Transverse thermal conductivity k_y (W/m K)	k_x/k_y (both are average values)
Graphite/epoxy plain-weave Fabric composite [8]	5.36	0.43~0.50	11.5
Hexcel F593 carbon/epoxy plain-weave pre-preq laminate[29]	2~3.5	0.5~0.8	4.2
Graphite/epoxy matrix lamina [108]	3.8~8.0	0.4~0.8	9.8
Carbon-fiber/epoxy used in this work [109]	-	0.3~0.8	-
Results from this work	5~7	0.5~0.8	10.4

Based on his work, a thermal conductivity of 6 W/mK will be used along the *x*, fibre direction and 0.65 W/mk transverse to the fibres in both the *y* and *z* directions.

In the *x* direction, *A* is equal to the pixel height (0.386 mm) multiplied by the ply thickness (0.281 mm), giving $A = 1.085 \text{ x } 10^{-7}$ m^2. It is assumed that the entire volume shown in red in the above schematic is 0.2 °C hotter than the surrounding material. The heat flow to the centre of the next pixel in the *x* direction is now calculated:

$$\Delta Q_x = -kA\frac{\Delta T}{\Delta x}\Delta t$$

$$\Delta Q_x = -6 * (1.085 \text{ x } 10^{-7}) * \frac{0.2}{0.386 \text{ x } 10^{-3}} * 3.2$$

$$\Delta Q_x = -1.079 \text{ x } 10^{-3}\text{J}$$

As heat will flow from equally from the top and bottom surface, this quantity is doubled to give the total heat flow in the x-direction:

$$\text{Total } \Delta Q_x = -2.159 \text{ x } 10^{-3}\text{J}$$

This is repeated for the y-direction

$$\Delta Q_y = -kA\frac{\Delta T}{\Delta x}\Delta t$$

$$\Delta Q_y = -0.65 * (1.085 \text{ x } 10^{-7}) * \frac{0.2}{0.386 \text{ x } 10^{-3}} * 3.2$$

$$\Delta Q_y = -1.170 \text{ x } 10^{-4}\text{J}$$

$$\text{Total } \Delta Q_y = -2.339 \text{ x } 10^{-4}\text{J}$$

And again for the through thickness *z*-direction, where the area now becomes the pixel width multiplied by the pixel height to give 1.490x10^{-7} m^2.

$$\Delta Q_z = -kA\frac{\Delta T}{\Delta x}\Delta t$$

$$\Delta Q_z = -0.65 * (1.49 \text{ x } 10^{-7}) * \frac{0.2}{0.386 \text{ x } 10^{-3}} * 3.2$$

$$\Delta Q_z = -1.606 \text{ x } 10^{-4}\text{J}$$

$$\text{Total } \Delta Q_z = -3.212 \text{ x } 10^{-4}\text{J}$$

The total change in heat within the volume is therefore:

$$\text{Total } \Delta Q_x + \text{ Total } \Delta Q_y + \text{ Total } \Delta Q_z = -2.714 \text{ x } 10^{-3}\text{J}$$

Using the following relationship for specific heat:

$$\Delta Q = \rho V c_p \Delta T$$

$$\Delta T = \frac{\Delta Q}{\rho V C_p}$$

where ρ is the material density, C_p is the specific heat capacity and ΔT is the change in temperature.

Using the density of epoxy (1.2 g/cm^3), the density of raw carbon fibres (1.772 g/cm^3) an estimate for the CFRP density material based on fibre volume fraction (75%) is 1628 kg/m^3. Using a similar analysis based on the C_p of epoxy (0.64 J/gK) and the C_p of carbon fibre (0.80 J/gK) gives a total C_p of 760 J/kgK. Volume = pixel height x pixel width x ply height (4.187 x 10^{-11} m^3)

$$\Delta T = \frac{-2.714 \text{ x } 10^{-3}}{1628 * 4.187 \text{ x } 10^{-11} * 760}$$

$$\Delta T = -52 \text{ °C}$$

A significant temperature drop would therefore be experienced by the material due to conduction effects. In reality, the temperature within the volume would continuously decrease due to conduction effects, so the total heat transfer would be considerably lower.

Using the same analysis, when a crack forms instantaneously across one pixel within one IR frame period (0.001 seconds), the temperature drop due to conduction was found to be:

$$\Delta T = -1.93\text{x}10^{-3} \text{ °C}$$

This is extremely small and shows why the cracks that occur near-instantaneously within area 1 and area 2 in Figure 69 remain above the threshold value for longer than 1 frame period.